Solution Processed Nanocarbon-Based Materials for Use in Photovoltaic Systems

Thesis submitted to the School of Chemical and Physical Sciences,

Faculty of Science and Engineering, Flinders University

In fulfilment of the requirements for the degree of

Doctor of Philosophy

June 2016

Lachlan J. Larsen

Supervisors: Joe Shapter and Amanda Ellis

The truth is, of course, that there is no journey. We are arriving and departing all at the same time.

- David Bowie

Table of Contents

Summary

The application of solution processed nanocarbon-based materials in a number of photovoltaic systems was investigated and the performance of these systems optimised. These systems included the use of solution processed single-walled carbon nanotubes (SWNTs) in the working electrodes of photoelectrochemical solar cells, along with surfactant-assisted exfoliated graphene and reduced graphene oxide (RGO) in solid state nanocarbon-based material-silicon solar cells.

Vertically aligned arrays of SWNTs were chemically attached to fluorinated tin oxide (FTO) substrates. These arrays were subsequently sensitised by the addition of a layer of 7,14-bis[2-[tris(1-methylethyl)silyl]ethynyl]dibenzo[*b,def*]chrysene (TIPS-DBC), a polycyclic aromatic hydrocarbon used in organic photovoltaics. These new TIPS-DBC/SWNT/FTO electrodes were then used as the working electrodes in dye-sensitised solar cell- (DSC) like photoelectrochemical cells. Addition of the TIPS-DBC to the working electrodes significantly enhanced the photovoltaic performance of the cells, due to the photoresponse of the TIPS-DBC. The response of the cells was then tuned by controlling the concentration of TIPS-DBC solution used to deposit the TIPS-DBC layer, as well as by controlling the spin speed used during deposition. Following this procedure, the maximum power conversion efficiency (PCE) was found for these cells, outperforming previously reported DSCs using vertically aligned arrays of SWNTs as the main photoactive material.

Aqueous dispersions of the non-ionic surfactant Tween-60 were found to be capable of producing surfactant-assisted exfoliated graphene dispersions containing few layer graphene. These dispersions were then vacuum filtered to make conductive films with highly reproducible optical transparencies and sheet resistances. By controlling the volume of dispersion filtered, the optical transparency of the films could be controlled, and two thickness regimes could be formed. In the thin regime, films were found to be non-continuous, leaving areas of exposed substrate, while in the thick regime continuous films with thicknesses on the order of hundreds of nanometres were formed. Both thin and thick films were then used to form graphene-silicon (G-Si) Schottky junction solar cells, which were found to be highly durable. The effect of graphene film thickness on the photovoltaic performance of G-Si Schottky junction solar cells was then investigated, along with the effects of thermal annealing of the graphene films. Chemical doping with the common dopants nitric acid and gold chloride was also investigated, with both found to have beneficial effects on cell PCE.

Aqueous dispersions of graphene oxide (GO) were vacuum filtered to produce thin GO films. These films were then deposited onto silicon substrates and annealed at a range of temperatures under forming gas, to produce RGO-Si Schottky junction solar cells. The effect of annealing temperature on cell performance was investigated, along with previously unseen beneficial aging effects observed at higher temperatures. The effects of RGO film thickness were then investigated using the optimal annealing temperature. The effects of chemical doping using both thionyl chloride and gold chloride were investigated both at different annealing temperatures and different RGO film thicknesses and these effects were compared with those of chemical doping on G-Si Schottky junction solar cells. The effect of using different sources of GO for the RGO film production was also investigated.

Declaration

I certify that this thesis does not incorporate without acknowledgment any material previously submitted for a degree or diploma in any university; and that to the best of my knowledge and belief it does not contain any material previously published or written by another person except where due reference is made in the text.

Lachlan J. Larsen

Acknowledgements

I would like to firstly acknowledge my supervisor Joe Shapter and co-supervisor Amanda Ellis, as without them this Thesis would not have been possible. Joe originally took me on as an Honours student and allowed me to choose my research topic from a number of choices he had available. This early freedom was afforded to me throughout my whole Honours year as well as throughout my Ph.D. candidature. Amanda, too, was also happy for me to explore the areas that interested me throughout my studies. Both Joe and Amanda have been supportive throughout, and have helped me develop not only research skills but a raft of other life skills, not the least of which are presentation and communication skills of which I am extremely grateful for. Another opportunity afforded to me under the supervision of Joe and Amanda was to be a co-author of a book chapter on the wet chemical fabrication of graphene and graphene oxide and its spectroscopic characterisation, with the section of this chapter that I was responsible for, the wet-chemical exfoliation of graphene, being included within the introduction of this Thesis.

As a student of Joe's I have worked in the Smart Surface Structures group at Flinders University since my Honours year. Here, again, I have been lucky to have a great group to spend so much time with. This has included other academics such as Jamie and Chris, along with numerous post-graduate students such as Adam, Mark, Anders, Daniel Tune and Cameron Shearer. All of these people have always been happy to offer advice, talk about science, or have a chat about anything but science when a change was needed. I would also like to further acknowledge Dan Tune and Cameron Shearer, who were co-authors on the journal articles which contributed to the work within this Thesis. Dan helped me perform the EQE analysis seen in Chapter 3, while Cameron performed the AFM seen in Chapters 4 and 5.

I have also had a great support network throughout my time at Flinders. I was lucky enough to spend time at the International Center for Materials Nanoarchitectonics (MANA) in Japan during my Ph.D. under the supervision of Tomo Nakayama. Closer to home, Leigh, Gos, Caitlyn, Karen and Krysta have all been there to share the good times and vent during the bad times, with many a conversation spent with Leigh debating the weekends AFL results and the prospects of my beloved Tigers. Special thanks should also go to Kathy Brady, who not only employed me towards the

end of my candidature but was able to help give me encouragement and advice along the way in that seemingly long period of “almost there”.

Finally, I would like to thank my parents Mark and Melissa. They have helped me out wherever they could throughout my many long years of study, despite it no doubt seeming like my quest for knowledge may never end. Despite this, they have always been happy to help, without which I would never have made it to where I am today. For this, I am forever grateful.

List of Figures

List of Tables

List of Abbreviations

0D – zero dimensional

1D – one dimensional

2D – two dimensional

3D – three dimensional

Φ_{bn} – Schottky barrier

Φ_{G} – work function of graphene

Φ_{Si} – work function of silicon

$\mathbf{\Omega}$ - frequency of phonon

α – absorption coefficient

ω_{L} – frequency of incoming photon

ω_{Sc} – frequency of scattered photon

χ_{Si} – electron affinity of graphene

%T – percent transmittance

AFM – atomic force microscopy

AM – air mass

AM0 – extra-terrestrial spectral irradiance

AM1.0 – spectral irradiance at surface of the Earth when the Sun is directly overhead

AM1.5G – global solar irradiance spectrum with the Sun at an angle of 42°

BOE – buffered oxide etch

$\mathbf{C_h}$ – chiral vector

CE – counter electrode

CNT – carbon nanotube

CNT-Si – carbon nanotube-silicon

COP21/CMP11 – 21st Conference of the Parties to the United Nations Framework Convention on Climate Change

CRG – chemically reduced graphene

CVD – chemical vapour deposition

DBC – dibenzo[*b,def*]chrysene

DCC – dicyclohexylcarbodiimide

DGU – density gradient ultracentrifugation

DMF – N,N-dimethylformamide

DMSO – dimethylsulphoxide

DSC – dye-sensitised solar cell
DWNT – double-walled carbon nanotubes
E_C – conduction band energy of silicon
E_F – Fermi level
E_g – bandgap of silicon
E_V – valence band energy of silicon
eGaIn – eutectic gallium indium
e-h – electron hole pair
EQE – external quantum efficiency
FF – fill factor
FLG – few layer graphene
FTO – fluorinated tin oxide
GO – graphene oxide
G-Si – graphene-silicon
HF – hydrofluoric acid
HI – hydroiodic acid
HNO_3 – nitric acid
HOMO – highest occupied molecular orbital
HOPG – highly ordered pyrolytic graphite
IEA – International Energy Agency
ITO – indium tin oxide
J_{MP} – current density at maximum power point
J_{SC} – short circuit current density
J-V – current density-voltage
LUMO – lowest unoccupied molecular orbital
MCE – mixed cellulose ester
MIS – metal insulator semiconductor
MoO_x – molybdenum oxide
MPII – 1-methyl-3-propylimidazolium iodide
MPN – 3-methoxypropionitrile
MTOE – million tonnes of oil equivalent
MWNT – multi-walled carbon nanotubes
Nd:YAG – neodymium-doped yttrium aluminium garnet
NMP – N-methylpyrrolidone

n-Si – n-type silicon

P3HT – poly(3-hexylthiophene-2,5-diyl)

PAMAM – poly(amidoamine)

PCBM – [6,6]-phenyl-C_{61}-butyric acid methyl ester

PCE – power conversion efficiency

PEDOT:PSS – poly(3,4-ethylenedioxythiophene) polystyrene sulfonate

PEO – polyethylene oxide

PET – polyethylene terephthalate

RBM – radial breathing mode

RGO – reduced graphene oxide

RGO-Si – reduced graphene oxide-silicon

SDBS – sodium dodecylbenzene sulfonate

SLG – single layer graphene

SWNT – single-walled carbon nanotubes

TCO – transparent conducting electrode

TEM – transmission electron microscopy

TFSA – bis(trifluoromethanesulfonyl)amide[($(CF_3SO_2)_2NH$)]

TIPS-DBC – 7,14-bis[2-[tris(1-methylethyl)silyl]ethynyl]dibenzo[*b,def*]chrysene

UHV – ultra-high vacuum

V_{bi} – in-built potential

V_{bias} – forward potential

V_{MP} – voltage at maximum power point

V_{OC} – open circuit voltage

XPS – x-ray photoelectron spectroscopy

List of Publications

[1] Yu, Y, Bandaru, NM, Larsen, LJ, Shapter, JG & Ellis, AV 2016, 'Wet chemical fabrication of graphene and graphene oxide and spectroscopic characterization', in M Aliofkhazraei, N Ali, WI Milne, CS Ozkan, S Mitura & JL Gervasoni (eds) *Graphene science handbook fabrication methods*, CRC Press, Boca Raton, Florida, pp. 319 – 334.

[2] Larsen, LJ, Tune, DD, Kemppinen, P, Winzenberg, KN, Watkins, SE & Shapter, JG 2012, 'Increased performance of single walled carbon nanotube photovoltaic cells through the addition of dibenzo[b,def]chrysene derivative', *Journal of Photochemistry and Photobiology A: Chemistry*, vol. 235, pp. 72-6.

[3] Larsen, LJ, Shearer, CJ, Ellis, AV & Shapter, JG 2015, 'Solution processed graphene-silicon Schottky junction solar cells', *RSC Advances*, vol. 5, no. 49, pp. 38851-8.

[4] Larsen, LJ, Shearer, CJ, Ellis, AV & Shapter, JG 2016, 'Optimization and doping of reduced graphene oxide–silicon solar cells', *The Journal of Physical Chemistry C*, vol. 120, no. 29, pp. 15648-56.

Parts of the above publications have been reproduced in this Thesis as follows:

- Chapter 1 contains material from [1]
- Chapter 2 contains material from [3] and [4]
- Chapter 3 contains material from [2]
- Chapter 4 contains material from [3]
- Chapter 5 contains material from [4]

Chapter 1

Introduction

Background information relative to this Thesis is given with focus upon three nanocarbon-based materials, specifically carbon nanotubes, graphene and graphene oxide. The structure, properties, production methods and application of these nanocarbon-based materials is discussed. Furthermore, background information on photovoltaics and the implementation of nanocarbon-based materials in this field is discussed.

This chapter contains material previously published in:

Yu, Y, Bandaru, NM, Larsen, LJ, Shapter, JG & Ellis, AV 2016, 'Wet chemical fabrication of graphene and graphene oxide and spectroscopic characterization', in M Aliofkhazraei, N Ali, WI Milne, CS Ozkan, S Mitura & JL Gervasoni (eds) *Graphene science handbook: Fabrication methods*, CRC Press, Boca Raton, Florida, pp. 319 – 334.

1.1 Overview

The world's total energy consumption has doubled over the past four decades, from 4,667 million tonnes of oil equivalent (MTOE) in 1973 to 9,301 MTOE in 2013 [1]. Over this same time frame, the percentage of energy consumed as electricity has risen from 9.4 % to 18.0 % [1]. The International Energy Agency (IEA), projects electricity demand will further rise by more than 70 % by 2040 [2], driven in part by the push for universal access to energy and connecting the 1.2 billion people worldwide still without electricity by 2030 [3].

Given that coal, natural gas and oil still make up two thirds of the world's electricity generation and their role in CO_2 emissions, one may be forgiven for feelings of misgivings about these projections. However, there is growing recognition and commitment from governments around the world, recently highlighted by the adoption in 2015 of the Paris Agreement at the 21st Conference of the Parties to the United Nations Framework Convention on Climate Change (COP21/CMP11), that commits governments to develop policies to keep global temperatures "well below 2 ºC above pre-industrial levels and pursue efforts to limit the temperature increase to 1.5 ºC" and for global CO_2 emissions to peak "as soon as possible" [4].

Encouragingly, according to the IEA, renewable sources of electricity had the fastest rate of expansion in 2014, contributing to nearly 45 % of net additions [5]. These renewable sources include hydroelectricity, biofuels, geothermal, wind, heat and solar photovoltaics [2]. Of these options, solar photovoltaics is a particularly promising area, due to the fact that there are no associated hazardous waste products (nuclear fission), encroachment of arable land (biofuels) or a large reliance on geographical locations (hydroelectricity, wind) [6]. With solar photovoltaics projected to have the second largest growth of renewable sources (behind onshore wind) [5], investigating new photovoltaic systems continues to be a highly relevant research priority.

Keen scientific research into photovoltaic devices was generated by the first report in 1954 of a silicon p-n junction solar cell showing power conversion efficiencies of 6 % [7]. Since this time, a large variety of photovoltaic devices have been investigated, including but not limited to, thin film solar cells [8, 9], organic photovoltaics [10, 11] and dye-sensitised solar cells [12, 13]. Research to this day continues to explore a number of avenues towards producing cheap and efficient solar cells for integration into the world's electricity generation network, with photovoltaic systems containing nanocarbons in some aspect of their design becoming increasingly popular over the past decade.

Graphene, itself a nanocarbon, is one of the most fundamental allotropes of carbon, consisting of a single two dimensional (2D) sheet of hexagonally packed sp^2 hybridised carbon atoms. A number of other nanocarbons, shown in Figure 1.1, can be obtained using, or considering, graphene as a building block, including zero dimensional (0D) buckminsterfullerenes, such as C_{60} [14], and one dimensional (1D) carbon nanotubes (CNTs) [15, 16]. Along with these nanocarbons, graphene also serves as the building block of the three dimensional (3D) graphite, with large numbers of graphene sheets AB stacking upon one another to form bulk graphite. A variety of graphene production methods use bulk graphite as a precursor and it can also be chemically modified to produce graphene oxide (GO) [17, 18], a further form of nanocarbon-based material.

These nanoscopic forms of carbon hold a special appeal in that their nanoscopic dimensions lend them a number of remarkable physical and chemical properties, such as high conductivities and tensile strength. For example, the direction in which a graphene sheet can be considered to have been "rolled up" in the formation of a CNT can change the physical properties of the resultant tube from exhibiting semiconductor or metallic behaviour [19]. It is hoped that these properties, combined with the abundance of carbon as a raw material, and in some cases, energy efficient production methods, may lead to cheaper, more efficient solar photovoltaics which also have energy efficient production processes. As energy efficiency is forecast to play a key role in limiting global CO_2 emissions while growing the global economy and moving towards universal energy access, efficient production processes are very worthy of consideration.

This thesis presents work investigating several different types of nanocarbon-based materials, viz. CNTs, graphene, and graphene oxide in several photovoltaic systems. In each of the applications, attention is paid to the potential and ability for scale-up and the low energy cost of the production methods, i.e., solution processing in atmospheric conditions. Each system was optimised according to a number of parameters arising from the production methods and the implications for further research are considered.

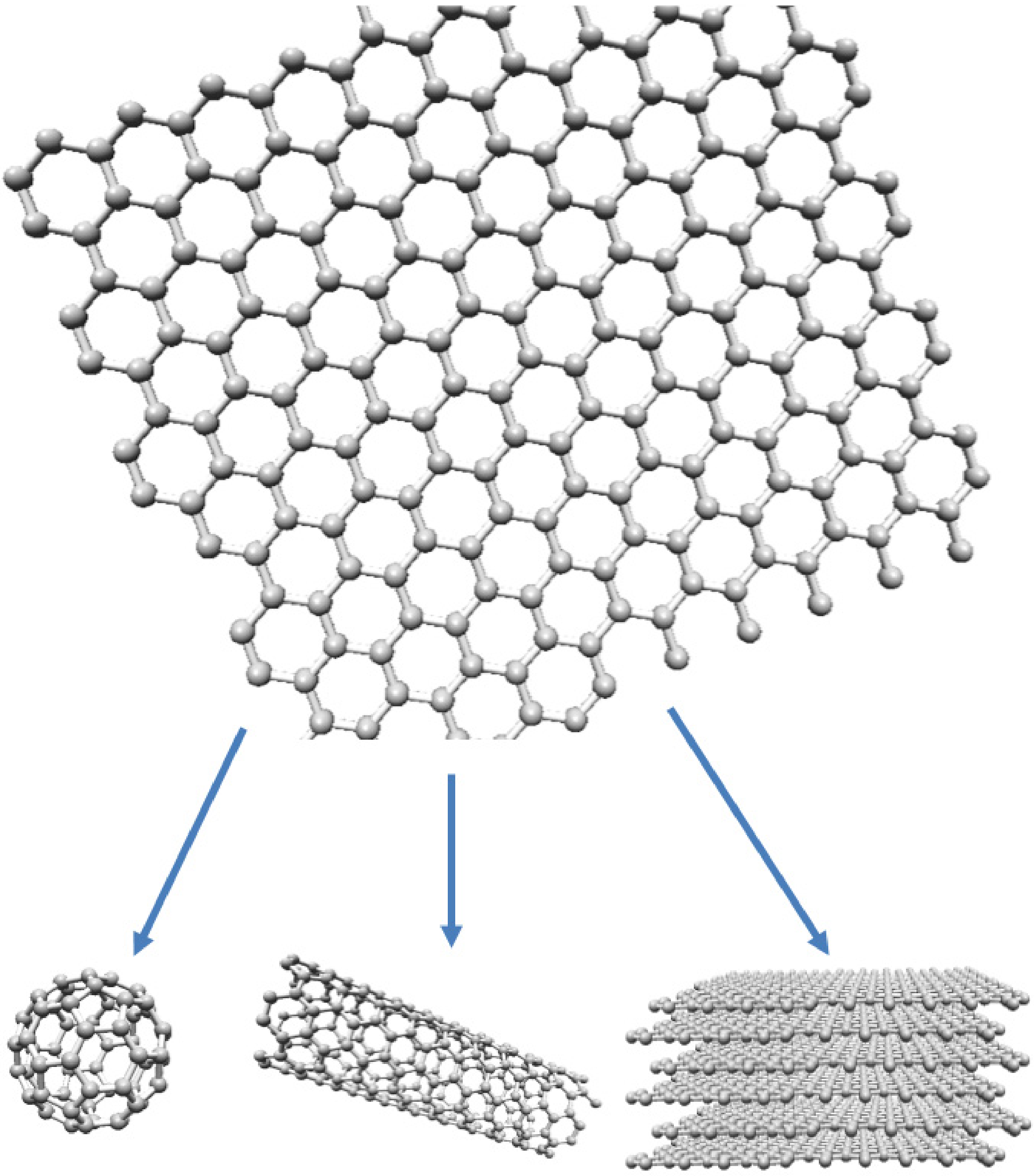

Figure 1.1: Two dimensional graphene as a building block for further nanocarbons, e.g., zero dimensional C_{60} (left) and 1 dimensional carbon nanotubes (middle), as well as three dimensional graphite (right) (adapted from [20]).

1.2 Carbon Nanotubes

1.2.1 History and Overview

Images of hollow carbon fibrils or filaments were published as early as 1952 [21] and these structures continued to be investigated throughout the following decades [22, 23]. It was not until 1991 however, that Iijima's [15] seminal report of "helical microtubules of graphitic carbon" prompted keen scientific interest in carbon nanotubes. In this paper, Iijima presented transmission electron microscopy (TEM) images of "microtubules of graphitic carbon" that were up to 1 µm long and consisted of between two to fifty sheets of carbon concentrically rolled around each other. Today, this is recognised as the first report of multi-walled carbon nanotubes (MWNTs). This report was closely followed by two independent papers published in Nature in 1993, by Bethune et al. [16] and Iijima and Ichihashi [24] describing CNTs with "single-atomic-layer" walls [16] and 1 nm diameters [24]; that is single-walled carbon nanotubes (SWNTs).

Figure 1.2 shows that the popularity of CNTs amongst researchers grew exponentially since these early papers by Iijima and Bethune, with almost 50,000 publications indexed by Scopus in the last five years alone (2011 – 2015). The majority of these publications are classified in the subject areas of materials science, physics and astronomy, engineering, and chemistry for reasons which will become apparent in the following sections detailing the structure and properties of CNTs and their myriad applications.

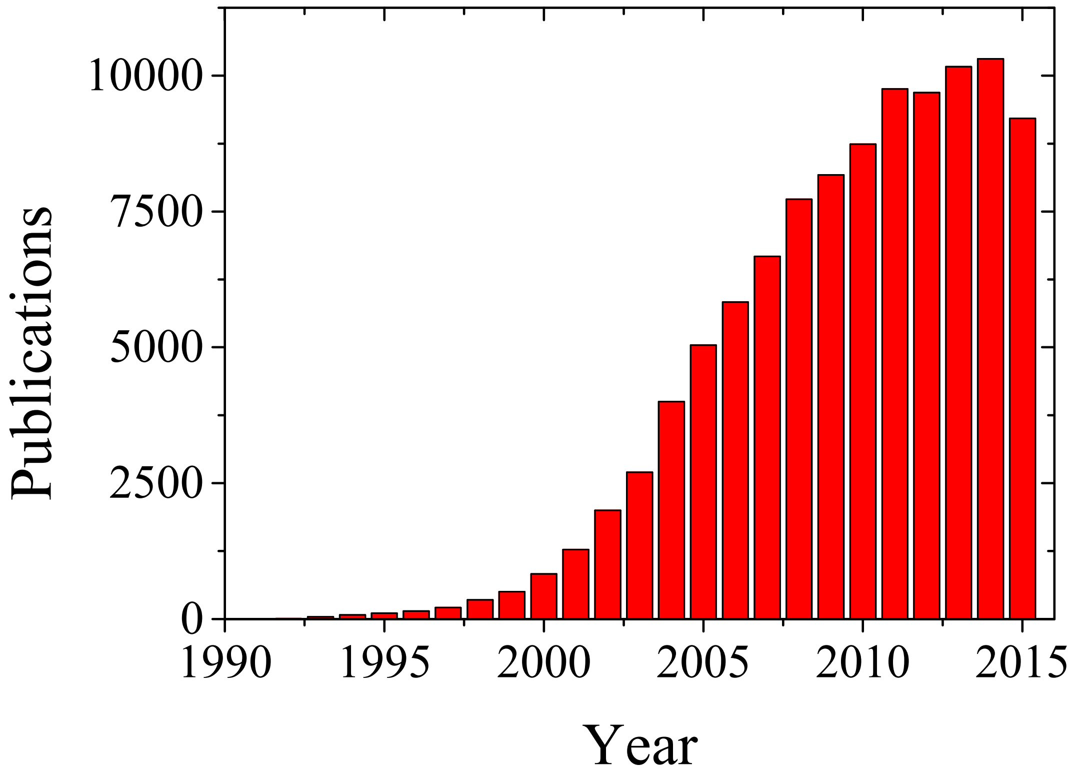

Figure 1.2: Publications per year containing carbon nanotubes in the title abstract or keywords as archived by Scopus up to and including 2015 (search query (TITLE-ABS-KEY ("carbon nanotubes")), search performed 1 February 2016.

1.2.2 Structure and Properties

As alluded to previously, and depicted in Figure 1.1, CNTs are 1D objects, which can be conceptualised as rolled up sheets of hexagonally packed sp^2 hybridised carbon atoms (graphene). If only one sheet of graphene is rolled up, the CNT is referred to as a SWNT. However, it is also possible to form tubes with two (double-walled carbon nanotubes (DWNTs)) or more walls, MWNTs. This conceptualisation of rolling up sheets of graphene is useful as it allows for the complete description of a SWNT's electronic properties, as well as its physical properties except for length, following a method depicted in Figure 1.3. A chiral vector, $\mathbf{C_h}$, can be defined along the graphene sheet, in the direction along which the sheet will be rolled to form the CNT such that:

$$\boldsymbol{C_h} = n\boldsymbol{a_1} + m\boldsymbol{a_2} = (n, m)$$

Equation 1.1

where $\boldsymbol{a_1}$ and $\boldsymbol{a_2}$ are the unit cell vectors of the carbon sheet and n and m are integers [25]. $\boldsymbol{C_h}$ can thus take on any value between two limiting cases, one where $\boldsymbol{C_h}$ is equal to $(n, 0)$, the red line in Figure 1.3, and two where $\boldsymbol{C_h}$ is equal to (n, n). The carbon atoms along the chiral vector form the circumference of the top of the CNT, with these two special cases commonly referred to as zigzag $(n, 0)$ and armchair (n, n) nanotubes, as this is the pattern the carbon atoms will form when viewed perpendicular to the nanotube long axis, $\boldsymbol{T}$. If known, $\boldsymbol{C_h}$ can thus also be used to determine the diameter of a CNT, with SWNTs having diameters on the order of 0.8 – 2 nm, and MWNTs typically between 5 – 20 nm [26].

The electronic properties of a CNT can also be elucidated by using the $\boldsymbol{C_h}$. Indeed, for any CNT with a $\boldsymbol{C_h}$ of (n, m), if

$$|n - m| = 3q$$

Equation 1.2

where q is an integer, the CNT will be "metallic", otherwise it will be semiconducting [27]. In reality, however, due to the curved nature of CNTs only armchair (n, n) nanotubes are truly metallic, with other metallic qualifying nanotubes exhibiting small chirality dependent energy gaps at low temperatures [27].

Due to their unique structure and one-dimensional nature, CNTs exhibit a number of remarkable physical properties. For example, CNTs have been found to exhibit electron mobilities of up to 1×10^5 $\mathrm{cm^2 \cdot V^{-1} \cdot s^{-1}}$ [28] and maximum current densities of $1 - 10 \times 10^9$ $\mathrm{A \cdot cm^{-2}}$ [29] while also having thermal conductivities of between 2000 - 5000 $\mathrm{W \cdot m \cdot K^{-1}}$. Furthermore, MWNTs have displayed a Young's modulus of 1 TPa and a tensile strength of 100 GPa [30]. CNTs are also known to be photoactive [31-35], which will be discussed in more detail in Section 1.6. These properties mean that CNTs have good potential for use in a myriad of applications, although due to the consequences of their production, practical CNT application has not flourished as much as had been anticipated when they were first discovered.

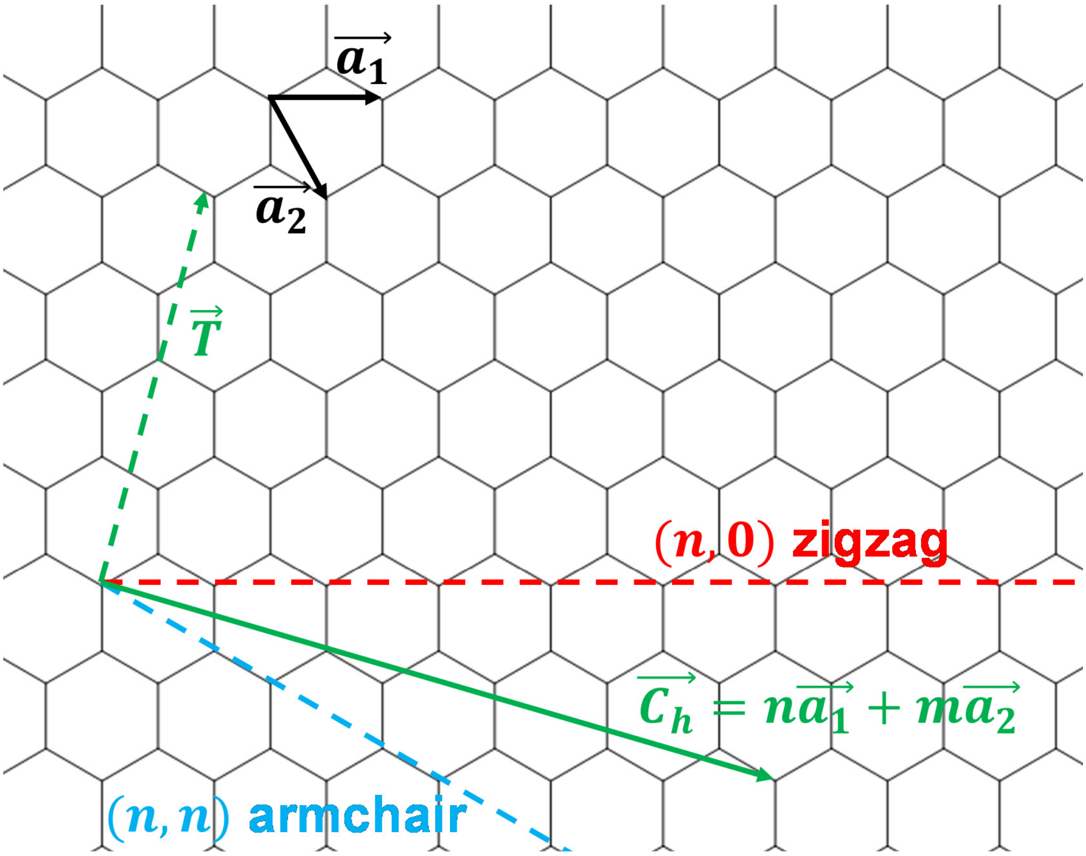

Figure 1.3: Diagram showing a graphene sheet, with a unit cell showing vectors $\mathbf{a}_1$ and $\mathbf{a}_2$ along with a chiral vector $\mathbf{C}_h$ (green), denoting the direction along which the graphene sheet is rolled to form a carbon nanotube, with the vector **T** (dashed green) showing the direction of the long axis of the nanotube. The dashed red line shows a chiral vector in the (n, 0) direction, resulting in zigzag nanotubes, while the dashed blue line shows a chiral vector in the (n, n) direction, resulting in armchair nanotubes (adapted from [25]).

1.2.3 Production Methods

There are three main methods for CNT synthesis, viz. arc discharge, laser ablation and chemical vapour deposition (CVD) [36].

The arc discharge was the method used by Iijima in both his first MWNT [15] and SWNT articles [24], as well as Bethune et al. [16]. In arc discharge synthesis, a basic schematic of which can be seen in Figure 1.4, an electrical current is passed between two electrodes inducing electrical breakdown of a gas, such as helium, thereby generating a plasma [36]. The first electrode, the anode, generally contains a powdered carbon precursor and potentially a catalyst, while the cathode is usually pure graphite [37]. Catalysts are excluded from the anode for the production of MWNTs, while transition metal catalysts such as cobalt and nickel are commonly included for SWNT synthesis [36]. The generated plasma can cause carbon sublimation from the anode, which can aggregate in the gas phase and eventually condenses on the cathode where it is collected and the produced CNTs recovered. This process can take place in either vapour or liquid phases [36] at a range of pressures (50 – 7600 Torr) [38], and generates high temperatures in the plasma in excess of 3000 ºC [38].

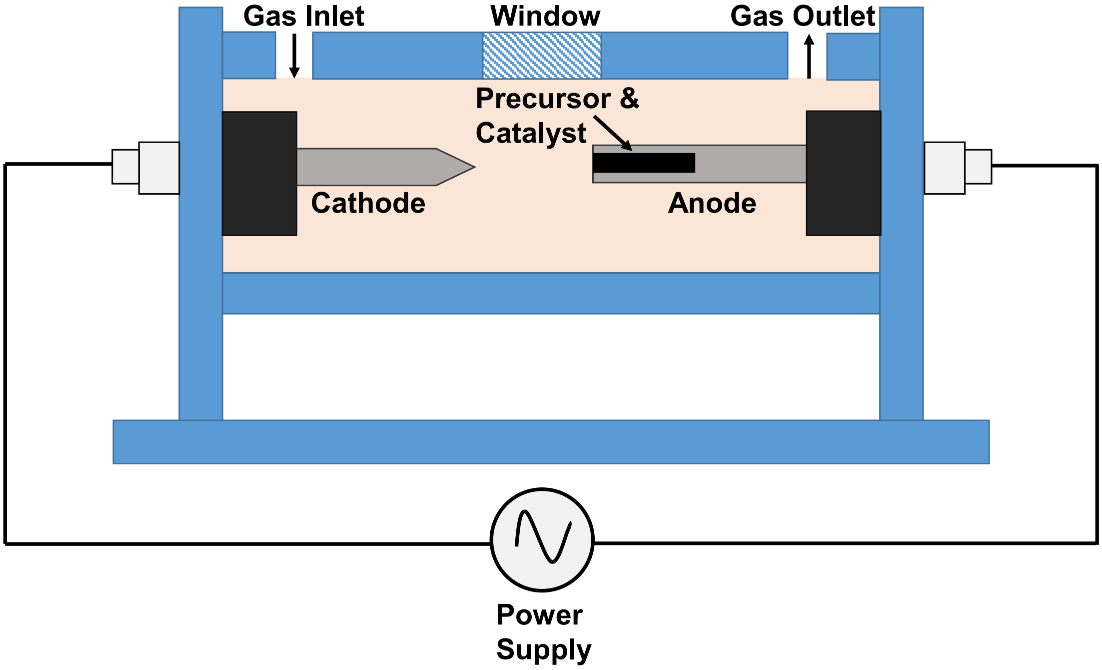

Figure 1.4: Basic schematic of an arc-discharge system used for SWNT synthesis, showing an anode, containing the precursor and catalyst, and cathode present in a gas filled chamber (adapted from [37]).

The synthesis of CNTs using laser ablation is quite similar to arc discharge and was first reported in 1995 by Guo et al. [39]. Rather than using electrical current, laser ablation uses a pulsed laser, such as a Nd:Yag or CO_2 laser, to provide the energy necessary to cause sublimation of a graphite target containing catalysts such as nickel or cobalt [36]. Like arc discharge this production method generates high temperatures in excess of 3000 ºC and is capable of producing both SWNTs and MWNTs, although unlike arc discharge the process only occurs under vacuum at low pressures (200 to 750 Torr) [38].

CVD synthesis of CNTs involves the catalytic decomposition of a hydrocarbon feedstock such as ethylene over a substrate seeded with metal catalyst particles that also act as nucleation centres for nanotube growth [36] (see Figure 1.5 for a schematic diagram). This method is highly versatile in that it can produce CNTs on a wide range of substrates from conductive surfaces such as silicon and copper to insulating surfaces such as silicon dioxide and glass [36]. As well as this potential substrate variety, CVD synthesis also allows for in situ atomic doping of CNTs [38]. For example, CNTs can be doped with nitrogen atoms by the addition of nitrogen containing feedstock gases such as ammonia [40] and amines [41]. There are a wide range of different types of CVD synthesis of CNTs such as water assisted [42], plasma assisted [43] and oxygen assisted [44] CVD, allowing for a wide range of operating conditions. CNT synthesis using CVD can occur at temperatures between 500 – 1200 ºC and at pressures between 760 – 7600 Torr [38].

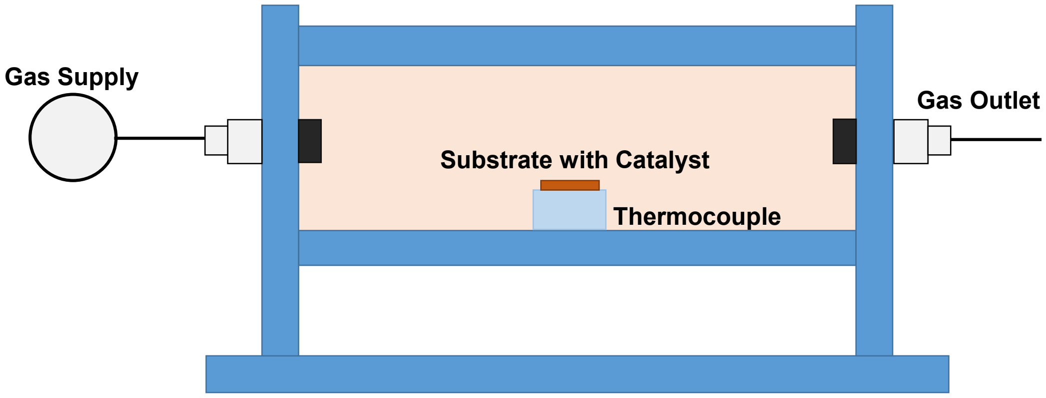

Figure 1.5: Basic schematic of a CVD furnace for CNT production (adapted from [45]).

As can be seen, each of the three methods has advantages and disadvantages, with arc discharge and laser ablation producing good quality CNTs but requiring high temperatures, generally low pressures and being difficult to scale up, while CVD allows for synthesis on a range of substrates but producing lower quality CNTs with more impurities [38]. Furthermore, all three techniques generally produce CNT mixtures with a wide range of chiralities, and due to the chemical inertness of the resultant nanotubes, practical application of CNTs typically require numerous further processing steps.

1.2.4 Processing Methods

One such early processing method for CNTs of particular interest for this Thesis, was a chemical process called “cutting”, in which as produced CNTs are ultrasonicated in highly acidic mixtures [46, 47]. In this process, CNTs are added to a 3:1 mixture of concentrated sulphuric and nitric acid and ultrasonication induced cavitation leads to breakage sites along the CNT walls [46]. These breaks are then sites for oxidative attack by the acids present, leading to further scission of the nanotubes and chemical functionalisation of the CNT ends and sidewalls with oxygen containing moieties, such as carboxylic acid groups [47]. Thus, this process produces a mixture of CNTs of various lengths, functionalised with numerous oxygen containing functional groups. As well as this functionalisation, the cutting process has also been shown to preferentially attack metallic CNTs, leading to a semiconductor enriched nanotube mix [48], useful for numerous electronic applications. After filtering the resultant tubes to remove any excess acid, they can be resuspended in a range of organic solvents, allowing for further solution processing of CNTs [49, 50].

There are a number of other methods for the dispersal of CNTs that do not require chemical modification of the nanotubes, allowing for both aqueous and organic CNT dispersions. Ultrasonication of CNTs in surfactant solutions can yield aqueous CNT dispersions, and this is possible with cationic, anionic, non-ionic and polymeric surfactants [51, 52]. For example, using anionic surfactants such as sodium dodecyl sulphate, aqueous dispersions of up to 20 $mg{\cdot}mL^{-1}$ can be obtained. Various polymers can also be used to disperse CNTs including block co-polymers [53] and aromatic polymers [54]. “Natural” agents such as sodium lignosulphonate [55] and single-stranded DNA [56] have also been found to disperse CNTs in aqueous suspensions with the help of ultrasonication. Surfactant-assisted dispersions of CNTs have also led to advances in the separation of nanotube chiralities through a number of different methods including density differentiation [57], and gel chromatography [58, 59], with recent advances in this field working to improve the scalability of this technique.

Numerous researchers have also focused on the ability to disperse and use CNTs without the need for extra molecules such as surfactants that may interfere with the CNTs’ desirable physical properties, or the need for ultrasonication which can cause damage to the walls of the nanotubes. One example of this approach is the use of superacids such as chlorosulphonic acid [60] which can make liquid crystal solutions with concentrations of up to 0.5 wt.% [61]. Another approach is the reduction of CNTs with alkali metals, which can be used to create “nanotubide” solutions, i.e., the nanotubes are negatively charged and dissolved within polar organic solvents [62]. Sodium naphthalide, for example, has been used to give SWNT Na^+ solutions with concentrations of over 2 $mg{\cdot}mL^{-1}$ [63], while elemental sodium has recently been found to dissolve SWNTs in dimethylacetamide at liquid crystal concentrations of up to 4 $mg{\cdot}mL^{-1}$ [64].

1.2.5 Application of Carbon Nanotubes

While it is beyond the scope of this Thesis to describe every application of CNTs, a number of recent reviews and research papers highlight some of the breadth of CNT application. For example, CNTs have found applications in a wide variety of composite materials, including as conductive fillers or strength enhancers in plastics as well as in fibre composites and yarns [26]. Lawal [65] delivers a comprehensive review of CNT use in electrochemical biosensors, including among others, CNT-inorganic nanocomposites as well as biosensors based on direct enzymatic attachment to CNTs. In the field of medical research, CNTs have not only been used in bio-imaging [66], for example, through their intrinsic fluorescence properties or with fluorescent labelling, but have also been used for drug and gene delivery [67]. Due to the strength of CNTs, along with their high aspect ratios, MWNTs and SWNTs have also found success in the field of atomic force microscopy (AFM), where they can be attached to the tips of both normal and fast-scan AFM cantilevers, improving both resolution and wear resistance [68]. Finally, the use of CNTs in electron field emission has been reviewed comprehensively by Li et al. [69], who include examples of prototype applications for flat panel displays and x-ray generation using CNT field emission.

1.3 Graphene

1.3.1 History and Overview

The concept of a 2D sheet of hexagonally bonded carbon atoms was first introduced in 1946 in a theoretical consideration of the physical properties of graphite by Wallace [70] and this work was further refined over the following years and decades [71]. At the time, it was assumed that 2D monolayer graphene would not be stable in ambient conditions, rolling or folding itself into smaller networks like fullerenes or nanotubes due to the energy of their dangling bonds [72]. Indeed, early examples of "monolayer graphite" or single-layer graphite, produced for example by introduction of a polymeric intercalation agent and its subsequent removal showed folding behaviour [73]. Alternatively, single layer "films" grown by the reaction of carbon feed gases on surfaces such as Pt(111) [74] and TiC(111) [75, 76] showed numerous graphene-substrate interactions.

Novoselov et al. [77] thus became the first to fully realise the potential of graphene when they isolated monolayer and few layer graphene (FLG) by mechanical cleavage of highly ordered pyrolytic graphite (HOPG) on an oxidised Si substrate, commonly referred to now as the "Scotch tape" method. The presence of the oxidised Si substrate allowed visual screening for mono- and few layer graphene under a microscope due to the slight colour contrast observed between the flakes and the underlying substrate [78]. Continuing to use this method, it was soon discovered that graphene exhibited unusual electronic properties, with its electrons acting as a two-dimensional gas of massless Dirac fermions, and its anomalous integer quantum Hall effect [79].

As Figure 1.6 shows, since these seminal papers the growth of graphene research has been exponential, with 2014 and 2015 each having almost 10,000 publications containing graphene (and not graphene oxide) in the title, abstract or keywords. It should be noted that while the original papers by Novoselov and Geim would themselves not be included within this search, papers published relating to graphene prior to these papers mostly dealt with considerations of other nanocarbons such as fullerenes and nanotubes.

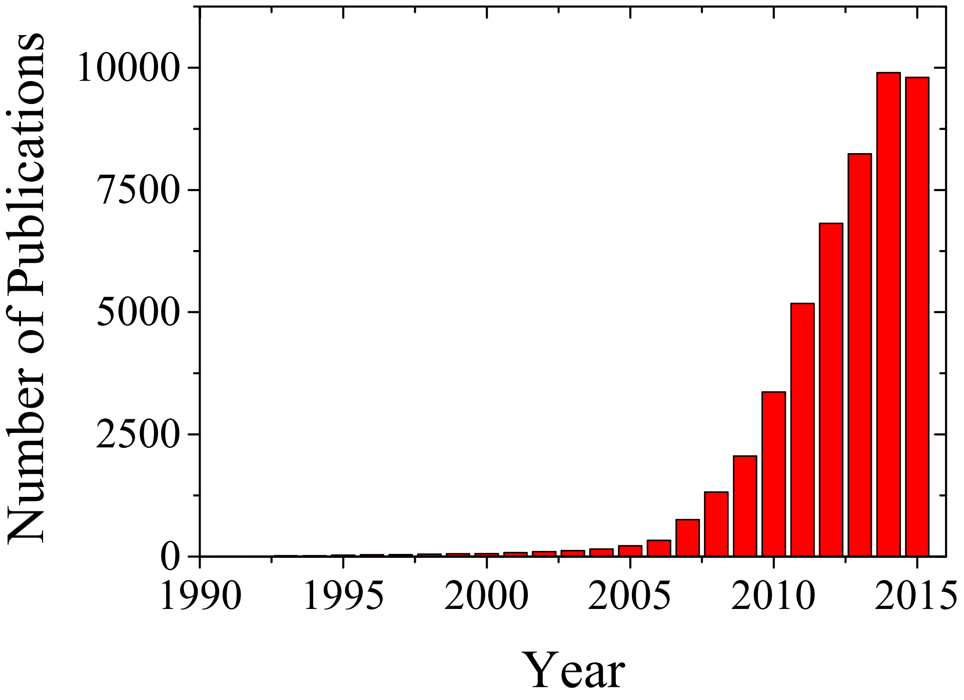

Figure 1.6: Publications per year containing graphene, and not graphene oxide, in the title, abstract or keywords as archived by Scopus up to and including 2015 (search query (TITLE-ABS-KEY (graphene AND NOT "graphene oxide")), search performed 8 January 2016).

1.3.2 Structure and Properties

As has been previously mentioned, mono- or single layer graphene (SLG) consists of a single layer of hexagonally bonded sp^2 hybridised carbon atoms. However, many also refer to multi-layer graphene (MLG), which generally consists of graphene sheets or flakes which have between 2 – 5 layers of graphene. These layers may Bernal, that is AB stack, upon one another, especially in the case of bi-layer graphene or in the case of MLG may exhibit random stacking [80]. Stacking order is important as it can drastically change the electrical properties of the graphene [81]. Adding yet further confusion, when multiple films of SLG are deposited one on top of the other, they do not re-stack AB and as such these composite films exhibit further different electrical properties [82, 83]. Thus, comparison of graphene films and their properties must always take into account both the number of layers of graphene present in a film, and the stacking order in which they are arranged. Given the large volume of graphene literature and the scope of this Thesis, here we briefly touch upon the properties of SLG, and later its production, but focus mainly on the production and applications of solution processed graphene.

Owing to its physical structure, SLG has a number of remarkable physical properties. It is the thinnest known material in the universe [84], and exhibits a number of relativistic and quantum mechanical effects. For example, charge carriers in graphene are found to resemble relativistic 2D massless Dirac fermions, governed by the Dirac equation [79]. Among the large number of effects that this has on pristine graphene's electronic properties are that it exhibits an anomalous quantum Hall effect [79] while electrons also display the Klein paradox, whereby the probability of an electron tunnelling through an energy barrier reaches unity [85]. Electron mobilities of up to 200,000 $cm^2 \cdot V^{-1} \cdot s^{-1}$ have been recorded in suspended pristine single layer graphene [86], an order of magnitude higher than electron mobilities currently found in silicon based transistors [87].

Pristine graphene is also remarkably physically robust, despite its thinness. Monolayer graphene has been found to have a Young's modulus of 1.0 terapascals, one of the highest values reported for known materials [88]. Monolayer graphene has also been found to be impermeable to a number of gases, including helium, which gives rise to a number of potential applications, including pressure sensing and ultrafiltration [89]. Indeed, it has recently been shown that SLG is impermeable to all materials other than electrons, hydrogen ions [90] and, to a lesser extent, deuterons [91].

Another useful property of graphene is its high optical transparency. Nair et al. [82] found that the drop in transmittance of white light through a monolayer sheet of graphene was equal to the product of π with the fine structure constant, or 2.3 %. Subsequent layers of graphene were found to reduce the transmittance by the same amount, up to a total of 5 layers. Graphene's optical transparency, combined with its significant conductivity, has led to a large amount of interest in potential applications, ranging from transistors to photovoltaics.

1.3.3 Production Methods

Many techniques exist that can produce either single- or few layer graphene, or both, consisting of both top-down and bottom-up approaches. These approaches can be broadly categorised into three categories; they are micromechanical cleavage, chemical vapour deposition and solution processing. All of these approaches have advantages and disadvantages, generally related to either the quality of the graphene they produce, their throughput and scalability or both and these will be discussed in the following sections, with special focus afforded to the solution processing techniques.

1.3.3.1 Micromechanical Cleavage

Pristine single- and few layer graphene can most reliably be produced what is commonly referred to as the "Scotch tape" method. This aforementioned method of micromechanical cleavage was used by Novoselov and Geim to prepare their original graphene samples [77, 78]. In short, free-standing mesas of HOPG were embedded in a photoresist, and Scotch tape was then used to repeatedly cleave off flakes of the HOPG until only thin flakes remained embedded within. These were then released by dissolving the photoresist in acetone and the flakes were subsequently deposited onto Si substrates which had 300 nm thick SiO_2 layers on top, with the change in the optical path length of reflected light allowing graphene flakes of very few layers to be visible under an optical microscope. This visibility was key for further analysis of the flakes and confirmation of their one-dimensional nature. It also gives the ability to pick desired flakes for transfer to other substrates for device fabrication. For example, using wet methods [92], a polymer coating can be spun on top of the graphene and SiO_2 substrate, with the substrate subsequently etched away and the polymer dissolved in acetone, allowing the graphene flake to be "picked up" by a new target substrate. Alternatively, using dry methods [93], van der Waals forces can be used to transfer graphene from a SiO_2 surface to a substrate with a higher affinity for graphene, such as boron nitride. While this approach remains the best technique for obtaining pristine monolayer graphene for fundamental research purposes [90, 91, 94-97], it lacks the high throughput and scalability required for applied research.

1.3.3.2 Chemical Vapour Deposition

Chemical vapour deposition (CVD) is a bottom-up approach that has been successful in making single- and few layer graphene in large quantities. Early work focused on Ni substrates [80, 98-100], but several other metal substrates such as Ru, Co, Au and Pt were also investigated [101]. While these substrates did produce areas of SLG, there were also substantial areas of bi-layer and few-layer graphene as well as crystal boundary issues. Most success, however, has come with the use of Cu substrates, first reported in 2009 [102], which shows a much larger proportion of SLG than other substrates. Further refinement of Cu substrate growth conditions has seen significant process made, with single crystal SLG being grown with lateral size dimensions of 5 mm [103], and claims of seamless stitching of single crystal domains up to 6 cm × 3 cm [104]. While these achievements are quite impressive and have a high potential for application and upscaling, there are still several drawbacks. Both Ni and Cu substrates generally require annealing at temperatures of up to 900 – 1000 ºC and growth conditions of up to 1000 ºC, and in the cases of some Cu growth conditions, low vacuum [105]. These conditions are very energy intensive and as such, the energy efficiency of applications made containing these graphene films will be low. On top of this, once grown on the target substrate, the films must still be transferred to the desired substrate, in most cases using wet transfer methods, a technique flaw shared with solution processed graphene.

1.3.3.3 Wet-Chemical Exfoliation

A less energy intensive route for single- and few layer graphene is the top-down approach of liquid phase exfoliation of graphite into graphene, which has been studied since early 2008. As will be discussed in more detail later in this section, this technique does not produce high yield SLG like CVD, but it is similarly scalable for industrial settings. Secondly, the liquid phase exfoliation of graphite oxide into graphene oxide, which will be discussed in more detail in Section 1.4.2, produces numerous oxidative defects into the graphene lattice and subsequent reduction techniques cannot repair the graphene oxide to levels comparable to that of pristine graphene [106]. In response to these issues, two independent groups were the first to publish reports of the exfoliation of bulk graphite into single- and few layer graphene by ultrasonication of graphite in the organic solvents *N,N*-dimethylformamide (DMF) and *N*-methylpyrrolidone (NMP) [107, 108], the chemical structures of which can be seen in Figure 1.7.

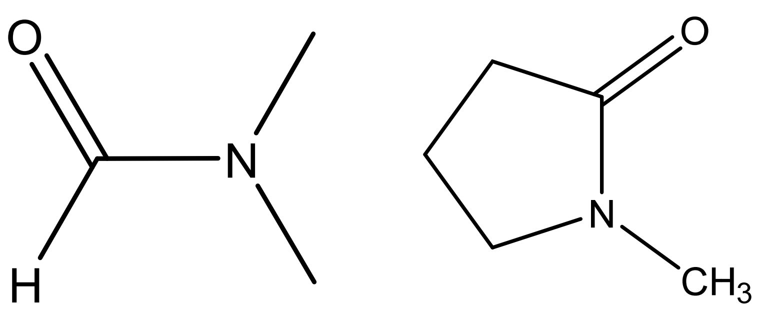

Figure 1.7: Chemical structures of the organic solvents (a) *N,N*-dimethylformamide and (b) *N*-methylpyrrolidone.

In the first report, Blake et al. [107] showed that ultrasonication of natural graphite in DMF, for periods over three hours, led to exfoliation of the graphite. After centrifugation, dispersions containing single- and few layer graphene flakes with submicron size dimensions were obtained, with the dispersions subsequently used to spray coat centimetre scale glass slides, producing transparent conductive films. This method was more thoroughly investigated by Hernandez et al. [108] who investigated the efficacy of 12 different organic solvents in exfoliating graphite. Hernandez et al. [106] theorised that the energy required to exfoliate graphene should be balanced by the solvent-graphene interaction for solvents whose surface energies match that of graphene, analogous to the similar exfoliation of SWNTs in organic solvents [109]. Using this approach, the solvent NMP was found to produce a SLG yield of ~1 wt%, relative to the initial concentration of graphite, and give dispersions of overall graphene concentrations of ~0.01 $mg \cdot mL^{-1}$. These dispersions were found to be stable for long time periods, up to several months, and in certain solvents, such as NMP, almost all flakes analysed after ultrasonication and centrifugation were found to be exfoliated to less than five layers. Indeed, 28 % of all flakes produced in NMP which were analysed under TEM were found to be monolayers. Raman analysis, combined with TEM and x-ray photoelectron spectroscopy (XPS) analysis, of films produced by filtration of the resultant dispersions showed that the graphene flakes were relatively free of basal plane defects, with the disorder bands observed in the Raman spectra found to be caused by the edges of the graphene flakes.

This method was further expanded by Bourlinos et al. [110] who used perfluorinated aromatic solvents, such as pentafluorobenzonitrile, to disperse graphene at concentrations of up to 0.1 $mg \cdot mL^{-1}$. Hernandez et al. [111] also expanded on their own work by testing a further 28 solvents for their suitability for graphene exfoliation in 2009. The main motivation for this study was to determine whether solubility parameters could be used to determine ideal solvents for graphene exfoliation. Concentrations ranged from 0.16 ± 0.05 $\mu g \cdot mL^{-1}$ in the worst solvent (pentane) up to 8.5 ± 1.3 $\mu g \cdot mL^{-1}$ in cyclopentanone, with greater than 70 % of the graphene remaining dispersed in good solvents after 250 hours. There was however a discrepancy between the ability of a solvent to disperse graphene and its ability to exfoliate FLG. For example, NMP was found to be the eighth best solvent tested in terms of dispersion concentration but the best when analysing the mean number of graphene layers per flake.

Other solvents investigated for exfoliation and dispersion have included benzylamine, used to produce concentrations of ~0.5 mg·mL^{-1} [112] and ortho-dichlorobenzene [113, 114], which has the advantage of being non-hygroscopic and not highly polar, when compared to popular solvents such as NMP.

While these approaches were successful in producing single- and few layer graphene in their respective solvents, the yield was still quite low compared to the 1 mg·mL^{-1} possible when exfoliating graphene oxide in organic solvents. The challenge of producing high concentration graphene dispersions was taken up by Coleman et al. [115] in two subsequent studies. In the first, they hypothesised that the amount of graphene exfoliated and dispersed was limited by the amount of energy added to the initial graphite/solvent system. Using low power ultrasonication baths, these initial solutions were ultrasonicated for up to 460 hours, resulting in graphene dispersions of up to 1.2 mg·mL^{-1} containing 4 wt/% SLG. It was found that the concentration of the final dispersion was proportional to the square root of the ultrasonication time, while the mean number of layers per flake was constant at ~3 for all times. In a further improvement [116], dispersion concentrations of up to 63 mg·mL^{-1} were achieved by centrifuging dispersions after the initial ultrasonication, filtering the supernatant and subsequently re-dispersing the filtrate with ultrasonication. The final dispersions had between 3 – 4 layers per flake and were of comparable size dimensions to the previously reported methods. Such high concentration dispersions were found to be stable only over a period of days, although dispersions with concentrations of up to 26 – 28 mg·mL^{-1} remained stably dispersed "indefinitely".

Despite the large steps forward in terms of dispersion concentrations that had been achieved in solvent exfoliation, there were still problems that needed to be addressed. Chief among these was the ultimate usefulness of the graphene dispersions. Nearly all prior work conducted in solvent exfoliation had been performed in high boiling point solvents. As well as being generally expensive and toxic, their high boiling point meant that it was hard to use these dispersions for subsequent applications, as waiting for solvents to evaporate led to aggregation of graphene flakes into undesirable bulk crystallite structures. This problem was addressed by a number of groups, including O'Neill et al. [117] and Choi et al. [118]. O'Neill et al. [117] used three common low boiling point solvents, namely chloroform, isopropanol and acetone, to exfoliate graphite. While previous work had shown they were poor at dispersing graphene (concentrations of 1-3 μg·mL^{-1} for all three solvents), all of their boiling points are well below 100 °C. By using the procedures honed by work with high boiling point solvents, the concentration of these dispersions was increased to 0.1 – 0.5 mg·mL^{-1}, with all flakes analysed having 7 or less layers, with a mean of 3.2 layers per flake. The dispersions were also found to be quite stable, with 96 % of the original graphene dispersion stable after over 200 hours in isopropanol. Choi et al. [118] meanwhile used 1-propanol, which has a boiling point of 97 °C. While these dispersions were not as concentrated as those prepared by O'Neill et al. [115] (25 μg·mL^{-1} compared with 100 – 500 μg·mL^{-1}), the lateral dimensions of the flakes were found to be up to 15 μm, which was an improvement. While the mean number of layers per graphene flake was poor (high) in these studies, their main advantage is that the low boiling point solvents were easily evaporated in ambient conditions, with no solvent residues left to contaminate the graphene samples, and very little flake to flake aggregation occurring. This would potentially allow for better processing and application of these dispersions when compared to the high boiling point solvents used to achieve higher ratios of SLG and FLG. More recently, however, numerous works have investigated the use of the high-boiling point NMP exfoliated graphene for use in ink-jet printing, with successful results [119, 120].

Surfactant assisted exfoliation of graphite to graphene is another top-down solution processing approach to the exfoliation of graphene. While the majority of solvent exfoliation techniques already discussed in this Section involved expensive solvents which require special care when handling and have high boiling points, aqueous surfactant solutions are cheap and easily processable. With this motivation, Lotya et al. [121] in 2009 used the common ionic surfactant sodium dodecylbenzene sulfonate (SDBS) to produce graphene dispersions with concentrations of up to 0.05 mg·mL^{-1}. Optimised dispersions contained 43 % FLG flakes with less than 5 layers and an overall SLG yield of 3 %. Unlike solvent exfoliated graphene dispersions, these flakes had an effective charge due to the absorption of surfactant anions and as such the dispersions were stabilised in a manner consistent with DLVO theory.

Green and Hersam [122] were able to selectively control the thickness of surfactant exfoliated graphene flakes using density gradient ultracentrifugation (DGU). Using the planar amphiphilic surfactant sodium cholate, natural flake graphite and horn sonication, graphene dispersions were produced. After centrifugation at

15,000 rpm for one hour, the resultant supernatant solutions with concentrations in excess of 90 $\mu g \cdot mL^{-1}$ were stable for several weeks. These dispersions were then processed using DGU for 24 hours at 141,000 g, after which fractions of varying thicknesses, defined by the number of layers of graphene per flake, could be collected.

Lotya et al. [123] expanded upon the sodium cholate method in 2010, using bath ultrasonication for extended periods of time of up to 400 hours, similar to their previously discussed solvent exfoliation approach. They found that the final dispersion concentration was dependent on the initial graphite concentration, surfactant concentration, centrifugation rate, and sonication time. Optimisation of these parameters resulted in maximum concentrations of up to 0.3 $mg \cdot mL^{-1}$. Unlike solvent exfoliated graphene though, it was found that the concentration of the dispersion did not scale with the square root of the sonication time and the size of the graphene flakes did not continue to decrease with increased sonication time. This was found to be likely due to surfactant slippage at the graphene/surfactant/water double surface reducing the amount of sonication induced scission.

Other examples of ionic surfactant assisted exfoliation of graphene have come from Hasan et al. [114], who used sodium deoxycholate to produce polymer composites, Zhang et al. [124] who used pyrene derivatives to form aqueous dispersions, Vadukumpully et al. [125] who used cationic cetyltrimethylammonium bromide in glacial acetic acid to make dispersions which could then be filtered and resuspended in DMF solutions and Sampath et al. [126] who used diazaperopyrenium dications to intercalate natural graphite and then stabilise the exfoliated graphene sheets through electrostatic repulsion.

One of the most successful examples of surfactant assisted exfoliation of graphene came from Guardia et al. [127] who performed a study to compare the use of ionic and non-ionic surfactants in the exfoliation of graphene, investigating nine different non-ionic and eight ionic surfactants. While not optimised, the concentration of surfactant solutions used was kept above the critical micelle concentration for all surfactants. Under these conditions, it was found that non-ionic surfactants generally outperformed ionic surfactants in dispersing high concentrations of graphene. Indeed the best non-ionic surfactants Tween-80 and Pluronic® P-123, the chemical structures of which can be seen contrasted with that of the common ionic surfactant SDBS in Figure 1.8, achieved dispersion concentrations of 0.5 – 1 $mg \cdot mL^{-1}$ compared with 0.01 – 0.10 $mg \cdot mL^{-1}$ for ionic surfactants. This result led the authors to propose that the steric repulsion provided by the hydrophilic part of the non-ionic surfactants extending into the water phase was more efficient at stabilising graphene sheets than the electrostatic repulsion provided by ionic surfactants. This explanation was also supported by Smith et al. [128], who found that steric stabilisation played a large role in the final concentration of non-ionic graphene dispersions. At the same time however, Smith et al. [126] also concluded that favourable water interaction with ether and acid groups along with possible electrostatic interactions are additive to this stabilisation.

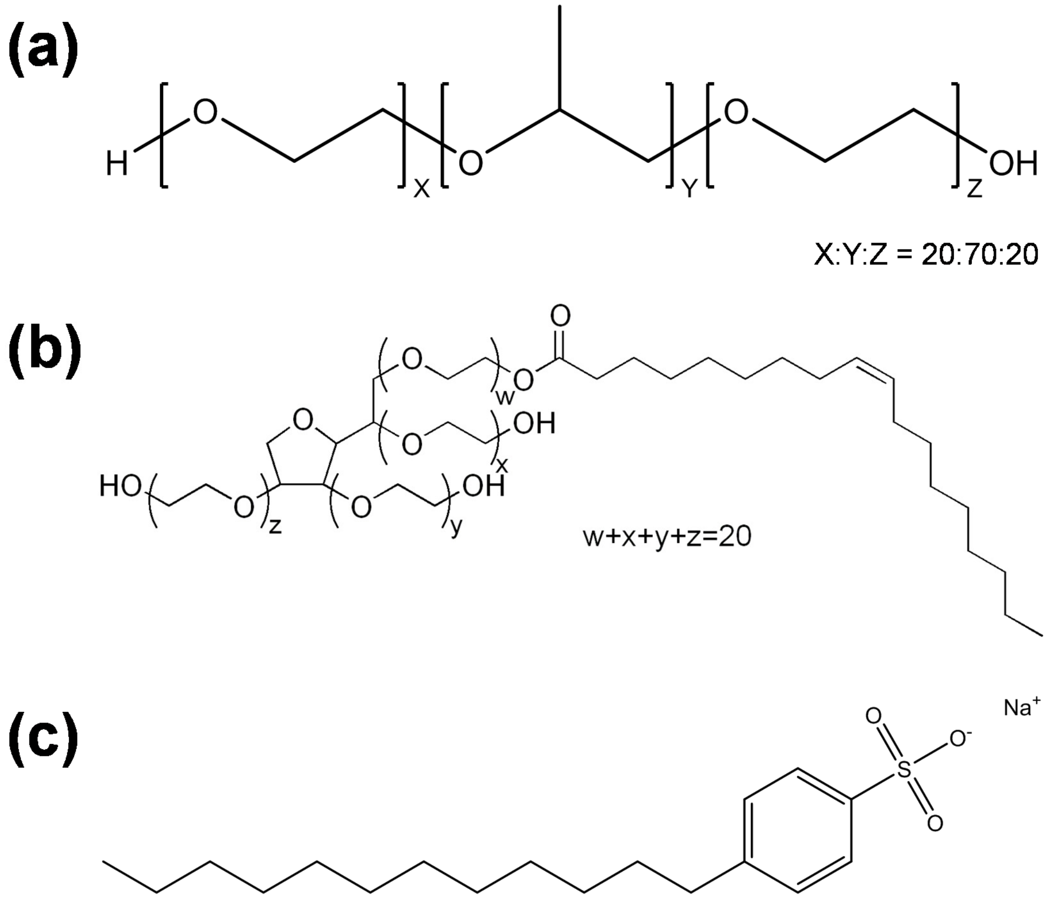

Figure 1.8: Chemical structures of the non-ionic surfactants (a) Pluronic® P-123 and (b) Tween-80 and (c) the chemical structure of the common ionic surfactant SDBS.

These reports clearly show the potential for aqueous dispersions of surfactant-exfoliated graphene. They are easy to produce, requiring little more than water, surfactant and an ultrasonicator and are easy to produce transparent conductive films through numerous methods capable of scale up.

1.3.3.4 Further Solution Processing Methods

While not focused on during the work completed in this Thesis, there are a number of other solution processing techniques which can produce non-chemically modified graphene. For example, electrolytic exfoliation can be performed using suitable electrolytes [129] or intercalating agents [130]. Another approach is the exfoliation of expanded, and or intercalated, graphite through ultrasonication in suitable solvents [131, 132]. More recent efforts include using shear forces in the exfoliation process, either in NMP [133, 134], or surfactant-water solutions [134, 135].

1.3.4 Applications of Graphene

Early reports of solvent assisted exfoliated graphene focused on preparing conducting films [107, 108, 115], graphene-polymer composites [108, 114], or subsequent chemical modification of the suspended graphene flakes [110, 112, 113]. While these reports showed the potential of these dispersions to create conducting films and polymer composites, Hasan et al. [114] were the only ones to use their graphene-polymer composite in a functioning device, making a photonic device. The more recent examples of solvent assisted exfoliated graphene have shown application as fillers in glue [136] and as photocatalytic enhancers of ZnO degradation of dyes [137]. When using shear to help exfoliate rather than ultrasonication, solvent assisted exfoliated graphene has been used in an array of applications such as dye sensitised solar cell counter electrodes, capacitors and strain sensors [134]. Similarly, recent examples of solvent assisted exfoliated graphene used in ink-jet printing applications have been used to make heterostructure photodiodes [119] and transparent flexible films on polyethylene terephthalate [138].

Early reports of surfactant assisted exfoliated graphene also focussed almost exclusively on preparing vacuum filtered films [121, 122, 124, 139] to produce either transparent conducting or thicker composite papers [123, 127]. More recently, surfactant assisted exfoliated graphene has been used to make TiO_2 composites for photocatalytic NO_X removal [140], graphene-manganese oxide hybrid supercapacitors [141], catalytic graphene-metallic hybrid nanoparticles [142], as electrode enhancers [143] and as an additive for water-based lubricants [144].

1.4 Graphene Oxide

1.4.1 History and Overview

Another solution processing method of graphene production commonly found in the literature is the use of chemically reduced graphene (CRG) [145]. This method involves the heavy oxidation of graphite into graphite oxide, which can then be dispersed into aqueous solutions. These dispersions contain flakes of graphene oxide of varying thicknesses, including single layer graphene oxide. The GO can then either be further processed into films before reduction to CRG or reduced while in solution and then used in further applications.

Methods for the production of graphite oxide have been known since the work of Brodie [17] in the mid-nineteenth century, while it is also acknowledged by Geim [146], that the earliest known observation of atomically thin sheets of chemically reduced graphene was reported by Boehm et al. in 1962 [147, 148]. It is generally accepted [149] that the production of GO is ubiquitously performed using modified versions of methods of either Brodie [17], Hummers and Offeman [150] or Staudenmaier [18] (itself a modification of the Brodie method) with these methods discussed in more detail in Section 1.4.2.

While atomically thin sheets of reduced graphene oxide may have been observed decades earlier, a search of the literature shows that since the first report of graphene in 2004, publications including graphene oxide in their title, abstract or keywords have grown exponentially, as seen in red in Figure 1.9. Interest in graphite oxide also grew in the same time period, with publication numbers in the single digits in the years from 1950 onwards increasing to the hundreds in the mid 2000's, as seen in blue in Figure 1.9. Unlike GO however, this interest appears to have waned in more recent years.

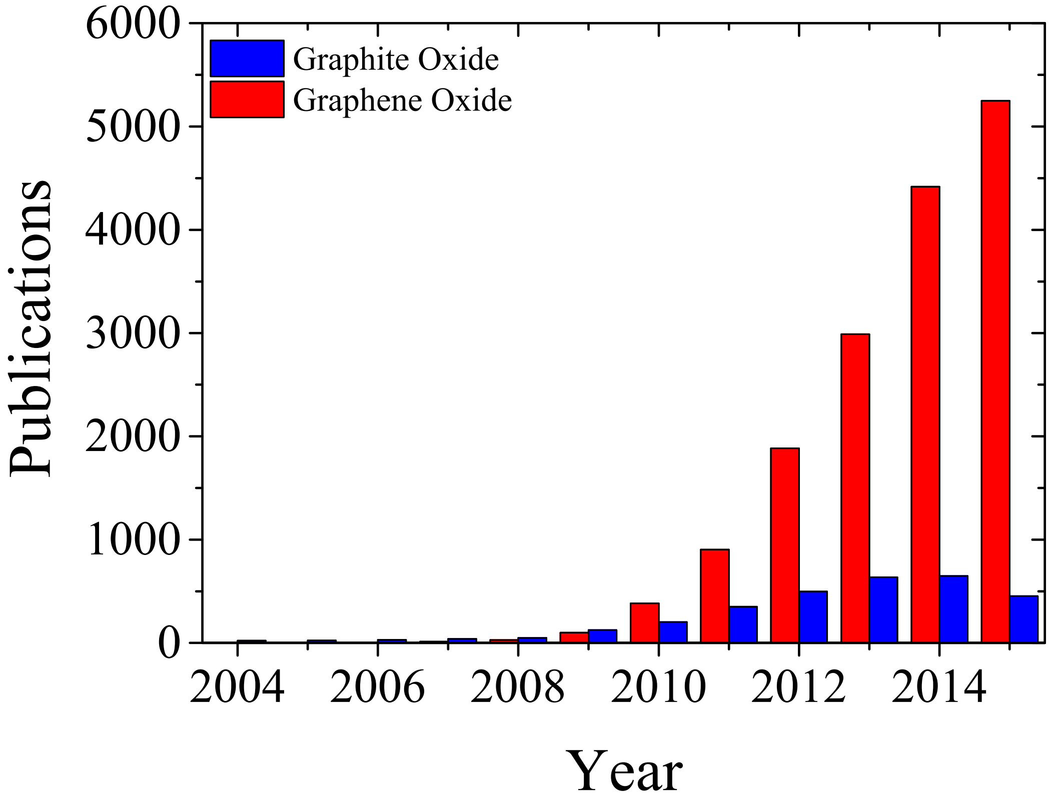

Figure 1.9: Publications per year containing graphene oxide, or graphite oxide, in the title, abstract or keywords as archived by Scopus up to and including 2015 (search query (TITLE-ABS-KEY("graphene oxide")) and (TITLE-ABS-KEY ("graphite oxide”)), searches performed 15 January 2016).

1.4.2 Production Methods

The Hummers’ method was published in 1958 by Hummers and Offeman [150]. Motivated by the time consuming and hazardous nature of previous production methods of graphite oxide, such as those reported by Brodie [17] and Staudenmaier [18], they reported a method of oxidation of graphite using an anhydrous mixture of sulphuric acid, sodium nitrate and potassium permanganate. This method took less than two hours to perform, however it required over two litres of concentrated sulphuric acid to oxidise 100 grams of graphite, along with copious dilution (up to 14 litres) with water. Also, while technically less hazardous than Brodie’s method, the Hummers’ method still generates toxic gases due to the use of sodium nitrate.

Modified Hummers’ methods typically involve extending the oxidation of graphite in sodium nitrate, potassium permanganate and concentrated sulphuric acid for up to five days to increase the oxidation and intercalation of the graphite [151, 152]. These modified methods however still generate the toxic gases associated with the Hummers' method due to the presence of sodium nitrate.

The graphene oxide produced during these methods is finally filtered, and after copious rinsing with water, a filter cake of GO is produced. These GO cakes can either be redispersed in water via ultrasonication to produce aqueous GO dispersions, or dried to produce GO powders for further applications.

Marcano et al. [153] developed a method for the production of graphene oxide which excluded sodium nitrate and therefore did not generate any toxic gases. This method involved the addition of graphite to a 9:1 mixture of concentrated sulphuric acid to phosphoric acid, and potassium permanganate, followed by stirring of the mixture for 12 hours. It was found that this method was much more efficient at producing GO from the starting graphite material and that the product was still as easily reduced as GO produced using the Hummers' or modified Hummers' methods [153].

Examples of other GO production methods include the unzipping of carbon nanohorns to form GO [154], using graphite produced from cokes of petroleum and coal derivatives [155], large scale GO production in continuous stirred tank reactors [156] and "eco-friendly" Hummers methods that leave out $NaNO_3$ [157]. Despite these "new" methods however, the modified Hummer's approach remains the gold standard, with modifications such as those mentioned previously focusing on incremental improvements, rather than new techniques [149].

1.4.3 Structure and Properties

The structure of graphene oxide is still subject to some debate within the literature, owing in part to the difficulties involved with characterising its irregular structure [149]. The Lerf-Klinowski model [158, 159] is currently the generally accepted model [160], but new models are still being proposed [161]. Briefly, the Lerf-Klinowski model shows a random, non-repeating structure, containing regions of aromatic benzene rings, along with aliphatic six membered rings. Throughout the GO flake in non-aromatic regions there are hydroxyl and ketone groups, as seen in Figure 1.10(a & b). This model also proposes that there is a small number of carboxylic acid groups present on the edges of the GO basal plane, although as can also be seen in Figure 1.10(b), these are sometimes left out of structures "for clarity". Other models, such as the Zsabo-Dakeny model however, reject the presence of carboxylic acid groups, and present a repeating structure of cyclohexanes and flat hexagons, functionalised with various oxygen moieties such as tertiary hydroxyls, ketones and quinones, as seen in Figure 1.10(c).

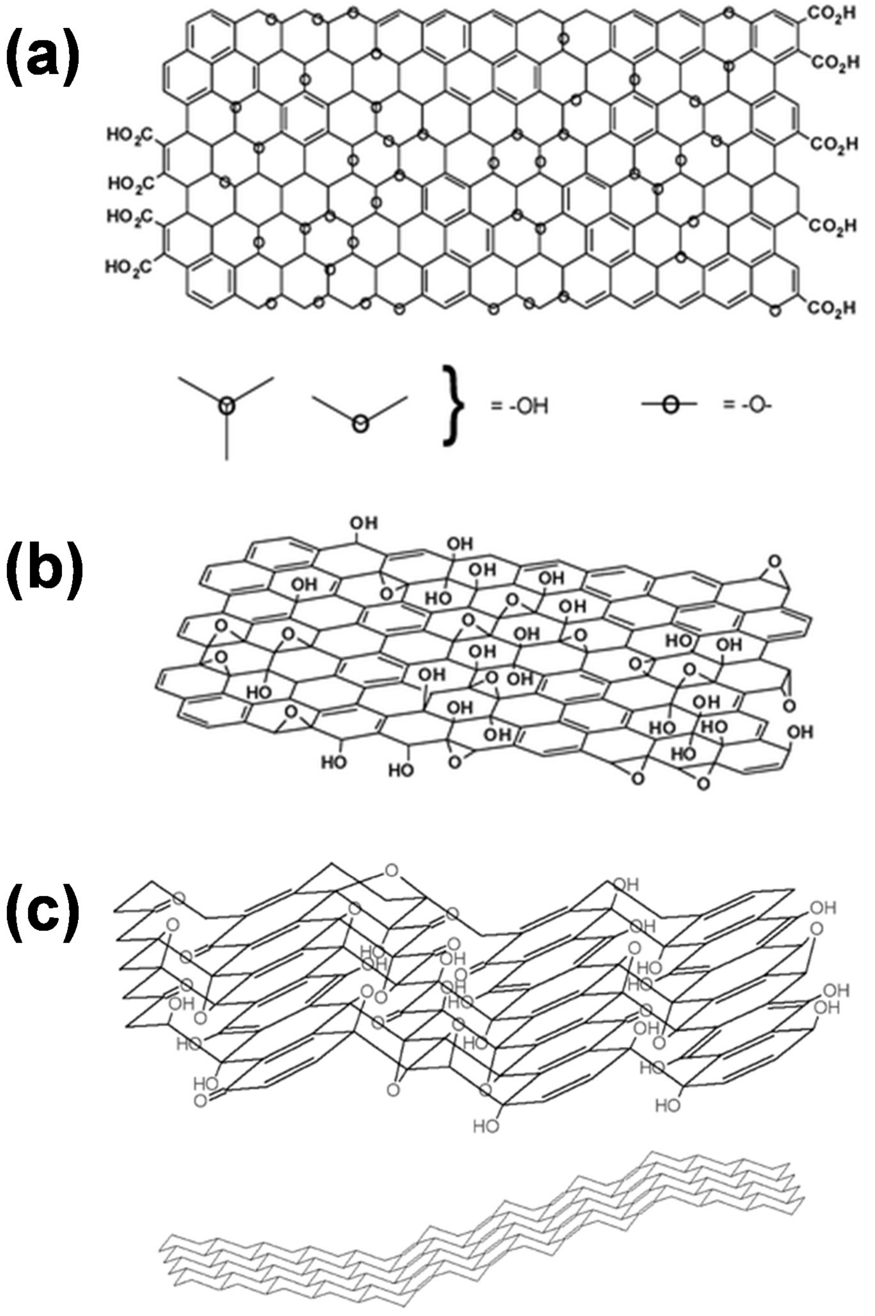

Figure 1.10: Two different chemical structures proposed by Lerf and Klinowski; (both from [149]) (a) carboxylic acid groups are present on the edges of the basal plane, while they are absent in the model proposed in (b), with (c) showing the repeating structure of the Zsabo-Dakeny model ([161]).

What is not under debate, however, is that the introduction of the oxygen containing moieties seen in Figure 1.10 destroys the pristine aromatic nature of the graphene sheet. This results in a large amount of disorder in the sp^2 network, as sp^3 bonding is introduced throughout the basal plane and edges of the graphene sheets. This disruption of the pure graphene lattice results in a large decrease in the conductivity of graphene oxide, when compared to pristine graphene. Gómez-Navarro et al. [162] reported that the conductivity of graphene oxide sheets before reduction was $1 – 5 \times 10^{-3}$ $S \cdot cm^{-1}$, a value close to that of an insulator. Similarly, Stankovich et al. [163] reported conductivities of graphene oxide films ranging from $10^{-4} – 10^{-3}$ $S \cdot m^{-1}$, while Gilje et al. [164] found that the sheet resistance of graphene oxide films was approximately 4×10^{10} $\Omega \cdot square^{-1}$.

Disruption of the aromatic carbon sheet with oxygen moieties does however bring several processing advantages, that were recognised quite early in the post-graphene boom of research [106]. GO can be dispersed in water quite readily, with commercial suppliers offering aqueous dispersions containing 80 % single layer GO of concentrations up to 6 $mg \cdot mL^{-1}$ [165]. Furthermore, GO can also be stably dispersed in organic solvents such as ethylene glycol, DMF and NMP for extended periods at concentrations of up to 0.5 $mg \cdot mL^{-1}$ [166], while the chemically reactive oxygen sites allow for chemical modification of the GO flakes to allow for stable dispersions in organic solvents such as DMF at concentrations in the 1 $mg \cdot mL^{-1}$ range [167].

1.4.4 Reduction of Graphene Oxide

A variety of methods have been reported in the literature that aim to reduce graphene oxide in order to restore the conjugated electronic nature of graphene and thus increase the conductivity of the resultant material [106, 168, 169]. These methods include chemical reduction using reagents such as hydrazine [170], thermal reductions [171], a combination of chemical and annealing methods [172], or more unique techniques such as electrochemical methods [173].

Hydrazine reduction of graphene oxide [174] is a very common technique used to prepare films of reduced graphene oxide (RGO) for a variety of purposes. This technique is popular as it results in increases of several orders of magnitude in the conductivity of thin films of RGO, as reported in the aforementioned papers by Gómez-Navarro, Stankovich and Gilje et al. [162-164]. Other reducing agents that have been used to reduce GO include sodium borohydride ($NaBH_4$) [175], borane (BH_3) [176], hydroiodic acid (HI) [177]. Although large increases in conductivity can be achieved through the chemical reduction of GO, it does not completely remove all traces of oxygen within the sample. Indeed, while hydrazine treatment removes hydroxyl and epoxy groups present on the basal plane of the GO, edge groups, such as carboxylic acids, remain [178]. Another drawback to the use of hydrazine, its derivatives, such as dimethylhydrazine [179], is that they are highly flammable, explosive, toxic by inhalation, ingestion and contact with the skin and toxic to aquatic organisms, which gives rise to environmental concerns. One potential work around to these issues is the use of "nature based" reagents for the reduction of GO with vitamins such as vitamin C [180, 181], along with saccharides and amino acids to name a few [182].

Thermal reduction of graphene oxide is another more environmentally friendly, albeit energy intensive, technique used to prepare samples of reduced GO for a variety of purposes. Thermal reduction can lead to the removal of oxygen from a large majority of the basal plane of graphene, although as per hydrazine reduction, oxygen containing groups are still left on the edges of the graphene [183]. Unfortunately, the best results in terms of the reduction of oxygen present and the increased conductivity of resultant films of reduced graphene are generally obtained at high temperatures, often in excess of 500 °C [183, 184]. For example, thermal reduction taking place in ultra-high vacuum conditions (UHV), at temperatures in excess of 900 ºC was found to produce the highest C1s/O1s ratio upon XPS analysis when compared with heat treatment in inert (Ar) or reducing (forming gas, Ar/H_2) atmospheres [185]. Thermal annealing in a reducing atmosphere, such as forming gas, has been found to significantly increase the conductivity of RGO films, but the effect is most significant at temperatures above 700 ºC [186]. Another more novel technique is thermal reduction followed by the introduction of a carbon feedstock at temperatures in excess of 800 ºC, which then promotes CVD "repair" of the films, leading to very low sheet resistances [187, 188]. The elevated temperatures of all these techniques, however, rule out the use of certain substrates, in particular plastics, and as such these processes can be detrimental to device design.

Other less common techniques have also been used to reduce graphene oxide to form films of RGO. Electrochemical techniques have seen the reduction of GO using a number of different electrodes and surfaces [173, 189, 190], while microwave assisted reduction [191], solvothermal reduction [192] and UV-Vis assisted TiO_2 photocatalytic reduction [193] have all been found to successfully reduce GO to some extent.

1.4.5 Applications of Graphene Oxide

GO and RGO have found use in a myriad of applications due to their ease of processing and ample opportunities for chemical modification. While the full breadth cannot be covered within the scope of this Thesis, this section details a number of current reviews which summarise a wide range of applications across a number of fields. A wide ranging review by Li et al. [194] reviews the use of GO and RGO for the chemical and physical storage of hydrogen, photocatalytic water splitting, cathode and anode enhancement in lithium ion batteries, improving supercapacitors and GO/RGO composites for water purification. Filtration applications of GO and RGO have also been reviewed in terms of desalination applications [195] as well as the improved antimicrobial and antifouling properties of GO/RGO containing desalination membranes [196], and nano- and ultra-filtration and forward osmosis [197]. GO and RGO have also found applications in gas sensing, with reviews by Gupta Chatterjee et al. [198] focusing on toxic gas sensing, and Toda, Furue and Hayami [199] also including water vapour, H_2 and organic vapour sensing in their review. A large number of catalytic applications have been investigated with GO and RGO, with reviews focusing on the use of metal-free catalysis using GO [200], GO as a platform/tether for catalytic species [200], and metal nanoparticle hybrid catalysis [201]. Finally, GO and RGO have found a number of uses in the biological and medical fields, being used for biological imaging and sensing such as photoluminescence [202], chemiluminescence, and electrochemiluminescence [203] as well as in cancer therapeutics, such as photothermal and photodynamic therapy and drug delivery [204].

1.5 Introduction to Photovoltaics

The most ubiquitous photovoltaic system in the eyes of the public is that of the crystalline silicon heterojunction solar cell [205]. While this may be the limit of the layman's appreciation of "solar cells", there are a vast number of other alternatives that use a wide variety of materials to convert sunlight into electrical energy [206]. These include so-called III-V cells such as GaAs thin film cells [207], thin film chalcogenide cells such as $CuInGaSe_2$ cells [208], polymer containing organic thin-film solar cells [209], dye sensitised solar cells [210] and, more recently, perovskite thin-film solar cells [211].

While the exact operating mechanisms of how these solar cells are able to harvest light energy for power production is beyond the scope of this Thesis, the way in which these cells are tested and their performance reported is both consistent and relevant. In general, to test the photovoltaic performance of a solar cell, the cell is first exposed to a light source while connected to an external circuit containing a source-measurement unit. This source-measurement unit applies a potential to the cell that is then swept across a defined range while measuring the current that is generated within the circuit. If the active area of the cell, that is the area that is actively participating in photocurrent generation, is known, the current output can be converted to current density, allowing for the production of a current density-voltage (J-V) curve, an example of which can be seen in Figure 1.11. By measuring J-V curves, comparisons between cells with different active areas can be made if the conditions used during their testing, such as temperature and the profile of light being used, are identical.

Although a J-V curve is generally taken across a set voltage range such as -1 V – 1 V, the main quadrants of interest are either the second or fourth quadrant. Within these quadrants the photocurrent being generated is in the opposite direction to the applied voltage and hence power is being generated by the cell. Measuring a J-V curve allows one to determine three key points which can be used to summarise the photovoltaic performance of a solar cell, with these points depicted on the example J-V curve in Figure 1.11. The first point of interest is the short circuit current density (J_{SC}), which is the current the cell produces at zero bias. The second point of interest is the open circuit voltage (V_{OC}) of the cell, which is the voltage that occurs within the cell when there is no net current flow throughout. The third point of interest is the maximum power point, which occurs at (V_{MP}, J_{MP}).

These three points can then be used to help define the fill factor (FF) of the cell using the following equation:

$$\mathrm{FF} = \frac{\mathrm{J_{MP}} \times \mathrm{V_{MP}}}{\mathrm{J_{SC}} \times \mathrm{V_{OC}}}$$

Equation 1.3

FF is the ratio of the maximum power generated by the cell ($V_{MP} \times J_{MP}$) to the maximum potential power that could be generated by the cell ($V_{OC} \times J_{SC}$) and is a measure of the "squareness" of a cell's J-V curve. Graphically, this can be seen in Figure 1.11 as the ratio of the light grey rectangle bounded by the origin and the cell's maximum power point to the dark grey rectangle bounded by the origin and the straight lines passing through the cell's V_{OC} and J_{SC}. Ideally, a solar cell would continue to produce a current density equal to that of its J_{SC} across the whole positive bias range until it reached its V_{OC}, producing a perfectly rectangular J-V curve, but due to a number of reasons, including charge recombination, this does not occur in practical solar cells.

With its J_{SC}, V_{OC} and FF known, the power conversion efficiency (PCE) of a cell can be determined using the following equation [212]:

$$\eta = \frac{\mathrm{J_{SC}} \times \mathrm{V_{OC}} \times \mathrm{FF}}{\mathrm{Is}}$$

Equation 1.4

where η is the PCE of the cell measured in percent, J_{SC} is measured in $mA \cdot cm^{-2}$, V_{OC} is measured in V, FF is the fill factor of the cell and I_S is the intensity of the incident light measured in $mW \cdot cm^{-2}$.

The J-V curve seen in Figure 1.11 was obtained from a cell being measured under 100 $mW \cdot cm^{-2}$ light. As such, this example curve shows a cell with a J_{SC} of 1.42 $mA \cdot cm^{-2}$, V_{OC} of 0.466 V and a maximum power point occurring at (0.306 V, 0.878 $mA \cdot cm^{-2}$). Using Equation 1.3, the FF of the cell is 0.41 and thus using Equation 1.4, its PCE is 0.27 %. These parameters will be used throughout Sections 1.6 - 1.7 and Chapters 3 – 5 in order to draw comparisons between the photovoltaic performance of different types of solar cells, viz. CNT containing photoelectrochemical solar cells, and carbon-silicon solar cells.

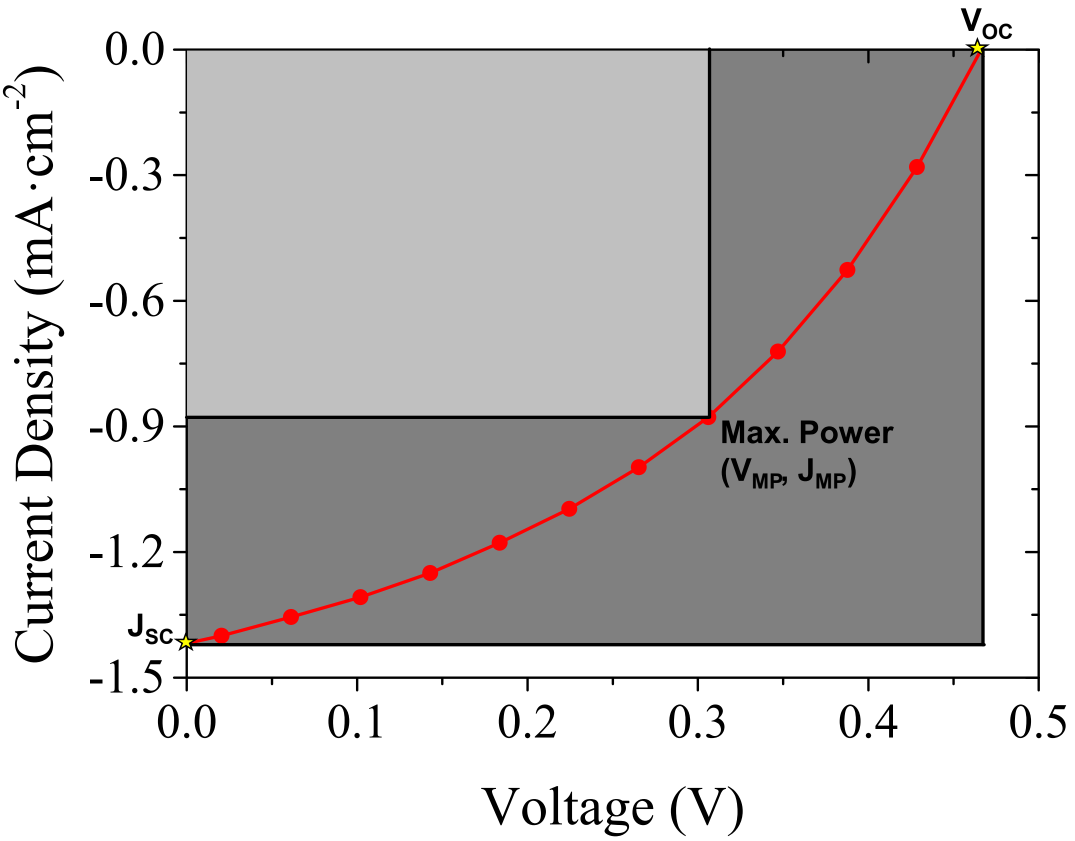

Figure 1.11: An example J-V curve, showing the maximum power point at (V_{MP}, J_{MP}) as well as the short circuit current density, J_{SC}, and open circuit voltage, V_{OC}. Also represented are the areas of the rectangles bounded by the origin and the maximum power point (light grey) and the origin and the maximum theoretical power point (dark grey).

1.6 Carbon Nanotubes in Dye-Sensitised Solar Cells

1.6.1 History and Overview

The archetypal dye-sensitised solar cell (DSC) was first reported by O'Regan and Grätzel [213] in 1991. Figure 1.12(a) shows a schematic for a generalised DSC design, showing the numerous design components [214]. While there have been some changes to this generalised scheme since the DSCs inception, this model is very useful for developing an understanding of their construction and operating mechanisms. The first main component of a DSC is the photoanode (shown on the left of the cell), which generally consists of a glass substrate with a transparent conducting oxide (TCO) layer such as fluorinated tin oxide (FTO) or indium tin oxide (ITO). On top of this TCO, a micron sized layer of a semiconductor such as mesoporous TiO_2 nanoparticles is deposited. Once deposited, this mesoporous TiO_2 is sensitised with a layer of dye molecules, for example, transition metal complexes like the ruthenium based dyes N3 and N719. The second component of the DSC is the counter electrode (CE) (shown on the right of the cell), which again generally consists of a TCO covered glass substrate, coated with a thin layer of platinum. To complete the DSC, the photoanode and CE are sealed together and the final component, a redox electrolyte, is back-filled through the CE, filling the void between the two electrodes [214]. In the first generation of DSCs, the redox electrolyte consisted of a mixture of I_2 and an iodide species dissolved in an organic solvent. Triiodide (I_3^-) is formed in the electrolyte by the following equilibrium reaction:

$$\mathrm{I^- + I_2 \rightleftharpoons I_3^-}$$

Equation 1.5

Figure 1.12(b) shows the energy level diagram for this generalised DSC design [215]. When light is incident on the DSC through the photoanode, a dye molecule (S^O in Figure 1.12(b)) can absorb photon and excite an electron from the highest occupied molecular orbital (HOMO) to the lowest unoccupied molecular orbital (LUMO), leaving the dye molecule in an excited state (S^*). The excited electron can then get injected into the n-type TiO_2 scaffold, where it is conducted to the TCO layer and into the external circuit, leaving the dye in a cationic state (S^+). Once the electron has passed through the load of the external circuit it arrives back at the platinised CE. Here, the platinum layer of the CE can catalyse the reduction of the I_3^- in the redox electrolyte by the following equilibrium equation:

$$I_3^- + 2e^- \rightleftharpoons 3I^-$$

Equation 1.6

The I^- produced as a result of Equation 1.6 occurring at the CE then diffuses across the cell to the photoanode whereby it undergoes a series of redox reactions with the dye cation, ultimately regenerating the dye to its original state (S^O) and reforming I_3^-, which is then able to diffuse back across the cell to the CE. With the dye regenerated, it is again able to absorb incident photons, and the cell is in this way able to continue producing photocurrent while it is illuminated. Finally, as seen in Figure 1.12(b), the maximum possible V_{OC} of these cells is determined by the difference in potentials between the Fermi level of the TiO_2, which sits just below the TiO_2 conduction band edge, and the potential of the I^-/I_3^- redox couple [216].

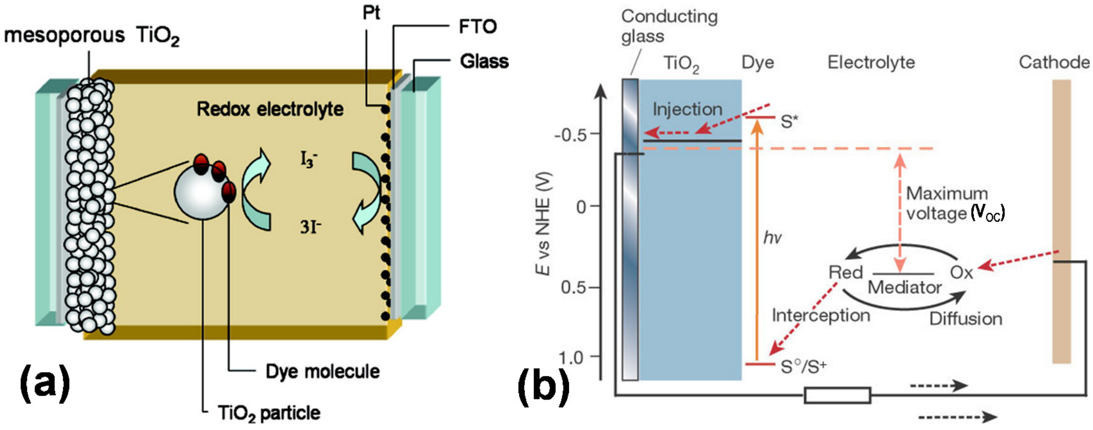

Figure 1.12: (a) Schematic showing a generalised dye-sensitised solar cell design (from [214]) with (b) depicting a generalised energy level diagram for a dye-sensitised solar cell showing the direction of electron flow within the cell and the external circuit (modified from [215]).

Since O'Regan and Grätzel's first DSC paper [213], there has been a plethora of methods proposed for improving the photovoltaic performance of DSCs. These include molecular engineering of new dyes, changing the semiconductor present on the photoanode, electrolyte modification including changing the redox couples and using solid state electrolytes, and changing the composition of the CE. For a comprehensive review on the alternatives that have been investigated in the first two decades since the O'Regan and Grätzel, readers are encouraged to view Hagfeldt et al.'s comprehensive 2010 review [214].

With an understanding of the operating mechanism of DSCs it is clear that the addition of CNTs to a number of areas could result in improvements to cell PCE [217]. For example, CNTs may be used to replace the TCOs in the photanode and CE, as a scaffold or additive for the semiconductor layer of the photanode, as a replacement catalytic coating for the CE or as a photoactive material themselves. Indeed, the following sections will explore some of these potential CNT applications in more detail.

1.6.2 Carbon Nanotubes as a Replacement for Transparent Conducting Oxide Layers

CNTs have been used in a number of different ways to replace the TCO layer present on both the photoanode and the CE of DSCs. For example, nitrogen doped CNTs, in conjunction with a layer of pure CNTs, have been used to replace the traditional FTO/Pt CE [218], with a Pt/CNT hybrid material TCO free CE found to be almost as effective as the normal platinised CE [219]. It has also been found that CNT films covered with a thin TiO_2 recombination-blocking layer can replace the TCO layer in the photoanode of a DSC [220]. Alternatively, multiple groups have also used CNTs to replace TCOs on flexible plastic substrates, in both the CE [221] and the photoanode of ZnO DSCs [222, 223]. Furthermore, CNTs have also successfully been used as counter electrodes in more recent fibre-, or wire-shaped, DSCs [224-226]. These fibre-shaped DSCs eschew the normal planar DSC design, instead incorporating a titanium fibre that is sensitised with dye, with the counter electrode wrapped around the wire.

1.6.3 Carbon Nanotubes as a Catalytic Replacement for Platinum

A more successful approach to incorporating CNTs into DSCs involves using them to replace the platinum layer on the CE [227], first demonstrated by Suzuki et al. [228]. MWNTs have frequently been shown to be good candidates for replacing platinum, either by themselves [229, 230] or as composites [231]. Similar to one of the aforementioned TCO replacement systems, nitrogen doped CNTs, this time decorated with cobalt or nickel nanoparticles, have also been shown to have good catalytic activities when used in I^-/I_3^- based DSCs [232].

1.6.4 Carbon Nanotubes within the Photoanode

Much work has also investigated the effect of adding CNTs into the semiconductor layer present on the photoanode of DSCs, as the CNTs should help increase the electrical conductivity and provide more direct routes for injected electrons to reach the TCO and hence the external circuit [233]. Both MWNTs [234, 235] and SWNTs [236-238] have been used in this approach, with both showing good potential. For example, a photoanode made through deposition of a mixed MWNTs-TiO_2 solution demonstrated a PCE of 10.29 % [235], while a photoanode made with TiO_2 coated semiconducting SWNTs that were also decorated with TiO_2 particles demonstrated a PCE of 10.6 %, the best PCE achieved to date with a SWNT/TiO_2 composite electrode [237].

1.6.5 Carbon Nanotubes as the Photoactive Material

Prior to 2010, there were very few examples in the literature in which CNTs were used as the photoactive material in photoelectrochemical cells using the typical DSC architecture. Using electrophoretically deposited SWNTs to form a working electrode in a photoelectrochemical cell, Barazzouk et al. [33], achieved photocurrents of approximately 8 $\mu A \cdot cm^{-2}$ and photovoltages of only 12 mV. Although these photovoltages are below the thermal voltage at room temperature (~26 mV), they exhibited a reproducible on/off effect when repeatedly exposed to light over a 10 min period. Later, Kongkanand et al. [239], used electrophoretically deposited SWNTs as a scaffold for unsensitised TiO_2 particles, achieving larger photocurrents of approximately 50 $\mu A \cdot cm^{-2}$. Wei et al. [240] used a gel-centrifugation method to prepare high purity semiconducting SWNTs. Vacuum filtration was then used to prepare thin films containing the high purity semiconducting SWNTs and unsorted SWNTs. These random films were then deposited onto ITO substrates and used as the working electrode in a photoelectrochemical cell. Although the photocurrents produced were less than 1 μA, the photocurrent produced when using semiconducting SWNT films was up to 35 % higher than cells made with unsorted SWNT films [240].

Bissett and Shapter [35], however, recognised that the random nature of electrophoretically deposited or vacuum filtered CNT networks was undesirable for the efficient transport of charge from the site of photon absorption to the TCO layer of the substrate. As such, they proposed to use a chemical attachment method [49, 241] to produce vertically aligned arrays of SWNTs on an FTO substrate, thereby reducing electron-hole recombination and increasing photocurrent. This method exploits the carboxylic acid groups present on the ends and sidewalls of the acid "cut" SWNTs described Section 1.2.4, creating ester bonds between a hydroxylated substrate and the SWNTs, resulting in vertically aligned SWNTs on the substrate.

Using this method, Bissett and Shapter produced a cell with a SWNT/FTO working electrode and a platinised FTO CE, using a standard I^-/I_3^- electrolyte, as shown in Figure 1.13(a). Cells made with these SWNT/FTO working electrodes showed a rapid photoresponse upon illumination of less than 200 ms, produced solely by the SWNTs. It was found that modifying the attachment time and the "cutting" time of the SWNTs could tune the photovoltaic performance of the cells. Despite this tuning however, the maximum J_{SC} observed in the cells was 4.7 $\mu A \cdot cm^{-2}$, lower than previous efforts. Although the cells did produce larger V_{OC}s of 40 mV, their FFs were still low (approximately 0.3) and hence their PCE was found to be 4.7×10^{-5} %, orders of magnitude below the PCE found in conventional DSCs. The authors did note though, that considering the very low amount of photoactive material present on their working electrodes compared to conventional DSCs that the results were indeed promising.

This work was further expanded upon by the Shapter group in the following years, investigating the sensitisation of these SWNT electrodes with dendrons [242] and conventional DSC dyes [50], as well as the effect that using different types of CNTs had on cell performance [243]. Tune et al. [50] used the same chemistry as Bissett and Shapter to chemically attach SWNTs to ITO substrates, which were then sensitised by the covalent attachment of the conventional DSC dye N3, as seen in Figure 1.13(b). Following the attachment of one layer of SWNTs, the CNT networks were built up by resubmerging the SWNT/ITO substrate into an appropriate SWNT solution containing a linker molecule, ethylenediamine. This allowed amide bonding between CNTs, resulting in a larger network of SWNTs that could then be functionalised with N3 dye, as seen in Figure 1.13(c). It was found that increasing the number of SWNT layers increased the J_{SC} of the cells (2.0 $\mu A \cdot cm^{-2}$ for one layer to 4.9 $\mu A \cdot cm^{-2}$ for five layers), while slightly decreasing the V_{OC} (47 – 43 mV). Addition of N3 dye to each layer also improved the J_{SC} of the cells (2.8 $\mu A \cdot cm^{-2}$ for one layer of sensitised SWNTs to 6.2 $\mu A \cdot cm^{-2}$ for five layers of sensitised SWNTs), while decreasing V_{OC} (43 – 36 mV). Both increasing the size of the SWNT network and sensitising the network resulted in slight increases of FF (from 0.28 to approximately 0.32), although the cells still remained at PCEs comparable to those of Bissett and Shapter.

Similar improvements were observed when polyamidoamine (PAMAM) dendrons were “grown” on SWNT/FTO electrodes, via ethylenediamine attachment to the SWNTs [242]. With optimised dendron growth, a J_{SC} of approximately 14 μA·cm^{-2} and V_{OC} of approximately 43 mV was achieved, although again, the maximum FF observed was 0.31. Bissett et al. [243] also investigated whether CNT type could be used to improve the performance of these cells, comparing chemically attached SWNTs and MWNTs with CVD SWNTs and MWNTs. Ultimately, it was found that chemically attached CNTs vastly outperformed their CVD counterparts and that in both cases SWNTs performed better than MWNTs.

While these studies displayed very low PCEs when compared with conventional DSCs, the improvements observed in photovoltaic performance after sensitisation with other photoactive molecules showed good promise for further research. Chen et al. [244] further improved the use of aligned CNTs in photoelectrochemical cells by sensitising MWNT fibres with N719 dye. These sensitised fibres were deposited on an FTO electrode which was then used as the working electrode for the photoelectrochemical cell. The aligned nature of the MWNTs comprising the fibre led to much higher values of PCE than previous works, with a maximum PCE of 4 % achieved [244]. This fibre-based design became the template for the fibre-shaped DSCs discussed in Section 1.6.2 [224-226].

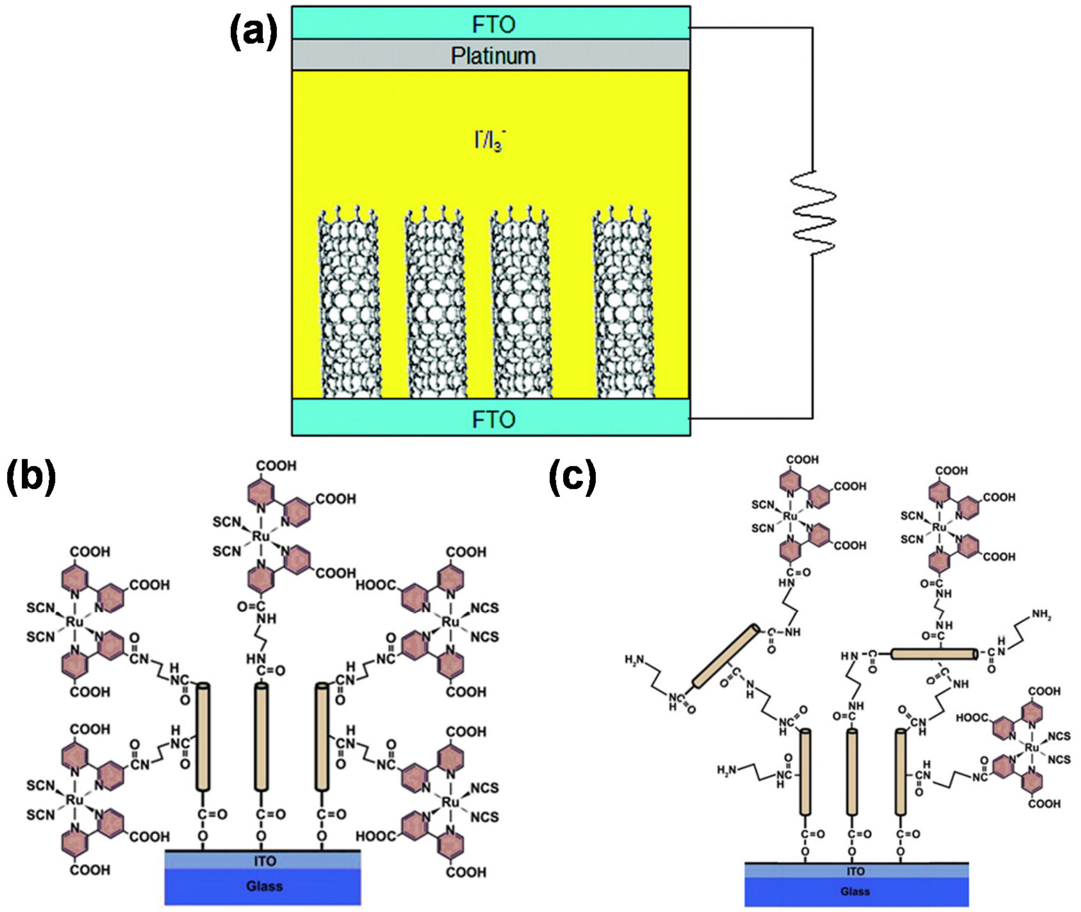

Figure 1.13: (a) Cell design for Bissett and Shapter's CNT DSC, with a photocathode consisting of chemically attached SWNTs to a FTO substrate (modified from [35]) and (b) The dye-sensitised photocathode of Tune et al. showing covalent attachment of dye to SWNTs covalently attached to an ITO substrate, with (c) showing how the SWNT network can be built up by covalent attachment of SWNTs to an existing layer of SWNTs and then sensitised (modified from [50]).

1.7 Carbon-Silicon Solar Cells

1.7.1 History and Overview

Carbon-silicon photovoltaics have been investigated as potential alternatives to p-n silicon photovoltaics for the past two decades. Initial interest focused on the use of amorphous carbonaceous thin films, which could be produced on n-type silicon by CVD of carbon feedstocks such as 2,5-dimethyl-*p*-benzoquinone [245] and camphor [246]. Following this approach, interest increased in nanocarbon films, with C_{60} being investigated on p-Si and n-Si substrates [247, 248]. However, as thin films of C_{60} are insulating, focus quickly moved to doping via ion-implantation, which causes the breakdown of C_{60} and formation of conducting amorphous carbonaceous films. Both p- and n-type doping was investigated, with phosphorous ion implantation of C_{60} on p-type silicon [249] and boron implantation of C_{60} on n-type silicon [250]. Control of ion implantation depth was also investigated as a means of improving the low efficiencies of these cells (generally <1 %), in order to create p-i-n solar cells [251], although this did not significantly improve efficiencies.

Nanocarbon-silicon photovoltaics have further developed in the last decade with the advent of carbon nanotube-silicon (CNT-Si) heterojunctions [252]. The first of these heterojunctions was developed by Wei et al. [11], who used CVD to grow a DWNT film. This fim was then suspended in distilled water and picked up on a pre-patterned n-type silicon substrate to create a p(CNT)-n(Si) junction, with a power conversion efficiency (PCE) of 1.31 %. SWNTs were soon used in the design [253, 254], and recent progress has seen the effect of chiralty mixing also investigated [255]. It was also found that chemical doping of the CNTs improved the PCE of the cells, with $SOCl_2$ doping seeing an increase in PCE to [253] and acid doping with HNO_3 leading to a PCE of 13.8 % [256]. Further investigations have changed the architecture of the cells for example, by adding conductive polymers [257], anti-reflection layers [258] or polymer interlayers between the CNTs and Si substrate [259]. The most successful architecture modification however was achieved by evaporating a layer of molybdenum oxide (MoO_x) onto the CNTs before the deposition of a gold front electrode [260]. This metal oxide layer acted as an antireflection coating, carrier dopant and carrier transport layer, increasing the PCE of the cells to 17.0 %, the highest published to date (albeit with an active area of 0.008 cm^{-2}) [260, 261].

While the exact mechanism by which these CNT-Si heterojunctions function, that is, whether they are Schottky or p-n junctions [64, 262] or metal-insulator-semiconductor junctions [263], is still debated, several of the CNTs' roles are clear. Importantly, the CNTs act as transparent conducting electrodes, transporting holes that are generated at the CNT-Si interface. However, these holes are generated as a result of charge separation at the CNT-Si interface, which is generated in part by the presence of the CNTs.

1.7.2 Graphene–Silicon Solar Cells

Graphene-silicon (G-Si) solar cells are a more recent example of carbon-silicon solar cells, first reported by Li et al. [264] in 2010, who investigated their potential as solar cells. Figure 1.14(a) shows a schematic of Li et al.'s [264] cell, with a schematic view showing the direction of charge flow in Figure 1.14(b) and a photograph of a the completed cell in Figure 1.14(c). These cells were produced by transferring CVD graphene sheets (GS Figure 1.14(b)) onto pre-patterned n-type silicon (n-Si) substrates. These n-Si substrates had a 300 nm oxide (SiO_2) layer, which serves as insulation between the graphene and the silicon, and, the top gold electrode and the silicon. By using photolithography and hydrofluoric acid (HF) etching, a window of exposed n-Si can be obtained. Following this etching, the gold front electrode and Ti/Pd/Ag back electrodes were sputtered onto the SiO_2 surface and exposed n-Si respectively. Finally, the graphene sheet can be transferred to the top of the cell, forming an interface with the exposed n-Si, which defines the active area, and the Au front electrode.

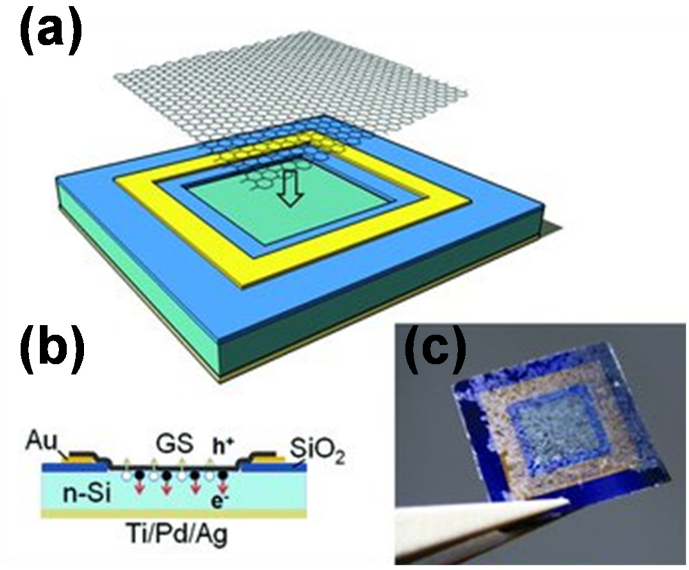

Figure 1.14: (a) A schematic of the first graphene-silicon Schottky junction solar cell, (b) a cross-sectional view of the cell, including direction of electron and hole flow and (c) photograph of the assembled cell (modified from [264]).

Despite the ambiguity described in Section 1.7.1 regarding the operating mechanisms of CNT-Si heterojunctions, Li et al. [264] described these cells as being Schottky junctions, and the description has been accepted [265]. A Schottky junction may be formed when a metal is brought into contact with a semiconductor if the work function of the metal is sufficiently larger than the work function of the semiconductor [266]. Figure 1.15(a) shows the energy band diagram at thermal equilibrium of a graphene-n-type silicon Schottky junction, where graphene acts as a metal. When the graphene is brought into contact with the n-Si, the Fermi levels (E_F) of the two materials become pinned to each other causing band bending in the n-Si, with electrons flowing from the n-Si into the graphene. This flow of electrons generates a depletion region in the n-Si with an in built potential (V_{bi}), seen in Figure 1.15(a), along with a Schottky barrier (Φ_{bn}). In the ideal case, the height of this Φ_{bn} is equal to the difference between the work function of the graphene (Φ_G) and the electron affinity of the n-Si (χ_{Si}).

Forward biasing a G-Si Schottky junction will cause the E_F of the n-Si to be shifted upwards, as seen in Figure 1.15(b). When this forward biased cell is under illumination, as is the case in Figure 1.15(b), then light with energy equal to that of the bandgap of silicon (i.e., $h\nu = E_g$) can generate an exciton, with an electron from the valence band (E_V) of the n-Si promoted to the conduction band (E_C) of the n-Si, leaving a hole in the E_V. The V_{bi} caused by the depletion region is then able to separate the exciton, driving the electron into the external circuit, with the hole transported away by the graphene, as depicted in Figure 1.15(b). Thus, similarly to the CNTs in CNT-Si heterojunctions, the graphene in these G-Si Schottky junctions functions not only as a transparent conducting electrode, but also as a key component in the ability to separate charge within the system.

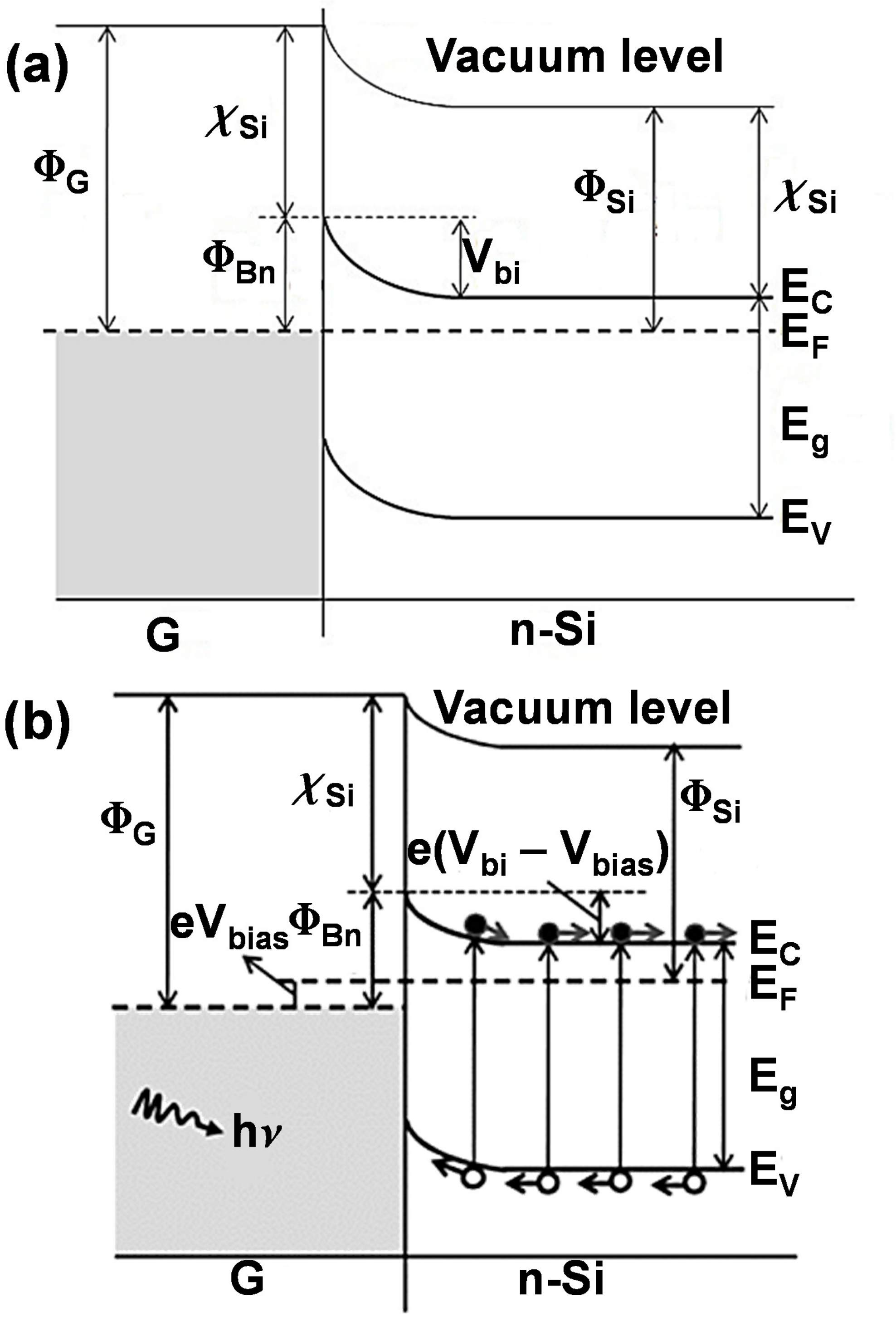

Figure 1.15: The energy band diagram (a) at thermal equilibrium of a graphene-silicon Schottky junction in the dark and (b) of a forward biased graphene-silicon Schottky junction under illumination, where Φ_G and Φ_{Si} are the work functions of graphene and silicon, χ_{Si} is the electron affinity of silicon, E_g is the bandgap of silicon, E_C is the conduction band energy of silicon, E_V is the valence band energy of silicon, E_F is the Fermi level, Φ_{bn} is the Schottky barrier height, V_{bi} is the built in potential barrier and V_{bias} is the forward bias potential (modified from [264]).

The solar cells produced by Li et al. [264] showed promising photovoltaic properties, with J_{SC}s of between 4 – 6.5 mA·cm^{-2}, V_{OC}s of between 0.42 – 0.48 V and FFs of between 0.45 – 0.56, leading to a PCE of 1.3 % under AM 1.5 illumination. While not performing as well as previous amorphous carbon-silicon solar cells or CNT-Si heterojunction solar cells, these cells nonetheless showed good potential future work along with good stability, retaining their performance over a two month period.

One early form of modification to this G-Si architecture was to replace the planar n-Si at the interface with a nanowire or pillar array [267-269]. These nanowire or silicon pillar arrays can be fabricated through either chemical etching [267] or plasma etching respectively [268, 269]. Using these nanostructured interfaces, the solar cell reflectance is decreased, and the distance that electrons and holes must travel before collection is also reduced. This architectural modification saw improvements to the PCE of the cells, despite the smaller "true" active area of the cells due to the nanowire configuration. Further architectural modifications made to the G-Si solar cell have included using conductive polymers such as poly(3,4-ethylenedioxythiophene) polystyrene sulfonate (PEDOT:PSS) on top of the graphene-silicon pillar array interface [269], where it acts as a more efficient hole transport layer, placing polymers interlayers such as poly(3-hexylthiophene) (P3HT) between the G-Si interface [270], where the P3HT can act as both a hole transport layer and an electron blocking layer, or growing insulating carbon interlayers on the n-Si to act as both an insulating layer and surface pacifier [271].

Another more obvious form of modification to the G-Si system is modulating the number graphene layers present over the active area, as the number of layers of graphene is directly related to the Φ_G [272, 273]. Ihm et al. [274] were the first to specifically investigate the effect that the number of layers of graphene had on the photovoltaic parameters of G-Si solar cells, albeit in a system using p-type silicon (p-Si) substrates rather than the normal n-Si. Although they used layer-by-layer stacking of CVD grown SLG, they found that the Φ_G increased as the number of layers increased, but due to their use of p-Si the V_{OC} and PCE of the cells decreased. Indeed, using n-Si Li et al. [275] found that as the work function of CVD graphene increased as the number of layers increased from one to six, the V_{OC} of their G-Si solar cells increased, indicating that the V_{bi} of the Schottky junction also increased. However, the J_{SC}, and hence PCE, of the cells was maximised at a graphene thickness of four layers, as further increases in thickness decreased the optical transmittance limiting the amount of photons incident on the G-Si interface. Interestingly, it has also been found in n-Si systems that despite its lower sheet resistance and similar optical transparency, G-Si solar cells made with five layers of layer-by-layer stacked SLG are still outperformed by G-Si solar cells made with five to seven layer thick SLG [276].

Significant research has also been directed towards enhancing the photovoltaic performance of G-Si Schottky junction solar cells via chemical doping methods. The first chemical dopant to be reported was thionyl chloride ($SOCl_2$) [267], a dopant commonly used in CNT-Si heterojunction solar cells [252]. As well as $SOCl_2$ [277], gold chloride ($AuCl_3$) [278, 279], bis(trifluoromethanesulfonyl)amide [($(CF_3SO_2)_2NH$)] (TFSA) [280, 281], silver nanoparticles [282], and exposure to HNO_3 vapour [269, 276, 277, 283, 284]. Generally, all of these dopants cause an increase in cell PCE by two somewhat interrelated methods. Firstly, the dopants cause p-type doping of the graphene, which causes an increase in Φ_G, hence increasing V_{bi} and in turn the V_{OC} of the cells. This p-doping of the graphene also serves to decrease the sheet resistance which in turn increases the J_{SC} of the cells and these two factors combined lead to significantly increased cell PCEs. Several studies did however find that the J_{SC} of G-Si cells made with FLG films was slightly decreased upon doping with HNO_3 [276, 277] and $SOCl_2$ [277] although in all instances these decreases accounted for a less than 5 % change in J_{SC}. Despite its frequent use as a chemical dopant for G-Si systems, HNO_3 doping is not stable over time [271], although its effect can be recovered with re-exposure of the cells to HNO_3 vapour [285]. $AuCl_3$ is generally seen as a more stable dopant [271], with reductions in cell performance as little as 10 % over a period of two weeks [279]. Finally, chemical doping methods can also be used in conjunction with antireflection coatings. In these cells, colloidal TiO_2 solutions are used to deposit anti-reflection layers on top of the graphene with both HNO_3 [285] and $AuCl_3$ [286] then being used to dope the cell. This approach, when used in conjunction with optimising the thickness of the native oxide layer present between the graphene and silicon at the interface has led to the current record PCE for G-Si Schottky junction solar cells of 15.6 % by Song et al. [286].

It is worth noting that all of the G-Si investigations discussed in this section have so far been carried out exclusively using CVD graphene, with no work conducted on solution processed G-Si Schottky junction solar cells.

1.7.3 Graphene Oxide–Silicon Solar Cells

While G-Si solar cell research has expanded considerably since 2010, there has comparatively little investigation into GO-Si or RGO-Si solar cells. A small number of papers have investigated GO or RGO heterojunctions with silicon for either solar cell [287-291] or photo-sensing applications [292, 293]. These photovoltaic applications have been undertaken using both n-Si [287-289] and p-Si [290, 291], with GO or RGO taking the place of graphene in the same architecture as seen in G-Si solar cells. Similar to G-Si solar cells, to date the best photovoltaic performance has been achieved with n-Si substrates (PCE of 0.31 %) [288]. Although not purely GO- or RGO-Si solar cells, GO has also been used as an interlayer, additive, or both, in hybrid organic-silicon heterojunctions, to great effect [294, 295]. Liu et al. [294] first used GO as an interlayer, first depositing a thick GO layer, the top of which was then plasma reduced leaving a RGO-GO-Si junction. This produced a PCE of 6.62 %, much higher than any reported RGO-Si junction. They then used a thinner layer of GO as an interlayer between PEDOT:PSS and Si, producing a PEDOT:PSS-GO-Si interface, which achieved a PCE of 8.09%. Finally they produced a PEDOT:PSS:GO composite and did away with the GO interlayer, achieving a PCE of 10.7 %, slightly higher than Tang et al. [295] who achieved a PCE of 10.3 % while also using PEDOT:PSS:GO composites.

The mechanism behind RGO-Si solar cells photovoltaic performance is again generally considered to be Schottky in nature [288-290], analogous to the G-Si mechanism discussed in Section 1.7.2. Thus, the difference in the work functions of RGO and n-Si causes Fermi level equilibration and band bending in the n-Si, with a corresponding depletion region set up at the RGO-Si interface. The photovoltaic performance of RGO-Si solar cells has to date not been as successful as either the organic-Si heterojunctions mentioned earlier, or as early CVD G-Si solar cells. They are often plagued by low J_{SC} (maximum of 4.28 mA·cm^{-2} [287]), low V_{OC} (maximum of 0.3 V [288]) and low FF (maximum of 0.35 [288]), leading to a current record PCE of 0.31 %. This low photovoltaic performance may be due to a number of factors, including poor work function engineering, large sheet resistance of the RGO films (several kΩ·square^{-1} to 745 kΩ·square^{-1} [287, 288]), poor optical transparency of the RGO films (30 – 35 % [288]), or a combination of all three. While Zhu et al. [288] did investigate the effect of thermal annealing on the photovoltaic performance of their RGO-Si cells, to date no work has investigated the effect that chemical doping might have on photovoltaic performance, despite its ability to both tune the work function of RGO and also decrease its sheet resistance.

1.8 Motivation

It is clear that for world electricity consumption to continue to increase, without a concomitant increase in CO_2 emissions, existing photovoltaic systems should be improved, in conjunction with other renewable energy sources. While these improvements may lead to increases in the maximum PCEs achieved, increasing the energy efficiency of their production is also a worthy goal.

Given their remarkable physical properties and the ability to use solution processing for their deposition and application, nanocarbon-based materials such as CNTs, graphene and graphene oxide present an obvious route for trying to increase both PCE and energy efficiency of current solar cell designs.

In this regard, the preceding literature review identified several areas that could be investigated including:

- The addition of photoactive molecules onto SWNT/FTO working electrodes for photoelectrochemical cells.
- Using solution processed, rather than CVD, graphene to make G-Si Schottky junction solar cells.
- Investigating the effects of annealing and chemical doping on RGO-Si Schottky junction solar cells.

1.9 Thesis Outline

This Thesis consists of:

- An experimental methods and materials chapter (Chapter 2), containing a brief overview of the common experimental techniques used throughout the Thesis and their expected results along with experimental methods that are common to more than one chapter.

- A chapter detailing the enhanced photovoltaic performance of a CNT photoelectrochemical solar cell following the addition of a polyaromatic hydrocarbon, found in organic solar cells, to the SWNT/FTO working electrode (Chapter 3).

- A chapter detailing the surfactant-assisted exfoliation of graphene and the subsequent use of this aqueous graphene dispersion to form G-Si Schottky junction solar cells (Chapter 4). These cells are optimised by tuning the thickness of the graphene films used to make them, along with thermal annealing and chemical doping.

- A chapter detailing the effects of thermal annealing and chemical doping on RGO-Si Schottky junction solar cells (Chapter 5). Comparisons between thermal annealing effects seen previously in the literature are made, along with the novel effects seen after chemical doping. These effects are compared and contrasted with those seen with the G-Si Schottky junction solar cells of the preceding chapter.

- A concluding chapter (Chapter 6), summarising the results found and their implications for further research.

1.10 References

1. International Energy Agency 2015, *Key world energy statistics*, International Energy Agency, Paris.

2. International Energy Agency 2015, *World energy outlook 2015: Executive summary*, International Energy Agency, Paris.

3. Division for Sustainable Development 2015, *Transforming our world: The 2030 agenda for sustainable development*, United Nations.

4. Framework Convention on Climate Change 2015, *Adoption of the Paris agreement*, United Nations.

5. International Energy Agency 2015, *Medium-term renewable energy market report 2015: Executive summary*, International Energy Agency, Paris.

6. Schiermeier, Q, Tollefson, J, Scully, T, Witze, A & Morton, O 2008, 'Electricity without carbon', *Nature*, vol. 454, no. 7206, pp. 816-23.

7. Chapin, DM, Fuller, CS & Pearson, GL 1954, *A new silicon p/n junction photocell for converting solar radiation into electrical power*, vol. 25, AIP.

8. Reinhard, P, Buecheler, S & Tiwari, AN 2013, 'Technological status of Cu(In,Ga)(Se,S)$_2$-based photovoltaics', *Solar Energy Materials and Solar Cells*, vol. 119, pp. 287-90.

9. Salomé, PMP, Rodriguez-Alvarez, H & Sadewasser, S 2015, 'Incorporation of alkali metals in chalcogenide solar cells', *Solar Energy Materials and Solar Cells*, vol. 143, pp. 9-20.

10. Mazzio, KA & Luscombe, CK 2015, 'The future of organic photovoltaics', *Chemical Society Reviews*, vol. 44, no. 1, pp. 78-90.

11. Lu, L, Kelly, MA, You, W & Yu, L 2015, 'Status and prospects for ternary organic photovoltaics', *Nature Photonics*, vol. 9, no. 8, pp. 491-500.

12. Ye, M, Wen, X, Wang, M, Iocozzia, J, Zhang, N, Lin, C & Lin, Z 2015, 'Recent advances in dye-sensitized solar cells: From photoanodes, sensitizers and electrolytes to counter electrodes', *Materials Today*, vol. 18, no. 3, pp. 155-62.

13. Sugathan, V, John, E & Sudhakar, K 2015, 'Recent improvements in dye sensitized solar cells: A review', *Renewable and Sustainable Energy Reviews*, vol. 52, pp. 54-64.

14. Kroto, HW, Heath, JR, O'Brien, SC, Curl, RF & Smalley, RE 1985, 'C_{60}: Buckminsterfullerene', *Nature*, vol. 318, no. 6042, pp. 162-3.

15. Iijima, S 1991, 'Helical microtubules of graphitic carbon', *Nature*, vol. 354, no. 6348, pp. 56-8.

16. Bethune, DS, Klang, CH, de Vries, MS, Gorman, G, Savoy, R, Vazquez, J & Beyers, R 1993, 'Cobalt-catalysed growth of carbon nanotubes with single-atomic-layer walls', *Nature*, vol. 363, no. 6430, pp. 605-7.

17. Brodie, BC 1859, 'On the atomic weight of graphite', *Philosophical Transactions of the Royal Society of London*, vol. 149, pp. 249-59.

18. Staudenmaier, L 1898, 'Verfahren zur darstellung der graphitsäure', *Berichte der deutschen chemischen Gesellschaft*, vol. 31, no. 2, pp. 1481-7.

19. Dresselhaus, MS, Dresselhaus, G & Hofmann, M 2008, 'Raman spectroscopy as a probe of graphene and carbon nanotubes', *Philosophical Transactions of the Royal Society A: Mathematical, Physical and Engineering Sciences*, vol. 366, no. 1863, pp. 231-6.

20. Geim, AK & Novoselov, KS 2007, 'The rise of graphene', *Nature Materials*, vol. 6, no. 3, pp. 183-91.

21. Radushkevich, L & Lukyanovich, V 1952, 'O strukture ugleroda, obrazujucegosja pri termiceskom razlozenii okisi ugleroda na zeleznom kontakte', *Russian Journal of Physical Chemistry*, vol. 26, pp. 88-95.

22. Hillert, M & Lange, N 1958, 'The structure of graphite filaments', *Zeitschrift für Kristallographie*, vol. 111, pp. 24-34.

23. Boehm, HP 1973, 'Carbon from carbon monoxide disproportionation on nickel and iron catalysts: Morphological studies and possible growth mechanisms', *Carbon*, vol. 11, no. 6, pp. 583-90.

24. Iijima, S & Ichihashi, T 1993, 'Single-shell carbon nanotubes of 1-nm diameter', *Nature*, vol. 363, no. 6430, pp. 603-5.

25. Belin, T & Epron, F 2005, 'Characterization methods of carbon nanotubes: A review', *Materials Science and Engineering: B*, vol. 119, no. 2, pp. 105-18.

26. De Volder, MFL, Tawfick, SH, Baughman, RH & Hart, AJ 2013, 'Carbon nanotubes: Present and future commercial applications', *Science*, vol. 339, no. 6119, pp. 535-9.

27. Dresselhaus, MS, Dresselhaus, G, Saito, R & Jorio, A 2005, 'Raman spectroscopy of carbon nanotubes', *Physics Reports*, vol. 409, no. 2, pp. 47-99.

28. Dürkop, T, Getty, SA, Cobas, E & Fuhrer, MS 2004, 'Extraordinary mobility in semiconducting carbon nanotubes', *Nano Letters*, vol. 4, no. 1, pp. 35-9.

29. Wei, BQ, Vajtai, R & Ajayan, PM 2001, 'Reliability and current carrying capacity of carbon nanotubes', *Applied Physics Letters*, vol. 79, no. 8, pp. 1172-4.

30. Peng, B, Locascio, M, Zapol, P, Li, S, Mielke, SL, Schatz, GC & Espinosa, HD 2008, 'Measurements of near-ultimate strength for multiwalled carbon nanotubes and irradiation-induced crosslinking improvements', *Nature Nanotechnology*, vol. 3, no. 10, pp. 626-31.

31. Zhang, Y & Iijima, S 1999, 'Elastic response of carbon nanotube bundles to visible light', *Physical Review Letters*, vol. 82, no. 17, p. 3472.

32. Shi, Y, Fu, D, Marsh, DH, Rance, GA, Khlobystov, AN & Li, L-J 2008, 'Photoresponse in self-assembled films of carbon nanotubes', *The Journal of Physical Chemistry C*, vol. 112, no. 33, pp. 13004-9.

33. Barazzouk, S, Hotchandani, S, Vinodgopal, K & Kamat, PV 2004, 'Single-wall carbon nanotube films for photocurrent generation. A prompt response to visible-light irradiation', *The Journal of Physical Chemistry B*, vol. 108, no. 44, pp. 17015-8.

34. Lee, JU 2005, 'Photovoltaic effect in ideal carbon nanotube diodes', *Applied Physics Letters*, vol. 87, no. 7, p. 073101.

35. Bissett, MA & Shapter, JG 2010, 'Photocurrent response from vertically aligned single-walled carbon nanotube arrays', *The Journal of Physical Chemistry C*, vol. 114, no. 14, pp. 6778-83.

36. Prasek, J, Drbohlavova, J, Chomoucka, J, Hubalek, J, Jasek, O, Adam, V & Kizek, R 2011, 'Methods for carbon nanotubes synthesis-review', *Journal of Materials Chemistry*, vol. 21, no. 40, pp. 15872-84.

37. Arora, N & Sharma, NN 2014, 'Arc discharge synthesis of carbon nanotubes: Comprehensive review', *Diamond and Related Materials*, vol. 50, pp. 135-50.

38. Yan, Y, Miao, J, Yang, Z, Xiao, F-X, Yang, HB, Liu, B & Yang, Y 2015, 'Carbon nanotube catalysts: Recent advances in synthesis, characterization and applications', *Chemical Society Reviews*, vol. 44, no. 10, pp. 3295-346.

39. Guo, T, Nikolaev, P, Thess, A, Colbert, DT & Smalley, RE 1995, 'Catalytic growth of single-walled manotubes by laser vaporization', *Chemical Physics Letters*, vol. 243, no. 1–2, pp. 49-54.

40. Chizari, K, Vena, A, Laurentius, L & Sundararaj, U 2014, 'The effect of temperature on the morphology and chemical surface properties of nitrogen-doped carbon nanotubes', *Carbon*, vol. 68, pp. 369-79.

41. Adjizian, J-J, Leghrib, R, Koos, AA, Suarez-Martinez, I, Crossley, A, Wagner, P, Grobert, N, Llobet, E & Ewels, CP 2014, 'Boron- and nitrogen-doped multi-wall carbon nanotubes for gas detection', *Carbon*, vol. 66, pp. 662-73.

42. Hata, K, Futaba, DN, Mizuno, K, Namai, T, Yumura, M & Iijima, S 2004, 'Water-assisted highly efficient synthesis of impurity-free single-walled carbon nanotubes', *Science*, vol. 306, no. 5700, pp. 1362-4.

43. Meyyappan, M, Lance, D, Alan, C & David, H 2003, 'Carbon nanotube growth by PECVD: A review', *Plasma Sources Science and Technology*, vol. 12, no. 2, p. 205.

44. Zhang, G, Mann, D, Zhang, L, Javey, A, Li, Y, Yenilmez, E, Wang, Q, McVittie, JP, Nishi, Y, Gibbons, J & Dai, H 2005, 'Ultra-high-yield growth of vertical single-walled carbon nanotubes: Hidden roles of hydrogen and oxygen', *Proceedings of the National Academy of Sciences of the United States of America*, vol. 102, no. 45, pp. 16141-5.

45. Sivakumar, VM, Mohamed, AR, Abdullah, AZ & Chai, S-P 2010, 'Role of reaction and factors of carbon nanotubes growth in chemical vapour decomposition process using methane - a highlight', *Journal of Nanomaterials*, vol. 2010, p. 11.

46. Liu, J, Rinzler, AG, Dai, H, Hafner, JH, Bradley, RK, Boul, PJ, Lu, A, Iverson, T, Shelimov, K, Huffman, CB, Rodriguez-Macias, F, Shon, Y-S, Lee, TR, Colbert, DT & Smalley, RE 1998, 'Fullerene pipes', *Science*, vol. 280, no. 5367, pp. 1253-6.

47. Liu, Z, Shen, Z, Zhu, T, Hou, S, Ying, L, Shi, Z & Gu, Z 2000, 'Organizing single-walled carbon nanotubes on gold using a wet chemical self-assembling technique', *Langmuir*, vol. 16, no. 8, pp. 3569-73.

48. Yang, C-M, Park, JS, An, KH, Lim, SC, Seo, K, Kim, B, Park, KA, Han, S, Park, CY & Lee, YH 2005, 'Selective removal of metallic single-walled carbon nanotubes with small diameters by using nitric and sulfuric acids', *The Journal of Physical Chemistry B*, vol. 109, no. 41, pp. 19242-8.

49. Yu, J, Shapter, JG, Quinton, JS, Johnston, MR & Beattie, DA 2007, 'Direct attachment of well-aligned single-walled carbon nanotube architectures to silicon (100) surfaces: A simple approach for device assembly', *Physical Chemistry Chemical Physics*, vol. 9, no. 4, pp. 510-20.

50. Tune, DD, Flavel, BS, Quinton, JS, Ellis, AV & Shapter, JG 2010, 'Single walled carbon nanotube network electrodes for dye solar cells', *Solar Energy Materials and Solar Cells*, vol. 94, no. 10, pp. 1665-72.

51. Blanch, AJ, Lenehan, CE & Quinton, JS 2010, 'Optimizing surfactant concentrations for dispersion of single-walled carbon nanotubes in aqueous solution', *The Journal of Physical Chemistry B*, vol. 114, no. 30, pp. 9805-11.

52. Moore, VC, Strano, MS, Haroz, EH, Hauge, RH, Smalley, RE, Schmidt, J & Talmon, Y 2003, 'Individually suspended single-walled carbon nanotubes in various surfactants', *Nano Letters*, vol. 3, no. 10, pp. 1379-82.

53. Sinani, VA, Gheith, MK, Yaroslavov, AA, Rakhnyanskaya, AA, Sun, K, Mamedov, AA, Wicksted, JP & Kotov, NA 2005, 'Aqueous dispersions of single-wall and multiwall carbon nanotubes with designed amphiphilic polycations', *Journal of the American Chemical Society*, vol. 127, no. 10, pp. 3463-72.

54. Nish, A, Hwang, J-Y, Doig, J & Nicholas, RJ 2007, 'Highly selective dispersion of single-walled carbon nanotubes using aromatic polymers', *Nature Nanotechnology*, vol. 2, no. 10, pp. 640-6.

55. Liu, Y, Gao, L, Zheng, S, Wang, Y, Sun, J, Kajiura, H, Li, Y & Noda, K 2007, 'Debundling of single-walled carbon nanotubes by using natural polyelectrolytes', *Nanotechnology*, vol. 18, no. 36, p. 365702.

56. Zheng, M, Jagota, A, Semke, ED, Diner, BA, McLean, RS, Lustig, SR, Richardson, RE & Tassi, NG 2003, 'DNA-assisted dispersion and separation of carbon nanotubes', *Nature Materials*, vol. 2, no. 5, pp. 338-42.

57. Arnold, MS, Green, AA, Hulvat, JF, Stupp, SI & Hersam, MC 2006, 'Sorting carbon nanotubes by electronic structure using density differentiation', *Nature Nanotechnology*, vol. 1, no. 1, pp. 60-5.

58. Liu, H, Nishide, D, Tanaka, T & Kataura, H 2011, 'Large-scale single-chirality separation of single-wall carbon nanotubes by simple gel chromatography', *Nature Communications*, vol. 2, p. 309.

59. Flavel, BS, Moore, KE, Pfohl, M, Kappes, MM & Hennrich, F 2014, 'Separation of single-walled carbon nanotubes with a gel permeation chromatography system', *ACS Nano*, vol. 8, no. 2, pp. 1817-26.

60. Li, X, Jung, Y, Sakimoto, K, Goh, T-H, Reed, MA & Taylor, AD 2013, 'Improved efficiency of smooth and aligned single walled carbon nanotube/silicon hybrid solar cells', *Energy & Environmental Science*, vol. 6, no. 3, pp. 879-87.

61. Davis, VA, Parra-Vasquez, ANG, Green, MJ, Rai, PK, Behabtu, N, Prieto, V, Booker, RD, Schmidt, J, Kesselman, E, Zhou, W, Fan, H, Adams, WW, Hauge, RH, Fischer, JE, Cohen, Y, Talmon, Y, Smalley, RE & Pasquali, M 2009, 'True solutions of single-walled carbon nanotubes for assembly into macroscopic materials', *Nature Nanotechnology*, vol. 4, no. 12, pp. 830-4.

62. Pénicaud, A, Poulin, P, Derré, A, Anglaret, E & Petit, P 2005, 'Spontaneous dissolution of a single-wall carbon nanotube salt', *Journal of the American Chemical Society*, vol. 127, no. 1, pp. 8-9.

63. Clancy, AJ, Melbourne, J & Shaffer, MSP 2015, 'A one-step route to solubilised, purified or functionalised single-walled carbon nanotubes', *Journal of Materials Chemistry A*, vol. 3, no. 32, pp. 16708-15.

64. Tune, DD, Blanch, AJ, Shearer, CJ, Moore, KE, Pfohl, M, Shapter, JG & Flavel, BS 2015, 'Aligned carbon nanotube thin films from liquid crystal polyelectrolyte inks', *ACS Applied Materials & Interfaces*, vol. 7, no. 46, pp. 25857-64.

65. Lawal, AT 2016, 'Synthesis and utilization of carbon nanotubes for fabrication of electrochemical biosensors', *Materials Research Bulletin*, vol. 73, pp. 308-50.

66. Bartelmess, J, Quinn, SJ & Giordani, S 2015, 'Carbon nanomaterials: Multi-functional agents for biomedical fluorescence and Raman imaging', *Chemical Society Reviews*, vol. 44, no. 14, pp. 4672-98.

67. Karimi, M, Solati, N, Ghasemi, A, Estiar, MA, Hashemkhani, M, Kiani, P, Mohamed, E, Saeidi, A, Taheri, M, Avci, P, Aref, AR, Amiri, M, Baniasadi, F & Hamblin, MR 2015, 'Carbon nanotubes part ii: A remarkable carrier for drug and gene delivery', *Expert Opinion on Drug Delivery*, vol. 12, no. 7, pp. 1089-105.

68. Slattery, AD, Blanch, AJ, Quinton, JS & Gibson, CT 2013, 'Efficient attachment of carbon nanotubes to conventional and high-frequency afm probes enhanced by electron beam processes', *Nanotechnology*, vol. 24, no. 23, p. 235705.

69. Li, Y, Sun, Y & Yeow, JTW 2015, 'Nanotube field electron emission: Principles, development, and applications', *Nanotechnology*, vol. 26, no. 24, p. 242001.

70. Wallace, PR 1947, 'The band theory of graphite', *Physical Review*, vol. 71, no. 9, p. 622.

71. Slonczewski, JC & Weiss, PR 1958, 'Band structure of graphite', *Physical Review*, vol. 109, no. 2, p. 272.

72. Krishnan, A, Dujardin, E, Treacy, MMJ, Hugdahl, J, Lynum, S & Ebbesen, TW 1997, 'Graphitic cones and the nucleation of curved carbon surfaces', *Nature*, vol. 388, no. 6641, pp. 451-4.

73. Shioyama, H 2001, 'Cleavage of graphite to graphene', *Journal of Materials Science Letters*, vol. 20, no. 6, pp. 499-500.

74. Land, TA, Michely, T, Behm, RJ, Hemminger, JC & Comsa, G 1992, 'Stm investigation of single layer graphite structures produced on Pt(111) by hydrocarbon decomposition', *Surface Science*, vol. 264, no. 3, pp. 261-70.

75. Nagashima, A, Nuka, K, Itoh, H, Ichinokawa, T, Oshima, C & Otani, S 1993, 'Electronic states of monolayer graphite formed on TiC(111) surface', *Surface Science*, vol. 291, no. 1–2, pp. 93-8.

76. Kobayashi, K & Tsukada, M 1994, 'Electronic structure of monolayer graphite on a TiC(111) surface', *Physical Review B*, vol. 49, no. 11, pp. 7660-9.

77. Novoselov, KS, Geim, AK, Morozov, SV, Jiang, D, Zhang, Y, Dubonos, SV, Grigorieva, IV & Firsov, AA 2004, 'Electric field effect in atomically thin carbon films', *Science*, vol. 306, no. 5696, pp. 666-9.

78. Novoselov, KS, Jiang, D, Schedin, F, Booth, TJ, Khotkevich, VV, Morozov, SV & Geim, AK 2005, 'Two-dimensional atomic crystals', *Proceedings of the National Academy of Sciences of the United States of America*, vol. 102, no. 30, pp. 10451-3.

79. Novoselov, KS, Geim, AK, Morozov, SV, Jiang, D, Katsnelson, MI, Grigorieva, IV, Dubonos, SV & Firsov, AA 2005, 'Two-dimensional gas of massless Dirac fermions in graphene', *Nature*, vol. 438, no. 7065, pp. 197-200.

80. Reina, A, Jia, X, Ho, J, Nezich, D, Son, H, Bulovic, V, Dresselhaus, MS & Kong, J 2008, 'Large area, few-layer graphene films on arbitrary substrates by chemical vapor deposition', *Nano Letters*, vol. 9, no. 1, pp. 30-5.

81. Castro Neto, AH, Guinea, F, Peres, NMR, Novoselov, KS & Geim, AK 2009, 'The electronic properties of graphene', *Reviews of Modern Physics*, vol. 81, no. 1, pp. 109-62.

82. Nair, RR, Blake, P, Grigorenko, AN, Novoselov, KS, Booth, TJ, Stauber, T, Peres, NMR & Geim, AK 2008, 'Fine structure constant defines visual transparency of graphene', *Science*, vol. 320, no. 5881, p. 1308.

83. Bae, S, Kim, H, Lee, Y, Xu, X, Park, J-S, Zheng, Y, Balakrishnan, J, Lei, T, Ri Kim, H, Song, YI, Kim, Y-J, Kim, KS, Ozyilmaz, B, Ahn, J-H, Hong, BH & Iijima, S 2010, 'Roll-to-roll production of 30-inch graphene films for transparent electrodes', *Nature Nanotechnology*, vol. 5, no. 8, pp. 574-8.

84. Geim, AK & MacDonald, AH 2007, *Graphene: Exploring carbon flatland*, vol. 60, AIP.

85. Katsnelson, MI, Novoselov, KS & Geim, AK 2006, 'Chiral tunnelling and the klein paradox in graphene', *Nature Physics*, vol. 2, no. 9, pp. 620-5.

86. Bolotin, KI, Sikes, KJ, Jiang, Z, Klima, M, Fudenberg, G, Hone, J, Kim, P & Stormer, HL 2008, 'Ultrahigh electron mobility in suspended graphene', *Solid State Communications*, vol. 146, no. 9-10, pp. 351-5.

87. Katsnelson, MI 'Graphene: Carbon in two dimensions', *Materials Today*, vol. 10, no. 1-2, pp. 20-7.

88. Lee, C, Wei, X, Kysar, JW & Hone, J 2008, 'Measurement of the elastic properties and intrinsic strength of monolayer graphene', *Science*, vol. 321, no. 5887, pp. 385-8.

89. Bunch, JS, Verbridge, SS, Alden, JS, van der Zande, AM, Parpia, JM, Craighead, HG & McEuen, PL 2008, 'Impermeable atomic membranes from graphene sheets', *Nano Letters*, vol. 8, no. 8, pp. 2458-62.

90. Hu, S, Lozada-Hidalgo, M, Wang, FC, Mishchenko, A, Schedin, F, Nair, RR, Hill, EW, Boukhvalov, DW, Katsnelson, MI, Dryfe, RAW, Grigorieva, IV, Wu, HA & Geim, AK 2014, 'Proton transport through one-atom-thick crystals', *Nature*, vol. 516, no. 7530, pp. 227-30.

91. Lozada-Hidalgo, M, Hu, S, Marshall, O, Mishchenko, A, Grigorenko, AN, Dryfe, RAW, Radha, B, Grigorieva, IV & Geim, AK 2016, 'Sieving hydrogen isotopes through two-dimensional crystals', *Science*, vol. 351, no. 6268, pp. 68-70.

92. Nair, RR, Blake, P, Blake, JR, Zan, R, Anissimova, S, Bangert, U, Golovanov, AP, Morozov, SV, Geim, AK, Novoselov, KS & Latychevskaia, T 2010, 'Graphene as a transparent conductive support for studying biological molecules by transmission electron microscopy', *Applied Physics Letters*, vol. 97, no. 15, p. 153102.

93. Wang, L, Meric, I, Huang, PY, Gao, Q, Gao, Y, Tran, H, Taniguchi, T, Watanabe, K, Campos, LM, Muller, DA, Guo, J, Kim, P, Hone, J, Shepard, KL & Dean, CR 2013, 'One-dimensional electrical contact to a two-dimensional material', *Science*, vol. 342, no. 6158, pp. 614-7.

94. Zhang, W, Lin, C-T, Liu, K-K, Tite, T, Su, C-Y, Chang, C-H, Lee, Y-H, Chu, C-W, Wei, K-H, Kuo, J-L & Li, L-J 2011, 'Opening an electrical band gap of bilayer graphene with molecular doping', *ACS Nano*, vol. 5, no. 9, pp. 7517-24.

95. Xu, H, Xie, L, Zhang, H & Zhang, J 2011, 'Effect of graphene fermi level on the Raman scattering intensity of molecules on graphene', *ACS Nano*, vol. 5, no. 7, pp. 5338-44.

96. Yoon, D, Son, Y-W & Cheong, H 2011, 'Negative thermal expansion coefficient of graphene measured by Raman spectroscopy', *Nano Letters*, vol. 11, no. 8, pp. 3227-31.

97. Cançado, LG, Jorio, A, Ferreira, EHM, Stavale, F, Achete, CA, Capaz, RB, Moutinho, MVO, Lombardo, A, Kulmala, TS & Ferrari, AC 2011, 'Quantifying defects in graphene via Raman spectroscopy at different excitation energies', *Nano Letters*, vol. 11, no. 8, pp. 3190-6.

98. Yu, Q, Lian, J, Siriponglert, S, Li, H, Chen, YP & Pei, S-S 2008, 'Graphene segregated on Ni surfaces and transferred to insulators', *Applied Physics Letters*, vol. 93, no. 11, p. 113103.

99. De Arco, LG, Yi, Z, Kumar, A & Chongwu, Z 2009, 'Synthesis, transfer, and devices of single- and few-layer graphene by chemical vapor deposition', *IEEE Transactions on Nanotechnology*, vol. 8, no. 2, pp. 135-8.

100. Kim, KS, Zhao, Y, Jang, H, Lee, SY, Kim, JM, Kim, KS, Ahn, J-H, Kim, P, Choi, J-Y & Hong, BH 2009, 'Large-scale pattern growth of graphene films for stretchable transparent electrodes', *Nature*, vol. 457, no. 7230, pp. 706-10.

101. Kitaura, R, Miyata, Y, Xiang, R, Hone, J, Kong, J, Ruoff, RS & Maruyama, S 2015, 'Chemical vapor deposition growth of graphene and related materials', *Journal of the Physical Society of Japan*, vol. 84, no. 12, p. 121013.

102. Li, X, Cai, W, An, J, Kim, S, Nah, J, Yang, D, Piner, R, Velamakanni, A, Jung, I, Tutuc, E, Banerjee, SK, Colombo, L & Ruoff, RS 2009, 'Large-area synthesis of high-quality and uniform graphene films on copper foils', *Science*, vol. 324, no. 5932, pp. 1312-4.

103. Zhou, H, Yu, WJ, Liu, L, Cheng, R, Chen, Y, Huang, X, Liu, Y, Wang, Y, Huang, Y & Duan, X 2013, 'Chemical vapour deposition growth of large single crystals of monolayer and bilayer graphene', *Nature Communications*, vol. 4.

104. Nguyen, VL, Shin, BG, Duong, DL, Kim, ST, Perello, D, Lim, YJ, Yuan, QH, Ding, F, Jeong, HY, Shin, HS, Lee, SM, Chae, SH, Vu, QA, Lee, SH & Lee, YH 2015, 'Seamless stitching of graphene domains on polished copper (111) foil', *Advanced Materials*, vol. 27, no. 8, pp. 1376-82.

105. Zhang, Y, Zhang, L & Zhou, C 2013, 'Review of chemical vapor deposition of graphene and related applications', *Accounts of Chemical Research*, vol. 46, no. 10, pp. 2329-39.

106. Park, S & Ruoff, RS 2009, 'Chemical methods for the production of graphenes', *Nature Nanotechnology*, vol. 4, no. 4, pp. 217-24.

107. Blake, P, Brimicombe, PD, Nair, RR, Booth, TJ, Jiang, D, Schedin, F, Ponomarenko, LA, Morozov, SV, Gleeson, HF, Hill, EW, Geim, AK & Novoselov, KS 2008, 'Graphene-based liquid crystal device', *Nano Letters*, vol. 8, no. 6, pp. 1704-8.

108. Hernandez, Y, Nicolosi, V, Lotya, M, Blighe, FM, Sun, Z, De, S, McGovern, IT, Holland, B, Byrne, M, Gun'Ko, YK, Boland, JJ, Niraj, P, Duesberg, G, Krishnamurthy, S, Goodhue, R, Hutchison, J, Scardaci, V, Ferrari, AC & Coleman, JN 2008, 'High-yield production of graphene by liquid-phase exfoliation of graphite', *Nature Nanotechnology*, vol. 3, no. 9, pp. 563-8.

109. Giordani, S, Bergin, SD, Nicolosi, V, Lebedkin, S, Kappes, MM, Blau, WJ & Coleman, JN 2006, 'Debundling of single-walled nanotubes by dilution: Observation of large populations of individual nanotubes in amide solvent dispersions', *The Journal of Physical Chemistry B*, vol. 110, no. 32, pp. 15708-18.

110. Bourlinos, AB, Georgakilas, V, Zboril, R, Steriotis, TA & Stubos, AK 2009, 'Liquid-phase exfoliation of graphite towards solubilized graphenes', *Small*, vol. 5, no. 16, pp. 1841-5.

111. Hernandez, Y, Lotya, M, Rickard, D, Bergin, SD & Coleman, JN 2009, 'Measurement of multicomponent solubility parameters for graphene facilitates solvent discovery', *Langmuir*, vol. 26, no. 5, pp. 3208-13.

112. Economopoulos, SP, Rotas, G, Miyata, Y, Shinohara, H & Tagmatarchis, N 2010, 'Exfoliation and chemical modification using microwave irradiation affording highly functionalized graphene', *ACS Nano*, vol. 4, no. 12, pp. 7499-507.

113. Hamilton, CE, Lomeda, JR, Sun, Z, Tour, JM & Barron, AR 2009, 'High-yield organic dispersions of unfunctionalized graphene', *Nano Letters*, vol. 9, no. 10, pp. 3460-2.

114. Hasan, T, Torrisi, F, Sun, Z, Popa, D, Nicolosi, V, Privitera, G, Bonaccorso, F & Ferrari, AC 2010, 'Solution-phase exfoliation of graphite for ultrafast photonics', *physica status solidi (b)*, vol. 247, no. 11-12, pp. 2953-7.

115. Khan, U, O'Neill, A, Lotya, M, De, S & Coleman, JN 2010, 'High-concentration solvent exfoliation of graphene', *Small*, vol. 6, no. 7, pp. 864-71.

116. Khan, U, Porwal, H, O’Neill, A, Nawaz, K, May, P & Coleman, JN 2011, 'Solvent-exfoliated graphene at extremely high concentration', *Langmuir*, vol. 27, no. 15, pp. 9077-82.

117. O’Neill, A, Khan, U, Nirmalraj, PN, Boland, J & Coleman, JN 2011, 'Graphene dispersion and exfoliation in low boiling point solvents', *The Journal of Physical Chemistry C*, vol. 115, no. 13, pp. 5422-8.

118. Choi, E-Y, Choi, WS, Lee, YB & Noh, Y-Y 2011, 'Production of graphene by exfoliation of graphite in a volatile organic solvent', *Nanotechnology*, vol. 22, no. 36, p. 365601.

119. Withers, F, Yang, H, Britnell, L, Rooney, AP, Lewis, E, Felten, A, Woods, CR, Sanchez Romaguera, V, Georgiou, T, Eckmann, A, Kim, YJ, Yeates, SG, Haigh, SJ, Geim, AK, Novoselov, KS & Casiraghi, C 2014, 'Heterostructures produced from nanosheet-based inks', *Nano Letters*, vol. 14, no. 7, pp. 3987-92.

120. Finn, DJ, Lotya, M, Cunningham, G, Smith, RJ, McCloskey, D, Donegan, JF & Coleman, JN 2014, 'Inkjet deposition of liquid-exfoliated graphene and MoS_2 nanosheets for printed device applications', *Journal of Materials Chemistry C*, vol. 2, no. 5, pp. 925-32.

121. Lotya, M, Hernandez, Y, King, PJ, Smith, RJ, Nicolosi, V, Karlsson, LS, Blighe, FM, De, S, Wang, Z, McGovern, IT, Duesberg, GS & Coleman, JN 2009, 'Liquid phase production of graphene by exfoliation of graphite in surfactant/water solutions', *Journal of the American Chemical Society*, vol. 131, no. 10, pp. 3611-20.

122. Green, AA & Hersam, MC 2009, 'Solution phase production of graphene with controlled thickness via density differentiation', *Nano Letters*, vol. 9, no. 12, pp. 4031-6.

123. Lotya, M, King, PJ, Khan, U, De, S & Coleman, JN 2010, 'High-concentration, surfactant-stabilized graphene dispersions', *ACS Nano*, vol. 4, no. 6, pp. 3155-62.

124. Zhang, M, Parajuli, RR, Mastrogiovanni, D, Dai, B, Lo, P, Cheung, W, Brukh, R, Chiu, PL, Zhou, T, Liu, Z, Garfunkel, E & He, H 2010, 'Production of graphene sheets by direct dispersion with aromatic healing agents', *Small*, vol. 6, no. 10, pp. 1100-7.

125. Vadukumpully, S, Paul, J & Valiyaveettil, S 2009, 'Cationic surfactant mediated exfoliation of graphite into graphene flakes', *Carbon*, vol. 47, no. 14, pp. 3288-94.

126. Sampath, S, Basuray, AN, Hartlieb, KJ, Aytun, T, Stupp, SI & Stoddart, JF 2013, 'Direct exfoliation of graphite to graphene in aqueous media with diazaperopyrenium dications', *Advanced Materials*, vol. 25, no. 19, pp. 2740-5.

127. Guardia, L, Fernández-Merino, MJ, Paredes, JI, Solís-Fernández, P, Villar-Rodil, S, Martínez-Alonso, A & Tascón, JMD 2011, 'High-throughput production of pristine graphene in an aqueous dispersion assisted by non-ionic surfactants', *Carbon*, vol. 49, no. 5, pp. 1653-62.

128. Smith, RJ, Lotya, M & Coleman, JN 2010, 'The importance of repulsive potential barriers for the dispersion of graphene using surfactants', *New Journal of Physics*, vol. 12, no. 12, p. 125008.

129. Wang, G, Wang, B, Park, J, Wang, Y, Sun, B & Yao, J 2009, 'Highly efficient and large-scale synthesis of graphene by electrolytic exfoliation', *Carbon*, vol. 47, no. 14, pp. 3242-6.

130. Huang, H, Xia, Y, Tao, X, Du, J, Fang, J, Gan, Y & Zhang, W 2012, 'Highly efficient electrolytic exfoliation of graphite into graphene sheets based on li ions intercalation-expansion-microexplosion mechanism', *Journal of Materials Chemistry*, vol. 22, no. 21, pp. 10452-6.

131. Zhu, L, Zhao, X, Li, Y, Yu, X, Li, C & Zhang, Q 2013, 'High-quality production of graphene by liquid-phase exfoliation of expanded graphite', *Materials Chemistry and Physics*, vol. 137, no. 3, pp. 984-90.

132. Qian, W, Hao, R, Hou, Y, Tian, Y, Shen, C, Gao, H & Liang, X 2009, 'Solvothermal-assisted exfoliation process to produce graphene with high yield and high quality', *Nano Research*, vol. 2, no. 9, pp. 706-12.

133. Chen, X, Dobson, JF & Raston, CL 2012, 'Vortex fluidic exfoliation of graphite and boron nitride', *Chemical Communications*, vol. 48, no. 31, pp. 3703-5.

134. Paton, KR, Varrla, E, Backes, C, Smith, RJ, Khan, U, O'Neill, A, Boland, C, Lotya, M, Istrate, OM, King, P, Higgins, T, Barwich, S, May, P, Puczkarski, P, Ahmed, I, Moebius, M, Pettersson, H, Long, E, Coelho, J, O'Brien, SE, McGuire, EK, Sanchez, BM, Duesberg, GS, McEvoy, N, Pennycook, TJ, Downing, C, Crossley, A, Nicolosi, V & Coleman, JN 2014, 'Scalable production of large quantities of defect-free few-layer graphene by shear exfoliation in liquids', *Nature Materials*, vol. 13, no. 6, pp. 624-30.

135. Varrla, E, Paton, KR, Backes, C, Harvey, A, Smith, RJ, McCauley, J & Coleman, JN 2014, 'Turbulence-assisted shear exfoliation of graphene using household detergent and a kitchen blender', *Nanoscale*, vol. 6, no. 20, pp. 11810-9.

136. Khan, U, May, P, Porwal, H, Nawaz, K & Coleman, JN 2013, 'Improved adhesive strength and toughness of polyvinyl acetate glue on addition of small quantities of graphene', *ACS Applied Materials & Interfaces*, vol. 5, no. 4, pp. 1423-8.

137. Ong, W-J, Voon, S-Y, Tan, L-L, Goh, BT, Yong, S-T & Chai, S-P 2014, 'Enhanced daylight-induced photocatalytic activity of solvent exfoliated graphene (SEG)/ZnO hybrid nanocomposites toward degradation of reactive black 5', *Industrial & Engineering Chemistry Research*, vol. 53, no. 44, pp. 17333-44.

138. Capasso, A, Del Rio Castillo, AE, Sun, H, Ansaldo, A, Pellegrini, V & Bonaccorso, F 2015, 'Ink-jet printing of graphene for flexible electronics: An environmentally-friendly approach', *Solid State Communications*, vol. 224, pp. 53-63.

139. De, S, King, PJ, Lotya, M, O'Neill, A, Doherty, EM, Hernandez, Y, Duesberg, GS & Coleman, JN 2010, 'Flexible, transparent, conducting films of randomly stacked graphene from surfactant-stabilized, oxide-free graphene dispersions', *Small*, vol. 6, no. 3, pp. 458-64.

140. Trapalis, A, Todorova, N, Giannakopoulou, T, Boukos, N, Speliotis, T, Dimotikali, D & Yu, J 2016, 'TiO_2/graphene composite photocatalysts for NO_x removal: A comparison of surfactant-stabilized graphene and reduced graphene oxide', *Applied Catalysis B: Environmental*, vol. 180, pp. 637-47.

141. Mendoza-Sánchez, B, Coelho, J, Pokle, A & Nicolosi, V 2015, 'A 2d graphene-manganese oxide nanosheet hybrid synthesized by a single step liquid-phase co-exfoliation method for supercapacitor applications', *Electrochimica Acta*, vol. 174, pp. 696-705.

142. Ayán-Varela, M, Paredes, JI, Guardia, L, Villar-Rodil, S, Munuera, JM, Díaz-González, M, Fernández-Sánchez, C, Martínez-Alonso, A & Tascón, JMD 2015, 'Achieving extremely concentrated aqueous dispersions of graphene flakes and catalytically efficient graphene-metal nanoparticle hybrids with flavin mononucleotide as a high-performance stabilizer', *ACS Applied Materials & Interfaces*, vol. 7, no. 19, pp. 10293-307.

143. Walch, NJ, Davis, F, Langford, N, Holmes, JL, Collyer, SD & Higson, SPJ 2015, 'Enhancement of electrode performance by a simple casting method using sonochemically exfoliated graphene', *Analytical Chemistry*, vol. 87, no. 18, pp. 9273-9.

144. Liang, S, Shen, Z, Yi, M, Liu, L, Zhang, X & Ma, S 2016, 'In-situ exfoliated graphene for high-performance water-based lubricants', *Carbon*, vol. 96, pp. 1181-90.

145. Allen, MJ, Tung, VC & Kaner, RB 2009, 'Honeycomb carbon: A review of graphene', *Chemical Reviews*, vol. 110, no. 1, pp. 132-45.

146. Geim, AK 2010, 'Many pioneers in graphene discovery', *APS News*, vol. 19, no. 1, January 2010.

147. Boehm, HP, Clauss, A, Fischer, GO & Hofmann, U 1962, 'Dünnste kohlenstoff-folien', *Z. Naturforschung*, vol. 17b, pp. 150-3.

148. Boehm, HP, Clauss, A, Fischer, GO & Hofmann, U 1962, 'Surface properties of extremely thin graphite lamellae', *Proceedings of the Fifth Conference On Carbon*, pp. 73-80.

149. Dreyer, DR, Park, S, Bielawski, CW & Ruoff, RS 2010, 'The chemistry of graphene oxide', *Chemical Society Reviews*, vol. 39, no. 1, pp. 228-40.

150. Hummers, WS & Offeman, RE 1958, 'Preparation of graphitic oxide', *Journal of the American Chemical Society*, vol. 80, no. 6, p. 1339.

151. Hirata, M, Gotou, T, Horiuchi, S, Fujiwara, M & Ohba, M 2004, 'Thin-film particles of graphite oxide 1:: High-yield synthesis and flexibility of the particles', *Carbon*, vol. 42, no. 14, pp. 2929-37.

152. Becerril, HA, Mao, J, Liu, Z, Stoltenberg, RM, Bao, Z & Chen, Y 2008, 'Evaluation of solution-processed reduced graphene oxide films as transparent conductors', *ACS Nano*, vol. 2, no. 3, pp. 463-70.

153. Marcano, DC, Kosynkin, DV, Berlin, JM, Sinitskii, A, Sun, Z, Slesarev, A, Alemany, LB, Lu, W & Tour, JM 2010, 'Improved synthesis of graphene oxide', *ACS Nano*, vol. 4, no. 8, pp. 4806-14.

154. Zhang, M, Okazaki, T, Iizumi, Y, Miyako, E, Yuge, R, Bandow, S, Iijima, S & Yudasaka, M 2016, 'Preparation of small-sized graphene oxide sheets and their biological applications', *Journal of Materials Chemistry B*, vol. 4, no. 1, pp. 121-7.

155. Sierra, U, Álvarez, P, Blanco, C, Granda, M, Santamaría, R & Menéndez, R 2016, 'Cokes of different origin as precursors of graphene oxide', *Fuel*, vol. 166, pp. 400-3.

156. Lee, S, Eom, SH, Chung, JS & Hur, SH 2013, 'Large-scale production of high-quality reduced graphene oxide', *Chemical Engineering Journal*, vol. 233, pp. 297-304.

157. Chen, J, Yao, B, Li, C & Shi, G 2013, 'An improved hummers method for eco-friendly synthesis of graphene oxide', *Carbon*, vol. 64, pp. 225-9.

158. He, H, Klinowski, J, Forster, M & Lerf, A 1998, 'A new structural model for graphite oxide', *Chemical Physics Letters*, vol. 287, no. 1-2, pp. 53-6.

159. Lerf, A, He, H, Forster, M & Klinowski, J 1998, 'Structure of graphite oxide revisited', *The Journal of Physical Chemistry B*, vol. 102, no. 23, pp. 4477-82.

160. Mao, S, Pu, H & Chen, J 2012, 'Graphene oxide and its reduction: Modeling and experimental progress', *RSC Advances*, vol. 2, no. 7, pp. 2643-62.

161. Szabó, T, Berkesi, O, Forgó, P, Josepovits, K, Sanakis, Y, Petridis, D & Dékány, I 2006, 'Evolution of surface functional groups in a series of progressively oxidized graphite oxides', *Chemistry of Materials*, vol. 18, no. 11, pp. 2740-9.

162. Gómez-Navarro, C, Weitz, RT, Bittner, AM, Scolari, M, Mews, A, Burghard, M & Kern, K 2007, 'Electronic transport properties of individual chemically reduced graphene oxide sheets', *Nano Letters*, vol. 7, no. 11, pp. 3499-503.

163. Stankovich, S, Dikin, DA, Piner, RD, Kohlhaas, KA, Kleinhammes, A, Jia, Y, Wu, Y, Nguyen, ST & Ruoff, RS 2007, 'Synthesis of graphene-based nanosheets via chemical reduction of exfoliated graphite oxide', *Carbon*, vol. 45, no. 7, pp. 1558-65.

164. Gilje, S, Han, S, Wang, M, Wang, KL & Kaner, RB 2007, 'A chemical route to graphene for device applications', *Nano Letters*, vol. 7, no. 11, pp. 3394-8.

165. Graphene Supermarket 2016, *Ultra highly concentrated single-layer graphene oxide, 175 ml*, Graphene Supermarket, viewed 18 January 2016, <https://graphene-supermarket.com/Ultra-Highly-Concentrated-Single-Layer-Graphene-Oxide-175ml.html>.

166. Paredes, JI, Villar-Rodil, S, Martínez-Alonso, A & Tascón, JMD 2008, 'Graphene oxide dispersions in organic solvents', *Langmuir*, vol. 24, no. 19, pp. 10560-4.

167. Stankovich, S, Piner, RD, Nguyen, ST & Ruoff, RS 2006, 'Synthesis and exfoliation of isocyanate-treated graphene oxide nanoplatelets', *Carbon*, vol. 44, no. 15, pp. 3342-7.

168. Pei, S & Cheng, H-M 2012, 'The reduction of graphene oxide', *Carbon*, vol. 50, no. 9, pp. 3210-28.

169. Park, S & Ruoff, RS 2015, 'Synthesis and characterization of chemically modified graphenes', *Current Opinion in Colloid & Interface Science*, vol. 20, no. 5–6, pp. 322-8.

170. Li, D, Muller, MB, Gilje, S, Kaner, RB & Wallace, GG 2008, 'Processable aqueous dispersions of graphene nanosheets', *Nature Nanotechnology*, vol. 3, no. 2, pp. 101-5.

171. Jung, I, Dikin, DA, Piner, RD & Ruoff, RS 2008, 'Tunable electrical conductivity of individual graphene oxide sheets reduced at “low” temperatures', *Nano Letters*, vol. 8, no. 12, pp. 4283-7.

172. Eda, G, Fanchini, G & Chhowalla, M 2008, 'Large-area ultrathin films of reduced graphene oxide as a transparent and flexible electronic material', *Nature Nanotechnology*, vol. 3, no. 5, pp. 270-4.

173. Guo, H-L, Wang, X-F, Qian, Q-Y, Wang, F-B & Xia, X-H 2009, 'A green approach to the synthesis of graphene nanosheets', *ACS Nano*, vol. 3, no. 9, pp. 2653-9.

174. Stankovich, S, Piner, RD, Chen, X, Wu, N, Nguyen, ST & Ruoff, RS 2006, 'Stable aqueous dispersions of graphitic nanoplatelets via the reduction of exfoliated

graphite oxide in the presence of poly(sodium 4-styrenesulfonate)', *Journal of Materials Chemistry*, vol. 16, no. 2, pp. 155-8.

175. Si, Y & Samulski, ET 2008, 'Synthesis of water soluble graphene', *Nano Letters*, vol. 8, no. 6, pp. 1679-82.

176. Han, J, Zhang, LL, Lee, S, Oh, J, Lee, K-S, Potts, JR, Ji, J, Zhao, X, Ruoff, RS & Park, S 2013, 'Generation of B-doped graphene nanoplatelets using a solution process and their supercapacitor applications', *ACS Nano*, vol. 7, no. 1, pp. 19-26.

177. Zhao, J, Pei, S, Ren, W, Gao, L & Cheng, H-M 2010, 'Efficient preparation of large-area graphene oxide sheets for transparent conductive films', *ACS Nano*, vol. 4, no. 9, pp. 5245-52.

178. Eda, G & Chhowalla, M 2010, 'Chemically derived graphene oxide: Towards large-area thin-film electronics and optoelectronics', *Advanced Materials*, vol. 22, no. 22, pp. 2392-415.

179. Stankovich, S, Dikin, DA, Dommett, GHB, Kohlhaas, KM, Zimney, EJ, Stach, EA, Piner, RD, Nguyen, ST & Ruoff, RS 2006, 'Graphene-based composite materials', *Nature*, vol. 442, no. 7100, pp. 282-6.

180. Eigler, S, Grimm, S, Enzelberger-Heim, M, Muller, P & Hirsch, A 2013, 'Graphene oxide: Efficiency of reducing agents', *Chemical Communications*, vol. 49, no. 67, pp. 7391-3.

181. Fernández-Merino, MJ, Guardia, L, Paredes, JI, Villar-Rodil, S, Solís-Fernández, P, Martínez-Alonso, A & Tascón, JMD 2010, 'Vitamin C is an ideal substitute for hydrazine in the reduction of graphene oxide suspensions', *The Journal of Physical Chemistry C*, vol. 114, no. 14, pp. 6426-32.

182. Thakur, S & Karak, N 2015, 'Alternative methods and nature-based reagents for the reduction of graphene oxide: A review', *Carbon*, vol. 94, pp. 224-42.

183. Acik, M, Lee, G, Mattevi, C, Chhowalla, M, Cho, K & Chabal, YJ 2010, 'Unusual infrared-absorption mechanism in thermally reduced graphene oxide', *Nature Materials*, vol. 9, no. 10, pp. 840-5.

184. Mattevi, C, Eda, G, Agnoli, S, Miller, S, Mkhoyan, KA, Celik, O, Mastrogiovanni, D, Granozzi, G, Garfunkel, E & Chhowalla, M 2009, 'Evolution of electrical, chemical, and structural properties of transparent and conducting chemically derived graphene thin films', *Advanced Functional Materials*, vol. 19, no. 16, pp. 2577-83.

185. Yang, D, Velamakanni, A, Bozoklu, G, Park, S, Stoller, M, Piner, RD, Stankovich, S, Jung, I, Field, DA, Ventrice Jr, CA & Ruoff, RS 2009, 'Chemical analysis of graphene oxide films after heat and chemical treatments by x-ray photoelectron and micro-Raman spectroscopy', *Carbon*, vol. 47, no. 1, pp. 145-52.

186. Wang, X, Zhi, L & Mullen, K 2007, 'Transparent, conductive graphene electrodes for dye-sensitized solar cells', *Nano Letters*, vol. 8, no. 1, pp. 323-7.

187. López, V, Sundaram, RS, Gómez-Navarro, C, Olea, D, Burghard, M, Gómez-Herrero, J, Zamora, F & Kern, K 2009, 'Chemical vapor deposition repair of graphene oxide: A route to highly-conductive graphene monolayers', *Advanced Materials*, vol. 21, no. 46, pp. 4683-6.

188. Su, C-Y, Xu, Y, Zhang, W, Zhao, J, Liu, A, Tang, X, Tsai, C-H, Huang, Y & Li, L-J 2010, 'Highly efficient restoration of graphitic structure in graphene oxide using alcohol vapors', *ACS Nano*, vol. 4, no. 9, pp. 5285-92.

189. Ekiz, OOn, Ürel, M, Güner, H, Mizrak, AK & Dâna, A 2011, 'Reversible electrical reduction and oxidation of graphene oxide', *ACS Nano*, vol. 5, no. 4, pp. 2475-82.

190. Zhou, M, Wang, Y, Zhai, Y, Zhai, J, Ren, W, Wang, F & Dong, S 2009, 'Controlled synthesis of large-area and patterned electrochemically reduced graphene oxide films', *Chemistry – A European Journal*, vol. 15, no. 25, pp. 6116-20.

191. Zhu, Y, Murali, S, Stoller, MD, Velamakanni, A, Piner, RD & Ruoff, RS 2010, 'Microwave assisted exfoliation and reduction of graphite oxide for ultracapacitors', *Carbon*, vol. 48, no. 7, pp. 2118-22.

192. Dubin, S, Gilje, S, Wang, K, Tung, VC, Cha, K, Hall, AS, Farrar, J, Varshneya, R, Yang, Y & Kaner, RB 2010, 'A one-step, solvothermal reduction method for producing reduced graphene oxide dispersions in organic solvents', *ACS Nano*, vol. 4, no. 7, pp. 3845-52.

193. Williams, G, Seger, B & Kamat, PV 2008, 'TiO_2-graphene nanocomposites. UV-assisted photocatalytic reduction of graphene oxide', *ACS Nano*, vol. 2, no. 7, pp. 1487-91.

194. Li, F, Jiang, X, Zhao, J & Zhang, S 2015, 'Graphene oxide: A promising nanomaterial for energy and environmental applications', *Nano Energy*, vol. 16, pp. 488-515.

195. Aghigh, A, Alizadeh, V, Wong, HY, Islam, MS, Amin, N & Zaman, M 2015, 'Recent advances in utilization of graphene for filtration and desalination of water: A review', *Desalination*, vol. 365, pp. 389-97.

196. Hegab, HM & Zou, L 2015, 'Graphene oxide-assisted membranes: Fabrication and potential applications in desalination and water purification', *Journal of Membrane Science*, vol. 484, pp. 95-106.

197. Liu, G, Jin, W & Xu, N 2015, 'Graphene-based membranes', *Chemical Society Reviews*, vol. 44, no. 15, pp. 5016-30.

198. Gupta Chatterjee, S, Chatterjee, S, Ray, AK & Chakraborty, AK 2015, 'Graphene–metal oxide nanohybrids for toxic gas sensor: A review', *Sensors and Actuators B: Chemical*, vol. 221, pp. 1170-81.

199. Toda, K, Furue, R & Hayami, S 2015, 'Recent progress in applications of graphene oxide for gas sensing: A review', *Analytica Chimica Acta*, vol. 878, pp. 43-53.

200. Haag, D & Kung, HH 2013, 'Metal free graphene based catalysts: A review', *Topics in Catalysis*, vol. 57, no. 6, pp. 762-73.

201. Wu, D, Zhang, F, Liang, H & Feng, X 2012, 'Nanocomposites and macroscopic materials: Assembly of chemically modified graphene sheets', *Chemical Society Reviews*, vol. 41, no. 18, pp. 6160-77.

202. Yoo, JM, Kang, JH & Hong, BH 2015, 'Graphene-based nanomaterials for versatile imaging studies', *Chemical Society Reviews*, vol. 44, no. 14, pp. 4835-52.

203. Su, Y & Lv, Y 2014, 'Graphene and graphene oxides: Recent advances in chemiluminescence and electrochemiluminescence', *RSC Advances*, vol. 4, no. 55, pp. 29324-39.

204. Shanmugam, V, Selvakumar, S & Yeh, C-S 2014, 'Near-infrared light-responsive nanomaterials in cancer therapeutics', *Chemical Society Reviews*, vol. 43, no. 17, pp. 6254-87.

205. Masuko, K, Shigematsu, M, Hashiguchi, T, Fujishima, D, Kai, M, Yoshimura, N, Yamaguchi, T, Ichihashi, Y, Mishima, T, Matsubara, N, Yamanishi, T, Takahama, T, Taguchi, M, Maruyama, E & Okamoto, S 2014, 'Achievement of more than 25% conversion efficiency with crystalline silicon heterojunction solar cell', *IEEE Journal of Photovoltaics*, vol. 4, no. 6, pp. 1433-5.

206. Green, MA, Emery, K, Hishikawa, Y, Warta, W & Dunlop, ED 2016, 'Solar cell efficiency tables (version 47)', *Progress in Photovoltaics: Research and Applications*, vol. 24, no. 1, pp. 3-11.

207. Kayes, BM, Hui, N, Twist, R, Spruytte, SG, Reinhardt, F, Kizilyalli, IC & Higashi, GS 2011, '27.6% conversion efficiency, a new record for single-junction solar cells under 1 sun illumination', in *Photovoltaic Specialists Conference (PVSC), 2011 37th IEEE*, pp. 4-8.

208. Wallin, E, Malm, U, Jarmar, T, Edoff, OLM & Stolt, L 2012, 'World-record Cu(In,Ga)Se_2-based thin-film sub-module with 17.4% efficiency', *Progress in Photovoltaics: Research and Applications*, vol. 20, no. 7, pp. 851-4.

209. Hosoya, M, Oooka, H, Nakao, H, Gotanda, T, Mori, S, Shida, N, Hayase, R, Nakano, Y & Saito, M 2013, 'Organic thin film photovoltaic modules', in *Proceedings, 93rd Annual Meeting of the Chemical Society of Japan*, pp. 21-37.

210. Mathew, S, Yella, A, Gao, P, Humphry-Baker, R, CurchodBasile, FE, Ashari-Astani, N, Tavernelli, I, Rothlisberger, U, NazeeruddinMd, K & Grätzel, M 2014, 'Dye-sensitized solar cells with 13% efficiency achieved through the molecular engineering of porphyrin sensitizers', *Nature Chemistry*, vol. 6, no. 3, pp. 242-7.

211. Heo, JH, Im, SH, Noh, JH, Mandal, TN, Lim, C-S, Chang, JA, Lee, YH, Kim, H-j, Sarkar, A, NazeeruddinMd, K, Gratzel, M & Seok, SI 2013, 'Efficient inorganic-organic hybrid heterojunction solar cells containing perovskite compound and polymeric hole conductors', *Nature Photonics*, vol. 7, no. 6, pp. 486-91.

212. Grätzel, M 2005, 'Solar energy conversion by dye-sensitized photovoltaic cells', *Inorganic Chemistry*, vol. 44, no. 20, pp. 6841-51.

213. O'Regan, B & Grätzel, M 1991, 'A low-cost, high-efficiency solar cell based on dye-sensitized colloidal TiO_2 films', *Nature*, vol. 353, no. 6346, pp. 737-40.

214. Hagfeldt, A, Boschloo, G, Sun, L, Kloo, L & Pettersson, H 2010, 'Dye-sensitized solar cells', *Chemical Reviews*, vol. 110, no. 11, pp. 6595-663.

215. Grätzel, M 2001, 'Photoelectrochemical cells', *Nature*, vol. 414, no. 6861, pp. 338-44.

216. Boschloo, G & Hagfeldt, A 2009, 'Characteristics of the iodide/triiodide redox mediator in dye-sensitized solar cells', *Accounts of Chemical Research*, vol. 42, no. 11, pp. 1819-26.

217. Batmunkh, M, Biggs, MJ & Shapter, JG 2015, 'Carbon nanotubes for dye-sensitized solar cells', *Small*, vol. 11, no. 25, pp. 2963-89.

218. Tantang, H, Kyaw, AKK, Zhao, Y, Chan-Park, MB, Tok, AIY, Hu, Z, Li, L-J, Sun, XW & Zhang, Q 2012, 'Nitrogen-doped carbon nanotube-based bilayer thin film as transparent counter electrode for dye-sensitized solar cells (DSSCs)', *Chemistry – An Asian Journal*, vol. 7, no. 3, pp. 541-5.

219. Liu, C-T, Wang, Y-C, Dong, R-X, Wang, C-C, Huang, K-C, Vittal, R, Ho, K-C & Lin, J-J 2012, 'A dual-functional Pt/CNT TCO-free counter electrode for dye-sensitized solar cell', *Journal of Materials Chemistry*, vol. 22, no. 48, pp. 25311-5.

220. Kyaw, AKK, Tantang, H, Wu, T, Ke, L, Peh, C, Huang, ZH, Zeng, XT, Demir, HV, Zhang, Q & Sun, XW 2011, 'Dye-sensitized solar cell with a titanium-oxide-modified carbon nanotube transparent electrode', *Applied Physics Letters*, vol. 99, no. 2, p. 021107.

221. Aitola, K, Kaskela, A, Halme, J, Ruiz, V, Nasibulin, AG, Kauppinen, EI & Lund, PD 2010, 'Single-walled carbon nanotube thin-film counter electrodes for indium tin oxide-free plastic dye solar cells', *Journal of The Electrochemical Society*, vol. 157, no. 12, pp. B1831-B7.

222. Wei, D, Unalan, HE, Han, D, Zhang, Q, Niu, L, Amaratunga, G & Ryhanen, T 2008, 'A solid-state dye-sensitized solar cell based on a novel ionic liquid gel and ZnO

nanoparticles on a flexible polymer substrate', *Nanotechnology*, vol. 19, no. 42, p. 424006.

223. Du, J, Bittner, F, Hecht, DS, Ladous, C, Ellinger, J, Oekermann, T & Wark, M 2013, 'A carbon nanotube-based transparent conductive substrate for flexible ZnO dye-sensitized solar cells', *Thin Solid Films*, vol. 531, pp. 391-7.

224. Li, H, Yang, Z, Qiu, L, Fang, X, Sun, H, Chen, P, Pan, S & Peng, H 2014, 'Stable wire-shaped dye-sensitized solar cells based on eutectic melts', *Journal of Materials Chemistry A*, vol. 2, no. 11, pp. 3841-6.

225. Chen, T, Qiu, L, Yang, Z, Cai, Z, Ren, J, Li, H, Lin, H, Sun, X & Peng, H 2012, 'An integrated “energy wire” for both photoelectric conversion and energy storage', *Angewandte Chemie International Edition*, vol. 51, no. 48, pp. 11977-80.

226. Chen, T, Qiu, L, Cai, Z, Gong, F, Yang, Z, Wang, Z & Peng, H 2012, 'Intertwined aligned carbon nanotube fiber based dye-sensitized solar cells', *Nano Letters*, vol. 12, no. 5, pp. 2568-72.

227. Yun, S, Hagfeldt, A & Ma, T 2014, 'Pt-free counter electrode for dye-sensitized solar cells with high efficiency', *Advanced Materials*, vol. 26, no. 36, pp. 6210-37.

228. Suzuki, K, Yamaguchi, M, Kumagai, M & Yanagida, S 2003, 'Application of carbon nanotubes to counter electrodes of dye-sensitized solar cells', *Chemistry Letters*, vol. 32, no. 1, pp. 28-9.

229. Ramasamy, E, Lee, WJ, Lee, DY & Song, JS 2008, 'Spray coated multi-wall carbon nanotube counter electrode for tri-iodide reduction in dye-sensitized solar cells', *Electrochemistry Communications*, vol. 10, no. 7, pp. 1087-9.

230. Lee, WJ, Ramasamy, E, Lee, DY & Song, JS 2009, 'Efficient dye-sensitized solar cells with catalytic multiwall carbon nanotube counter electrodes', *ACS Applied Materials & Interfaces*, vol. 1, no. 6, pp. 1145-9.

231. Choi, HJ, Gong, HH, Park, J-Y & Hong, SC 2013, 'Characteristics of dye-sensitized solar cells with surface-modified multi-walled carbon nanotubes as counter electrodes', *Journal of Materials Science*, vol. 48, no. 2, pp. 906-12.

232. Xing, Y, Zheng, X, Wu, Y, Li, M, Zhang, W-H & Li, C 2015, 'Nitrogen-doped carbon nanotubes with metal nanoparticles as counter electrode materials for dye-sensitized solar cells', *Chemical Communications*, vol. 51, no. 38, pp. 8146-9.

233. Jang, S-R, Vittal, R & Kim, K-J 2004, 'Incorporation of functionalized single-wall carbon nanotubes in dye-sensitized TiO_2 solar cells', *Langmuir*, vol. 20, no. 22, pp. 9807-10.

234. Dembele, KT, Selopal, GS, Soldano, C, Nechache, R, Rimada, JC, Concina, I, Sberveglieri, G, Rosei, F & Vomiero, A 2013, 'Hybrid carbon nanotubes–TiO_2 photoanodes for high efficiency dye-sensitized solar cells', *The Journal of Physical Chemistry C*, vol. 117, no. 28, pp. 14510-7.

235. Sawatsuk, T, Chindaduang, A, Sae-kung, C, Pratontep, S & Tumcharern, G 2009, 'Dye-sensitized solar cells based on TiO_2–MWCNTs composite electrodes: Performance improvement and their mechanisms', *Diamond and Related Materials*, vol. 18, no. 2–3, pp. 524-7.

236. Brown, P, Takechi, K & Kamat, PV 2008, 'Single-walled carbon nanotube scaffolds for dye-sensitized solar cells', *The Journal of Physical Chemistry C*, vol. 112, no. 12, pp. 4776-82.

237. Dang, X, Yi, H, Ham, M-H, Qi, J, Yun, DS, Ladewski, R, Strano, MS, Hammond, PT & Belcher, AM 2011, 'Virus-templated self-assembled single-walled carbon nanotubes for highly efficient electron collection in photovoltaic devices', *Nature Nanotechnology*, vol. 6, no. 6, pp. 377-84.

238. Macdonald, TJ, Tune, DD, Dewi, MR, Gibson, CT, Shapter, JG & Nann, T 2015, 'A TiO2 nanofiber–carbon nanotube-composite photoanode for improved efficiency in dye-sensitized solar cells', *ChemSusChem*, vol. 8, no. 20, pp. 3396-400.

239. Kongkanand, A, Martínez Domínguez, R & Kamat, PV 2007, 'Single wall carbon nanotube scaffolds for photoelectrochemical solar cells. Capture and transport of photogenerated electrons', *Nano Letters*, vol. 7, no. 3, pp. 676-80.

240. Wei, L, Tezuka, N, Umeyama, T, Imahori, H & Chen, Y 2011, 'Formation of single-walled carbon nanotube thin films enriched with semiconducting nanotubes and their application in photoelectrochemical devices', *Nanoscale*, vol. 3, no. 4, pp. 1845-9.

241. Yu, J, Losic, D, Marshall, M, Böcking, T, Gooding, JJ & Shapter, JG 2006, 'Preparation and characterisation of an aligned carbon nanotube array on the silicon (100) surface', *Royal Society of Chemistry Journals*, vol. 2, no. 12, pp. 1081-8.

242. Bissett, MA, Koper, I, Quinton, JS & Shapter, JG 2011, 'Dendron growth from vertically aligned single-walled carbon nanotube thin layer arrays for photovoltaic devices', *Physical Chemistry Chemical Physics*, vol. 13, no. 13, pp. 6059-64.

243. Bissett, M, Barlow, A, Shearer, C, Quinton, J & Shapter, JG 2012, 'Comparison of carbon nanotube modified electrodes for photovoltaic devices', *Carbon*, vol. 50, no. 7, pp. 2431-41.

244. Chen, T, Wang, S, Yang, Z, Feng, Q, Sun, X, Li, L, Wang, Z-S & Peng, H 2011, 'Flexible, light-weight, ultrastrong, and semiconductive carbon nanotube fibers for a highly efficient solar cell', *Angewandte Chemie International Edition*, vol. 50, no. 8, pp. 1815-9.

245. Yu, HA, Kaneko, Y, Yoshimura, S & Otani, S 1996, 'Photovoltaic cell of carbonaceous film/n-type silicon', *Applied Physics Letters*, vol. 68, no. 4, pp. 547-9.

246. Mukhopadhyay, K, Mukhopadhyay, I, Sharon, M, Soga, T & Umeno, M 1997, 'Carbon photovoltaic cell', *Carbon*, vol. 35, no. 6, pp. 863-4.

247. Katz, EA, Faiman, D, Goren, S, Shtutina, S, Mishori, B & Shapira, Y 1998, 'A photovoltaic C_{60}-Si heterojunction', *Fullerene Science and Technology*, vol. 6, no. 1, pp. 103-11.

248. Kita, K, Wen, C, Ihara, M & Yamada, K 1996, 'Photovoltage generation of Si/C_{60} heterojunction', *Journal of Applied Physics*, vol. 79, no. 5, pp. 2798-800.

249. Narayanan, KL & Yamaguchi, M 2001, 'Phosphorous ion implantation in C_{60} for the photovoltaic applications', *Journal of Applied Physics*, vol. 89, no. 12, pp. 8331-5.

250. Narayanan, KL & Yamaguchi, M 1999, 'Boron ion-implanted C_{60} heterojunction photovoltaic devices', *Applied Physics Letters*, vol. 75, no. 14, pp. 2106-7.

251. Narayanan, KL & Yamaguchi, M 2003, 'Photovoltaic effects of a:C/C_{60}/Si (p–i–n) solar cell structures', *Solar Energy Materials and Solar Cells*, vol. 75, no. 3-4, pp. 345-50.

252. Tune, DD, Flavel, BS, Krupke, R & Shapter, JG 2012, 'Carbon nanotube-silicon solar cells', *Advanced Energy Materials*, vol. 2, no. 9, pp. 1043-55.

253. Li, Z, Kunets, VP, Saini, V, Xu, Y, Dervishi, E, Salamo, GJ, Biris, AR & Biris, AS 2009, 'Light-harvesting using high density p-type single wall carbon nanotube/n-type silicon heterojunctions', *ACS Nano*, vol. 3, no. 6, pp. 1407-14.

254. Tune, DD & Shapter, JG 2013, 'Effect of nanotube film thickness on the performance of nanotube-silicon hybrid solar cells', *Nanomaterials*, vol. 3, no. 4, pp. 655-73.

255. Tune, DD, Blanch, AJ, Krupke, R, Flavel, BS & Shapter, JG 2014, 'Nanotube film metallicity and its effect on the performance of carbon nanotube–silicon solar cells', *physica status solidi (a)*, vol. 211, no. 7, pp. 1479-87.

256. Jia, Y, Cao, A, Bai, X, Li, Z, Zhang, L, Guo, N, Wei, J, Wang, K, Zhu, H, Wu, D & Ajayan, PM 2011, 'Achieving high efficiency silicon-carbon nanotube heterojunction solar cells by acid doping', *Nano Letters*, vol. 11, no. 5, pp. 1901-5.

257. Tune, DD, Flavel, BS, Quinton, JS, Ellis, AV & Shapter, JG 2013, 'Single-walled carbon nanotube/polyaniline/n-silicon solar cells: Fabrication, characterization, and performance measurements', *ChemSusChem*, vol. 6, no. 2, pp. 320-7.

258. Yu, L, Tune, DD, Shearer, CJ & Shapter, JG 2015, 'Implementation of antireflection layers for improved efficiency of carbon nanotube–silicon heterojunction solar cells', *Solar Energy*, vol. 118, no. 0, pp. 592-9.

259. Yu, L, Tune, DD, Shearer, CJ & Shapter, JG 2015, 'Application of polymer interlayers in silicon–carbon nanotube heterojunction solar cells', *ChemNanoMat*, vol. 1, no. 2, pp. 115-21.

260. Wang, F, Kozawa, D, Miyauchi, Y, Hiraoka, K, Mouri, S, Ohno, Y & Matsuda, K 2015, 'Considerably improved photovoltaic performance of carbon nanotube-based solar cells using metal oxide layers', *Nature Communications*, vol. 6, p. 6305.

261. Li, X, Lv, Z & Zhu, H 2015, 'Carbon/silicon heterojunction solar cells: State of the art and prospects', *Advanced Materials*, vol. 27, no. 42, pp. 6549-74.

262. Harris, JM, Semler, MR, May, S, Fagan, JA & Hobbie, EK 2015, 'Nature of record efficiency fluid-processed nanotube–silicon heterojunctions', *The Journal of Physical Chemistry C*, vol. 119, no. 19, pp. 10295-303.

263. Pintossi, C, Pagliara, S, Drera, G, De Nicola, F, Castrucci, P, De Crescenzi, M, Crivellari, M, Boscardin, M & Sangaletti, L 2015, 'Steering the efficiency of carbon nanotube–silicon photovoltaic cells by acid vapor exposure: A real-time spectroscopic tracking', *ACS Applied Materials & Interfaces*, vol. 7, no. 18, pp. 9436-44.

264. Li, X, Zhu, H, Wang, K, Cao, A, Wei, J, Li, C, Jia, Y, Li, Z, Li, X & Wu, D 2010, 'Graphene-on-silicon Schottky junction solar cells', *Advanced Materials*, vol. 22, no. 25, pp. 2743-8.

265. Ye, Y & Dai, L 2012, 'Graphene-based Schottky junction solar cells', *Journal of Materials Chemistry*, vol. 22, no. 46, pp. 24224-9.

266. Sze, SM 1969, *Physics of semiconductor devices*, Wiley-Interscience, New York.

267. Fan, G, Zhu, H, Wang, K, Wei, J, Li, X, Shu, Q, Guo, N & Wu, D 2011, 'Graphene/silicon nanowire Schottky junction for enhanced light harvesting', *ACS Applied Materials & Interfaces*, vol. 3, no. 3, pp. 721-5.

268. Feng, T, Xie, D, Lin, Y, Zang, Y, Ren, T, Song, R, Zhao, H, Tian, H, Li, X, Zhu, H & Liu, L 2011, 'Graphene based Schottky junction solar cells on patterned silicon-pillar-array substrate', *Applied Physics Letters*, vol. 99, no. 23.

269. Feng, T, Xie, D, Lin, Y, Zhao, H, Chen, Y, Tian, H, Ren, T, Li, X, Li, Z, Wang, K, Wu, D & Zhu, H 2012, 'Efficiency enhancement of graphene/silicon-pillar-array solar cells by HNO_3 and PEDOT-PSS', *Nanoscale*, vol. 4, no. 6, pp. 2130-3.

270. Wu, Y, Zhang, X, Jie, J, Xie, C, Zhang, X, Sun, B, Wang, Y & Gao, P 2013, 'Graphene transparent conductive electrodes for highly efficient silicon nanostructures-based hybrid heterojunction solar cells', *The Journal of Physical Chemistry C*.

271. Jiao, T, Wei, D, Song, X, Sun, T, Yang, J, Yu, L, Feng, Y, Sun, W, Wei, W, Shi, H, Hu, C & Du, C 2016, 'High-efficiency, stable and non-chemically doped graphene-Si solar cells through interface engineering and pmma antireflection', *RSC Advances*, vol. 6, no. 12, pp. 10175-9.

272. Hibino, H, Kageshima, H, Kotsugi, M, Maeda, F, Guo, FZ & Watanabe, Y 2009, 'Dependence of electronic properties of epitaxial few-layer graphene on the number of layers investigated by photoelectron emission microscopy', *Physical Review B*, vol. 79, no. 12, p. 125437.

273. Lin, Y, Li, X, Xie, D, Feng, T, Chen, Y, Song, R, Tian, H, Ren, T, Zhong, M, Wang, K & Zhu, H 2013, 'Graphene/semiconductor heterojunction solar cells with modulated antireflection and graphene work function', *Energy & Environmental Science*, vol. 6, no. 1, pp. 108-15.

274. Ihm, K, Lim, JT, Lee, K-J, Kwon, JW, Kang, T-H, Chung, S, Bae, S, Kim, JH, Hong, BH & Yeom, GY 2010, 'Number of graphene layers as a modulator of the open-circuit voltage of graphene-based solar cell', *Applied Physics Letters*, vol. 97, no. 3, p. 032113.

275. Li, YF, Yang, W, Tu, ZQ, Liu, ZC, Yang, F, Zhang, LQ & Hatakeyama, R 2014, 'Schottky junction solar cells based on graphene with different numbers of layers', *Applied Physics Letters*, vol. 104, no. 4, p. 043903.

276. Li, X, Xie, D, Park, H, Zeng, TH, Wang, K, Wei, J, Zhong, M, Wu, D, Kong, J & Zhu, H 2013, 'Anomalous behaviors of graphene transparent conductors in graphene–silicon heterojunction solar cells', *Advanced Energy Materials*, vol. 3, no. 8, pp. 1029-34.

277. Li, X, Xie, D, Park, H, Zhu, M, Zeng, TH, Wang, K, Wei, J, Wu, D, Kong, J & Zhu, H 2013, 'Ion doping of graphene for high-efficiency heterojunction solar cells', *Nanoscale*, vol. 5, pp. 1945-8.

278. Shi, Y, Kim, KK, Reina, A, Hofmann, M, Li, L-J & Kong, J 2010, 'Work function engineering of graphene electrode via chemical doping', *ACS Nano*, vol. 4, no. 5, pp. 2689-94.

279. Liu, X, Zhang, XW, Yin, ZG, Meng, JH, Gao, HL, Zhang, LQ, Zhao, YJ & Wang, HL 2014, 'Enhanced efficiency of graphene-silicon Schottky junction solar cells by doping with Au nanoparticles', *Applied Physics Letters*, vol. 105, no. 18, p. 183901.

280. Miao, X, Tongay, S, Petterson, MK, Berke, K, Rinzler, AG, Appleton, BR & Hebard, AF 2012, 'High efficiency graphene solar cells by chemical doping', *Nano Letters*, vol. 12, no. 6, pp. 2745-50.

281. Ho, P-H, Liou, Y-T, Chuang, C-H, Lin, S-W, Tseng, C-Y, Wang, D-Y, Chen, C-C, Hung, W-Y, Wen, C-Y & Chen, C-W 2015, 'Self-crack-filled graphene films by metallic nanoparticles for high-performance graphene heterojunction solar cells', *Advanced Materials*, vol. 27, no. 10, pp. 1724-9.

282. Ayhan, ME, Kalita, G, Kondo, M & Tanemura, M 2014, 'Photoresponsivity of silver nanoparticles decorated graphene-silicon Schottky junction', *RSC Advances*, vol. 4, no. 51, pp. 26866-71.

283. Feng, T, Xie, D, Lin, Y, Zang, Y, Ren, T, Song, R, Zhao, H, Tian, H, Li, X, Zhu, H & Liu, L 2011, 'Graphene based Schottky junction solar cells on patterned silicon-pillar-array substrate', *Applied Physics Letters*, vol. 99, no. 23, pp. -.

284. Cui, T, Lv, R, Huang, Z-H, Chen, S, Zhang, Z, Gan, X, Jia, Y, Li, X, Wang, K & Wu, D 2013, 'Enhanced efficiency of graphene/silicon heterojunction solar cells by molecular doping', *Journal of Materials Chemistry A*, vol. 1, no. 18, pp. 5736-40.

285. Shi, E, Li, H, Yang, L, Zhang, L, Li, Z, Li, P, Shang, Y, Wu, S, Li, X, Wei, J, Wang, K, Zhu, H, Wu, D, Fang, Y & Cao, A 2013, 'Colloidal antireflection coating improves graphene–silicon solar cells', *Nano Letters*, vol. 13, no. 4, pp. 1776-81.

286. Song, Y, Li, X, Mackin, C, Zhang, X, Fang, W, Palacios, T, Zhu, H & Kong, J 2015, 'Role of interfacial oxide in high-efficiency graphene–silicon Schottky barrier solar cells', *Nano Letters*, vol. 15, no. 3, pp. 2104-10.

287. Kalita, G, Wakita, K, Umeno, M & Tanemura, M 2013, 'Fabrication and characteristics of solution-processed graphene oxide–silicon heterojunction', *physica status solidi (RRL)-Rapid Research Letters*, vol. 7, no. 5, pp. 340-3.

288. Zhu, M, Li, X, Guo, Y, Li, X, Sun, P, Zang, X, Wang, K, Zhong, M, Wu, D & Zhu, H 2014, 'Vertical junction photodetectors based on reduced graphene oxide/silicon Schottky diodes', *Nanoscale*, vol. 6, no. 9, pp. 4909-14.

289. Phan, DT, Gupta, RK, Chung, GS, Al-Ghamdi, AA, Al-Hartomy, OA, El-Tantawy, F & Yakuphanoglu, F 2012, 'Photodiodes based on graphene oxide–silicon junctions', *Solar Energy*, vol. 86, no. 10, pp. 2961-6.

290. Behura, SK, Nayak, S, Mukhopadhyay, I & Jani, O 2014, 'Junction characteristics of chemically-derived graphene/p-Si heterojunction solar cell', *Carbon*, vol. 67, pp. 766-74.

291. Batra, K, Nayak, S, Behura, SK & Jani, O 2015, 'Optimizing performance parameters of chemically-derived graphene/p-Si heterojunction solar cell', *Journal of Nanoscience and Nanotechnology*, vol. 15, no. 7, pp. 4877-82.

292. Fernandes, GE, Kim, JH, Oller, D & Xu, J 2015, 'Reduced graphene oxide mid-infrared photodetector at 300 k', *Applied Physics Letters*, vol. 107, no. 11, p. 111111.

293. Gupta, RK, Alahmed, ZA, Albrithen, HA & Yakuphanoglu, F 2014, 'Highly efficient photosensor based on reduced graphene oxide', *Journal of Nanoelectronics and Optoelectronics*, vol. 9, no. 4, pp. 474-8.

294. Liu, Q, Wanatabe, F, Hoshino, A, Ishikawa, R, Gotou, T, Ueno, K & Shirai, H 2012, 'Crystalline silicon/graphene oxide hybrid junction solar cells', *Japanese Journal of Applied Physics*, vol. 51, no. 10S, p. 10NE22.

295. Tang, Z, Liu, Q, Khatri, I, Ishikawa, R, Ueno, K & Shirai, H 2012, 'Optical properties and carrier transport in c-Si/conductive PEDOT:PSS(go) composite heterojunctions', *physica status solidi (c)*, vol. 9, no. 10-11, pp. 2075-8.

Chapter 2

Experimental Methods

Common experimental methods and materials that cover multiple chapters are described, with details of specific sections presented within each chapter. The fundamentals and representative data of common characterisation techniques used throughout the Thesis are also covered.

This chapter contains material previously published in:

Larsen, LJ, Shearer, CJ, Ellis, AV & Shapter, JG 2015, 'Solution processed graphene-silicon Schottky junction solar cells', *RSC Advances*, vol. 5, no. 49, pp. 38851-8.

Larsen, LJ, Shearer, CJ, Ellis, AV & Shapter, JG 2016, 'Optimization and doping of reduced graphene oxide–silicon solar cells', *The Journal of Physical Chemistry C*, vol. 120, no. 29, pp. 15648-56.

2.1 Experimental Methods

2.1.1 Graphene and Graphene Oxide Film Fabrication

Graphene and graphene oxide films with an area of 0.18 cm^2 were prepared for device fabrication while an area of 0.50 cm^2 was used for all other measurements. To form graphene and GO films, the respective dispersions were filtered through mixed cellulose ester (MCE) membranes (0.45 μm, HAWP, Millipore, USA). The UV-Vis transmittance at 550 nm of the resultant graphene films can be controlled by varying the volume of graphene or GO dispersion (mL) filtered per unit area of the final film (cm^{-2}). The amount of dispersion used to produce each film was controlled such that films of varying transmittances were produced for each purpose (sheet resistance measurements or solar cells etc.). These films were then rinsed thoroughly with MilliQ water before their application.

2.1.2 Nanocarbon-Based Materials-Silicon Solar Cell Fabrication

See Figure 2.1 for a cutaway schematic of the final solar cell architecture. Phosphorous doped n-type silicon wafers (CZ, 1-20 Ω·cm, <100>, ABC GmbH, Germany), polished on one side and with a 100 nm thermal silicon oxide layer were used for device fabrication. UV lithography was used to define holes (area of 0.08 cm^2) in the sputtered front metal contacts (Ti/Au 5 nm/145 nm) which were then used as a mask for buffered oxide etching (BOE) (6:1 40 % NH_4F: 48 % HF) of the oxide layer. Nanocarbon-based material (graphene or GO) films were deposited by placing the circular nanocarbon-based material-MCE membranes nanocarbon-based material side down over the etched hole. The membranes were wetted with MilliQ water, and a Teflon sheet placed on top of the membrane. The assembly was then compressed with a glass slide and baked at 80 °C for 15 min and then allowed to cool and subsequently immersed in acetone to dissolve the MCE, leaving a tightly physisorbed nanocarbon-based material membrane on the silicon/gold substrate. The oxide layer on the back of the silicon was then etched using BOE and an electrical contact was made between the silicon and a stainless steel back electrode using eutectic gallium indium (eGaIn, Sigma-Aldrich, Australia), consistent with the works of Tune et al. in their CNT-Si heterojunction cells [1-4]. Following assembly, the nanocarbon-based material-Si interface was etched by pipetting 2 % HF (diluted from 48 % HF, Sigma-Aldrich, Australia) onto the surface for 90 s before rinsing with MilliQ water and ethanol and drying under flowing nitrogen.

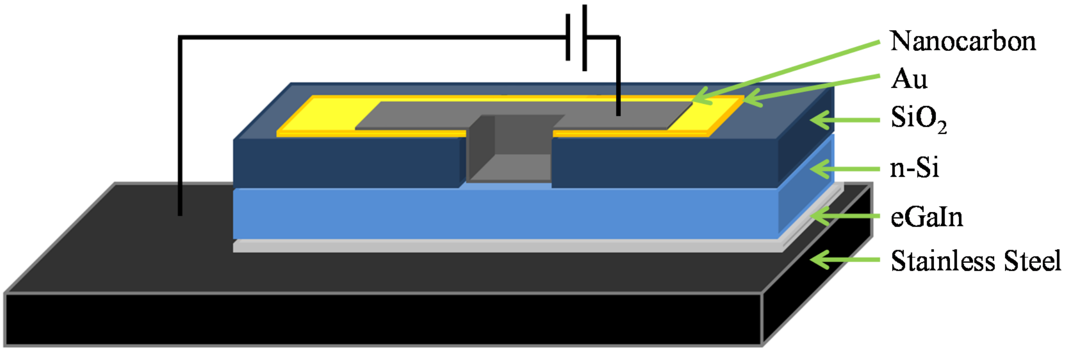

Figure 2.1: Cutaway schematic of nanocarbon-based material-Si solar cell.

2.1.3 Doping of Nanocarbon-Based Material-Silicon Solar Cells

The solar cells were doped using 3 different protocols. (1) Cells were doped with thionyl chloride ($SOCl_2$) by pipetting 2 drops onto the nanocarbon-based material films and allowing it to evaporate in a fume hood, (2) cells were doped with nitric acid (HNO_3) (70 %, Sigma-Aldrich, Australia) by exposing them to concentrated nitric acid vapour for 2 min and (3) cells were doped with gold chloride ($AuCl_3$) (99 %, Aldrich, Australia) by dynamic spin coating (30 s at 3000 rpm) of $AuCl_3$ dissolved in ethyl ether (10 mM).

2.1.4 Film Annealing

All thermal annealing was performed in a tube furnace under a forming gas atmosphere (1:20 H_2:Ar) for 2 h. Annealed films for non-solar cell related measurements were prepared by annealing the nanocarbon-based material films on glass. Annealed cells were prepared by annealing nanocarbon-based material-Si substrates in the same tube furnace conditions prior to back BOE etching.

2.1.5 Characterisation

UV-Vis spectra of nanocarbon-based material films on glass slides (deposited analogously to the previously described film deposition on silicon) were scanned over the range 300 – 850 nm with a resolution of 1 nm using a Varian Cary 50G spectrophotometer.

Raman spectra were collected with a WITec α300R microscope using a 40× objective (NA 0.9) and a 532 nm laser operating at constant power for each spectrum up to a possible maximum of 60 mW. Raman spectra were collected with an integration time of 6 s and 10 accumulations.

Sheet resistance measurements were taken from nanocarbon-based material films on glass using a four-point probe (KeithLink) in linear geometry and a multimeter (GDM-8261, GW Instek).

Atomic force microscopy (AFM) images were acquired in air using a Bruker Dimension FastScan AFM with Nanoscope V controller, operating in tapping mode. Silicon cantilevers (MikroMasch) with a fundamental resonance frequency of between 300 and 400 kHz were used. Images were obtained using a scan rate of 1 Hz with the set point, amplitude, and feedback control parameters optimised manually for each sample. The images presented have been flattened using NanoScope Analysis v1.4 software.

2.1.6 Nanocarbon-Based Material-Silicon Solar Cell Testing

After cell assembly, unless otherwise noted, the nanocarbon-based material-Si interface was treated with 2 % HF (diluted from 48 %, Sigma-Aldrich, Australia) to remove any native oxide layer that had grown back on the Si during the assembly process, and the first J-V test after this step was denoted as the 0 h test. Current-voltage data was collected using a Keithley 2400 SMU instrument and recorded using a custom LabView Virtual Instrument program. Cells were illuminated by collimated 100 mW·cm^{-2} light from a xenon-arc source passed through an AM1.5G filter with the irradiance at the sample plane being measured with a silicon reference cell (PV Measurements, NIST-traceable calibration). J-V curves were obtained by scanning from 1 V to -1 V.

J-V curves were also obtained after doping with $SOCl_2$, HNO_3 and $AuCl_3$. The first J-V test immediately after doping was denoted as the 0 h test, with the cell performance immediately prior to doping presented as a “negative time” value for comparison.

2.2 Characterisation Techniques

2.2.1 UV-Vis Spectroscopy

UV-Vis spectroscopy is a technique in which light, generally ranging in wavelength from 200 – 800 nm, is passed through a sample containing an analyte of interest and the intensity of the remaining light (I) at each wavelength is measured [5]. As the initial intensity of the light (I_0) is known, the transmittance (T) of the sample at any wavelength can be defined as:

$$T = \frac{I}{I_0}$$

Equation 2.1

The transmittance is often reported as percent transmittance (%T) which is calculated by multiplying the transmittance by 100. The %T allows one to quickly determine how much light at each wavelength can pass through the sample uninhibited. Alternatively, the amount of light attenuated, or absorbed, by a sample can be defined as its absorbance, A:

$$A = -\log T$$

Equation 2.2

When light of a certain wavelength passes through a sample, it will experience a decrease in intensity that is proportional to the sample's thickness and the concentration of the analyte [5]. A measure of this effect can be determined using the following equation known as Beer's Law:

$$A = \alpha l C$$

Equation 2.3

where α is the analyte's absorption coefficient (measured in $\text{cm}^{-1}\cdot\text{concentration}^{-1}$), l is the path length of light through the sample (in cm) and C is the concentration of the analyte (in $\text{mg}\cdot\text{mL}^{-1}$). The absorption coefficient α can be thought of as the probability that the analyte will absorb a photon of a given energy and thus is generally reported for a specific wavelength [5].

Vertically aligned arrays of CNTs chemically attached to TCO substrates generally show very little UV-Vis absorbance, unless the networks are built up via repeated ethylenediamine CNT linking [6], as seen in traces A-E of Figure 2.2(a).

Graphene (Figure 2.2(b)) as well as GO and RGO films (Figure 2.2(c)) display broad, featureless UV-Vis spectra throughout the UV-Vis region of 800 nm to approximately 600 nm. As the wavelength of light continues to decrease from 600 nm, the %T of these films begins to decrease, as chromophores present in their chemical structures begin to absorb photons. In graphene films, this involves the $\pi \rightarrow \pi^*$ electronic transition of carbon-carbon double bonds, and in GO and RGO films also includes the $\pi \rightarrow \pi^*$ transition of carbon-oxygen double bonds and the $n \rightarrow \pi^*$transition of carbon-oxygen double bonds [5]. Figure 2.2(b) reports the %T of SLG films layered on top of each other at 550 nm. This convention of transparent conducting film research, while not giving explicit transmittance details across the entire visible spectrum, allows for easy comparison between samples and literature reports [7]. Figure 2.2(d) also shows how the absorption coefficient of surfactant-exfoliated graphene can be determined. As previously described, the absorption coefficient is wavelength dependent, with 660 nm being the generally accepted convention for solution processed graphene [8]. For example, Lotya et al. [9] produced an aqueous dispersion of graphene by ultrasonication of flake graphite in an SDBS solution and vacuum filtration was used to determine the concentration of this dispersion in $\mu g \cdot mL^{-1}$. This dispersion was then used to make a series of dilutions. The UV-Vis absorbance at 660 nm of these dilutions divided by the path length of their cuvette was then plotted against the concentration of the dispersions. It can be seen from Equation 2.3 that the slope of a linear regression of this data will give the corresponding absorption coefficient of the original aqueous graphene dispersion, which in this instance was found to be 1390 $mL \cdot mg^{-1} \cdot m^{-1}$.

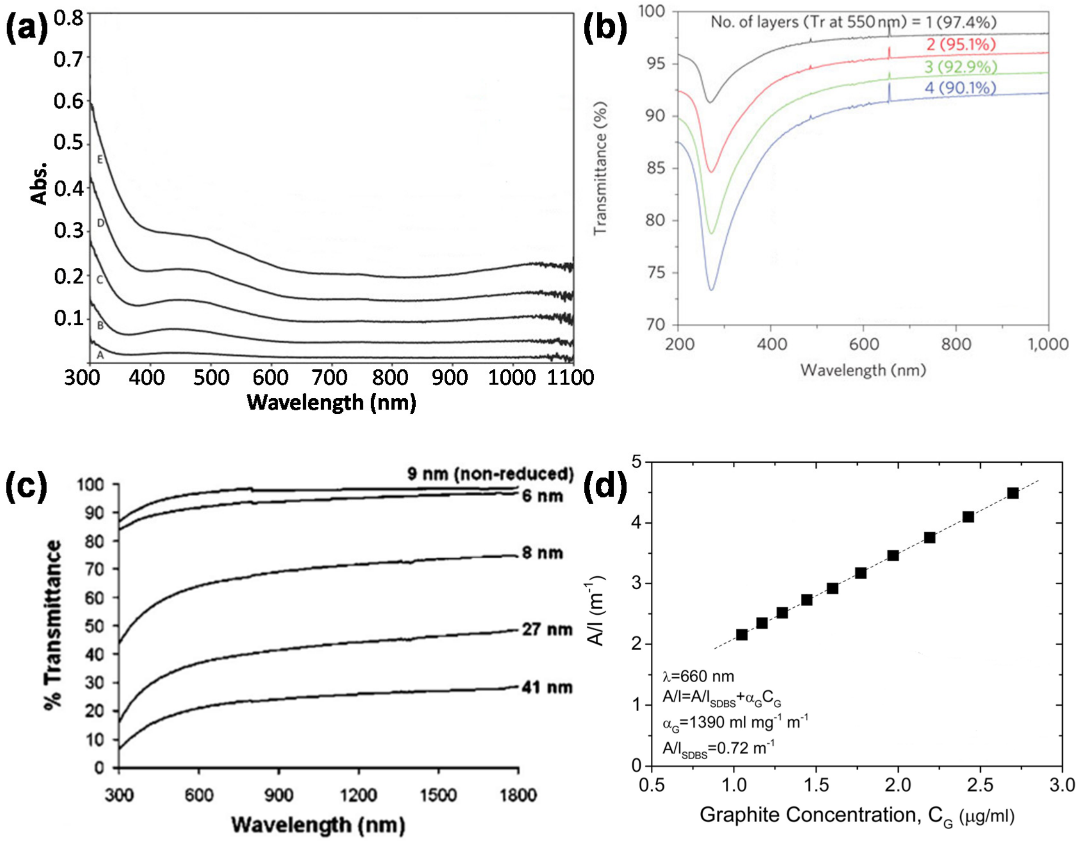

Figure 2.2: (a) Typical UV-Vis absorbance spectra of SWNT networks chemically attached to ITO substrates, with increasing absorbance corresponding with increasing size of the network (traces A-E) (modified from [6]) , (b) UV-Vis percent transmittance spectrum of CVD SLG graphene sheets stacked on top of each other (modified from [10]), (c) UV-Vis transmittance of GO and RGO films reduced using thermal annealing (modified from [11]) and (d) example calculation of the absorption coefficient at 660 nm of exfoliated graphene using the surfactant SDBS (modified from [9]).

2.2.2 Raman Spectroscopy

Raman spectroscopy studies the scattering of light by a sample of interest. When a photon of light of energy $\hbar\omega_L$ is incident on a sample, two types of scattering interactions are possible, viz. elastic and inelastic scattering. In elastic scattering, also known as Rayleigh scattering, the photon may be briefly absorbed by the sample, exciting an electron from the ground state into a “virtual state”, as seen in Figure 2.3(c). However, this virtual state is a forbidden energy level and the photon is quickly emitted by the sample, with the same incident frequency ω_L, returning the electron to its original ground state (again Figure 2.3(c)) [12].

However, in inelastic scattering, or Raman scattering, the frequency of the scattered photon, ω_{Sc}, is different to that of the incident photon. This can occur in one of two processes. In the first, more common, process called the Stokes process, the incident photon, $\hbar\omega_{L}$, again excites an electron-hole pair, e-h. This electron-hole pair however then decays into a phonon of energy $\hbar\Omega$ and a new electron-hole pair e-h′. When e-h′ recombines, the scattered photon will have a lower frequency, ω_{Sc}, than the incident light, ω_{L}, and the electron finishes in a vibrational state higher than its original ground state (see Figure 2.3(a & c)). In the less common process of anti-Stokes scattering, the excited electron may start in a vibrational state higher than the ground state of the sample (Figure 2.3(c)) or absorb a phonon, $\hbar\Omega$, after excitation (Figure 2.3(b)). In either case, the scattered photon emitted after the recombination of e-h′ has a higher frequency, ω_{Sc}, than the initial photon [12].

Finally, non-resonant Raman scattering is the name given to these processes when the excited energy levels of e-h do not correspond to allowed electronic states, as in the left hand side of Figure 2.3(c). If the excited states do correspond to allowed electronic states though, such as in the right hand side of Figure 2.3(c), the intensities of the scattered light are greatly enhanced and the process is said to be "resonant"[12]. Graphene's zero bandgap results in all energy states being resonant at all wavelengths of incident light making Raman a particularly powerful investigative tool [13], while in SWNTs resonance can be caused due to careful selection of wavelength as well as SWNT's unique density of states [14], allowing for relatively easy Raman spectroscopy of both systems.

To produce a Raman spectrum a laser, typically with a wavelength between 500 – 650 nm, is shone on the sample of interest and both the intensity and frequency of the scattered photons is measured. The intensity of the scattered light is then plotted as a function of the "Raman shift", that is, the difference of the incident and scattered photon frequencies, generally reported in wavenumbers (cm^{-1}).

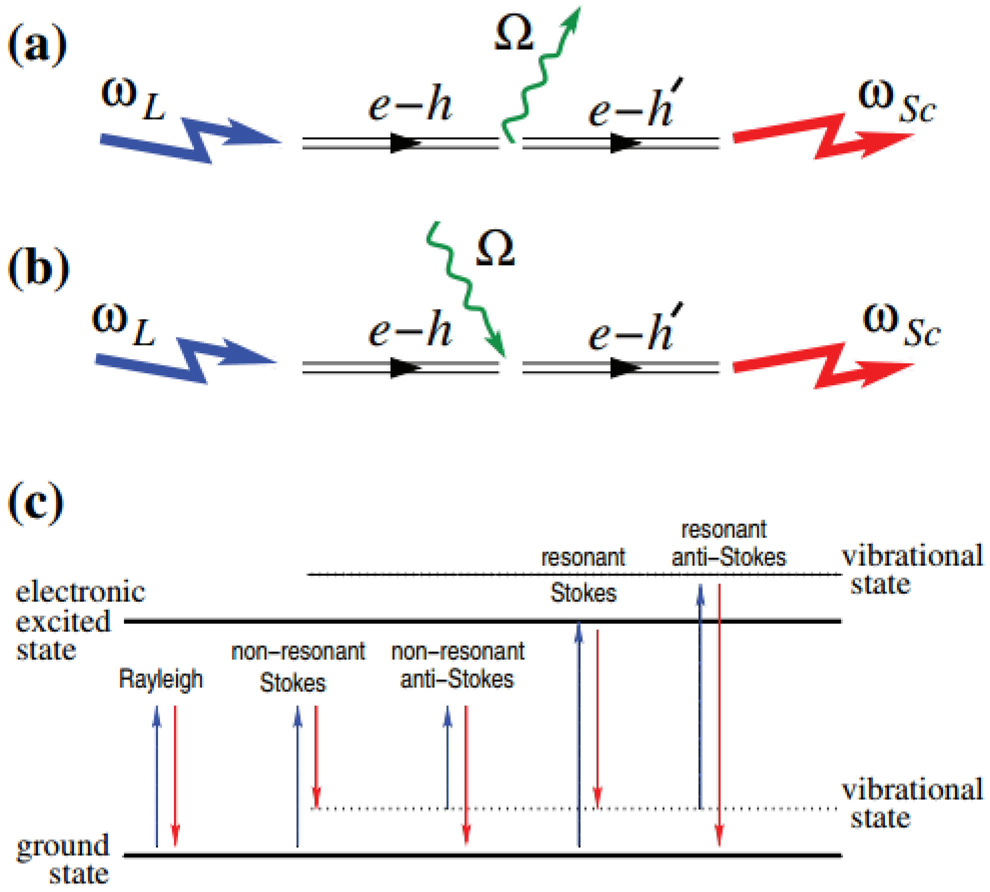

Figure 2.3: (a) Stokes scattering of an incident photon with frequency ω_L that excites an electron-hole pair e-h. This electron-hole pair then decays into a phonon, Ω, and another electron hole pair e-h′, which recombines, emitting a scattered photon of lower frequency ω_{Sc}, (b) anti-Stokes scattering, whereby a photon with the same frequency ω_L is excites an electron-hole pair that then absorbs a phonon, Ω, resulting in the electron-hole pair e-h′. When this electron-hole pair recombines, the scattered photon emitted has a higher frequency ω_{Sc}, (c) graphical representation of resonant and non-resonant Rayleigh, Stokes and anti-Stokes scattering (from [12]).

Raman spectra of CNTs have a number of typical Raman features, both first- and second-order, that can be observed in Figure 2.4(a) [14]. Although there are slight differences to the composition and shape of some of these features between metallic and semiconducting CNTs, the general position of the features remains the same across tube types. The lowest wavenumber first-order peak observed in the Raman spectra presented in Figure 2.4(a) is a SWNT signature feature, called the radial breathing mode (RBM). This feature corresponds to the vibration of carbon atoms in the radial direction of the tube, as if the tube were “breathing” with its diameter expanding and shrinking (Figure 2.4(b)). The RBM generally occurs between 120 – 350 cm^{-1} and can be used to determine the diameter and hence chirality of SWNTs present in a sample. The RBMs observed in Figure 2.4(a) are also a good demonstration of the resonance effect, as the RBM for the semiconducting tube is not in resonance with the wavelength of the laser being used to probe the surface (784 nm) and thus is not easily observed when compared to the resonant metallic RBM. The next important first-order Raman feature of CNTs is the G-band, which is also observed in other graphitic carbons such as graphene. This band generally occurs between 1560 – 1590 cm^{-1} and its corresponding sp^2 carbon vibrations can be observed in Figure 2.4(c). When analysing SWNTs, the G-band can be particularly useful for determining whether the nanotubes are semiconducting or metallic, based on the G-band line structure [14].

SWNT Raman spectra also have two second-order features commonly observed, viz. the D-band and the G′-, or 2D-, band. These features can also be seen in other graphitic carbons such as graphene and are double-resonance processes and thus may be observed quite strongly [14]. The D-band, also known as the disorder band, is observed due to atomic defects in the carbon lattice, or where there are dangling bonds or sp^3 hybridised carbon, for example at the ends of a CNT or sites of chemical modification [15]. This does mean however that if the carbon lattice of a SWNT is not defected in the area that the laser is incident, it is possible that a D-band will not be observed, as is the case in the metallic SWNT seen in Figure 2.4(a). If defects are present however, this band typically occurs at around 1350 cm^{-1}.The second, second-order feature observed in SWNTs (and, again, also other graphitic carbon such as graphene), is the G′-band. This band was originally designated as such during early Raman investigations of graphite, but it is in fact the second harmonic of the D-band and as such is now also referred to as the 2D-band [16]. However, unlike the D-band, the contributions causing the presence of the 2D-band do not need to occur due to defects in the carbon lattice, and as such this feature can always be observed in CNT Raman spectra. This is again displayed in the Raman spectrum of the metallic SWNT seen in Figure 2.4(a), where not only is the 2D-band (labelled G′) present but, due to its double resonance, is observed with a greater intensity than the first order G-band. The 2D band in CNT spectra generally occurs at around 2700 cm^{-1}, as would be expected from its status as the D-band's (~1350 cm^{-1}) second harmonic [14].

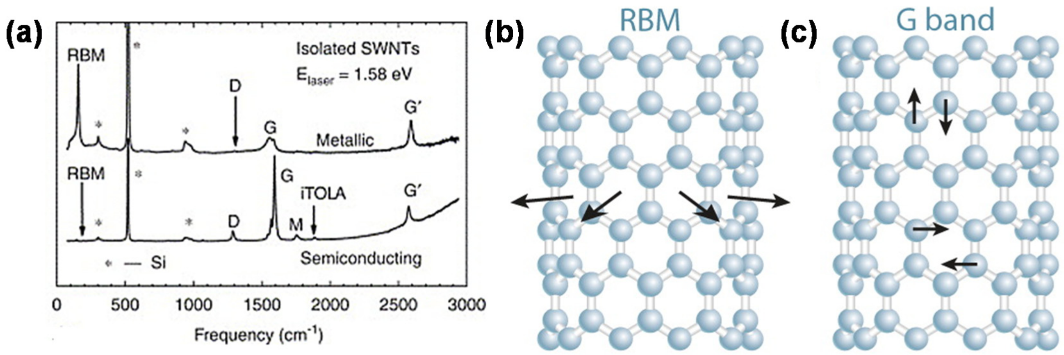

Figure 2.4: (a) Raman spectra of isolated metallic and semiconducting carbon nanotubes on a Si substrate showing the typical CNT Raman peaks of the radial breathing mode, D-band, G-band and G′ band, along with other weak CNT features (M and iTOLA) and silicon peaks marked with * (from [14]), (b) the direction of carbon-carbon bond stretching occurring when the radial breathing mode occurs and (c) when the G-band occurs (both (b) and (c) modified from [15]).

As previously eluded to, graphene and indeed GO, have quite similar Raman features to CNTs. Figure 2.5(a) shows the Raman spectrum of graphite, with a sharp G-band and a prominent 2D-band of lower intensity [17]. This is reversed in the Raman spectrum of single-layer graphene, also seen in Figure 2.5(a), where the 2D-band intensity can be up to four times greater than the intensity of the G-band. Another difference of note between the Raman spectra of graphite and graphene is the shape of the 2D-band. As seen in Figure 2.5(b), the 2D-band, which in graphite generally has its maximum after 2700 cm^{-1}, has a prominent shoulder on the lower wavenumber side. In single-layer graphene however, the 2D-band peak is downshifted, having a maximum before 2700 cm^{-1}, and consists of only one peak [18]. Thus, the 2D-band can be used to monitor the presence of single- and few layer graphene, with the 2D-band dropping in intensity and being composed of more than one peak as the number of layers of graphene increases (Figure 2.5(b)) [18].

Solution and surfactant-assisted exfoliated graphene have similar Raman spectra to each other, with Figure 2.5(c) presenting the Raman spectrum of surfactant-assisted exfoliated graphene, along with starting graphite material and chemically reduced graphene oxide [19]. Of note, in comparison to the mechanically exfoliated graphene shown in Figure 2.5(a), is the presence of a noticeable D-band in the exfoliated graphene and, to a lesser extent, the starting graphite. The presence of this D-band is related to the defects in the carbon lattice at the edges of both the graphite starting material and the exfoliated graphene flakes [8]. Due to the small size of graphene flakes made in solvent exfoliation techniques and the comparatively large spot size of the lasers used for Raman spectroscopy, light is unavoidably scattered off the edges of the graphene flakes and thus the D-band in these Raman spectra are not indicative of basal plane defects, as would be the case in RGO or chemically modified CNT spectra.

A typical Raman spectra of RGO can also be seen in Figure 2.5(c). Generally, RGO spectra consist of G- and D-bands of similar intensities, and much broader and low intensity 2D-bands. The presence of such large D-bands is to be expected due to the wide ranging defects and chemical functionalisation of the RGO flakes. Similarly, the low intensity, broad 2D-band is also due to disorder of the carbon lattice, as is the second peak at 2900 cm^{-1} sometimes observed in RGO Raman spectra [19].

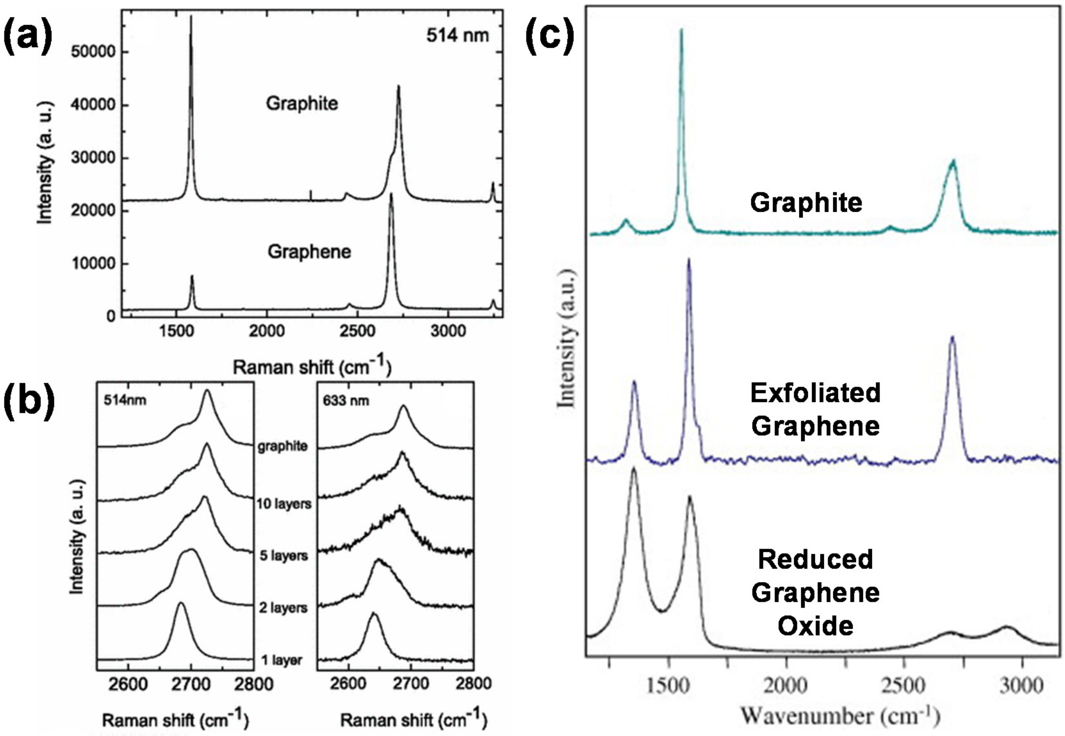

Figure 2.5: Raman spectrum of (a) graphite and single-layer graphene, (b) the 2D-band of graphite, 10 layer graphene, 5 layer graphene, 2 layer graphene and 1 layer graphene at two different laser wavelengths (a & b modified from [17]) and (c) graphite, surfactant assisted exfoliated graphene and chemically reduced graphene oxide (modified from [19]).

2.2.3 *Atomic Force Microscopy*

Atomic force microscopy is a scanning probe microscopy technique, originally developed by Binnig, Quate and Gerber [20]. The probe used in AFM has three constituents, viz. the chip, cantilever and tip (see Figure 2.6). The chip is the largest of the three components and is used for gross handling, for example loading of the probe into the AFM itself and subsequent course positioning. The cantilever is a much smaller structure that is attached to the chip, and at the end of the cantilever is the tip, which interacts directly with the surface of the sample. In a sample scanning AFM, the sample is mounted onto a piezoelectric scanner that is capable of scanning in three dimensions. This allows for the sample to be scanned across the tip both laterally, along the x and y axes, as well as vertically along the z axis. In the tapping mode of operation, the cantilever to which the tip is attached is oscillated at a known amplitude, close to its resonate frequency. When the scanner is used to bring the sample into contact with the oscillating tip, the amplitude and frequency of the cantilever oscillations will decrease. This change in amplitude is measured by monitoring the deflection of a laser beam that is reflected off of the end of the cantilever and onto a four quadrant photodetector. The scanner is then moved along the z axis through the use of feedback loops to maintain the initial amplitude of the cantilever, and thus gives topographic information related to the surface being probed. This process is then repeated as the sample is raster scanned in the lateral dimensions, giving nanometre topography details as the tip is tapped across micron sized areas [21]. A schematic of these basic AFM components can be seen in Figure 2.6.

AFM, in conjunction with other chemically specific techniques such as Raman spectroscopy, is a very popular technique for investigating the presence of nanocarbon-based materials such as CNTs, graphene, GO and RGO. Figure 2.7(a & b) shows representative AFM images of individual flakes of surfactant assisted exfoliated graphene that has been deposited onto a SiO_2/Si substrate. These images clearly show that the flakes vary in lateral dimensions from the tens of nanometres to the hundreds of nanometres, while the height profiles of the line sections shown in green indicate that these flakes are between 1-2 layers thick [19]. Figure 2.7(a) also potentially shows a thicker section of a flake to the left of the image which appears to show a graphene layer or layers mid-exfoliation. Figure 2.7(c & d) on the other hand show representative AFM images of RGO films that have been annealed at temperatures of 1100 ºC. Figure 2.7(c) shows a very thin spin coated RGO film that shows complete coverage of the substrate at a thickness of 3 nm, while the inset shows a sub-monolayer film clearly depicting isolated flakes across the substrate. Figure 2.7(d) shows a 67 nm RGO film also annealed at 1100 ºC. In this AFM image of a thicker film, the ability to resolve individual RGO flakes is lost but characteristic micron long wrinkles can be seen across the film [11].

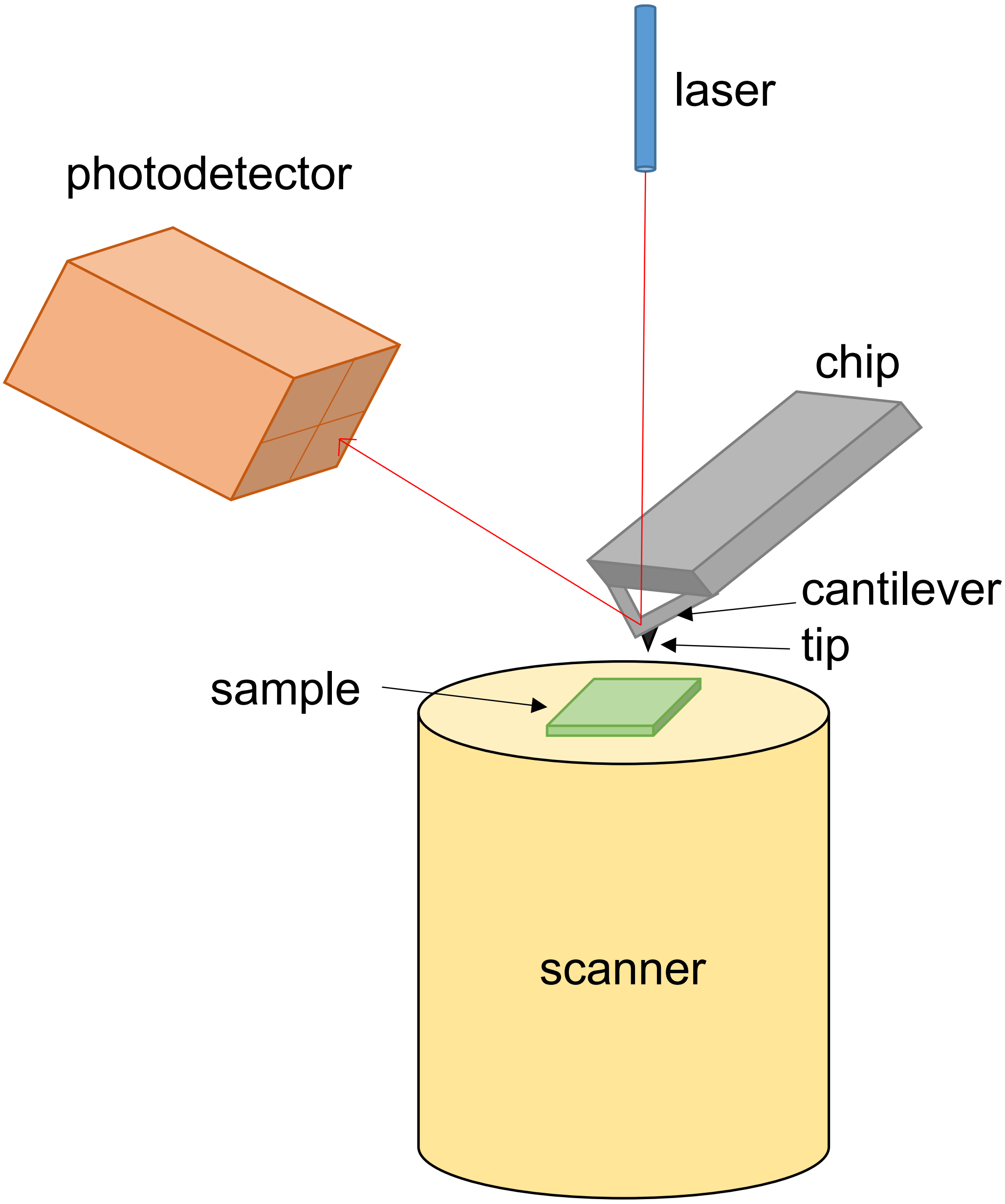

Figure 2.6: Basic schematic of an atomic force microscope, showing the probe and its individual constituents the chip, cantilever, and tip, along with the laser, scanner and photodetector and the sample being probed (adapted from [21]).

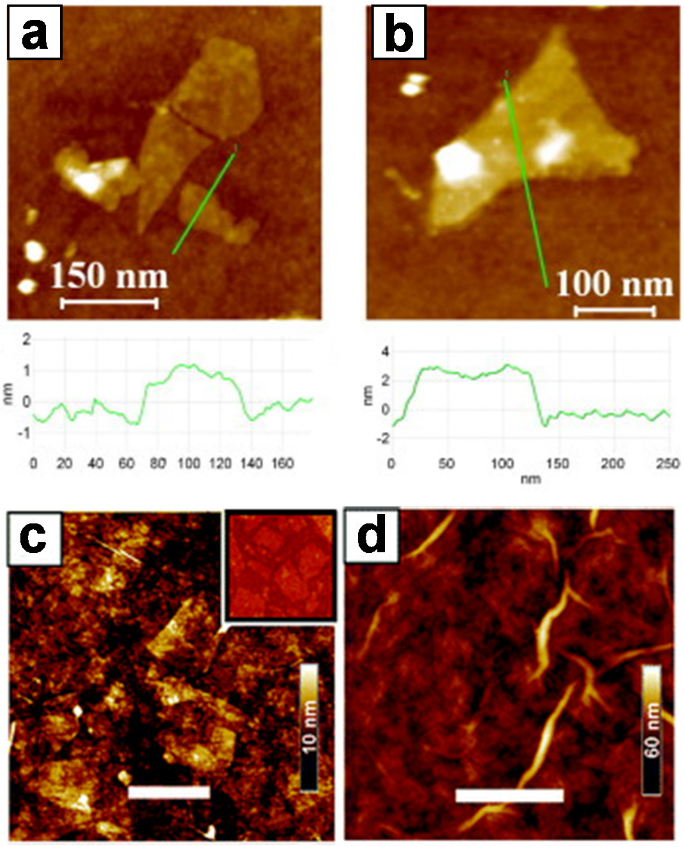

Figure 2.7: Representative AFM images of (a & b) surfactant assisted exfoliated graphene flakes deposited on SiO_2/Si substrates, showing height profiles of each line section (modified from [19]) and (c) tapping mode AFM image of spin coated 3 nm thick continuous GO film showing edges of flakes and inset a sub-monolayer film showing isolated flakes and (d) a 67 nm RGO film reduced at 1100 ºC showing characteristic wrinkling (Scale bars in c & d are 1 μm and both images are modified from [11]).

2.2.4 Solar Testing

The Sun emits electromagnetic radiation that approximates the spectrum of a blackbody at a temperature of 5760 K. Figure 2.8 shows the extra-terrestrial solar spectral irradiance experienced in space at the edge of the Earth's atmosphere in the blue trace. However, the spectral solar irradiance experienced at any point on the Earth's surface is not equivalent to this extra-terrestrial irradiance for a number of reasons, and in fact, differs all over the world. Molecules in the Earth's atmosphere both absorb and scatter light from the Sun before it can reach the Earth's surface. For example, ozone filters out a large section of the UV radiation, while water and CO_2 absorb heavily in the infrared region. The magnitude of these losses to the spectral irradiance experienced at the Earth's surface is minimised when the sun is directly overhead, i.e., the light incident at the surface has travelled through the least amount of atmosphere possible [22].

This distance, or path length, that light travels through the atmosphere before reaching the Earth's surface is referred to as the air mass (AM) and can be defined as follows:

$$\mathrm{AM} = \frac{1}{\cos \varphi}$$

Equation 2.4

where φ is the angle of elevation of the sun. Using Equation 2.4, two cases can immediately be defined, AM0 and AM1.0. AM0 refers to the previously defined extra-terrestrial spectral irradiance, experienced for example by orbiting satellites, while AM1.0 refers to the irradiance spectrum observed at the surface of the Earth when the sun is directly overhead ($\varphi = 0$) i.e., the shortest path length through the atmosphere. It can also be seen from Equation 2.4, that the effective AM at a point on the Earth's surface will vary not only due to the latitude of the location, but also on the relative position of the sun at that location, influenced by the time of day as well as the time of year [23]. Therefore in order to compare the relative performance of photovoltaic devices, one should use a reference standard solar spectral distribution, an agreed upon standard which can be used to accurately compare the performance of a device regardless of where or when it is being tested.

This standard was first defined in the 1970s by what is now known as ASTM International, with the most current reference being the ASTM G173-03 [23]. The actual solar spectral irradiance is referred to as the AM1.5G solar irradiance spectrum, where G stands for global, meaning that irradiance from diffuse reflectance from both the sky and ground is included in the total irradiance. AM1.5 is the solar irradiance spectrum when φ is equal to 42°, approximating the annual irradiance throughout the contiguous states of the United States of America as experienced by a 37° tilted sun-facing surface. This spectral irradiance can be seen as the red trace of Figure 2.8, where the effects of atmospheric scattering can most noticeably be observed by the lower solar irradiance at lower (UV) wavelengths when compared to the AM0 spectrum. The effects of atmospheric absorption are also visible, with a number of clearly defined absorption peaks occurring throughout the spectra including peaks caused by molecular oxygen at approximately 760 nm, water at 900, 1100, 1400 and 1900 nm, and CO_2 at 1800 and 2600 nm [22]. The total integrated irradiance across the spectrum of AM1.5G light is normalised to 1000 $W \cdot m^{-2}$, and is often referred to as 1 Sun when light intensity testing is carried out.

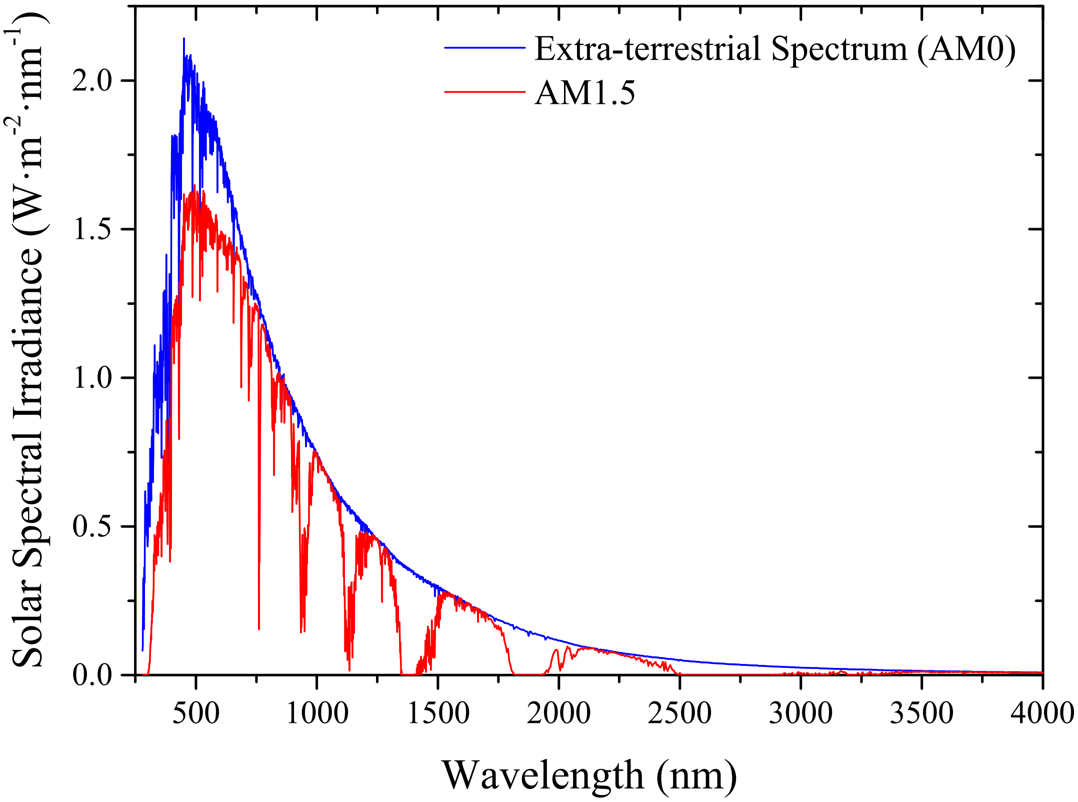

Figure 2.8: ASTM G173-03 reference spectra, showing both the extra-terrestrial (AM0) and AM.15G solar spectral irradiance [23].

AM1.5G light is often simulated in the laboratory through the use of “solar simulators” which use xenon lamps coupled with optical filters to produce the required spectrum and irradiance [24]. Several steps should be taken when using a solar simulator however to ensure that accurate photovoltaic testing can be performed. These include ensuring that the intensity profile of the light is uniform across the area of the cell being measured, calibrating the irradiance of the light using a reference cell of similar spectral response to the cell being investigated, accurately estimating the cell’s active area and ensuring appropriate anti-reflective surfaces are in place around the testing stage [24]. Even when all these factors are taken into account, the inherent limits of reproducibility of solar cells within batches means that average values of photovoltaic performance should be reported when possible [24].

2.3 References

1. Tune, DD, Flavel, BS, Krupke, R & Shapter, JG 2012, 'Carbon nanotube-silicon solar cells', *Advanced Energy Materials*, vol. 2, no. 9, pp. 1043-55.

2. Tune, DD, Flavel, BS, Quinton, JS, Ellis, AV & Shapter, JG 2013, 'Single-walled carbon nanotube/polyaniline/n-silicon solar cells: Fabrication, characterization, and performance measurements', *ChemSusChem*, vol. 6, no. 2, pp. 320-7.

3. Tune, DD & Shapter, JG 2013, 'Effect of nanotube film thickness on the performance of nanotube-silicon hybrid solar cells', *Nanomaterials*, vol. 3, no. 4, pp. 655-73.

4. Tune, DD, Blanch, AJ, Krupke, R, Flavel, BS & Shapter, JG 2014, 'Nanotube film metallicity and its effect on the performance of carbon nanotube–silicon solar cells', *Physica Status Solidi A: Applications and Materials Science*, vol. 211, no. 7, pp. 1479-87.

5. Harvey, D 2000, *Modern analytical chemistry*, McGraw Hill Higher Education, Kingsport.

6. Tune, DD, Flavel, BS, Quinton, JS, Ellis, AV & Shapter, JG 2010, 'Single walled carbon nanotube network electrodes for dye solar cells', *Solar Energy Materials and Solar Cells*, vol. 94, no. 10, pp. 1665-72.

7. Barnes, TM & Blackburn, JL 2010, 'Carbon nanotube transparent electrodes', in A Facchetti & TJ Marks (eds), *Transparent electronics: From synthesis to applications*, John Wiley & Sons Ltd, West Sussex, pp. 185-205.

8. Hernandez, Y, Nicolosi, V, Lotya, M, Blighe, FM, Sun, Z, De, S, McGovern, IT, Holland, B, Byrne, M, Gun'Ko, YK, Boland, JJ, Niraj, P, Duesberg, G, Krishnamurthy, S, Goodhue, R, Hutchison, J, Scardaci, V, Ferrari, AC & Coleman, JN 2008, 'High-yield production of graphene by liquid-phase exfoliation of graphite', *Nature Nanotechnology*, vol. 3, no. 9, pp. 563-8.

9. Lotya, M, Hernandez, Y, King, PJ, Smith, RJ, Nicolosi, V, Karlsson, LS, Blighe, FM, De, S, Wang, Z, McGovern, IT, Duesberg, GS & Coleman, JN 2009, 'Liquid phase production of graphene by exfoliation of graphite in surfactant/water solutions', *Journal of the American Chemical Society*, vol. 131, no. 10, pp. 3611-20.

10. Bae, S, Kim, H, Lee, Y, Xu, X, Park, J-S, Zheng, Y, Balakrishnan, J, Lei, T, Ri Kim, H, Song, YI, Kim, Y-J, Kim, KS, Ozyilmaz, B, Ahn, J-H, Hong, BH & Iijima, S 2010, 'Roll-to-roll production of 30-inch graphene films for transparent electrodes', *Nature Nanotechnology*, vol. 5, no. 8, pp. 574-8.

11. Becerril, HA, Mao, J, Liu, Z, Stoltenberg, RM, Bao, Z & Chen, Y 2008, 'Evaluation of solution-processed reduced graphene oxide films as transparent conductors', *ACS Nano*, vol. 2, no. 3, pp. 463-70.

12. Ferrari, AC & Basko, DM 2013, 'Raman spectroscopy as a versatile tool for studying the properties of graphene, suppl.', *Nature Nanotechnology*, vol. 8, no. 4, pp. 235-46.

13. Ferrari, AC & Basko, DM 2013, 'Raman spectroscopy as a versatile tool for studying the properties of graphene', *Nature Nanotechnology*, vol. 8, no. 4, pp. 235-46.

14. Dresselhaus, MS, Dresselhaus, G, Saito, R & Jorio, A 2005, 'Raman spectroscopy of carbon nanotubes', *Physics Reports*, vol. 409, no. 2, pp. 47-99.

15. Dresselhaus, MS, Jorio, A & Saito, R 2010, 'Characterizing graphene, graphite, and carbon nanotubes by Raman spectroscopy', *Annual Review of Condensed Matter Physics*, vol. 1, no. 1, pp. 89-108.

16. Ferrari, AC 2007, 'Raman spectroscopy of graphene and graphite: Disorder, electron-phonon coupling, doping and nonadiabatic effects', *Solid State Communications*, vol. 143, no. 1-2, pp. 47-57.

17. Ferrari, AC, Meyer, JC, Scardaci, V, Casiraghi, C, Lazzeri, M, Mauri, F, Piscanec, S, Jiang, D, Novoselov, KS, Roth, S & Geim, AK 2006, 'Raman spectrum of graphene and graphene layers', *Physical Review Letters*, vol. 97, no. 18, p. 187401.

18. Dresselhaus, MS, Dresselhaus, G & Hofmann, M 2008, 'Raman spectroscopy as a probe of graphene and carbon nanotubes', *Philosophical Transactions of the Royal Society A: Mathematical, Physical and Engineering Sciences*, vol. 366, no. 1863, pp. 231-6.

19. Guardia, L, Fernández-Merino, MJ, Paredes, JI, Solís-Fernández, P, Villar-Rodil, S, Martínez-Alonso, A & Tascón, JMD 2011, 'High-throughput production of pristine graphene in an aqueous dispersion assisted by non-ionic surfactants', *Carbon*, vol. 49, no. 5, pp. 1653-62.

20. Binnig, G, Quate, CF & Gerber, C 1986, 'Atomic force microscope', *Physical Review Letters*, vol. 56, no. 9, pp. 930-3.

21. Tsukruk, VV & Singamaneni, S 2012, 'Scanning probe microscopy basics', in *Scanning probe microscopy of soft matter: Fundamentals and practices*, Wiley-VCH Verlag & Co. KGaA, Weinheim, pp. 9-29.

22. Hagfeldt, A, Boschloo, G, Sun, L, Kloo, L & Pettersson, H 2010, 'Dye-sensitized solar cells', *Chemical Reviews*, vol. 110, no. 11, pp. 6595-663.

23. ASTM International 2012, *ASTM G173-03: Standard tables for reference solar spectral irradiances: Direct normal and hemispherical on 37° tilted surface*, ASTM International, West Conshohocken, PA.

24. Snaith, HJ 2012, 'The perils of solar cell efficiency measurements', *Nature Photonics*, vol. 6, no. 6, pp. 337-40.

Chapter 3

TIPS-DBC/SWNT/FTO Solar Cells

Vertically aligned arrays of SWNTs on FTO substrates were used to make working electrodes for photoelectrochemical solar cells. 7,14-bis[2-[tris(1-methylethyl)silyl]ethynyl]dibenzo[b,def]chrysene (TIPS-DBC) layers were then deposited onto the working electrodes and the enhanced photovoltaic properties of the new TIPS-DBC/SWNT/FTO electrodes were investigated. The TIPS-DBC deposition process was then optimised for maximum power conversion efficiency.

This chapter contains material previously published in:

Larsen, LJ, Tune, DD, Kemppinen, P, Winzenberg, KN, Watkins, SE & Shapter, JG 2012, 'Increased performance of single walled carbon nanotube photovoltaic cells through the addition of dibenzo[b,def]chrysene derivative', *Journal of Photochemistry and Photobiology A: Chemistry*, vol. 235, pp. 72-6.

3.1 Introduction

There has been a significant amount of investigation of DSCs since O'Regan and Grätzel's [1] initial paper in 1991. The majority of this investigation has generally focused on the archetypal DSC design discussed in Chapter 1 Section 1.6.1, viz. a photoanode consisting of a TCO layer with a mesoporous TiO_2 layer sensistised with a photoactive dye sandwiched together with a CE, with a redox electrolyte completing the electrical circuit [2].

CNTs have found applications within conventional DSC designs in a number of ways, helping to replace conventional TCO layers [3, 4], as additives in the photoanode [5, 6] or as a replacement for platinum in the CE [7, 8]. Alternatively, CNTs deposited using electrophoresis [9] or vacuum filtration [10] have been used to completely replace the TiO_2 layer while more success has recently been found using CNT-based fibre-shaped DSCs [11-14].

Non-fibre-based DSCs using CNTs as the basis of the working electrode suffered from large electron-hole recombination problems. Bissett and Shapter [15] thus proposed to reduce the amount of recombination occurring due to intertube interactions via the covalent attachment of SWNTs onto fluorine doped tin oxide (FTO) in vertically aligned arrays. This approach was successful in increasing the photoresponse obtained from the cell compared with thin film cells in terms of photocurrent and photovoltage produced, despite the overall low PCE generated (4.7×10^{-5} %). Tune et al. [16] further investigated the potential of CNT arrays covalently attached to indium tin oxide (ITO) electrodes. This work also investigated the chemical attachment of N3 dye, commonly found in Grätzel cells [17, 18], to the CNTs. While the introduction of the dye to the system resulted in an increase in the J_{SC} of the cells, V_{OC} and FF both decreased [16].

At the same time, work in the field of organic photovoltaics had focused on the replacement of conducting polymers used within the bulk heterojunction, such as P3HT, with small molecules such as acenes [19-21]. While the use of small molecules is advantageous with regards to cost and purity there are performance issues associated with their use within the heterojunction. Chief amongst these is the reactivity of acenes, such as pentacene, with fullerenes, which leads to a decrease in the efficiency of the bulk heterojunction [19]. Winzenberg et al. [22] reported the use of two derivatives of the polycyclic aromatic hydrocarbon dibenzo[*b,def*]chrysene (DBC) blended with [6,6]-phenyl-C_{61}-butyric acid methyl ester (PCBM) in bulk heterojunction cells. It was shown that DBC derivatives did not react with fullerenes such as PCBM. Cells based on one of the DBC derivatives, 7,14-bis[2-[tris(1-methylethyl)silyl]ethynyl]dibenzo[*b,def*]chrysene (TIPS-DBC), showed promising PCEs of 2.25 % [22]. Single crystal X-ray studies by Winzenberg et al. [22] also showed that this particular DBC derivative adopts a 1-D stack due to strong intermolecular π-π interactions.

The promising performance of these DBC cells, combined with the affinity of DBC derivatives for π-π stacking raises the possibility of combining DBC derivatives with SWNT photovoltaic architectures. Due to the aromatic nature of SWNT sidewalls, DBC derivatives should preferentially adsorb to the sidewalls of the SWNTs and hence promote efficient charge transfer between a photoexcited DBC derivative and the SWNT, resulting in an increased photovoltaic output of the cell. This chapter thus investigates and optimises the effect of adding a TIPS-DBC layer to SWNT/FTO electrodes via spin coating has on the photovoltaic performance of photoelectrochemical cells made with the subsequent TIPS-DCB/SWNT/FTO electrodes.

3.2 Experimental Methods

3.2.1 Electrode Preparation

Carbon nanotube arrays were prepared via an existing technique [15], the scheme of which is presented in Figure 3.1. SWNTs (P2-SWNT, Carbon Solutions Inc., California) were “cut” by adding them to a 3:1 v/v solution of H_2SO_4 (98 %):HNO_3 (70 %) at a concentration of 1 mg·mL^{-1}. The solution was ultrasonicated at 0 °C for 8 h, quenched and the resulting solution was filtered under vacuum using a 0.4 µm filter paper (Isopore HTTP, Millipore). The SWNTs were then suspended via ultrasonication in a solution of dimethylsulphoxide (DMSO) (99.9 % anhydrous, Sigma Aldrich) containing dicyclohexylcarbodiimide (DCC) (99 %, Sigma Aldrich) resulting in a 0.2 mg·mL^{-1} SWNT/DCC solution.

FTO coated glass (TCO22-15, Solaronix SA, 15 **Ω**·square^{-1}) was cleaned via ultrasonication in ethanol for five minutes. The cleaned FTO was then hydroxylated in a two-step process, Figure 3.1(a). The FTO was placed in a 1:1:5 v/v solution of NH_4OH (28-30 %, AR Grade, Sigma Aldrich), H_2O_2 (30 %, AR Grade, Chem-Supply) and MilliQ water and heated at 80 °C for 20 min. It was then rinsed with MilliQ water and placed in a 1:1:5 v/v solution of HCl (37 %, AR Grade, BDH Lab Supplies), H_2O_2 and MilliQ water and heated at 80 °C for 20 min before being rinsed with MilliQ water and dried thoroughly under nitrogen gas. Hydroxylated FTO was subsequently submerged in the SWNT/DCC solution and heated at 80 °C for 24 h under nitrogen, Figure 3.1(b). After heating, the SWNT/FTO electrodes, Figure 3.1(c), were rinsed thoroughly with isopropanol (≥99.5 %, AR Grade, Merck) and dried under nitrogen.

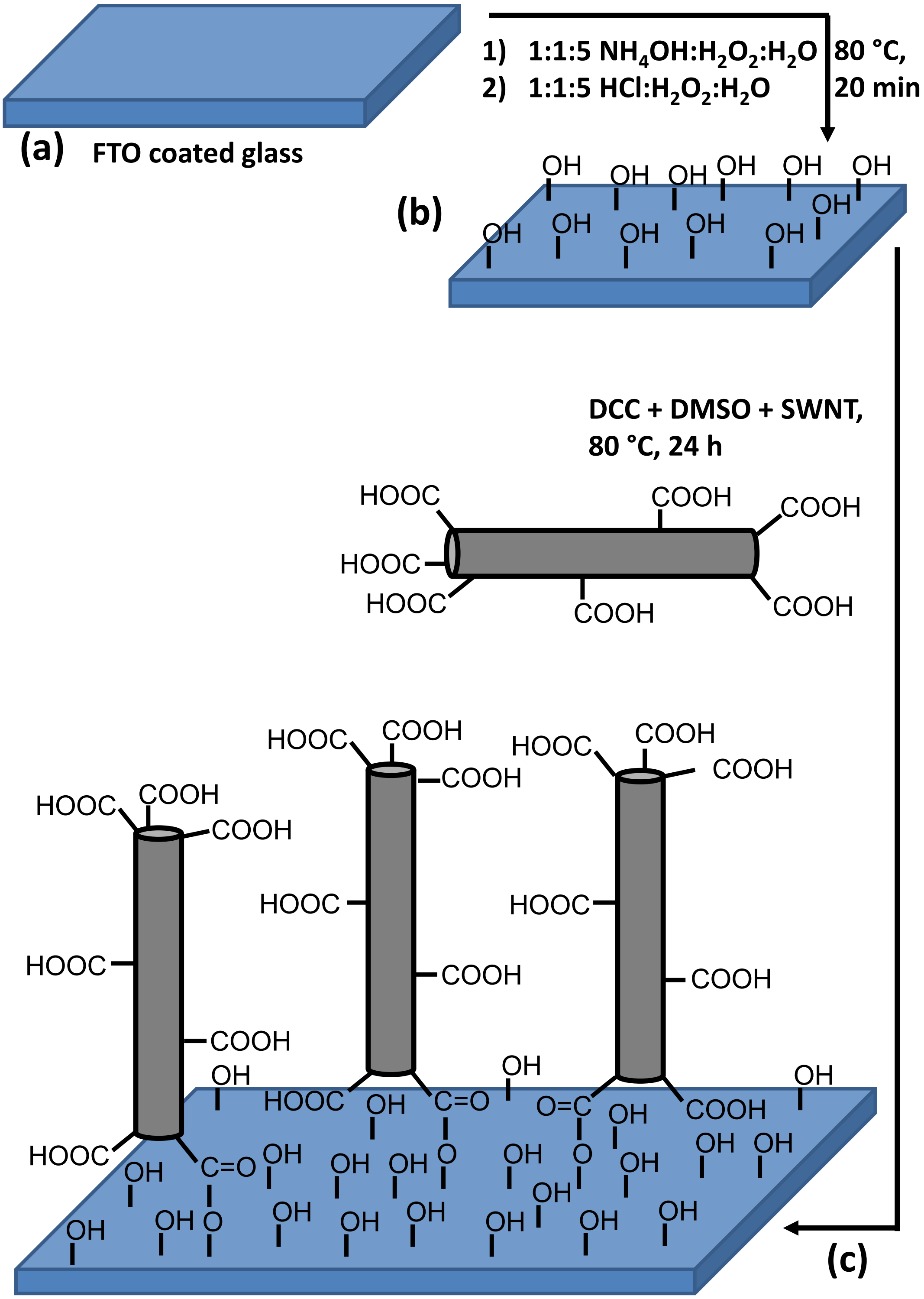

Figure 3.1: Scheme showing the preparation of SWNT/FTO working electrodes with (a) the preparation of hydroxylated FTO electrodes, (b) the addition of SWNT/DBC solution to the hydroxylated FTO substrate and (c) a vertically aligned SWNT/FTO electrode (not drawn to scale).

TIPS-DBC (prepared as previously described by Winzenberg et al. [22]) was dissolved in chloroform to make solutions ranging from 5 – 40 mg·mL^{-1}. TIPS-

DBC/SWNT/FTO electrodes were prepared by spin coating of the TIPS-DBC solutions onto the SWNT/FTO electrode, Figure 3.2. Dynamic spin coating was performed with a WS-400B-6NPP/Lite (Laurel Technologies) spin coater operating at the specified rpm.

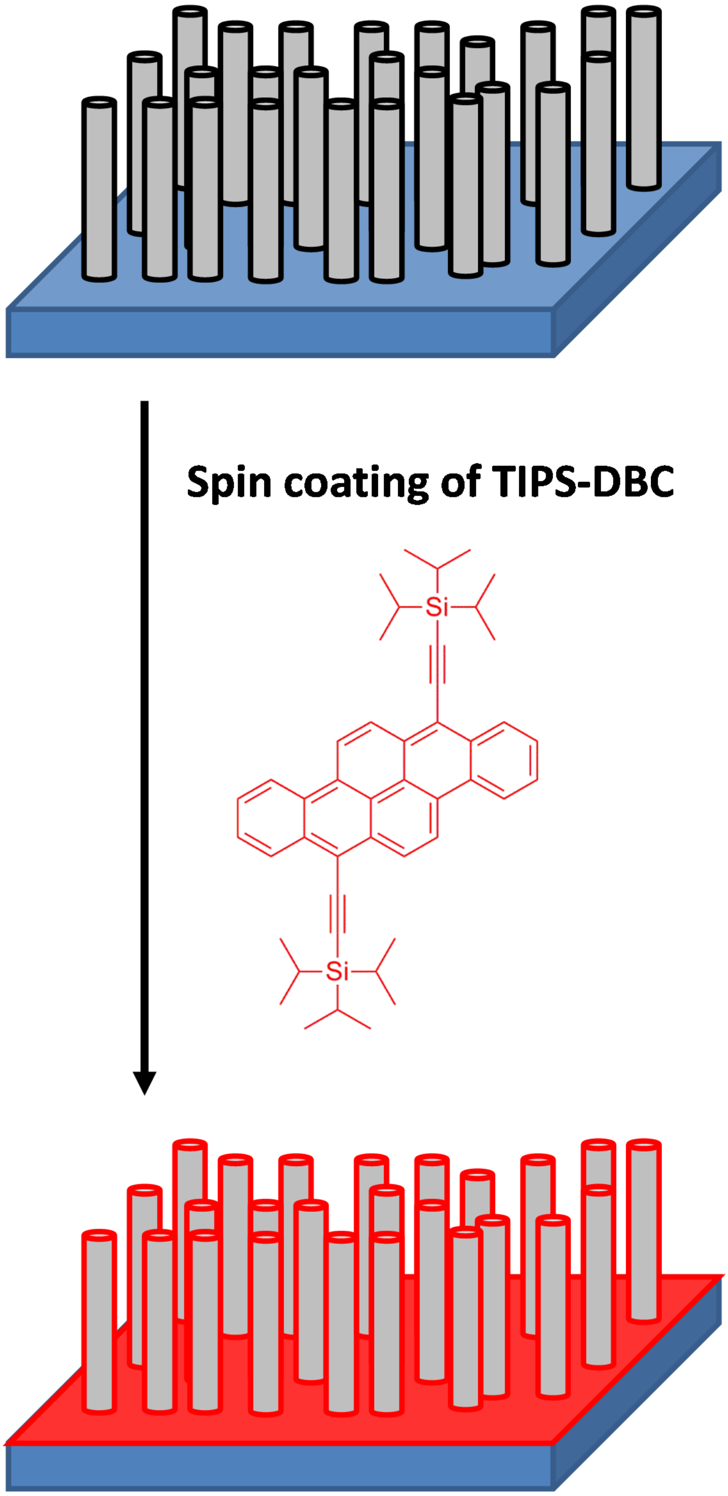

Figure 3.2: Preparation of TIPS-DBC/SWNT/FTO working electrodes (not drawn to scale).

SWNT solar cells were prepared using the SWNT/FTO working electrodes described previously. Pt/FTO counter electrodes were fabricated by sputtering a 5 nm thick layer of platinum onto FTO coated glass. The SWNT/FTO working electrode was then placed SWNT side down onto a Teflon spacer (which defined the active area of the cell) which was on top of the counter electrode and the three components were then sandwiched together. Once assembled, electrolyte consisting of 0.8 M 1-methyl-3-propylimidazolium iodide (MPII) (≥98.0 % HPLC, Aldrich) and 0.1 M I_2 (≥99 %, Sigma-Aldrich) in 3-methoxypropionitrile (MPN) (≥98.0 % HPLC, Aldrich) was introduced via capillary action. A schematic of the assembled cell can be seen in Figure 3.3(a). TIPS-DBC/SWNT/FTO solar cells were prepared in the same manner, with a schematic of an assembled cell shown in Figure 3.3(b).

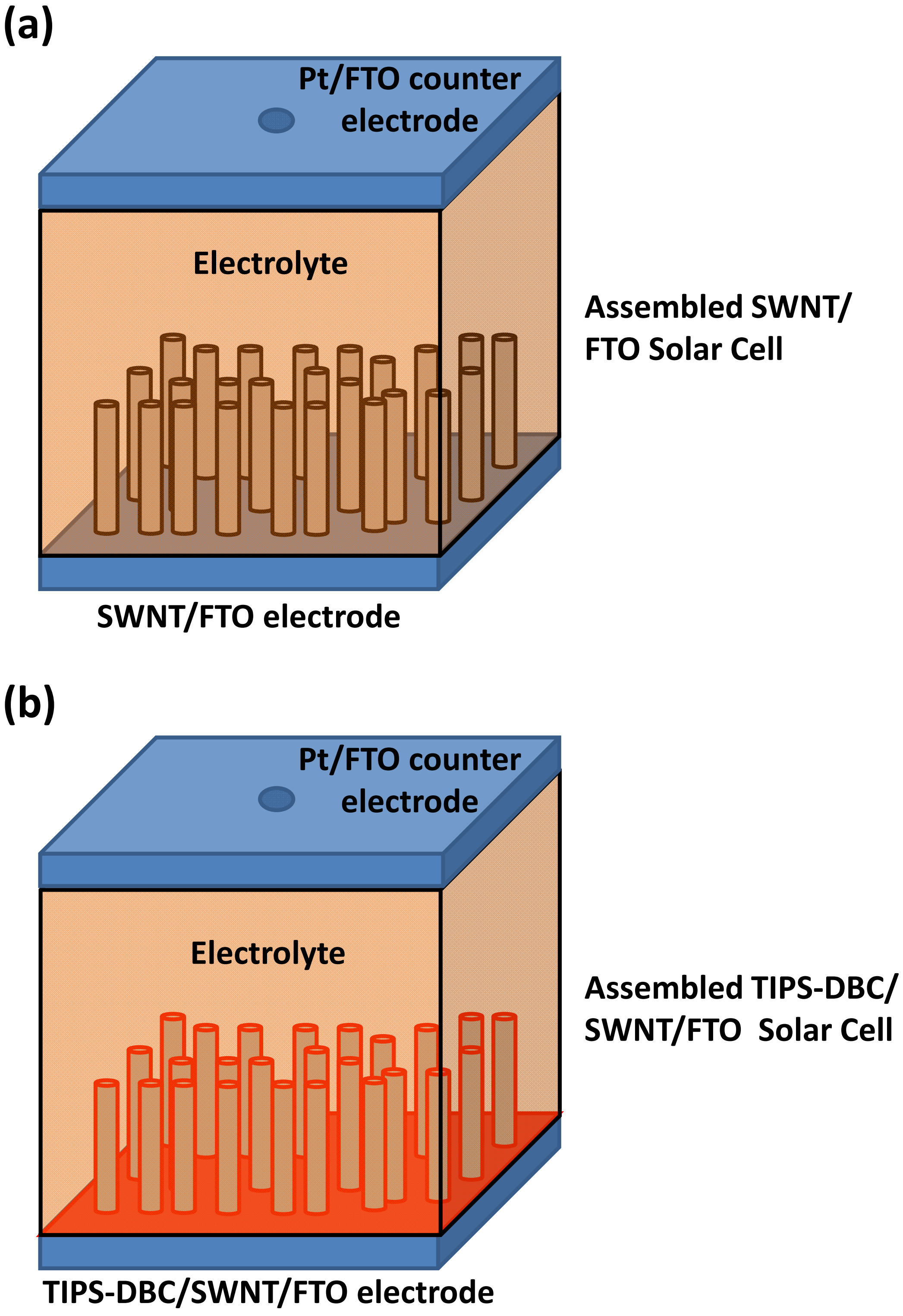

Figure 3.3: Schematic of (a) SWNT/FTO solar cell architecture and (b) TIPS-DBC/SWNT/FTO solar cell architecture (not drawn to scale).

3.2.2 Characterisation

Confocal Raman measurements were taken with a WITec α300R Microscope in Raman mode using a 100× objective, with a numerical aperture of 0.9. Measurements were taken using a 532 nm laser (2.33 eV) which was operated at constant power for each experiment. The surface was placed perpendicular to the excitation source during measurements. Single spectra were collected using an integration time of 5 s and averaged over 10 accumulations. Raman data was collected using WITec Control v2.04 software and analysed in the WITec Project v2.04 software.

UV-Vis spectra were obtained on a Varian Cary 50G with a resolution of 1 nm. In all experiments the spectrum of bare FTO coated glass was used as the baseline.

Current density-voltage (J-V) measurements of SWNT solar cells were taken using a Keithley 2400 Source-Measure unit which was interfaced with a National Instruments LabVIEW Virtual Instrument. J-V measurements were taken under illumination from a solar simulator LED light source at ~100 $mW\cdot cm^{-2}$. This intensity was monitored with a light meter (Newport Power Meter, model 1815-C). Three J-V curves were taken for each cell and an average J-V curve used for data analysis. All electrode configurations were tested in triplicate.

Photocurrent spectra were obtained at intervals of 2 nm in the range of 450 – 850 nm by illuminating a device of 1 cm^2 active area fabricated with a TIPS-DBC/SWNT/FTO working electrode. Light from a xenon arc lamp (Oriel) was passed through a monochromator (Jarrell Ash) and order sorting filters (390 nm and 650 nm long pass, Oriel). Since the photocurrent output of the test cell is low and a lock in analyser/chopper was not employed, the slit width was set wide (4 mm) to provide photocurrent densities in the μA range. External quantum efficiency (EQE) values were calculated by comparison of the baseline/noise corrected photocurrent output of the test cell with that from a 1 cm^2 NIST calibrated silicon cell (PVM 731, PV Measurements).

3.3 Electrode Characterisation

Raman spectroscopy, shown in Figure 3.4, was used to investigate the presence of carbon layers on the FTO substrates. From the black trace of Figure 3.4(i), it can be seen that the hydroxylated FTO substrate has a region of enhanced intensity from 125 – 750 cm^{-1}, typical of the normal Raman spectrum of glass, which is present beneath the FTO layer. After a 30 mg·mL^{-1} solution was used to deposit a layer of TIPS-DBC onto an FTO electrode, two prominent bands of equal intensity appeared in the Raman spectrum at 1344 cm^{-1} and 1597 cm^{-1} (red trace of Figure 3.4(ii)). These bands were assigned to the D-band and G-band respectively, which are commonly found in aromatic carbon compounds [23]. As discussed in Chapter 2 Section 2.2.2, the G-band corresponds to sp^2 carbon vibrations in a hexagonal carbon network, while the D-band corresponds to the presence of dangling bonds or sp^3 hybridised carbon in these networks. Therefore, the presence of these bands in the Raman spectrum of TIPS-DBC is expected due to the presence of the extended polycyclic aromatic hydrocarbon backbone of the molecule, seen in the inset of Figure 3.4.

The spectrum of a SWNT/FTO electrode (blue trace of Figure 3.4(iii)) had four prominent peaks, corresponding to the Raman fingerprint of SWNTs [24]. An RBM peak was seen to occur in the region of 130 – 140 cm^{-1}. D- and G-bands were also observed to occur at 1335 cm^{-1} and 1580 cm^{-1} respectively. Unlike in the TIPS-DBC spectrum however, the intensity of the G-band was much greater than that of the D-band. The 2D-band of the SWNTs was also clearly visible in the Raman spectrum of the SWNT/FTO electrode, occurring at 2650 cm^{-1}. When the Raman spectrum of a TIPS-DBC/SWNT/FTO electrode was obtained (green trace of Figure 3.4(iv)), it was seen that it was dominated by the presence of the SWNTs in the sample, displaying a clear RBM and 2D-band as well as a G-band that was much more intense in signal than the D-band. This is due to the large Raman cross section of SWNTs [25].

The black trace of Figure 3.5(i) shows the UV-Vis spectrum of an SWNT/FTO electrode, which agrees with previously published spectra of SWNT/ITO electrodes [16]. While the concentration of the SWNT solution used to prepare SWNT/FTO electrodes was kept constant throughout the experiments, the concentration of the TIPS-DBC chloroform solutions could be modified, due to the high solubility of the TIPS-DBC. Figure 3.5(ii, iv-v) shows the UV-Vis spectra of TIPS-DBC/SWNT/FTO electrodes made by depositing TIPS-DBC layers with chloroform solutions of increasing TIPS-DBC concentration. There is a clear increase in absorbance over the scanned region of 350 – 850 nm after the deposition of a TIPS-DBC layer using a 10 mg·mL^{-1} solution (red trace of Figure 3.5 (ii)). The two peaks seen at 500 nm and 540 nm show good alignment with peaks previously observed for TIPS-DBC by Winzenberg et al. [22] who observed peaks at approximately 485 nm and 530 nm when performing UV-Vis spectroscopy on TIPS-DBC layers deposited from chloroform. A series of TIPS-DBC chloroform solutions ranging in concentration from 5 mg·mL^{-1} to 40 mg·mL^{-1} were prepared and used to deposit TIPS-DBC layers on SWNT/FTO electrodes. There was a clear increase in the absorbance of the TIPS-DBC/SWNT/FTO electrodes at 540 nm, seen in the inset of Figure 3.5, as well as the spectra in the green and pink traces of Figure 3.5(iv and v) respectively. However, the UV-Vis spectrum of TIPS-DBC dissolved in chloroform (dashed trace of Figure 3.5(vi)) shows three defined peaks at 450, 480 and 512 nm. The combination of the loss of the highest energy peak and the red shifting and peak broadening of the TIPS/DBC/SWNT/FTO electrode spectra suggests that the TIPS-DBC forms an amorphous layer upon deposition onto the electrode. This is consistent with the work of Mori et al. [26] and Kim et al. [27] who found spin-coated films of a number of DBC derivatives are amorphous when analysed with AFM and XRD. Furthermore, the absorbance of the FTO-only electrode, where no SWNTs are present, prepared using the 30 mg·mL^{-1} TIPS-DBC solution (blue trace of Figure 3.5(iii)) has a much lower absorbance than the TIPS-DBC/SWNT/FTO electrode prepared using the same 30 mg·mL^{-1} solution (Figure 3.5(iv)). This highlights the affinity of the TIPS-DBC for the nanotubes as well as suggesting there is increased surface area available due to the vertically aligned array of SWNTs, making the production of the composite structure readily achievable.

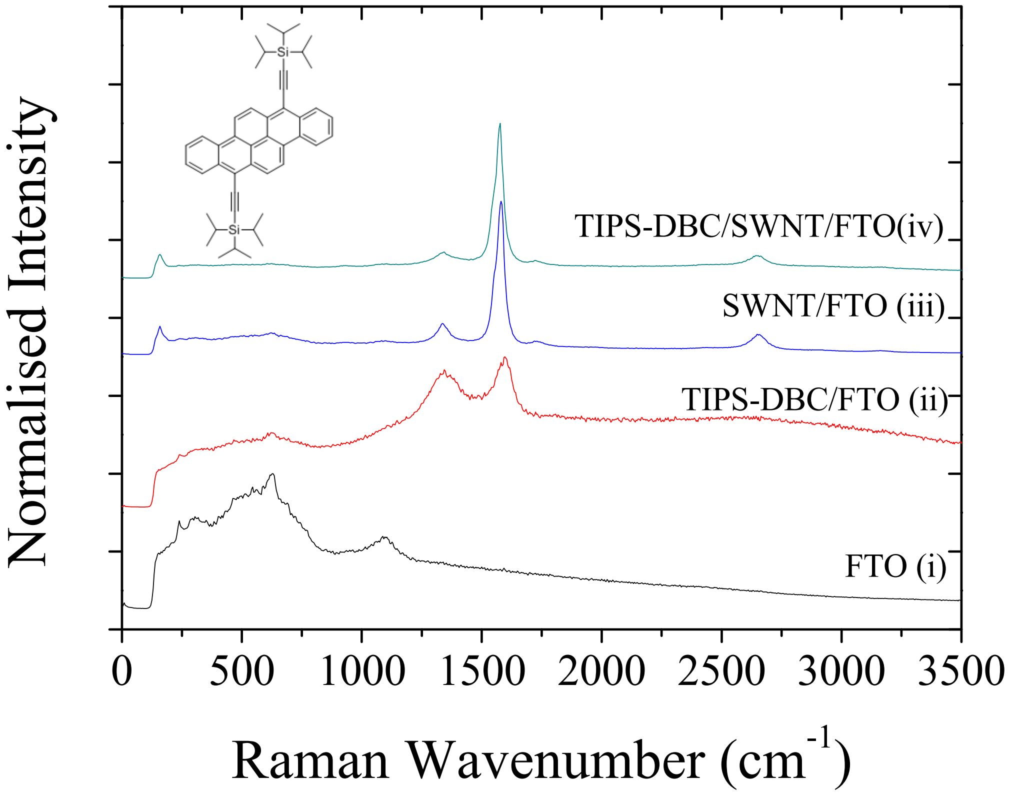

Figure 3.4: Raman spectra of (i) an FTO electrode, (ii)TIPS-DBC/FTO electrode, (iii) an SWNT/FTO electrode and (iv) a TIPS-DBC/SWNT/FTO electrode, and inset, a chemical diagram of TIPS-DBC.

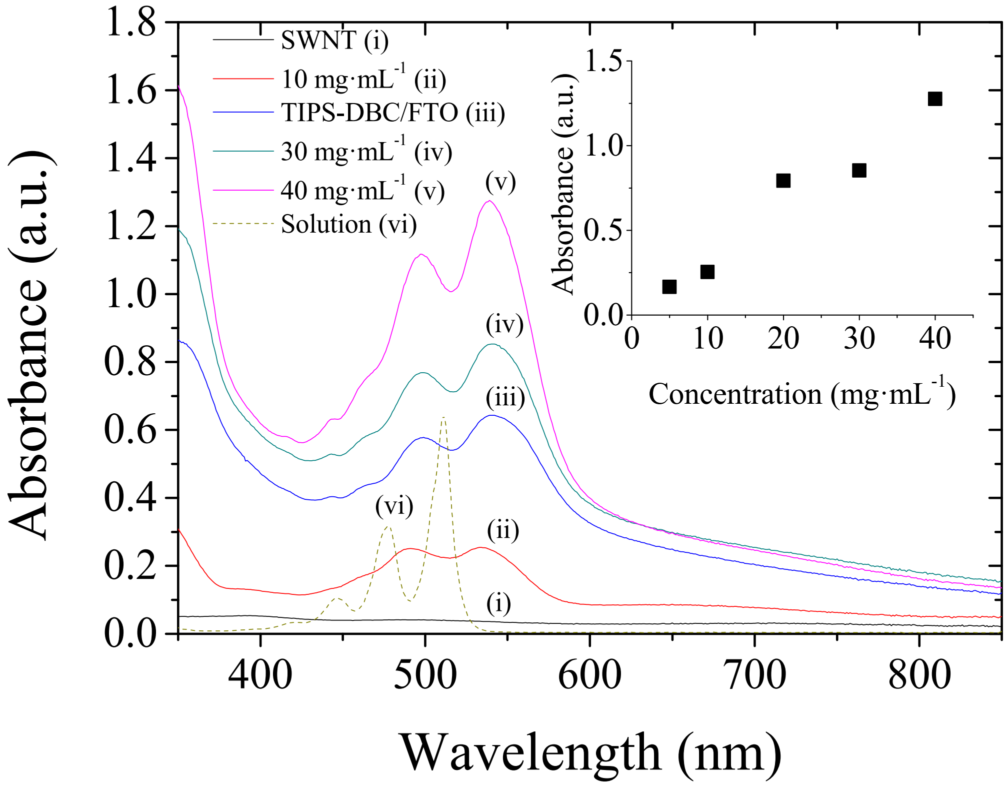

Figure 3.5: UV-Vis spectra of (i) a SWNT/FTO electrode, (ii, iv-v) TIPS-DBC/SWNT/FTO electrodes prepared with an increasing concentration of the TIPS-DBC solution, (iii) a TIPS-DBC/FTO electrode prepared with a 30 mg·mL^{-1} TIPS-DBC solution, (vi) a TIPS-DBC chloroform solution, and inset, variation in absorbance at 540 nm of TIPS-DBC/SWNT/FTO electrodes with increasing concentration of the deposited TIPS-DBC solution.

3.4 Effect of TIPS-DBC on Photovoltaic Performance

The initial SWNT/FTO solar cells, of which a representative J-V curve can be seen in the black trace of Figure 3.6(i), had a V_{OC} of -23.4 ± 0.46 mV and a J_{SC} of 10.1 ± 0.25 μA·cm^{-2}. A similar SWNT/FTO architecture reported by Bissett and Shapter [15] gave a V_{OC} of ~15 mV and a J_{SC} of 5.04 ± 0.11 μA·cm^{-2}, while a SWNT/ITO architecture from Tune et al. [16] gave a V_{OC} of 47 mV and J_{SC} of 2.0 μA·cm^{-2}. A possible reason for the lower V_{OC} and higher J_{SC} observed in this study is that the previous reports used polymer sealed solar cells, whereas in this study the cells were sandwiched together reversibly. This allows for atmospheric mixing of the electrolyte solution and the working electrode, which could conceivably affect their charge transport mechanisms.

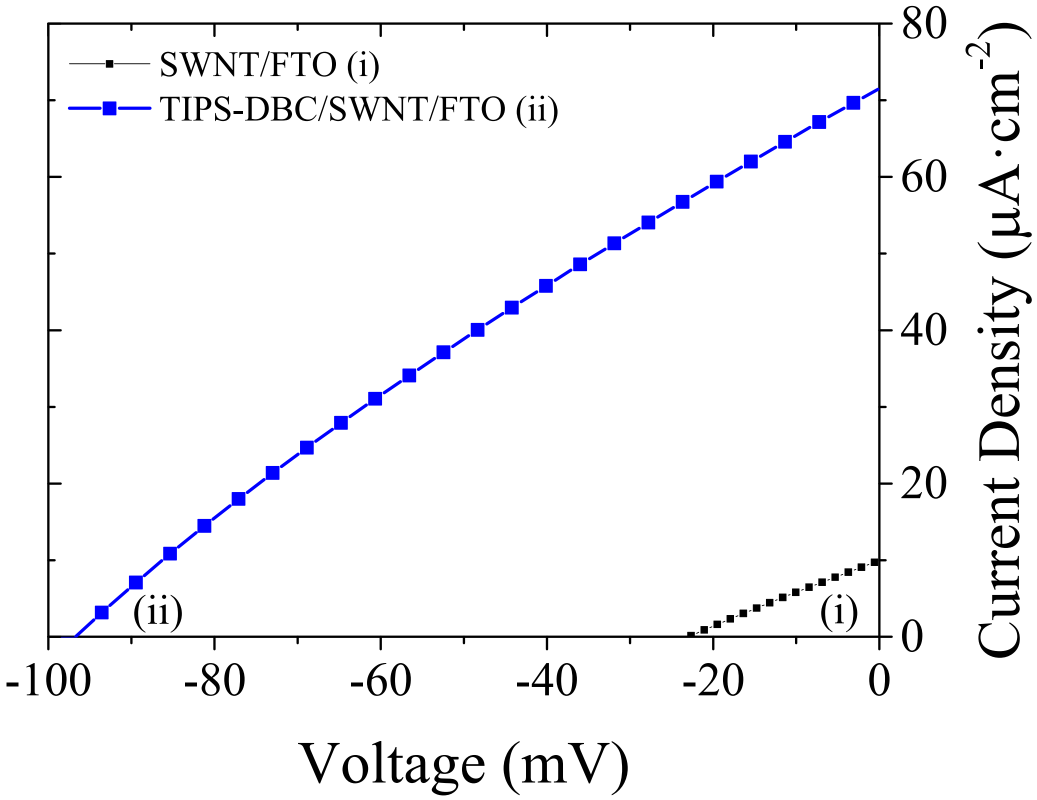

Figure 3.6: Representative J-V curves of (i) a solar cell made using a SWNT/FTO working electrode and (ii) a solar cell made using a TIPS-DBC/SWNT/FTO working electrode made using a 30 mg·mL^{-1} TIPS-DBC solution.

Deposition of a 30 mg·mL^{-1} TIPS-DBC solution onto a SWNT/FTO electrode via spin coating at 2000 rpm resulted in much improved photovoltaic performances of the resultant solar cells, a representative J-V curve of which can be seen in the blue trace of Figure 3.6(ii). With an almost five fold improvement in V_{OC} and seven fold improvement in J_{SC}, the TIPS-DBC/SWNT/FTO solar cells saw a large increase in their PCE compared with the SWNT/FTO solar cells.

To investigate whether this increased photovoltaic performance was due to an improved electronic configuration of the device, or due to the photoactive nature of TIPS-DBC, external quantum efficiency (EQE) measurements were performed on a TIPS-DBC/SWNT/FTO solar cell, as detailed in Section 3.2.2. The solid trace of Figure 3.7(i) shows the EQE of a solar cell fabricated using a TIPS-DBC/SWNT/FTO electrode made with a 30 $mg \cdot mL^{-1}$ solution. The cell exhibited no response below a threshold energy of ~600 nm but then displayed a steep increase in performance at higher energies, with this threshold energy matching the UV-Vis absorption onset also shown in the dashed trace of Figure 3.7(ii) (~600 nm). Two peaks of around 0.35 % are evident at 527 nm and 486 nm and these peaks in the EQE very closely correspond to those observed by Winzenberg et al. [22] for TIPS-DBC/PCBM devices. These results clearly demonstrate that the origin of the observed photocurrent is light harvesting by the TIPS-DBC molecules.

The inset of Figure 3.7 shows the proposed energy band diagram for a photoelectrochemical cell made with a TIPS-DBC/SWNT/FTO working electrode, iodide/triiodide electrolyte and Pt/FTO counter electrodes. Standard values for FTO and the redox potential of the iodide/triiodide redox couple are shown and the positions of the highest occupied molecular orbital (HOMO) and lowest unoccupied molecular orbital (LUMO) of TIPS-DBC were obtained from [22]. The SWNT HOMO and LUMO shown are representative of the major semiconducting chiralities present in the nanotube material used ((16,6) and (11,10), determined by curve fitting of solution UV-Vis spectra and comparison with data reported by Weisman and Bachilo [28]). These nanotubes have a fundamental optical bandgap of ~0.7 eV and can be assumed to have a Fermi level of ~4.8 eV, shifted from the intrinsic 4.65 eV by molecular oxygen adsorption and oxygen containing functionalities present as a result of acid purification [29]. It is proposed that electrons photogenerated in the TIPS-DBC are captured by the iodide/triiodide couple and transported to the Pt/FTO counter electrode whilst the resulting holes are transferred to the FTO working electrode via the SWNTs. In addition to hole transport, the nanotubes present on the electrode surface also serve the function of partially blocking the electron-hole recombination pathway between FTO and TIPS-DBC, however it must be noted that the coverage of nanotubes is incomplete and there is likely some contact between the TIPS-DBC and FTO. Although this proposed model adequately describes the predominant operation mechanism of the devices, a complete analysis would need to take into account the broad distribution of both semiconducting and metallic nanotube chiralities, any band bending due to interfacial charge transfer, especially between the SWNTs and FTO, and the relative kinetics of competing redox processes at the two electrode surfaces.

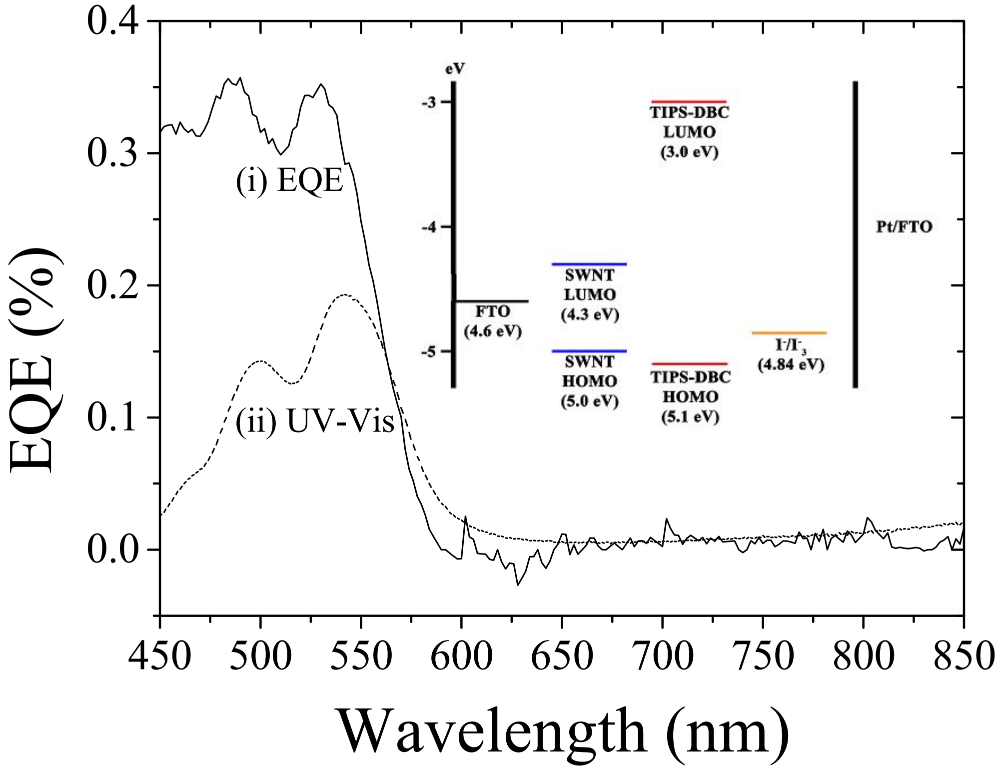

Figure 3.7: (i) EQE of the TIPS-DBC/SWNT/FTO device, (ii) a UV-Vis spectrum of a TIPS-DBC/SWNT/FTO electrode, and inset, a proposed energy diagram of the complete device.

3.5 Optimisation of Deposition Solution Concentration

After demonstrating the light harvesting action of the TIPS-DBC, the effect of the concentration of the TIPS-DBC deposition solution on the photovoltaic performance of the TIPS-DBC/SWNT/FTO solar cells was investigated. The active electrodes in the devices were prepared by dynamically spin coating a layer of TIPS-DBC dissolved in chloroform onto a SWNT/FTO electrode at a spin speed of 2000 rpm. As can be seen in Figure 3.9, the addition of a 5 mg·mL^{-1} solution resulted in a significant increase in both the V_{OC} (23.4 mV to 65.7 mV) and J_{SC} (10.1 µA·cm^{-2} to 27.9 µA·cm^{-2}) and hence the PCE of the resultant cells. Figure 3.8 and Figure 3.9 show that the PCE performance of the cells increases with increasing concentration of the TIPS-DBC solution up to a concentration of 30 mg·mL^{-1}. However, a further increase in concentration to 40 mg·mL^{-1} results in a slight decrease in the V_{OC} and J_{SC} and hence PCE of the cells, relative to those values obtained with the 30 mg·mL^{-1} solution.

The increased photovoltaic performance of the cells when a 30 mg·mL^{-1} TIPS-DBC solution is used to coat the SWNT/FTO electrodes is significant when compared to the bare SWNT/FTO electrodes, with a four fold increase in V_{OC} (23.4 mV to 98.3 mV) coupled with a near seven fold increase in J_{SC} (10.1 µA·cm^{-2} to 68.1 µA·cm^{-2}). Combined, these increases result in a more than thirty fold increase in cell PCE, although the PCE remains low in absolute terms (~0.002 %). This low PCE ultimately relates to the minimal amount of SWNTs present on the working electrodes and the recombination issues this causes, along with the relative kinetics of the competing redox processes at the two electrode surfaces. Compared with previous work using SWNT/FTO or SWNT/ITO cell architectures however, these results show significant potential. Functionalisation of multilayer SWNT/ITO electrodes with N3 dye by Tune et al. [16] showed a threefold increase in J_{SC}, but working from a much lower original current density (2.0 µA·cm^{-2} to 6.2 µA·cm^{-2}). Similarly, chemical attachment of PAMAM-type dendrons to an SWNT/FTO electrode by Bissett et al. [30] resulted in a 40 % increase in V_{OC} (from 30 mV to 43 mV) and a 16 % increase in J_{SC} (from 12 µA·cm^{-2} to 14 µA·cm^{-2}).

Several factors are believed to contribute to the marked increase in performance of the cells upon the addition of the TIPS-DBC layers. Firstly, as seen in the UV-Vis spectra of the electrodes in Figure 3.5, the working electrode absorbs a greater amount of incident light when TIPS-DBC is present compared to an SWNT/FTO electrode and hence a greater number of excitons can be generated within the cell. Coupled with this increase in excitons generated within the TIPS-DBC layer, is the ability of the p-type SWNTs to act as efficient hole transporters, enabling a much greater separation of charge to occur within the TIPS-DBC/SWNT/FTO cells compared to the SWNT/FTO cells. An increase in the separation of charge within the cell should result in the improved V_{OC} of the cells, while also contributing to the generation of a greater J_{SC}. While these factors may account for the increase in photovoltaic performance over the range of 5 – 30 mg·mL^{-1}, they do not however account for the decrease in performance when the concentration of the deposition solution is further increased to 40 mg·mL^{-1}. It is thought that the decrease in V_{OC} (from 98 ± 1.5 mV to 83.1 ± 0.86 mV) observed at this concentration is due to the increasingly large ratio of TIPS-DBC to SWNTs. As the thickness of the TIPS-DBC becomes too great, there is a greater likelihood of photogenerated electrons recombining with holes present in other TIPS-DBC molecules before they are transported to the triiodide within the electrolyte. This recombination would reduce the ability of the cell to separate and then collect charge, hence decreasing its V_{OC} and J_{SC}.

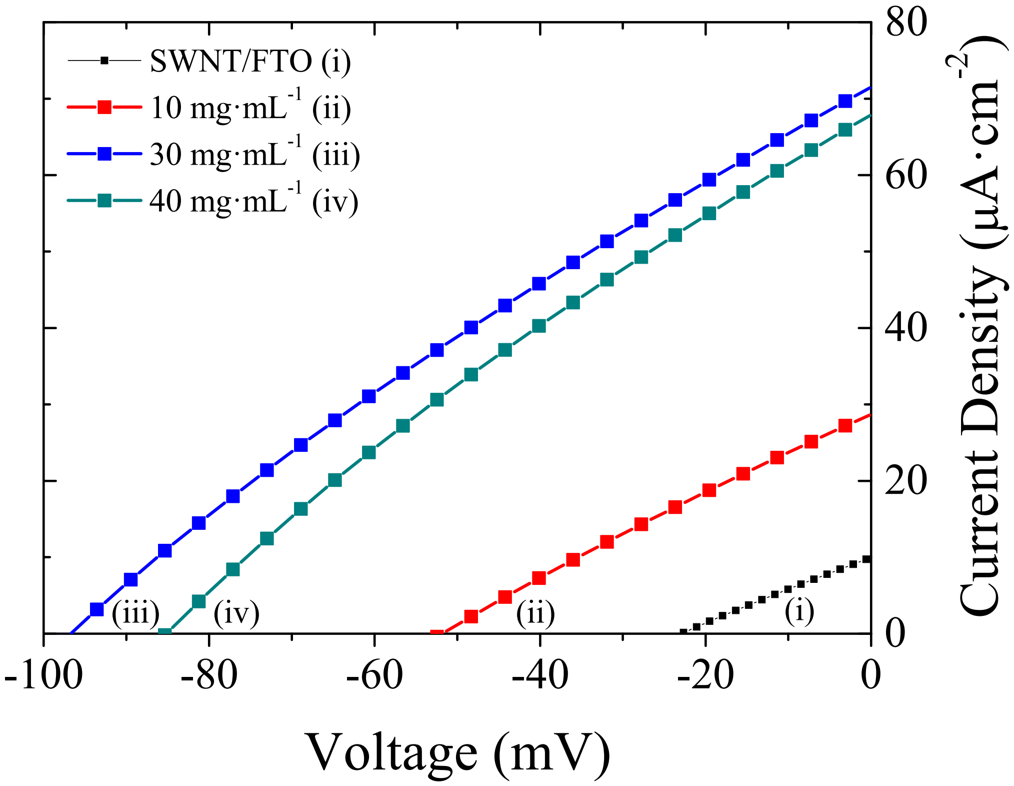

Figure 3.8: Representative J-V curves of (i) a SWNT/FTO working electrode solar cell and TIPS-DBC/SWNT/FTO solar cells made using deposition solutions with concentrations of (ii) 10 mg·mL^{-1}, (iii) 30 mg·mL^{-1} and (iv) 40 mg·mL^{-1}.

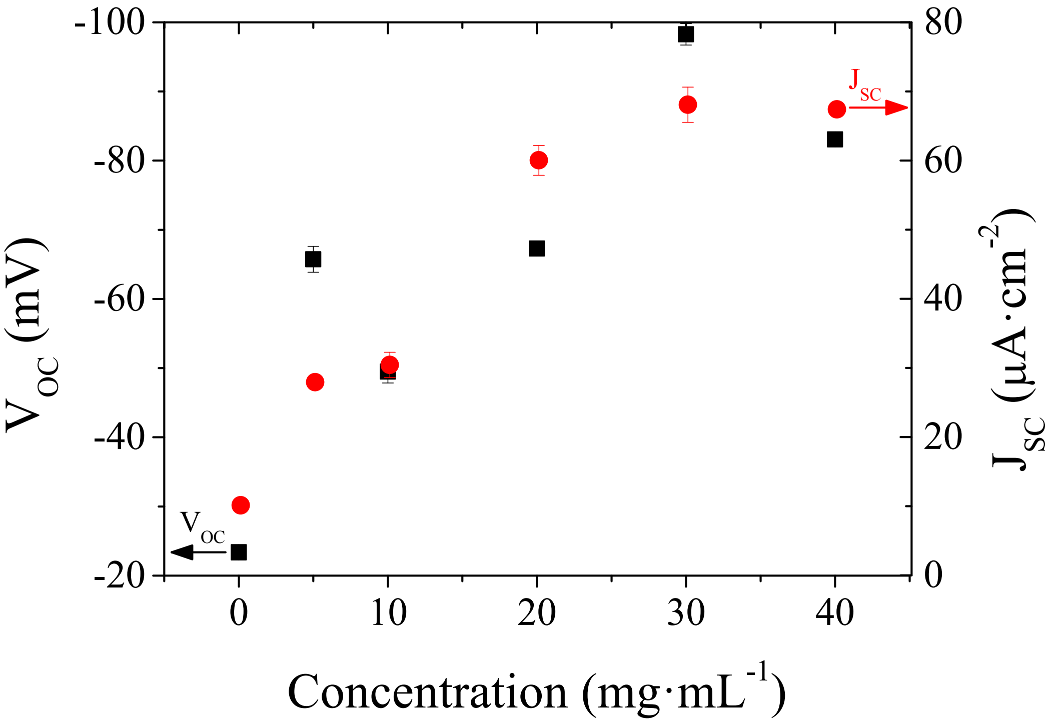

Figure 3.9: Effect of the concentration of the TIPS-DBC deposition solution on the V_{OC} (left axis) and J_{SC} (right axis) of the resultant TIPS-DBC/SWNT/FTO solar cells (error bars present on all data points and where not visible are within the data point).

3.6 Optimisation of Deposition Spin Speed

The final optimisation parameter investigated was the spin speed at which TIPS-DBC was deposited onto the SWNT/FTO electrodes. Figure 3.10 shows the effect that changing the spin speed of deposition of a 30 mg·mL^{-1} solution of TIPS-DBC has on the resultant TIPS-DBC/SWNT/FTO solar cells. Spin speed was found to have less of an effect on the PCE of the cells than the concentration of the deposition solution. Despite this however, there was a significant increase in both V_{OC} and J_{SC} when the spin speed was increased from 500 rpm to 2000 rpm. This is increase is postulated to be due to the increased ability of TIPS-DBC/SWNT/FTO electrodes to separate charge when TIPS-DBC is deposited at increased spin speeds. A higher spin speed should correlate to a greater uniformity in the TIPS-DBC layer covering the SWNT/FTO electrode and thus less intermolecular interactions within the layer. This would positively affect a number of processes within the cell, including the rate of charge separation, charge transport mobility and electron/hole separation. A decrease in V_{OC} and J_{SC} was observed upon deposition of TIPS-DBC at a spin speed of 4000 rpm. At this further increased speed, the rotation of the SWNT/FTO substrate may be high enough such that the deposited TIPS-DBC solution is spread much more thinly across the substrate, and thus the layer begins to resemble those deposited at slower spin speeds using solutions with lower concentrations of TIPS-DBC. Indeed, comparison of the V_{OC} (68.8 ± 4.8 mV) and J_{SC} (55.2 ± 4.8 μA·cm^{-2}) of this 4000 rpm cell seen in Figure 3.10 with the V_{OC} (67.3 ± 1.0 mV) and J_{SC} (60.0 ± 2.1 μA·cm^{-2}) of cells made at 2000 rpm with a 20 mg·mL^{-1} solution as seen in Figure 3.8 shows this is very likely the case.

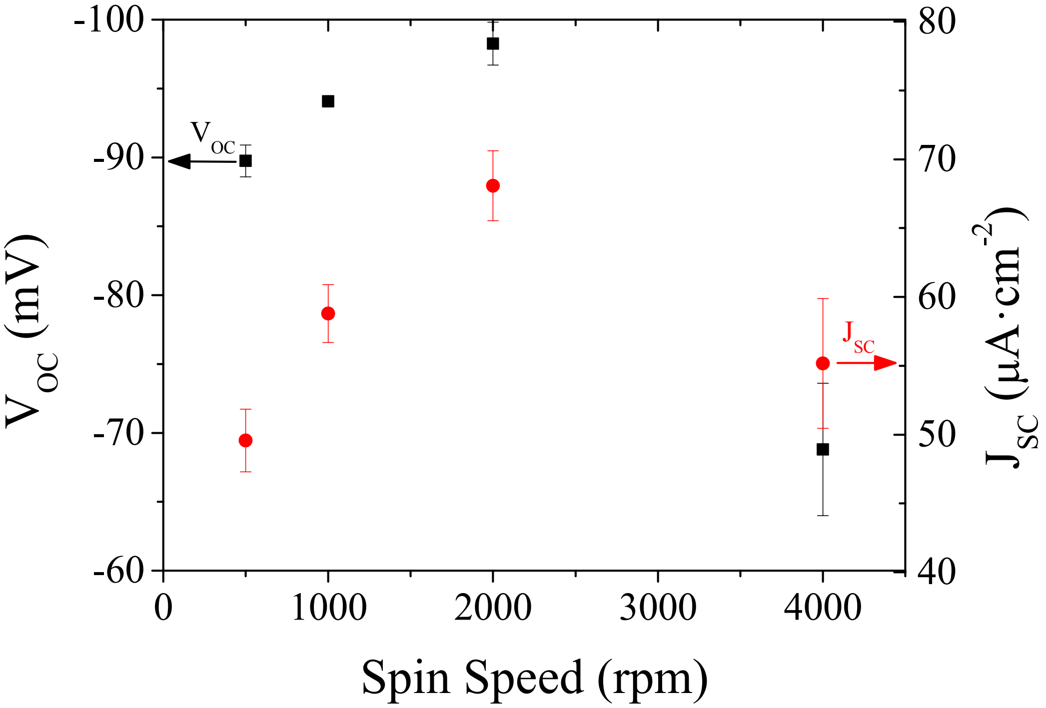

Figure 3.10: Effect of spin speed during deposition of a 30 mg·mL^{-1} TIPS-DBC solution on the V_{OC} (left axis) and J_{SC} (right axis) of resultant TIPS-DBC/SWNT/FTO solar cells (error bars present on all data points and where not visible are within the data point).

3.7 Conclusions

Vertically aligned SWNTs were chemically attached to FTO substrates and then further functionalised with a layer of TIPS-DBC. These electrodes were then used as the working electrodes in photoelectrochemical cells and the effect of the initial concentration of TIPS-DBC was investigated. It was found that the addition of TIPS-DBC onto an SWNT/FTO electrode resulted in a significant increase in the V_{OC} (23.4 mV to 98.3 mV) and J_{SC} (10.1 $\mu A \cdot cm^{-2}$ to 68.1 $\mu A \cdot cm^{-2}$) of the resultant cells, significantly increasing their PCE from ~6×10^{-5} % to ~0.002 %. Additionally, it was found that the spin speed at which the TIPS-DBC was deposited influenced the performance of the cells. Together, the optimal configuration was found to result from depositing a 30 $mg \cdot mL^{-1}$ TIPS-DBC solution at a spin speed of 2000 rpm. These results show a promising step towards efficient photoelectrochemical cells which use carbon based photoactive elements, as opposed to costly transition metal based dyes.

While the overall PCE of the cells reported here remains low after the introduction of TIPS-DBC, it still represents a greater than thirty fold increase over cells made using SWNT/FTO electrodes alone. While power generation from photovoltaic cells is the long-term goal of this research, these results also suggest other short-term applications. For example, these electrodes could be used in devices such as photodetectors, where a distinct current response from a cheap electrode is desirable.

3.8 References

1. O'Regan, B & Grätzel, M 1991, 'A low-cost, high-efficiency solar cell based on dye-sensitized colloidal TiO_2 films', *Nature*, vol. 353, no. 6346, pp. 737-40.

2. Hagfeldt, A, Boschloo, G, Sun, L, Kloo, L & Pettersson, H 2010, 'Dye-sensitized solar cells', *Chemical Reviews*, vol. 110, no. 11, pp. 6595-663.

3. Tantang, H, Kyaw, AKK, Zhao, Y, Chan-Park, MB, Tok, AIY, Hu, Z, Li, L-J, Sun, XW & Zhang, Q 2012, 'Nitrogen-doped carbon nanotube-based bilayer thin film as transparent counter electrode for dye-sensitized solar cells (DSSCs)', *Chemistry – An Asian Journal*, vol. 7, no. 3, pp. 541-5.

4. Liu, C-T, Wang, Y-C, Dong, R-X, Wang, C-C, Huang, K-C, Vittal, R, Ho, K-C & Lin, J-J 2012, 'A dual-functional Pt/CNT TCO-free counter electrode for dye-sensitized solar cell', *Journal of Materials Chemistry*, vol. 22, no. 48, pp. 25311-5.

5. Sawatsuk, T, Chindaduang, A, Sae-kung, C, Pratontep, S & Tumcharern, G 2009, 'Dye-sensitized solar cells based on TiO_2–MWCNTs composite electrodes: Performance improvement and their mechanisms', *Diamond and Related Materials*, vol. 18, no. 2–3, pp. 524-7.

6. Dang, X, Yi, H, Ham, M-H, Qi, J, Yun, DS, Ladewski, R, Strano, MS, Hammond, PT & Belcher, AM 2011, 'Virus-templated self-assembled single-walled carbon nanotubes for highly efficient electron collection in photovoltaic devices', *Nature Nanotechnology*, vol. 6, no. 6, pp. 377-84.

7. Ramasamy, E, Lee, WJ, Lee, DY & Song, JS 2008, 'Spray coated multi-wall carbon nanotube counter electrode for tri-iodide reduction in dye-sensitized solar cells', *Electrochemistry Communications*, vol. 10, no. 7, pp. 1087-9.

8. Lee, WJ, Ramasamy, E, Lee, DY & Song, JS 2009, 'Efficient dye-sensitized solar cells with catalytic multiwall carbon nanotube counter electrodes', *ACS Applied Materials & Interfaces*, vol. 1, no. 6, pp. 1145-9.

9. Barazzouk, S, Hotchandani, S, Vinodgopal, K & Kamat, PV 2004, 'Single-wall carbon nanotube films for photocurrent generation. A prompt response to visible-light irradiation', *The Journal of Physical Chemistry B*, vol. 108, no. 44, pp. 17015-8.

10. Wei, L, Tezuka, N, Umeyama, T, Imahori, H & Chen, Y 2011, 'Formation of single-walled carbon nanotube thin films enriched with semiconducting nanotubes and their application in photoelectrochemical devices', *Nanoscale*, vol. 3, no. 4, pp. 1845-9.

11. Chen, T, Wang, S, Yang, Z, Feng, Q, Sun, X, Li, L, Wang, Z-S & Peng, H 2011, 'Flexible, light-weight, ultrastrong, and semiconductive carbon nanotube fibers for a highly efficient solar cell', *Angewandte Chemie International Edition*, vol. 50, no. 8, pp. 1815-9.

12. Li, H, Yang, Z, Qiu, L, Fang, X, Sun, H, Chen, P, Pan, S & Peng, H 2014, 'Stable wire-shaped dye-sensitized solar cells based on eutectic melts', *Journal of Materials Chemistry A*, vol. 2, no. 11, pp. 3841-6.

13. Chen, T, Qiu, L, Yang, Z, Cai, Z, Ren, J, Li, H, Lin, H, Sun, X & Peng, H 2012, 'An integrated “energy wire” for both photoelectric conversion and energy storage', *Angewandte Chemie International Edition*, vol. 51, no. 48, pp. 11977-80.

14. Chen, T, Qiu, L, Cai, Z, Gong, F, Yang, Z, Wang, Z & Peng, H 2012, 'Intertwined aligned carbon nanotube fiber based dye-sensitized solar cells', *Nano Letters*, vol. 12, no. 5, pp. 2568-72.

15. Bissett, MA & Shapter, JG 2010, 'Photocurrent response from vertically aligned single-walled carbon nanotube arrays', *The Journal of Physical Chemistry C*, vol. 114, no. 14, pp. 6778-83.

16. Tune, DD, Flavel, BS, Quinton, JS, Ellis, AV & Shapter, JG 2010, 'Single walled carbon nanotube network electrodes for dye solar cells', *Solar Energy Materials and Solar Cells*, vol. 94, no. 10, pp. 1665-72.

17. Katoh, R, Furube, A, Yoshihara, T, Hara, K, Fujihashi, G, Takano, S, Murata, S, Arakawa, H & Tachiya, M 2004, 'Efficiencies of electron injection from excited N3 dye into nanocrystalline semiconductor (ZrO_2, TiO_2, ZnO, Nb_2O_5, SnO_2, In_2O_3) films', *The Journal of Physical Chemistry B*, vol. 108, no. 15, pp. 4818-22.

18. Grätzel, M 2003, 'Dye-sensitized solar cells', *Journal of Photochemistry and Photobiology C: Photochemistry Reviews*, vol. 4, no. 2, pp. 145-53.

19. Anthony, JE 2008, 'The larger acenes: Versatile organic semiconductors', *Angewandte Chemie International Edition*, vol. 47, no. 3, pp. 452-83.

20. Park, J-H, Chung, DS, Lee, DH, Kong, H, Jung, IH, Park, M-J, Cho, NS, Park, CE & Shim, H-K 2010, 'New anthracene-thiophene-based copolymers that absorb across the entire UV-Vis spectrum for application in organic solar cells', *Chemical Communications*, vol. 46, no. 11, pp. 1863-5.

21. Shu, Y, Lim, Y-F, Li, Z, Purushothaman, B, Hallani, R, Kim, JE, Parkin, SR, Malliaras, GG & Anthony, JE 2011, 'A survey of electron-deficient pentacenes as acceptors in polymer bulk heterojunction solar cells', *Chemical Science*, vol. 2, no. 2, pp. 363-8.

22. Winzenberg, KN, Kemppinen, P, Fanchini, G, Bown, M, Collis, GE, Forsyth, CM, Hegedus, K, Singh, TB & Watkins, SE 2009, 'Dibenzo[b,def]chrysene derivatives: Solution-processable small molecules that deliver high power-conversion efficiencies in bulk heterojunction solar cells', *Chemistry of Materials*, vol. 21, no. 24, pp. 5701-3.

23. Ferrari, AC 2007, 'Raman spectroscopy of graphene and graphite: Disorder, electron-phonon coupling, doping and nonadiabatic effects', *Solid State Communications*, vol. 143, no. 1-2, pp. 47-57.

24. Dresselhaus, MS, Dresselhaus, G, Saito, R & Jorio, A 2005, 'Raman spectroscopy of carbon nanotubes', *Physics Reports*, vol. 409, no. 2, pp. 47-99.

25. Dresselhaus, MS, Dresselhaus, G, Jorio, A, Souza Filho, AG & Saito, R 2002, 'Raman spectroscopy on isolated single wall carbon nanotubes', *Carbon*, vol. 40, no. 12, pp. 2043-61.

26. Mori, T, Fujita, K & Kimura, M 2010, 'Fabrication of organic thin-film transistor using soluble dibenzochrysene', *Journal of Photopolymer Science and Technology*, vol. 23, no. 3, pp. 317-22.

27. Kim, Y, Lee, SB, Jang, SH, An, TK, Kim, SH, Kim, Y-H & Park, CE 2016, 'Engineering the morphologies and charge transport properties of newly synthesized dibenzochrysene-based small molecules by attaching various side groups', *Dyes and Pigments*, vol. 130, pp. 176-82.

28. Weisman, RB & Bachilo, SM 2003, 'Dependence of optical transition energies on structure for single-walled carbon nanotubes in aqueous suspension: An empirical Kataura plot', *Nano Letters*, vol. 3, no. 9, pp. 1235-8.

29. Collins, PG, Bradley, K, Ishigami, M & Zettl, A 2000, 'Extreme oxygen sensitivity of electronic properties of carbon nanotubes', *Science*, vol. 287, no. 5459, pp. 1801-4.

30. Bissett, MA, Koper, I, Quinton, JS & Shapter, JG 2011, 'Dendron growth from vertically aligned single-walled carbon nanotube thin layer arrays for photovoltaic devices', *Physical Chemistry Chemical Physics*, vol. 13, no. 13, pp. 6059-64.

Chapter 4

G-Si Schottky Junctions

Surfactant-assisted exfoliated graphene dispersions were produced using the non-ionic surfactant Tween-60. These aqueous dispersions, and thin films produced via their vacuum filtration, were characterised and then investigated for their potential use in G-Si Schottky junction solar cells. The photovoltaic properties of the G-Si Schottky junctions were then optimised by investigating the effects of film thickness, film annealing and chemical doping.

This chapter contains material previously published in:

Larsen, LJ, Shearer, CJ, Ellis, AV & Shapter, JG 2015, 'Solution processed graphene-silicon Schottky junction solar cells', *RSC Advances*, vol. 5, no. 49, pp. 38851-8.

4.1 Introduction

As discussed in Chapter 1 Sections 1.7.1 and 1.7.2, the photovoltaic properties of nanocarbon-based material-silicon heterojunctions have been investigated for the past decade. Wei et al. [1] were the first to report a CNT-Si heterojunction in 2007 using DWNTs on a n-type silicon substrate. This work was expanded on by numerous researchers using a myriad of different nanotubes [2, 3], architectures [4, 5] and dopants [6, 7]. Li et al. [8] were the first to report G-Si heterojunctions and their photovoltaic potential. They used CVD graphene with n–type silicon to produce G-Si Schottky junctions with PCEs of up to 1.3 % under AM1.5G illumination [8] (see Figure 1.15 for a representative energy level diagram).

Since the seminal work of Li et al.[8], there have been a number of advances made to the PCE of G-Si Schottky junctions. These include changing the silicon at the interface from planar to nanowire or nanohole arrays [9-11] as well as changing the number of layers of CVD graphene present [12-14]. However, the majority of research has focused on chemical doping methods [15]. The first to report doping of G-Si Schottky junctions in a photovoltaic application was Fan et al. [9] who used $SOCl_2$ to dope G-Si nanowire Schottky junctions. The $SOCl_2$ doping increased the PCE from 0.68 % to 2.86 % after increases to the J_{SC}, V_{OC} and FF of the cells [9]. Interestingly, while the V_{OC} remained stable after doping, the J_{SC} and FF decreased over a period of two weeks before plateauing at a stable PCE of ~1.2 %. Following this result, a number of different dopants have been investigated including nitric acid [11, 14, 16, 17], poly(3,4-ethylenedioxythiophene) polystyrene sulfonate (PEDOT:PSS) [16], bis(trifluoromethanesulfonyl)amide [18], and gold chloride [17]. Chemical doping methods have also recently been combined with colloidal antireflection layers [19, 20] with a recent record PCE of 15.6 % set by Song et al. [20]. These examples highlight the interest in G-Si Schottky junctions but are limited in their scale up potential due to the use of graphene produced by CVD, which is both expensive and difficult to synthesise in large quantities. These properties of the CVD process limit its use in the industrial setting and cast doubt on whether such approaches could be used to economically produce solar cells.

There are several methods for the production of graphene using solution processing, viz. chemical modification of graphite, solvent-assisted exfoliation of graphite and surfactant-assisted exfoliation of graphite. While there are some examples of GO- or RGO-Si Schottky junction solar cells in the literature [21-24] (discussed in more detail in Chapter 5), there has been no research to date on G-Si Schottky junction solar cells made using more chemically pristine solvent-assisted exfoliated graphene or surfactant-assisted exfoliated graphene. This is despite the use of liquid-phase exfoliated graphene finding use in inkjet printing applications for other electronic devices [25, 26].

Blake et al. [27] and Hernandez et al. [28] were the first to produce solvent-assisted exfoliated graphene using organic solvents, in an attempt to produce large quantities of graphene without prior oxidation or the need for CVD. This process was expanded upon by numerous research groups in order to increase the concentration and quality of the graphene flakes produced. This was achieved through the investigation of numerous types of organic solvents [29-31], ultrasonication times [32], and introducing filtration and filtrate re-suspension [33]. While these methods succeeded in producing single- and few-layer graphene dispersions, they were limited in their application due to the presence of difficult to process organic solvents, which are typically toxic, have a high boiling point or both.

In order to mitigate the use of organic solvents Lotya et al. [34] reported a method for the liquid phase exfoliation of graphite in the absence of organic solvents. Using the common ionic surfactant sodium dodecylbenzene sulfonate (SDBS) they produced graphene dispersions at a concentration of up to 0.05 $mg \cdot mL^{-1}$. A number of different studies have been conducted using ionic surfactant-assisted exfoliation, for example by Green et al [35] and Hasan et al. [36]. Guardia et al. [37] showed that non-ionic surfactants outperformed ionic surfactants in making high concentration graphene dispersions even though the surfactant concentrations were not optimised. Indeed, using the non-ionic surfactants Tween-80 and P-123 graphene concentrations of $0.5 - 1\ mg \cdot mL^{-1}$ were achieved. Solution and surfactant-assisted exfoliation of graphene have the advantage over oxidation-assisted exfoliation, used to prepare GO, in that the basal planes of graphene remain pristine and thus retain their intrinsic mechanical and electrical properties [28].

Despite the existence of a simple method for FLG production and hence the ability to produce easily transferrable transparent, conducting graphene films, surfactant-assisted exfoliated graphene has thus far not been investigated in G-Si Schottky junctions for photovoltaics. This chapter presents a method for producing G-Si Schottky junctions from surfactant-assisted exfoliated graphene and investigates the effects of both film thickness and chemical doping on the photovoltaic properties of the heterojunctions.

4.2 Experimental Methods

4.2.1 Graphene Film Fabrication

Flake graphite (+100 mesh, Sigma Aldrich, Australia) was ultrasonicated (Elmasonic ElmaS30H, 80 W) in an aqueous Tween-60 solution (1 %w/v, Sigma Aldrich, Australia) at a concentration of 0.1 g·mL^{-1} for 2 h. Ultrasonication was halted every 15 min and the sample stirred with a magnetic stirrer to improve dispersion. The black dispersion was then centrifuged at 3200 rpm for 10 min and the supernatant removed via pipette. This resulted in an aqueous graphene dispersion at a concentration of ~0.1 mg·mL^{-1}.

Graphene films were prepared as per Chapter 2 Section 2.1.1. The UV-Vis transmittance at 550 nm of the resultant graphene films was controlled by varying the volume of graphene dispersion (mL) filtered per unit area of the final film (cm^{-2}). The amount of supernatant used to produce each film was such that transmittances of 13 %T to 76 %T were produced for each set of experiments (sheet resistance measurements or solar cells etc.). These films were then rinsed thoroughly with MilliQ water before their application.

4.2.2 Solar Cell Fabrication

Solar cell fabrication details followed those previously described in Chapter 2 Section 2.1.2.

4.2.3 Doping of Solar Cells

Solar cells were doped with $SOCl_2$ and $AuCl_3$ following the procedures described in Chapter 2 Section 2.1.3.

4.2.4 Film Annealing

All film annealing was performed as per Chapter 2 Section 2.1.4, at a temperature of 250 ºC.

4.3 Graphene Characterisation

Aqueous graphene dispersions were prepared using the non-ionic surfactant Tween-60, following a modified version of the Guardia et al. [37] method, as discussed in Section 4.2.1. While Guardia et al. [37] investigated Tween-80 and Tween-85, they did not use Tween-60. As such, an investigation to confirm the presence of graphene in the aqueous dispersions reported herein was carried out.

Figure 4.1(a) shows the Raman spectra of both the initial graphite flakes used in the ultrasonication process (see Section 4.2.1) and of a film made via vacuum filtration of the resultant dispersion deposited on glass (see Chapter 2 Section 2.1.1). The Raman spectrum of the graphene film (red trace) shows a 2D-band (2691 cm^{-1}) redshifted 18 cm^{-1} when compared with the 2D-band of the graphite starting material's Raman spectrum (2709 cm^{-1}). This shift, along with the disappearance of the characteristic graphite 2D shoulder (at 2685 cm^{-1}) and a broadening of the peak indicates the majority presence of few-layer graphene (FLG) flakes in the dispersion [38] as well as providing evidence that the graphene flakes do not restack in an AB pattern when being deposited in a film [39]. The redshift observed in the G-band of the graphene film (red trace, 1569 cm^{-1}) compared with the G-band of the starting graphite material (black trace, 1582 cm^{-1}) is also consistent with previously observed Raman spectra of thin films of solvent-assisted and surfactant-assisted exfoliated graphene [32, 40]. UV-Vis analysis of the films, inset of Figure 4.1, also shows the expected featureless absorption spectrum across the visible range characteristic of the Tween-60 surfactant-assisted exfoliated graphene [34].

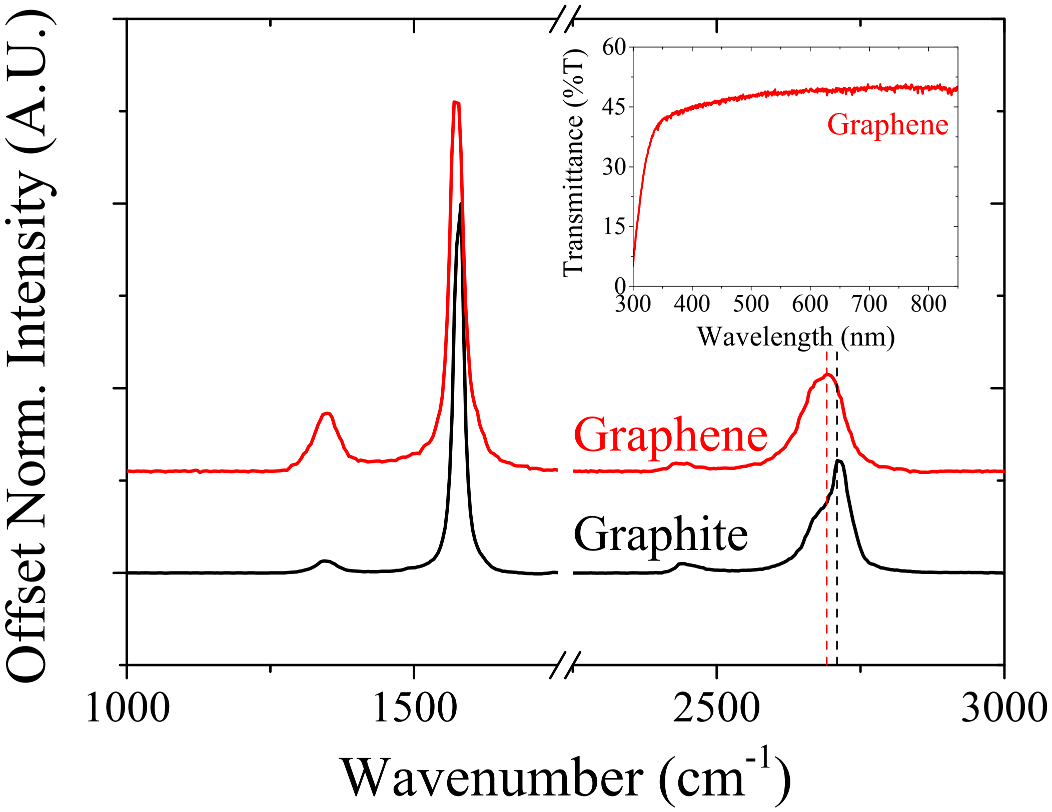

Figure 4.1: Offset normalised Raman spectra of the graphite flakes used as the starting material (black trace) and of a vacuum filtered graphene film deposited on a glass substrate (red trace), with the black and red dashed lines showing the position of the graphite and graphene 2D-band maxima respectively. The inset shows a UV-Vis spectrum of the graphene film.

To investigate the concentration of the graphene dispersions, five replicate solutions were made following the method outlined previously in Section 4.2.1. Following their centrifugation, 40 mL of the dispersion was pipetted into 2 L of MilliQ water and vacuum filtered through a pre-weighed filter paper. Once pipetted and rinsed thoroughly with 2 L of MilliQ water, the filter papers were placed in an oven in atmosphere for 24 h at 80 ºC. The filter papers were then weighed and placed back in the oven for a further 24 h before being weighed again. As the mass measured was the same after both of these drying steps, it was taken to be the true filtrate mass and hence the concentration of the solutions was determined. The average concentration of the dispersions was thus found to be 0.11 ± 0.03 mg·mL^{-1}.

Following the determination of the concentrations of the replicates, a series of dilutions of each replicate was prepared ranging from a one in five to one in twenty dilution. These solutions were then analysed using UV-Vis spectroscopy and their absorbance at 660 nm divided by the path length was plotted against the concentration of the solutions, as seen in Figure 4.2 (see Chapter 2 Section 2.2.1). A linear regression was then fitted to the data in order to determine the absorption coefficient (α) of the graphene dispersion. The absorption coefficient was found to be 2245 ± 117 mL$\cdot$mg$^{-1}\cdot$m^{-1}, which was significantly different to those previously reported in the literature for aqueous dispersions of graphene. The initial reports of organic solvent exfoliated graphene determined absorption coefficients at 660 nm of 2460 mL$\cdot$mg$^{-1}\cdot$m^{-1} in NMP, *N,N*-dimethylacetamide, *γ*-butyrolactone and 1,3-dimethyl-2-imidazolidinone [28]. However, to determine the concentration of their non-ionic surfactant solutions, Guardia et al. [37] used an absorption coefficient of 1390 mL$\cdot$mg$^{-1}\cdot$m^{-1}, which had been previously reported by Lotya et al. [34] for ionic surfactant SDBS exfoliated aqueous graphene dispersions. As Tween-60 is a non-ionic surfactant this may suggest that non-ionic solvents may change the absorption coefficient of the solutions and this factor should be taken into account in further work. It is worth noting however that Lotya et al. [34] did use thermogravimetric analysis to determine the percentage of actual graphitic content in their films and found that they were 64 ± 5 % graphitic with the rest of the mass attributed to surfactant. Every effort was made to remove any residual surfactant in the films used for analysis in this Thesis by copious rinsing of the films with MilliQ water, however, it is possible that some residual surfactant did remain. Thus, when considering Beer's Law (Chapter 2 Equation 2.3) the absorption coefficient presented here represents a lower limit.

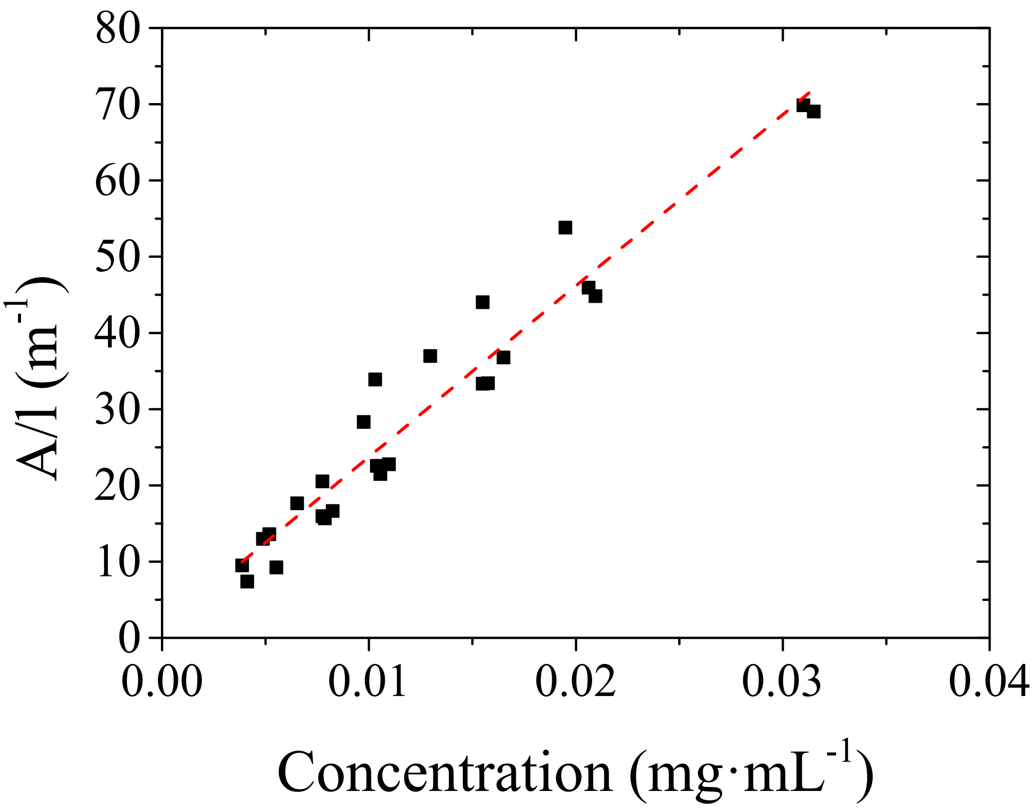

Figure 4.2: Concentration of diluted replicate dispersions versus UV-Vis absorbance at 660 nm divided by the path length. The dashed line is a fitted linear regression, with slope 2245 ± 117 mL·mg^{-1}·m^{-1} (Pearson's r = 0.97, $R^2 = 0.93854$).

Following confirmation of the presence of few layered graphene in the dispersions, the physical properties of the films made through its filtration were investigated. Films were investigated in their pristine condition, i.e., after deposition and removal of the MCE filter paper via acetone washing, and also after thermal annealing, as discussed in Section 2.1.4. Film annealing was investigated as it was hypothesised that thermal annealing may be able to reduce the amount of residual surfactant and MCE left over from the production process of the films, hence enhancing the physical properties of the films.

By controlling the volume of graphene dispersion filtered per unit area of the MCE membrane, the optical thickness of these films could be controlled. Figure 4.3(a) shows the volume per unit area (mL·cm^{-2}) versus the UV-Vis transmittance of the films at 550 nm. The transmittance of the graphene films at 550 nm was found to decrease nonlinearly with increased volume of graphene dispersion used for the preparation of the films. This non-linear behaviour suggests that there is a limit to the thickness of graphene films made using this deposition method, as the UV-Vis transmittance should scale linearly with an increasing number of graphene layers. This limit may arise due to the weight of the thicker films embedding the bottom graphene flakes more strongly into the MCE filters, causing these flakes to be washed away during the film's removal. Alternatively, at increased thicknesses, the water flow through the forming film may become equivalent to the water flow through the stencil membrane, causing graphene to be deposited outside of the desired film area. Regardless, the relationship between volume filtered and UV-Vis transmittance showed reasonable reproducibility, as evidenced by the standard deviations shown in Figure 4.3(a). As such, the films' thicknesses will be described from hereon in by their optical transparency, defined as their percentage transmittance at 550 nm (%T). Upon thermal annealing, the films showed no change in transmittance at 550 nm (Figure 4.3(a)).

Figure 4.3(b) shows the average sheet resistance of the graphene films of varying thickness in their pristine and annealed conditions. As expected the thickness of the graphene films significantly effects their sheet resistance, with the thickest 13 %T films having a drop in their sheet resistance of almost an order of magnitude compared to the 76 %T films ($4.0 \pm 0.2 \times 10^6\ \Omega\cdot\text{square}^{-1}$ and $2.7 \pm 0.2 \times 10^5\ \Omega\cdot\text{square}^{-1}$, respectively). The sheet resistance of the pristine films appears to show two regimes within the films, a thin film regime and a thick film regime. While the sheet resistance of the two thinnest films is the same within experimental error, the three thicker films show decreasing sheet resistance with increasing thickness. These two regimes were much more prominent when the sheet resistance of the films was measured again post annealing. As Figure 4.3(b) shows, the sheet resistance of the thinner 76 %T and 60 %T films remained constant, within experimental error, while there was a nearly three orders of magnitude decrease in sheet resistance for the thicker films, with the 23 %T film showing the best performance at $2.8 \pm 0.3 \times 10^3\ \Omega\cdot\text{square}^{-1}$. These sheet resistances compare favourably with other surfactant-assisted exfoliated graphene films such as those by Lotya et al. [34] (higher sheet resistance but higher transparency), De et al. [41] (comparable sheet resistance and transmittance but annealed at 500 °C) and Guardia et al. [37] (lower conductivities with opaque films).

It is hypothesised that there are two contributing factors to the changes in sheet resistance observed in the pristine and annealed films. The first difference between the two regimes is that the thin films are largely incomplete films, with graphene flakes acting as islands along the length of the film. Thus, electrons are unable to travel directly between flakes across large distances and must instead follow a hopping mechanism, increasing the sheet resistance of the films.

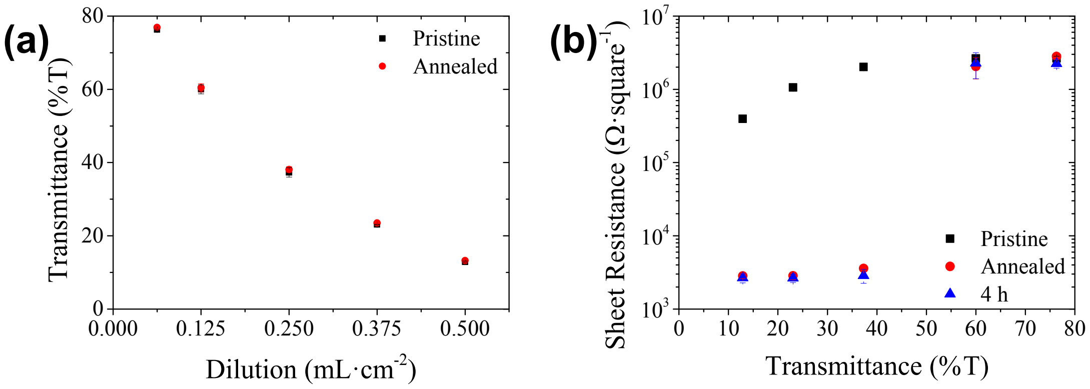

Figure 4.3: (a) UV-Vis transmittance at 550 nm of pristine (black squares) and annealed (red circles) graphene films of varying thicknesses on glass and (b) sheet resistance of graphene films of varying thickness on glass measured pristine, after annealing in forming gas for 2 h and then 4 h after annealing (error bars are present on all data points).

To investigate this potential factor, the film formation was observed by performing AFM on both 76 %T and 23 %T films that were deposited on silicon substrates, seen in Figure 4.4(a-c). Comparison of a 5 × 5 μm area on a 76 %T film (Figure 4.4(a)) and a 10 × 10 μm area on a 23 %T film (Figure 4.4(c)) shows a clear difference between the film morphologies in both lateral and vertical dimensions. Figure 4.4(a) shows several few-layer (and thicker) graphene flakes spread across the imaged area. Figure 4.4(b) shows a 1×1 μm zoom in of one of the few-layer flake seen in Figure 4.4(a) with the corresponding cross sections presented in Figure 4.4(d), showing an average flake thickness of 6.4 nm. This flake and others can be seen spread out from each other with the silicon substrate beneath clearly visible. Figure 4.4(c), however, shows a very densely packed film with no apparent silicon substrate visible underneath, with a greater maximum height scale of 400 nm.

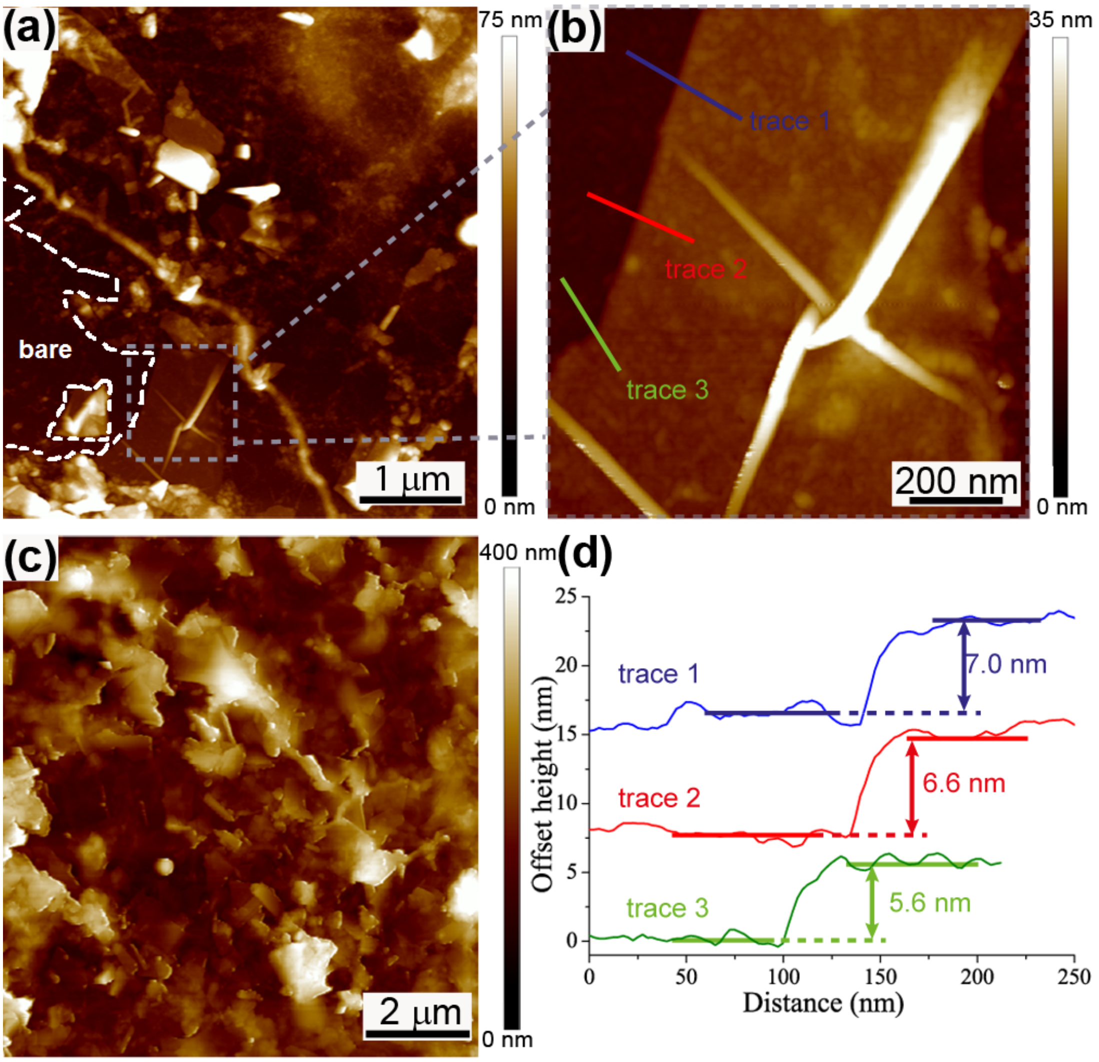

Figure 4.4: Representative AFM images of (a) 5×5 μm area of a 76 %T film on silicon substrate, (b) a zoom in on a 1×1 μm area showing an exfoliated graphene flake exhibiting characteristic wrinkling, (c) a 10×10 μm area of a 23 %T film on a silicon substrate, and (d) trace heights of the graphene flake seen in (b) showing an average height of 6.4 nm.

The second difference between the films arises from the film production method. Due to the small volumes of graphene dispersion being filtered, 45 μL in the case of the thinnest films, film inconsistencies occurred within filter papers if the dispersions were not first diluted before filtration. Thus, in order to ensure consistent film production, all films were prepared by diluting the volume of stock solution for the required thickness of the film in 1 L of water. It was therefore expected that the thinner films would have inherently less residual surfactant as the solution would be more dilute before filtering. Despite rinsing with copious amounts of water, the thicker films could still have more residual insulating surfactant between the graphene flakes, and hence a higher sheet resistance. When the films were then annealed, this residual surfactant decomposed and the graphene flakes were brought into better electrical contact with each other resulting in lower sheet resistances, with Figure 4.3(b) showing that this decrease in sheet resistance is stable at least 4 h after the annealing treatment.

4.4 Photovoltaic Characterisation of the Initial G-Si Solar Cells

The processing steps used in the initial photovoltaic characterisation of the G-Si Schottky junction solar cells are set out in Figure 4.5. Once the film had been applied (Figure 4.5(i)) there were still a number of steps that needed to be taken before the cell could be tested. In order to make an electrical connection between the silicon substrate and the stainless steel back electrode of the cell (Chapter 2 Figure 2.1), the 100 nm thermal oxide layer on the back of the Si substrate must be removed. This was achieved by etching the back of the cell with BOE (Figure 4.5(ii)), and after rinsing with MilliQ water and ethanol and drying under nitrogen eGaIn could be applied to both the Si substrate and the stainless steel plate, forming an electrical junction (Chapter 2 Section 2.1.2). At this stage, the cell was fully functional and its photovoltaic properties could be investigated.

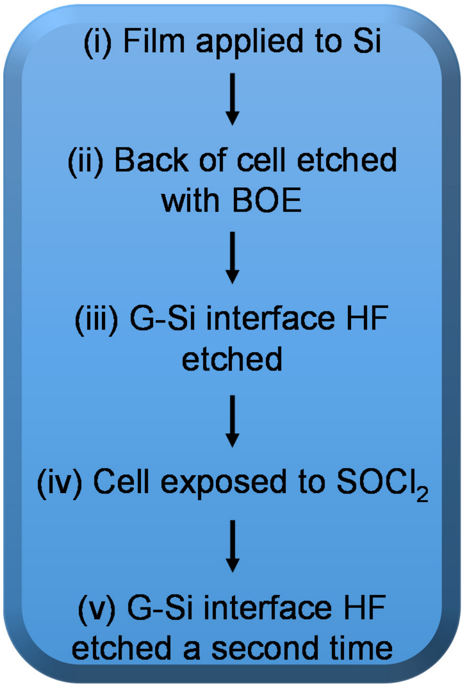

Figure 4.5: Scheme showing the processing steps used in the initial photovoltaic characterisation of the G-Si Schottky junction solar cells.

In order to understand the photovoltaic behaviour of the cells after each treatment step, the JSC, VOC, FF and PCE were plotted against time and shown in Figure 4.6, Figure 4.7, Figure 4.9 and Figure 4.10. Initially, straight after cell assembly (0 h), the cells exhibit low JSC (Figure 4.6(a)) and FF (Figure 4.6(c)) along with a moderate VOC (Figure 4.6(b)), with a representative J-V curve displayed in the black trace of Figure 4.8(i). Due to the low J_{SC} and FF the PCE of the cells is ultimately low (Figure 4.6(d)). However, when the cells were stored in ambient conditions and retested after 3 h and 5 h and again at 22 h and 24 h, an increase in their J_{SC} and V_{OC} was observed. In order to investigate this apparent gradual aging effect, the cells were stored in ambient conditions for 13 days (312 h) with periodical testing carried out over this time period. A gradual increase in both J_{SC} and V_{OC}, and thus PCE, was observed, before an eventual plateau after approximately 168 h (Figure 4.6 (a, b & d)). This same trend was not observed for the FF of the cells, which remained constant. This extended time dependence is proposed to be due to the gradual growth of the native oxide layer at the interface of the graphene film and the n-type silicon.

While the 100 nm thermal silicon oxide layer present on the Si substrate is removed with BOE etching prior to the application of the graphene films, it can regrow during both the cell assembly process, as well as post-assembly when the cells are exposed to atmosphere [19, 20, 42]. While graphene has been found to be impermeable to air [43], it has been observed that CVD grown graphene does not prevent the growth of native oxide at the G-Si interface [18, 19]. Native oxide growth has also been shown to continue growing after CNT deposition in CNT-Si solar cells [44, 45], which have a more comparable morphology to the patchwork nature of the films made from graphene flakes discussed here.

Song et al. [20] found an increase in V_{OC} with increasing silicon oxide thickness in their CVD G-Si Schottky junction solar cells, but observed a decrease in J_{SC} and FF. A possible reason for the difference in behaviour is that the CVD graphene of Song et al. [20] may make better morphological contact with their underlying substrate. Furthermore, they controlled their oxide thicknesses by changing the amount of time between their etching of the Si substrate and the deposition of their graphene, but did not repeatedly measure their cells again after their initial measurements, as was performed here.

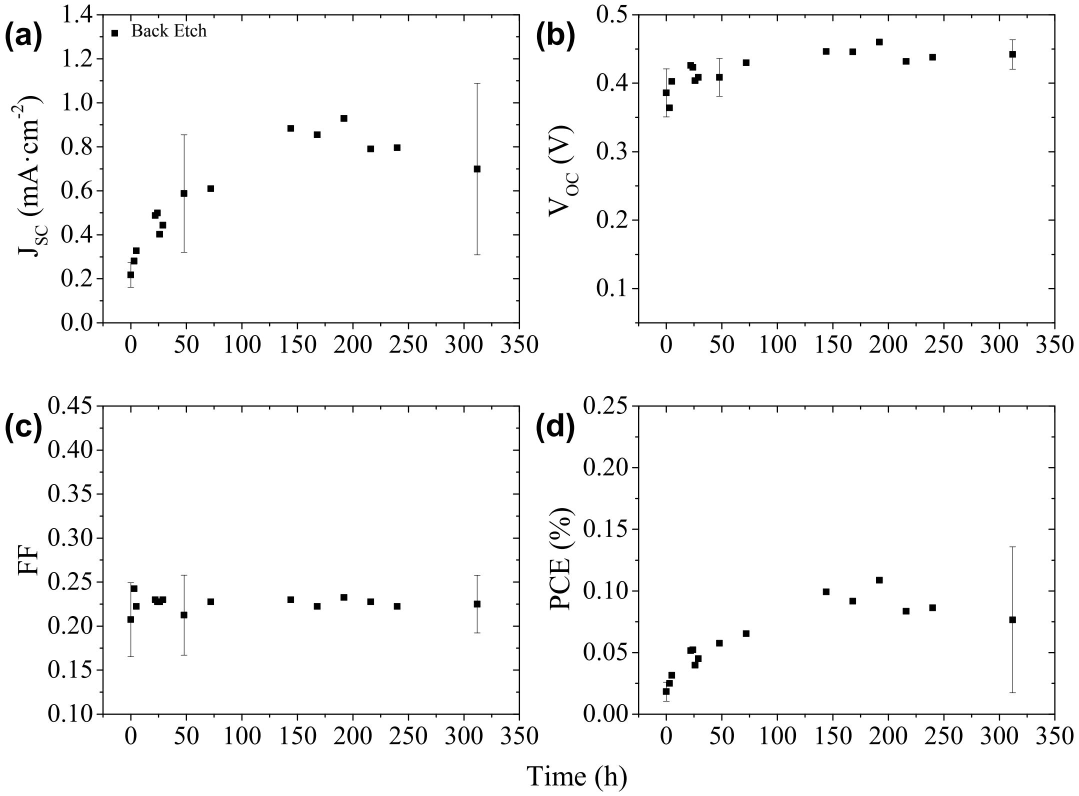

Figure 4.6: Effect of time on the photovoltaic properties of G-Si solar cells after BOE etching of the back of the silicon substrate, specifically (a) J_{SC}, (b) V_{OC}, (c) FF and (d) PCE.

It has been shown previously [4, 5] in the CNT-Si architecture that exposure of the CNT-Si interface to dilute HF acid can increase the PCE of the cells, specifically by increasing their FF. To investigate this effect on the G-Si architecture, the G-Si interface of the cells was exposed to dilute HF acid and the cells re-tested. Similarly to the CNT-Si cells, there was an immediate increase in the FF of the cells of approximately 40 %, seen in the red circles of Figure 4.7(c). Exposure of the G-Si interface to HF acid etches away the native oxide layer present between the two surfaces, bringing them into much better electrical contact with each other. This means that the ability of separated electron-hole pairs to recombine is reduced and the charge carriers can be more easily collected at their respective electrodes, resulting in an increased FF of the cells.

However, unlike in CNT-Si architectures [5], where the J_{SC} of the cells remained stable after HF etching and the V_{OC} was only slightly reduced (~10 %), in the G-Si solar cells, both the J_{SC} (Figure 4.7(a))and V_{OC} (Figure 4.7(b)) were reduced to values lower than initially measured immediately after BOE etching of the back contact. As mentioned in Section 4.1, the exact mechanism of action, e.g. Schottky junction, metal insulator semiconductor (MIS), or p-n junction, in the CNT-Si architecture is still debated and can be affected by a number of factors [46, 47]. In contrast to this, G-Si cells have been shown to follow a Schottky junction mechanism of action and it is therefore not unexpected that they would behave differently when exposed to HF etching. The subsequent removal of the native oxide layer decreases the size of the charge depletion region, decreasing the V_{OC} of the cells. This reduction in the V_{OC} would have a concomitant effect on the J_{SC} of the cells as they are now unable to drive as much charge throughout the circuit.

Periodic light testing of the G-Si cells after the HF etch showed that the reductions in J_{SC} (Figure 4.7(a)) and V_{OC} (Figure 4.7(b)) were not permanent, as they again increased over a period of approximately 216 h. These observed changes in V_{OC} occur on a similar scale to those reported by Song et al. [20]. Over the same period the FF also increased (Figure 4.7(c)), although the proportion of this increase was not as significant compared with the J_{SC} and V_{OC}. The increases in these photovoltaic properties are again attributed to the growth of an oxide layer between the G-Si interface. This occurs over the same time period as the initial growth which occurs during cell assembly, and would appear to reach similar levels, given the return of the J_{SC} and V_{OC} to their pre-HF etch values. This oxide layer however is in much better electrical contact with the two surfaces and as such the FF of the cells is preserved, and even increased, as it grows back. These factors ultimately led to the highest PCE for the cells being observed 240 h post HF etch, with a representative J-V curve of this shown in the red trace of Figure 4.8(ii).

Thionyl chloride has been shown to be an effective p-type dopant in CVD G-Si Schottky junctions [9, 17] as well as for CNT-Si heterojunctions [5, 6, 46]. Given the ubiquity of doping nanocarbon-based materials with $SOCl_2$, this was also used here for the G-Si solar cells as outlined in Chapter 2 Section 2.1.3. The resultant photovoltaic properties of the cells can be seen in Figure 4.9, with $SOCl_2$ exposure causing a decrease in J_{SC} (Figure 4.9(a)) and FF (Figure 4.9(c)) of the cells, resulting in an approximately two thirds reduction in cell PCE (Figure 4.9(d)). The decrease in FF may be expected, as the $SOCl_2$ may react with the silicon substrate and form a thicker oxide layer between it and the graphene [48], by passing through the flakes of the graphene films. This effect would not be observed in CVD G-Si Schottky junctions as these cells have more complete layers of graphene, which would prevent the $SOCl_2$ from reaching the underlying Si substrate. $SOCl_2$ has been shown to increase the work function of graphene films and decrease their sheet resistance [9, 17], thus increasing the V_{OC} and J_{SC} of G-Si solar cells made with $SOCl_2$ doped graphene. This increase in J_{SC} and V_{OC} may not be observed in the G-Si solar cells presented here however due to the artificially large silicon oxide layer $SOCl_2$ exposure creates in these systems.

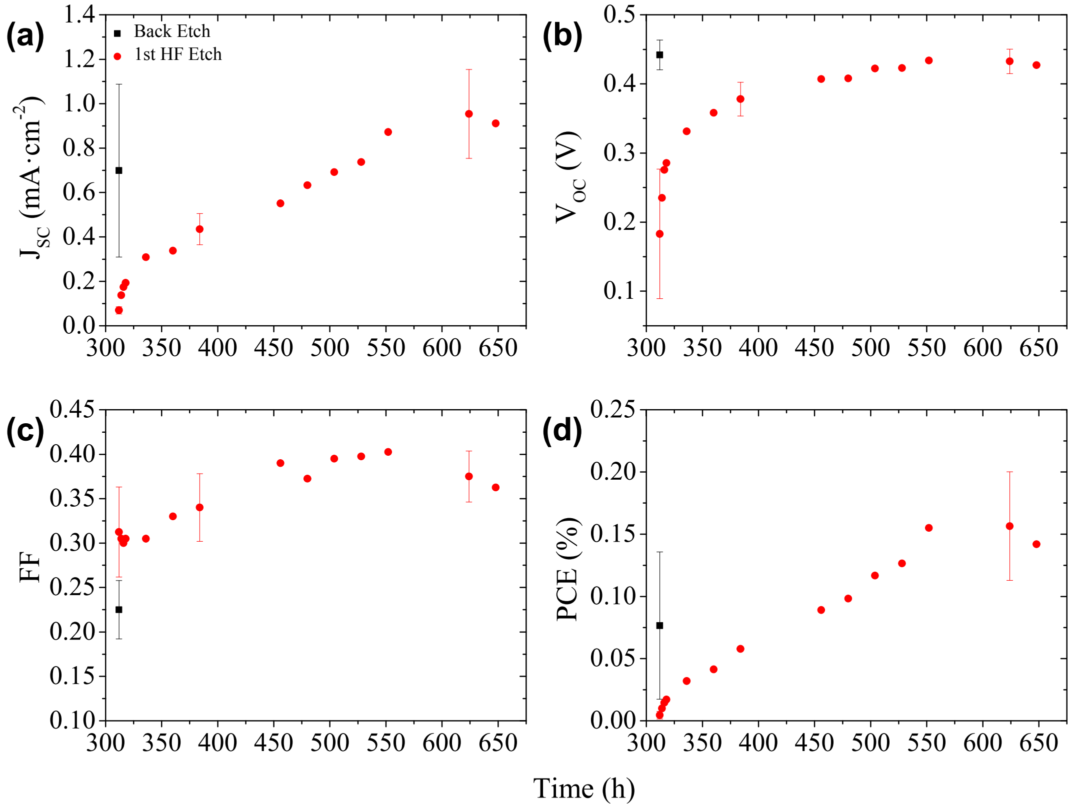

Figure 4.7: Effect of an HF etch on the G-Si interface on the photovoltaic properties of G-Si solar cells (red), specifically (a) J_{SC}, (b) V_{OC}, (c) FF and (d) PCE (prior values of the cells from the last back etch measurement are shown in black).

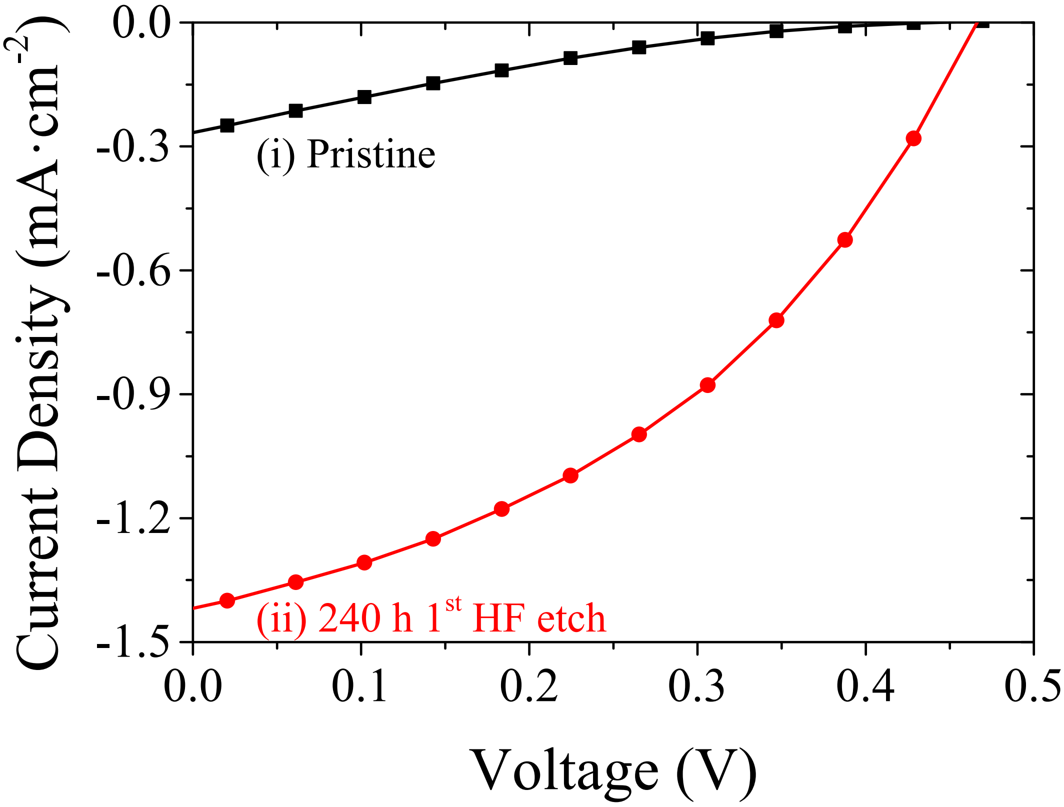

Figure 4.8: Representative J-V curves for (i) a pristine G-Si solar cell and (ii) a G-Si solar cell 240 h after its 1st HF etch.

In CNT-Si cells which also have a Si substrate easily reached by $SOCl_2$, subsequent exposure of the CNT-Si interface to dilute HF acid for a second time results in an increase in J_{SC} and FF, and hence PCE of the cells, with these values being greater than those achieved after the initial exposure [48]. To investigate whether this effect would be observed in the G-Si architecture, the cells were exposed to a second HF treatment, and their photovoltaic properties monitored over time, as seen in Figure 4.9. The cells showed the expected immediate improvement in their FF (Figure 4.9(c)), with a concomitant increase in J_{SC} (Figure 4.9(a)) and decrease in V_{OC} (Figure 4.9(b)). The initial increase in J_{SC} was replaced by a reduction over a period of 24 h, before the cell again showed improved J_{SC} values which began to plateau at values similar to their pre-$SOCl_2$ exposure. This trend was also observed in the V_{OC} of the cells, albeit on a longer time period, with plateauing not occurring until after approximately 48 h. These effects caused by the regrowth of the silicon oxide layer resulted in an eventual increase in the cells' PCE back to values approximately three quarters of their pre-$SOCl_2$ exposure (Figure 4.9(d)).

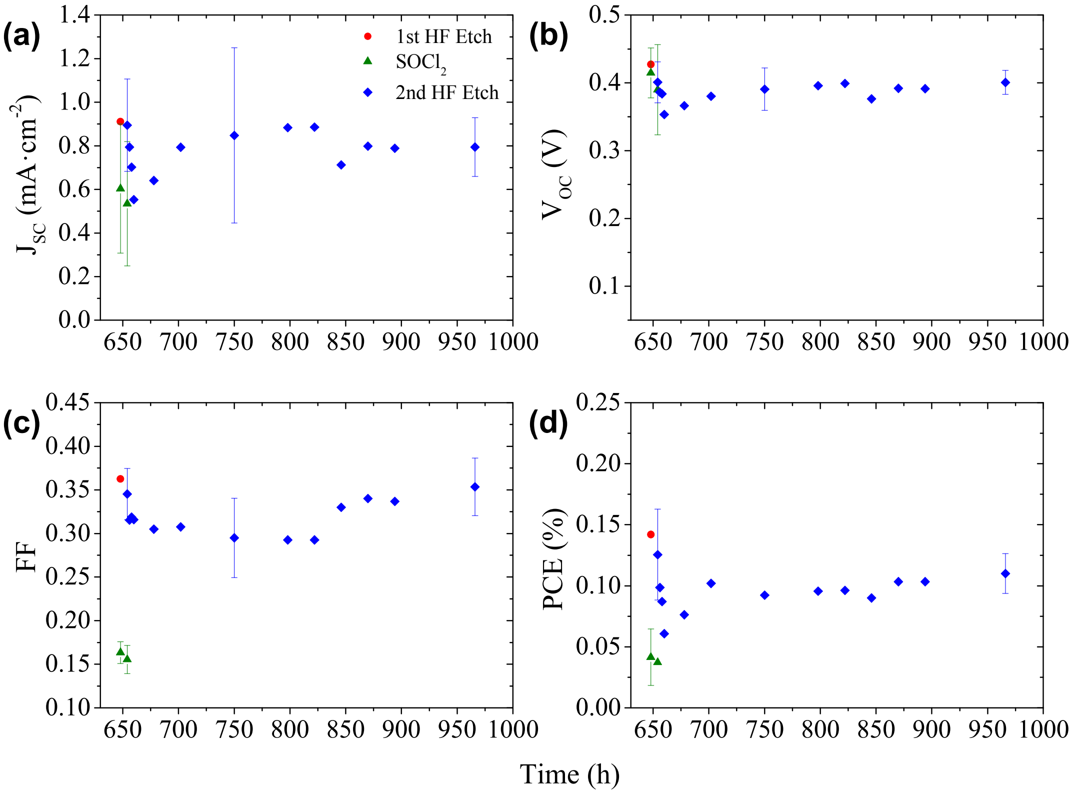

Figure 4.9: Effect of exposure to $SOCl_2$ (green) and then a second HF etch (blue) of the G-Si interface on the photovoltaic properties of G-Si solar cells, specifically (a) J_{SC}, (b) V_{OC}, (c) FF and (d) PCE (prior values of the cells from the first HF etch measurement are shown in red).

As well as giving valuable information about the effects of the native and regrown silicon oxide layer between the G-Si interface and the deleterious effects of $SOCl_2$ exposure on the cells, this initial photovoltaic characterisation provided a good indication of the robustness of these G-Si Schottky junctions. As Figure 4.10 shows, during the entire investigation, the cells were tested under AM1.5G conditions a total of 44 times, and the G-Si interface exposed to dilute HF acid twice, as well as $SOCl_2$. Despite these treatments, and the storage of the cells in ambient conditions in between light testing, they remained functional for 966 h, before testing was brought to a close due to the plateauing of the cells' performance.

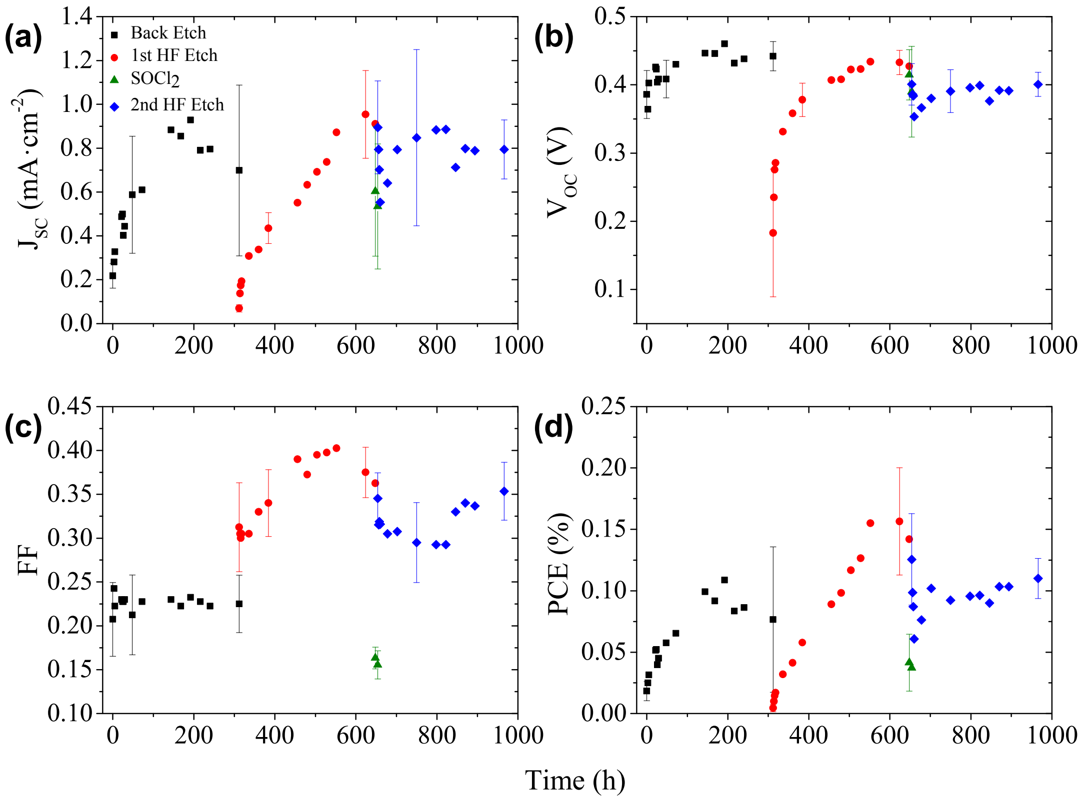

Figure 4.10: Effect of treatment steps and time on the photovoltaic properties of G-Si solar cells, specifically (a) J_{SC}, (b) V_{OC}, (c) FF and (d) PCE.

4.5 Effect of Film Thickness on Photovoltaic Performance

After the initial photovoltaic characterisation of the G-Si Schottky junction solar cells, the effect of the film thickness, measured by the film optical transmittance at 550 nm (as per Section 4.2.1), on the photovoltaic performance of the cells was investigated. It was expected that there would be a maximum PCE found in a series of thicknesses due to the trade-off between the amount of light that a film can let through to the G-Si interface with increasing optical transparency versus its increasing sheet resistance. Films of five thicknesses, with increasing optical transparencies at 550 nm of 13 %T, 23 %T, 37 %T, 60 %T and 76 %T, were used to make G-Si Schottky junctions which were then tested under AM1.5G conditions.

After the initial photovoltaic investigations, it was decided that the cells should be back etched, then immediately exposed to a front HF etch and then tested, denoted throughout as 0 h. The J_{SC} (Figure 4.11(a)), V_{OC} (Figure 4.11(c)), FF (Figure 4.11(e)) and PCE (Figure 4.11(g)) of cells of all film thicknesses were found to have a time dependence related to the HF etching of the front junction. This time dependence was most marked in the first 48 h after etching but began to plateau after approximately 150 h. The maximum post-HF etch J_{SC}, V_{OC}, FF and PCE can also be seen in Figure 4.11(b, d, f & h) respectively.

As can be seen in the pink and blue series of Figure 4.11(a), the G-Si Schottky junctions made with the two lowest optical transmittances, i.e. the two thickest films, both showed an eventual improvement in their J_{SC} after HF etching. Figure 4.11(b) also shows that their improved J_{SC} was also statistically significant compared with Schottky junctions made with the three higher optical transmittances. While the Schottky junctions with three higher optical transmittances did show improved J_{SC} over time, these values did not exceed their original post-etch value, and were also lower than the junctions made with the lowest transmittances. The Schottky junctions made with films with the highest optical transmittance, i.e., the thinnest films were found to have a significantly lower maximum J_{SC} than all other junctions. That a general trend of increasing J_{SC} with decreasing optical transmittance, and thus increasing film thickness, was observed is not surprising. It was shown in Section 4.3 Figure 4.3(b) that the sheet resistance of the films with lower optical transmittances was lower than that of films with high optical transmittances. Thus, although fewer photons reach the G-Si interface of cells made with low optical transmittance, the photocurrent that can be generated is able to travel through the circuit much more easily than current generated in cells with high optical transmittance.

Analysis of Figure 4.11(c) shows that the V_{OC} of the solar cells of all film thicknesses did not recover to their post-HF etch values. Figure 4.11(d) also shows that there was no significant difference between the maximum V_{OC} achieved post-HF etch between the solar cells made with graphene films of varying thicknesses. HF etching did however significantly reduce the inter-sample variation seen in the 76 %T cells (black series in Figure 4.11(d)).

Figure 4.11(e) shows that the cells made with 76 %T (black series), 60 %T (red series) and 23 %T (blue series) graphene films saw increases in their fill factors following HF etching, as expected. No significant change was seen in the FF of cells with the thickest 13 %T (pink series) films and a decrease in FF was observed in the cells made with the 37 %T films (green series). The HF etching had the largest effect on the FF of the cells made using the 76 %T and 60 %T films, with these FFs being significantly higher than the other three cells with thicker films (Figure 4.11(f)). This was an unexpected result, as these films are the least complete of the five thicknesses investigated and also have the highest sheet resistance. Although these thinner films are incomplete, removal of the native oxide layer may improve the electrical contact between the flakes as they move closer to each other and the underlying Si substrate post-etching, improving their FF. Furthermore, the thin nature of these films may reduce the number of flake-flake hopping events charge carriers require to travel from the G-Si interface into the graphene film for conduction, again increasing cell FF.

When the responses of the J_{SC}, V_{OC} and FF of the Schottky junctions were analysed via the PCE of the junctions, as seen in Figure 4.11(g and h), it can be seen that there was a decrease in PCE with an increase in optical transmittance. That is, as the thickness of the graphene films used to make the cells decreased, the overall photovoltaic performance of the cells decreased. However, there did appear to be a bimodal maximisation that occurred with cells with films of 23 %T and 60 %T. This again agrees with the existence of two film thickness regimes, consistent with the sheet resistance of the films discussed previously in Section 4.3 and seen in Figure 4.3(b).

The maximum PCE found for the pristine cells was 0.06 %, at a film thickness of 23 %T. This PCE was achieved with a J_{SC} of 0.68 $mA\cdot cm^{-2}$, V_{OC} of 0.41 V and a FF of 0.21. This PCE was low compared with the first CVD G-Si Schottky junction produced by Li et al. [8], however, agreement between the cell V_{OC} was reasonable (at 0.42 - 0.48 V for CVD compared with 0.41 V). This is further proof that the aqueous surfactant-assisted exfoliated graphene dispersions are indeed few-layer graphene.

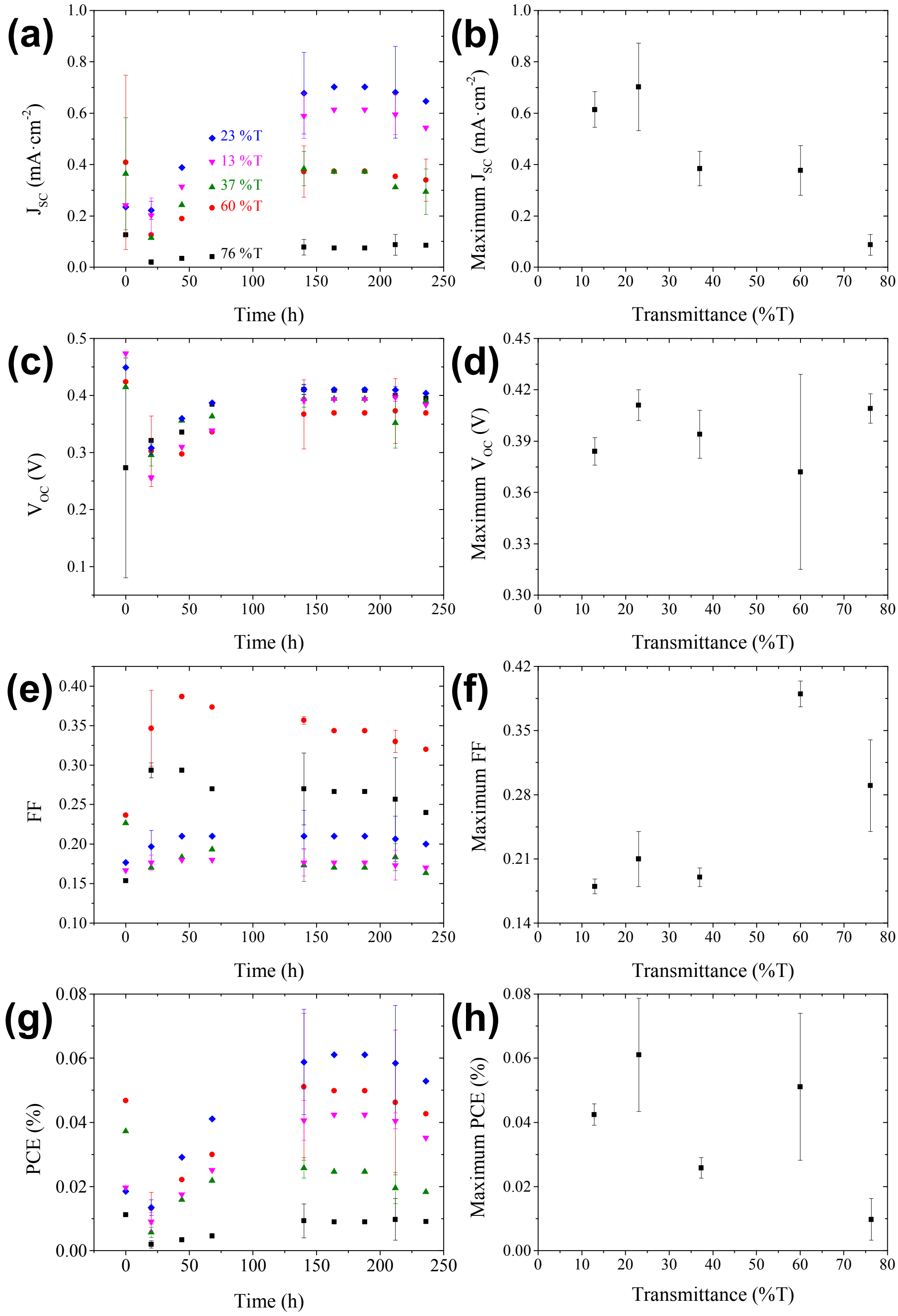

Figure 4.11: Effect of HF etching on the (a) J_{SC}, (c) V_{OC}, (e) FF and (g) PCE of G-Si Schottky junctions with graphene films of varying optical transmittance with the maximum (b) J_{SC}, (d) V_{OC}, (f) FF and (h) PCE acheived for by G-Si Schottky junctions with each optical transparency after the HF etch.

4.6 Effect of Thermal Annealing on Photovoltaic Performance

As the sheet resistance of the thicker graphene films was greatly reduced after annealing (Section 4.3), two sets of G-Si cells were prepared to investigate the effect of annealing the graphene film on the photovoltaic performance of the G-Si cells. The thin (60 %T) and thick films (23 %T) with the best photovoltaic performance, as shown in Figure 4.11(h), were prepared as per Chapter 2 Sections 2.1.1 and 2.1.2. Before the back etch step, the cells were annealed under the same conditions as the films on glass used for sheet resistance measurements. Once the cells were annealed they were back and front etched using BOE and HF respectively, as per Chapter 2 Section 2.1.2. Figure 4.12(a) shows representative dark and light J-V curves of G-Si Schottky junctions made with both pristine and annealed 60 %T and 23 %T graphene films over the range -1 to 1 V, with Figure 4.12(b) showing the light J-V curves in the power quadrant. Figure 4.13(d) shows the PCE of the annealed cells after back and front etching. Comparison of Figure 4.11(h) and Figure 4.13(d) shows that the same time dependent trend of cell PCE observed in pristine film cells is also observed in the annealed film cells. More importantly, while the thin film performance (red series) has been slightly reduced when compared to the pristine cells, the thicker 23 %T film cells (blue series) show an relative improvement in PCE of 50 % even upon initial testing, which rose to over 100 % relative increase over the course of 3 days (0.06 % to 0.13 %).

Figure 4.12(b) and Figure 4.13(a) show that the observed increase in the PCE of the solar cells was due mainly to the increase in the average J_{SC} of the junctions (a 200 % increase compared with the pristine cells, Figure 4.12(b)). There was no significant change in either the V_{OC} (Figure 4.13(b)) or FF (Figure 4.13(c)) of the cells made with 26 %T films (blue series) compared with their pristine equivalents. The comparatively larger increase in FF observed for solar cells made with pristine 60 %T films was again observed in the annealed samples (red series), although the maximum FF achieved was lower in the annealed junctions.

The increase in J_{SC} of the cells is in line with the observed decrease in sheet resistance of the annealed films in Figure 4.3(b). As the sheet resistance of the films was decreased, due to the loss of residual surfactant, it is easier for holes (charge carriers) to be transported from the graphene-silicon interface through the graphene to the front electrode and hence the measured J_{SC} is increased. As the annealing does not result in the knitting together of graphene flakes, there are still a large number of recombination sites within the graphene sheet suppressing the FF. However, this simple annealing step still further improved the J_{SC} of these junctions in comparison to early CVD G-Si cells, with the J_{SC} approaching 34 to 56 % of the CVD G-Si cells [8].

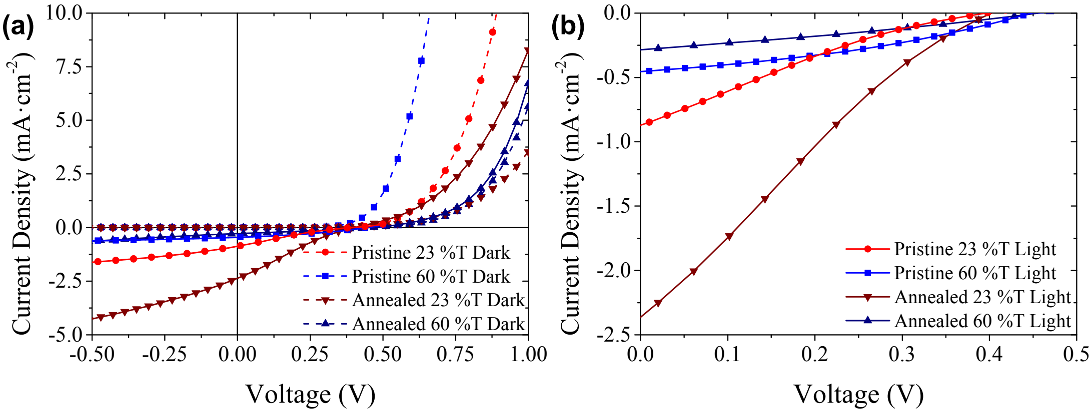

Figure 4.12: (a) Representative dark (dashed lines) and light J-V curves (solid lines) of G-Si Schottky junctions over the range -1 to 1 V, with (b) showing the light J-V curves in the power quadrant only.

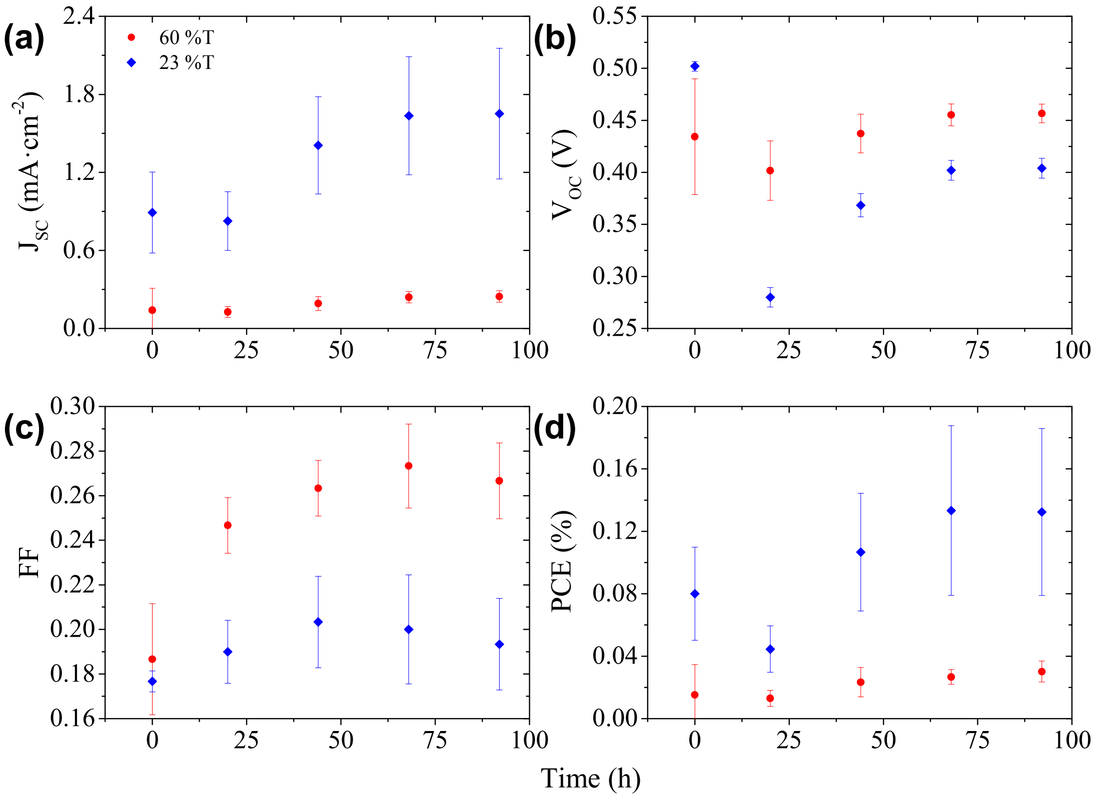

Figure 4.13: Effect of time on the photovoltaic performance of G-Si Schottky junctions made using annealed films of 60 %T (red) and 23 %T (blue) optical transmittance, specifically (a) J_{SC}, (b) V_{OC}, (c) FF and (d) PCE.

4.7 Effect of Chemical Doping on Photovoltaic Performance

Previous G-Si heterojunctions have shown marked improvement with doping of the graphene films. Figure 4.14(a) shows representative dark and light J-V curves of the best performed G-Si cells both pre- and post-doping with the chemical dopants HNO_3 and $AuCl_3$ (Chapter 2 Section 2.1.3), with Figure 4.14(b) showing the light J-V curves in the power quadrant only. Both HNO_3 [17, 49] and $AuCl_3$ [50] are known p-type dopants of graphene with similar charge transfer mechanisms of doping. In the case of HNO_3 vapour, HNO_3 molecules are adsorbed onto the surface of the graphene. Electrons are then donated from the graphene (p-doping the graphene) to the HNO_3 resulting in the release of NO_2 and H_2O, as seen in Equation 4.1 [51].

$$6\mathrm{HNO_3} + 25\mathrm{C} \rightarrow \mathrm{C_{25}^{+}NO_3^{-}} \cdot 4\mathrm{HNO_3} + \mathrm{NO_2} + 2\mathrm{H_2O}$$

Equation 4.1

Conversely $AuCl_3$ doping involves a two-step process, seen in Equation 4.2 and Equation 4.3 [52]. $AuCl_3$ is adsorbed onto the surface and can accept electrons from the graphene (p-doping the graphene), to form $AuCl_2^-$ and $AuCl_4$. The gold in these $AuCl_2^-$ complexes is then further reduced by the graphene, further p-doping it, to form gold nanoparticles [52].

$$2\mathrm{Graphene} + 2\mathrm{AuCl_3} \rightarrow 2\mathrm{Graphene^{+}} + \mathrm{AuCl_2^{-}} + \mathrm{AuCl_4}$$

Equation 4.2

$$3\mathrm{AuCl_2^{-}} \rightleftharpoons 2\mathrm{Au_0} \downarrow + \mathrm{AuCl_4^{-}} + 2\mathrm{Cl^{-}}$$

Equation 4.3

Figure 4.15 shows the PCE of pristine cells pre-doping (grey shaded area) with HNO_3 (Figure 4.15(a)) and $AuCl_3$ (Figure 4.15(b)) and post-doping. Exposing cells to concentrated HNO_3 fumes for 2 min resulted in a large initial increase in the PCE of all of the cells with the exception of the thinnest graphene film (76 %T, black trace of Figure 4.15(a)). This large increase in PCE, shown in the representative J-V curves in Figure 4.14(b), is mainly due to increases in the J_{SC} of the cells. Although there are slight increases in both the FF (10-20 %) and V_{OC} (10 %) of the cells when doped with HNO_3 and $AuCl_3$, they are not commensurate with the large increases often seen in the chemical doping of CVD G-Si Schottky junctions [9, 16]. A change in the CVD cell

V_{OC} is often attributed to the shifting of the graphene's work function [9, 17, 50], which raises the Schottky barrier height of the system and hence increases the V_{OC}. The current work however deals with films which consist of flakes of few-layer graphene stacked successively on top of each other. Work by Crowther et al. [53] with graphene of varying thickness of 1-10 layers has shown that while adsorbed NO_2 species can shift the Fermi level of graphene, only the two layers closest to the site of exposure are significantly doped, while no electric field is present deeper within the sample. This means that while the transport of electrons injected into the stacked graphene film should be enhanced due to the upper layers reduced sheet resistance [49], there is no large scale doping occurring right at the G-Si interface and hence a large change in V_{OC} is unlikely.

After this initial PCE increase due to the rise in J_{SC}, there is a decrease in the PCE of cells doped with HNO_3. However, for the three thicker films the PCE of the HNO_3 doped cells remains higher than the pre-doped values (pink, blue and green traces of Figure 4.15(a)). In contrast to this behaviour, the three thick film cells doped by spin coating of $AuCl_3$ (pink, blue and green traces of Figure 4.15(b)) showed an increase in PCE which was retained over the course of testing. This difference is most likely due to the different method in which the cells are exposed to the two dopants. In the case of exposure to concentrated HNO_3 vapour, HNO_3 can penetrate into the graphene films as well as adsorb onto the top of the film, allowing for supersaturation of the films. This accounts for the large increases in J_{SC} observed when the film was tested straight after doping. Testing the films however, along with the passage of time, allows for the excess HNO_3 to evaporate [19], and hence the PCE of the cells drops compared to the initial test but as some HNO_3 remains, the PCE still remains higher than the pre-doped instance. Doping of the cells with $AuCl_3$ however, occurs by dynamically spin coating $AuCl_3$ in ethyl ether solution onto the cells. In this method there is no chance for excess $AuCl_3$ to enter the films. The $AuCl_3$ that is deposited forms stable nanoparticles [52] and hence testing of the cells and passing of time does not result in any $AuCl_3$ being displaced and hence a drop in PCE is not observed. Indeed, gold nanoparticles can be used to dope G-Si solar cells by using radio frequency sputtering to deposit the gold and subsequently annealing the samples at 400 ºC for 10 min [54]. This non-solvent deposited gold was found to produce stable solar cell doping for up to 15 days with the cells being stored in ambient conditions [54].

Figure 4.15 also shows the PCE of annealed cells pre-doping (grey shaded area) and post-doping with HNO_3 (Figure 4.15(c)) and $AuCl_3$ (Figure 4.15(d)). The same trend that was present in the pristine cells is again apparent when annealed cells are doped, with both the thick and thin annealed film cells behaving in the same manner as their pristine counterparts. The overall magnitude of the lasting enhancement in both the HNO_3 and $AuCl_3$ cases is reduced in the annealed cells. In the case of the HNO_3 doping, this may be explained by the lack of residual surfactant present in the graphene films. It is conceivable that one of the reasons for the enhanced performance of the pristine cells when exposed to HNO_3 is that the HNO_3 removes residual surfactant from the films, reducing recombination sites and enhancing the PCE, prior to any chemical doping effects. In the case of annealed cells however, this enhancement has already taken place and hence the only effect that the HNO_3 can have is via chemical doping. In the case of $AuCl_3$ doping, the lack of surfactant may however be detrimental, as metal clusters have been shown to have a good affinity for reduction promoting crown-ether-like cavities in polyethylene oxide (PEO) surfactants, similar to Tween-60, and block copolymers [55, 56]. Hence, when exposed to annealed surfaces with less–to-no surfactant, less $AuCl_3$ is likely to be adsorbed and less chemical doping occurs.

These doping results show promising improvements in the PCE of the cells, with the thicker pristine $AuCl_3$ doped 23 %T cells showing an order of magnitude increase compared with the original, pristine and undoped cells. That these doped cell performances remain constant over the course of 7 days in ambient cell storage conditions, and that the cells in general remain stable over a period of three months (PCE $\approx$ 0.1 % for a non-optimised cell), shows that this aqueous solution processed approach to G-Si Schottky junction presents a promising new approach.

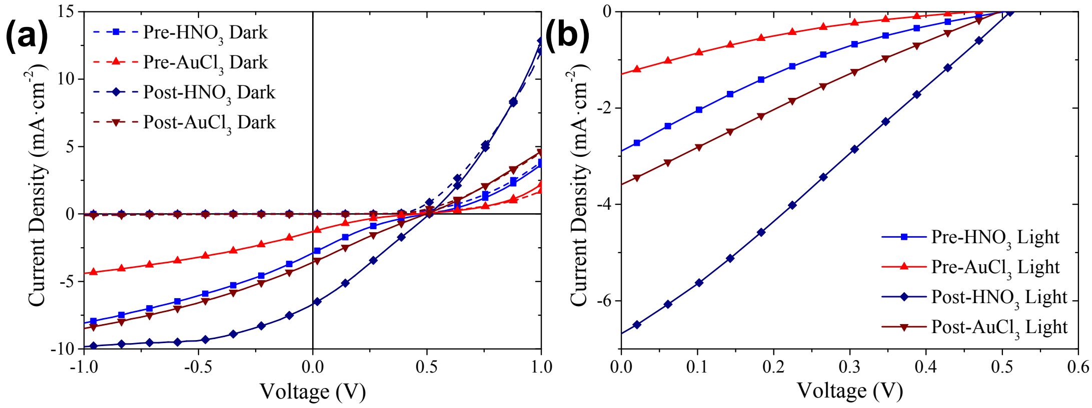

Figure 4.14: (a) Representative dark (dashed lines) and light (solid lines) J-V curves for G-Si cells pre-doping (squares and up triangles) and post- nitric acid (diamonds) and gold chloride (down triangles) doping and (b) the representative light J-V curves in the power quadrant only.

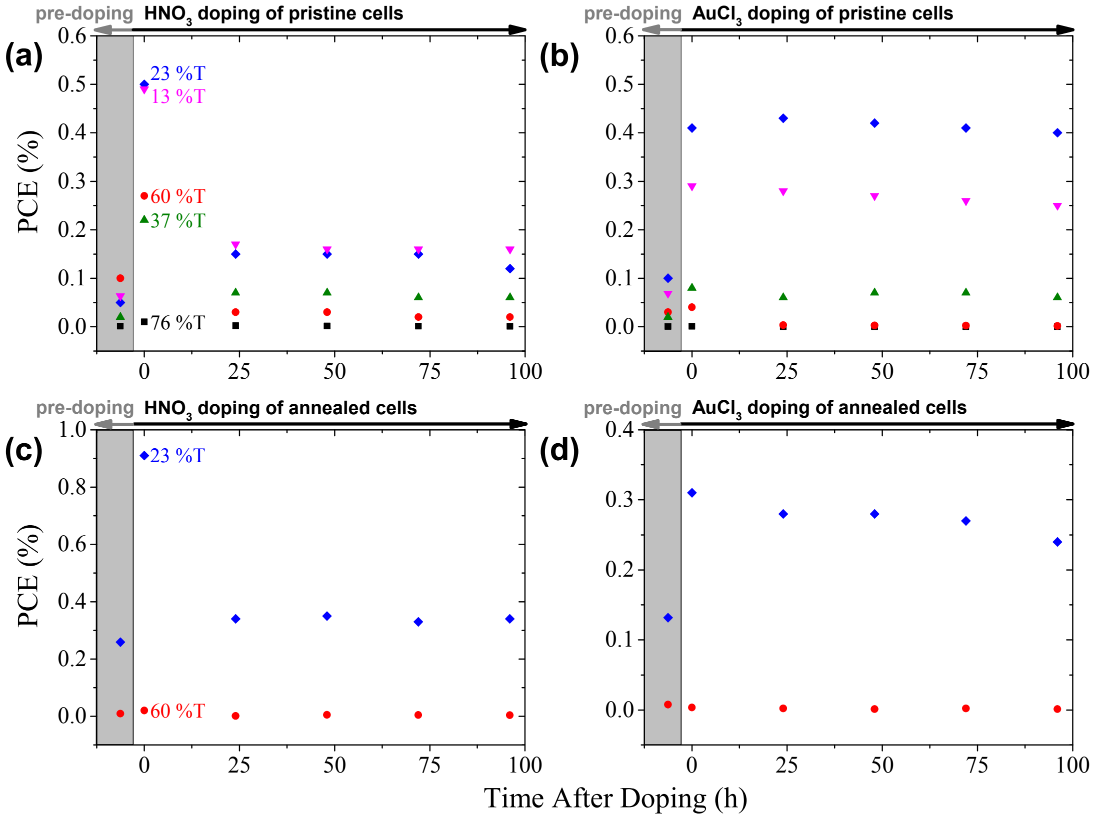

Figure 4.15: PCE of G-Si cells made with graphene films of various thicknesses both pre-doping (in grey area) and post- (a) nitric acid and (b) gold chloride doping as well as annealed film cell's PCEs both pre- and post- (c) nitric acid and (d) gold chloride doping.

4.8 Conclusions

With a maximum PCE of 0.9 % and optimised stable PCE of 0.4 %, the Tween-60 surfactant-assisted exfoliated graphene exhibited improved photovoltaic performance over reported GO and rGO cells of similar architecture (highest reported PCE of 0.3 %) [21]. This likely stems from improved conductivity in the pristine graphene flakes. However, G-Si cells fabricated from CVD produced graphene have shown higher PCEs of up to 15.6 % [20]. The improvement of the CVD derived films is a result of the larger graphene flake size reducing charge resistance related to flake-flake charge hopping. The higher conductivity allows for thinner films which increases transparency and allows for more light at the G-Si interface thus enhancing the effect of doping, as discussed earlier [53].

The solar cell performance should also be considered in terms of manufacturing cost and potential scalability of production. Solution processed graphene is capable of being fabricated on large scales from naturally occurring graphite with little input energy. In contrast, CVD growth is a high temperature process with limited scalability.

The initial reported PCE of CVD derived G-Si Schottky junction solar cell in 2010 was 1.65 % [8]. During the following 4 years gradual improvements have been achieved with the current record of 15.6 % recorded early 2015 [20]. It is foreseeable that surfactant-assisted exfoliated graphene could follow a similar path after the initial work reported in this Thesis with incremental increases likely by optimising film doping, uniformity and increasing graphene flake size.

Furthermore, the results shown here suggest that further work in this area should focus on increasing the lateral dimensions of the graphene flakes and the conductivity of the resultant films at higher optical transparencies, as higher transparencies will result in a larger photon flux reaching the G-Si interface.

In summary, surfactant-assisted exfoliated graphene was used to make transparent conducting electrodes which were then used for photovoltaic G-Si Schottky junctions. The effect of film thickness on the photovoltaic properties of these G-Si Schottky junctions was investigated and devices with an optimal film thickness of 23 %T were found to have a power conversion efficiency of 0.06 %. This efficiency was doubled (0.13 %) when the graphene films were annealed in mild conditions. Chemical doping with HNO_3 was able to increase the PCE for a short duration up to

0.9 % while doping with $AuCl_3$ was found to stably (> 100 h) increase the PCE to 0.4 %.

4.9 References

1. Wei, J, Jia, Y, Shu, Q, Gu, Z, Wang, K, Zhuang, D, Zhang, G, Wang, Z, Luo, J, Cao, A & Wu, D 2007, 'Double-walled carbon nanotube solar cells', *Nano Letters*, vol. 7, no. 8, pp. 2317-21.

2. Li, Z, Kunets, VP, Saini, V, Xu, Y, Dervishi, E, Salamo, GJ, Biris, AR & Biris, AS 2009, 'Light-harvesting using high density p-type single wall carbon nanotube/n-type silicon heterojunctions', *ACS Nano*, vol. 3, no. 6, pp. 1407-14.

3. Tune, DD, Blanch, AJ, Krupke, R, Flavel, BS & Shapter, JG 2014, 'Nanotube film metallicity and its effect on the performance of carbon nanotube–silicon solar cells', *Physica Status Solidi A: Applications and Materials Science*, vol. 211, no. 7, pp. 1479-87.

4. Tune, DD, Flavel, BS, Quinton, JS, Ellis, AV & Shapter, JG 2013, 'Single-walled carbon nanotube/polyaniline/n-silicon solar cells: Fabrication, characterization, and performance measurements', *ChemSusChem*, vol. 6, no. 2, pp. 320-7.

5. Tune, DD & Shapter, JG 2013, 'Effect of nanotube film thickness on the performance of nanotube-silicon hybrid solar cells', *Nanomaterials*, vol. 3, no. 4, pp. 655-73.

6. Li, Z, Kunets, VP, Saini, V, Xu, Y, Dervishi, E, Salamo, GJ, Biris, AR & Biris, AS 2008, '$SOCl_2$ enhanced photovoltaic conversion of single wall carbon nanotube/n-silicon heterojunctions', *Applied Physics Letters*, vol. 93, no. 24, pp. -.

7. Jung, Y, Li, X, Rajan, NK, Taylor, AD & Reed, MA 2012, 'Record high efficiency single-walled carbon nanotube/silicon p–n junction solar cells', *Nano Letters*.

8. Li, X, Zhu, H, Wang, K, Cao, A, Wei, J, Li, C, Jia, Y, Li, Z, Li, X & Wu, D 2010, 'Graphene-on-silicon Schottky junction solar cells', *Advanced Materials*, vol. 22, no. 25, pp. 2743-8.

9. Fan, G, Zhu, H, Wang, K, Wei, J, Li, X, Shu, Q, Guo, N & Wu, D 2011, 'Graphene/silicon nanowire Schottky junction for enhanced light harvesting', *ACS Applied Materials & Interfaces*, vol. 3, no. 3, pp. 721-5.

10. Wu, Y, Zhang, X, Jie, J, Xie, C, Zhang, X, Sun, B, Wang, Y & Gao, P 2013, 'Graphene transparent conductive electrodes for highly efficient silicon nanostructures-based hybrid heterojunction solar cells', *Journal of Physical Chemistry C*.

11. Feng, T, Xie, D, Lin, Y, Zang, Y, Ren, T, Song, R, Zhao, H, Tian, H, Li, X, Zhu, H & Liu, L 2011, 'Graphene based Schottky junction solar cells on patterned silicon-pillar-array substrate', *Applied Physics Letters*, vol. 99, no. 23.

12. Ihm, K, Lim, JT, Lee, K-J, Kwon, JW, Kang, T-H, Chung, S, Bae, S, Kim, JH, Hong, BH & Yeom, GY 2010, 'Number of graphene layers as a modulator of the open-circuit voltage of graphene-based solar cell', *Applied Physics Letters*, vol. 97, no. 3.

13. Bult, JB, Crisp, R, Perkins, CL & Blackburn, JL 2013, 'Role of dopants in long-range charge carrier transport for p-type and n-type graphene transparent conducting thin films', *ACS Nano*, vol. 7, no. 8, pp. 7251-61.

14. Li, X, Xie, D, Park, H, Zeng, TH, Wang, K, Wei, J, Zhong, M, Wu, D, Kong, J & Zhu, H 2013, 'Anomalous behaviors of graphene transparent conductors in graphene–silicon heterojunction solar cells', *Advanced Energy Materials*, vol. 3, no. 8, pp. 1029-34.

15. Jie, W & Hao, J 2014, 'Graphene-based hybrid structures combined with functional materials of ferroelectrics and semiconductors', *Nanoscale*, vol. 6, no. 12, pp. 6346-62.

16. Feng, T, Xie, D, Lin, Y, Zhao, H, Chen, Y, Tian, H, Ren, T, Li, X, Li, Z, Wang, K, Wu, D & Zhu, H 2012, 'Efficiency enhancement of graphene/silicon-pillar-array solar cells by HNO_3 and PEDOT-PSS', *Nanoscale*, vol. 4, no. 6, pp. 2130-3.

17. Li, X, Xie, D, Park, H, Zhu, M, Zeng, TH, Wang, K, Wei, J, Wu, D, Kong, J & Zhu, H 2013, 'Ion doping of graphene for high-efficiency heterojunction solar cells', *Nanoscale*, vol. 5, pp. 1945-8.

18. Miao, X, Tongay, S, Petterson, MK, Berke, K, Rinzler, AG, Appleton, BR & Hebard, AF 2012, 'High efficiency graphene solar cells by chemical doping', *Nano Letters*, vol. 12, no. 6, pp. 2745-50.

19. Shi, E, Li, H, Yang, L, Zhang, L, Li, Z, Li, P, Shang, Y, Wu, S, Li, X, Wei, J, Wang, K, Zhu, H, Wu, D, Fang, Y & Cao, A 2013, 'Colloidal antireflection coating improves graphene–silicon solar cells', *Nano Letters*, vol. 13, no. 4, pp. 1776-81.

20. Song, Y, Li, X, Mackin, C, Zhang, X, Fang, W, Palacios, T, Zhu, H & Kong, J 2015, 'Role of interfacial oxide in high-efficiency graphene–silicon Schottky barrier solar cells', *Nano Letters*, vol. 15, no. 3, pp. 2104-10.

21. Zhu, M, Li, X, Guo, Y, Li, X, Sun, P, Zang, X, Wang, K, Zhong, M, Wu, D & Zhu, H 2014, 'Vertical junction photodetectors based on reduced graphene oxide/silicon Schottky diodes', *Nanoscale*, vol. 6, no. 9, pp. 4909-14.

22. Phan, DT, Gupta, RK, Chung, GS, Al-Ghamdi, AA, Al-Hartomy, OA, El-Tantawy, F & Yakuphanoglu, F 2012, 'Photodiodes based on graphene oxide–silicon junctions', *Solar Energy*, vol. 86, no. 10, pp. 2961-6.

23. Kalita, G, Wakita, K, Umeno, M & Tanemura, M 2013, 'Fabrication and characteristics of solution-processed graphene oxide–silicon heterojunction', *Physica Status Solidi RRL: Rapid Research Letters*, vol. 7, no. 5, pp. 340-3.

24. Behura, SK, Nayak, S, Mukhopadhyay, I & Jani, O 2014, 'Junction characteristics of chemically-derived graphene/p-Si heterojunction solar cell', *Carbon*, vol. 67, pp. 766-74.

25. Finn, DJ, Lotya, M, Cunningham, G, Smith, RJ, McCloskey, D, Donegan, JF & Coleman, JN 2014, 'Inkjet deposition of liquid-exfoliated graphene and MoS_2 nanosheets for printed device applications', *Journal of Materials Chemistry C*, vol. 2, no. 5, pp. 925-32.

26. Withers, F, Yang, H, Britnell, L, Rooney, AP, Lewis, E, Felten, A, Woods, CR, Sanchez Romaguera, V, Georgiou, T, Eckmann, A, Kim, YJ, Yeates, SG, Haigh, SJ, Geim, AK, Novoselov, KS & Casiraghi, C 2014, 'Heterostructures produced from nanosheet-based inks', *Nano Letters*, vol. 14, no. 7, pp. 3987-92.

27. Blake, P, Brimicombe, PD, Nair, RR, Booth, TJ, Jiang, D, Schedin, F, Ponomarenko, LA, Morozov, SV, Gleeson, HF, Hill, EW, Geim, AK & Novoselov, KS 2008, 'Graphene-based liquid crystal device', *Nano Letters*, vol. 8, no. 6, pp. 1704-8.

28. Hernandez, Y, Nicolosi, V, Lotya, M, Blighe, FM, Sun, Z, De, S, McGovern, IT, Holland, B, Byrne, M, Gun'Ko, YK, Boland, JJ, Niraj, P, Duesberg, G, Krishnamurthy, S, Goodhue, R, Hutchison, J, Scardaci, V, Ferrari, AC & Coleman, JN 2008, 'High-yield production of graphene by liquid-phase exfoliation of graphite', *Nature Nanotechnology*, vol. 3, no. 9, pp. 563-8.

29. O'Neill, A, Khan, U, Nirmalraj, PN, Boland, J & Coleman, JN 2011, 'Graphene dispersion and exfoliation in low boiling point solvents', *Journal of Physical Chemistry C*, vol. 115, no. 13, pp. 5422-8.

30. Bourlinos, AB, Georgakilas, V, Zboril, R, Steriotis, TA & Stubos, AK 2009, 'Liquid-phase exfoliation of graphite towards solubilized graphenes', *Small*, vol. 5, no. 16, pp. 1841-5.

31. Hernandez, Y, Lotya, M, Rickard, D, Bergin, SD & Coleman, JN 2009, 'Measurement of multicomponent solubility parameters for graphene facilitates solvent discovery', *Langmuir*, vol. 26, no. 5, pp. 3208-13.

32. Khan, U, O'Neill, A, Lotya, M, De, S & Coleman, JN 2010, 'High-concentration solvent exfoliation of graphene', *Small*, vol. 6, no. 7, pp. 864-71.

33. Khan, U, Porwal, H, O'Neill, A, Nawaz, K, May, P & Coleman, JN 2011, 'Solvent-exfoliated graphene at extremely high concentration', *Langmuir*, vol. 27, no. 15, pp. 9077-82.

34. Lotya, M, Hernandez, Y, King, PJ, Smith, RJ, Nicolosi, V, Karlsson, LS, Blighe, FM, De, S, Wang, Z, McGovern, IT, Duesberg, GS & Coleman, JN 2009, 'Liquid phase production of graphene by exfoliation of graphite in surfactant/water solutions', *Journal of the American Chemical Society*, vol. 131, no. 10, pp. 3611-20.

35. Green, AA & Hersam, MC 2009, 'Solution phase production of graphene with controlled thickness via density differentiation', *Nano Letters*, vol. 9, no. 12, pp. 4031-6.

36. Hasan, T, Torrisi, F, Sun, Z, Popa, D, Nicolosi, V, Privitera, G, Bonaccorso, F & Ferrari, AC 2010, 'Solution-phase exfoliation of graphite for ultrafast photonics', *Physica Status Solidi B: Basic Solid State Physics*, vol. 247, no. 11-12, pp. 2953-7.

37. Guardia, L, Fernández-Merino, MJ, Paredes, JI, Solís-Fernández, P, Villar-Rodil, S, Martínez-Alonso, A & Tascón, JMD 2011, 'High-throughput production of pristine graphene in an aqueous dispersion assisted by non-ionic surfactants', *Carbon*, vol. 49, no. 5, pp. 1653-62.

38. Ferrari, AC, Meyer, JC, Scardaci, V, Casiraghi, C, Lazzeri, M, Mauri, F, Piscanec, S, Jiang, D, Novoselov, KS, Roth, S & Geim, AK 2006, 'Raman spectrum of graphene and graphene layers', *Physical Review Letters*, vol. 97, no. 18, p. 187401.

39. Bae, S, Kim, H, Lee, Y, Xu, X, Park, J-S, Zheng, Y, Balakrishnan, J, Lei, T, Ri Kim, H, Song, YI, Kim, Y-J, Kim, KS, Ozyilmaz, B, Ahn, J-H, Hong, BH & Iijima, S 2010, 'Roll-to-roll production of 30-inch graphene films for transparent electrodes', *Nature Nanotechnology*, vol. 5, no. 8, pp. 574-8.

40. Lotya, M, King, PJ, Khan, U, De, S & Coleman, JN 2010, 'High-concentration, surfactant-stabilized graphene dispersions', *ACS Nano*, vol. 4, no. 6, pp. 3155-62.

41. De, S, King, PJ, Lotya, M, O'Neill, A, Doherty, EM, Hernandez, Y, Duesberg, GS & Coleman, JN 2010, 'Flexible, transparent, conducting films of randomly stacked graphene from surfactant-stabilized, oxide-free graphene dispersions', *Small*, vol. 6, no. 3, pp. 458-64.

42. An, Y, Behnam, A, Pop, E, Bosman, G & Ural, A 2015, 'Forward-bias diode parameters, electronic noise, and photoresponse of graphene/silicon Schottky junctions with an interfacial native oxide layer', *Journal of Applied Physics*, vol. 118, no. 11, p. 114307.

43. Bunch, JS, Verbridge, SS, Alden, JS, van der Zande, AM, Parpia, JM, Craighead, HG & McEuen, PL 2008, 'Impermeable atomic membranes from graphene sheets', *Nano Letters*, vol. 8, no. 8, pp. 2458-62.

44. Petterson, MK, Lemaitre, MG, Shen, Y, Wadhwa, P, Hou, J, Vasilyeva, SV, Kravchenko, II & Rinzler, AG 2015, 'On field-effect photovoltaics: Gate enhancement of the power conversion efficiency in a nanotube/silicon-nanowire solar cell', *ACS Applied Materials & Interfaces*, vol. 7, no. 38, pp. 21182-7.

45. Jia, Y, Cao, A, Kang, F, Li, P, Gui, X, Zhang, L, Shi, E, Wei, J, Wang, K, Zhu, H & Wu, D 2012, 'Strong and reversible modulation of carbon nanotube-silicon heterojunction solar cells by an interfacial oxide layer', *Physical Chemistry Chemical Physics*.

46. Tune, DD, Blanch, AJ, Krupke, R, Flavel, BS & Shapter, JG 2014, 'Nanotube film metallicity and its effect on the performance of carbon nanotube–silicon solar cells', *physica status solidi (a)*, vol. 211, no. 7, pp. 1479-87.

47. Tune, DD, Flavel, BS, Krupke, R & Shapter, JG 2012, 'Carbon nanotube-silicon solar cells', *Advanced Energy Materials*, vol. 2, no. 9, pp. 1043-55.

48. Yu, L, Tune, DD, Shearer, CJ & Shapter, JG 2015, 'Implementation of antireflection layers for improved efficiency of carbon nanotube–silicon heterojunction solar cells', *Solar Energy*, vol. 118, no. 0, pp. 592-9.

49. Kasry, A, Kuroda, MA, Martyna, GJ, Tulevski, GS & Bol, AA 2010, 'Chemical doping of large-area stacked graphene films for use as transparent, conducting electrodes', *ACS Nano*, vol. 4, no. 7, pp. 3839-44.

50. Shi, Y, Kim, KK, Reina, A, Hofmann, M, Li, L-J & Kong, J 2010, 'Work function engineering of graphene electrode via chemical doping', *ACS Nano*, vol. 4, no. 5, pp. 2689-94.

51. Das, S, Sudhagar, P, Ito, E, Lee, D-y, Nagarajan, S, Lee, SY, Kang, YS & Choi, W 2012, 'Effect of HNO_3 functionalization on large scale graphene for enhanced tri-iodide reduction in dye-sensitized solar cells', *Journal of Materials Chemistry*.

52. Kim, KK, Reina, A, Shi, Y, Park, H, Li, L-J, Lee, YH & Kong, J 2010, 'Enhancing the conductivity of transparent graphene films via doping', *Nanotechnology*, vol. 21, no. 28, p. 285205.

53. Crowther, AC, Ghassaei, A, Jung, N & Brus, LE 2012, 'Strong charge-transfer doping of 1 to 10 layer graphene by NO_2', *ACS Nano*, vol. 6, no. 2, pp. 1865-75.

54. Liu, X, Zhang, XW, Yin, ZG, Meng, JH, Gao, HL, Zhang, LQ, Zhao, YJ & Wang, HL 2014, 'Enhanced efficiency of graphene-silicon Schottky junction solar cells by doping with Au nanoparticles', *Applied Physics Letters*, vol. 105, no. 18, p. 183901.

55. Sakai, T & Alexandridis, P 2005, 'Mechanism of gold metal ion reduction, nanoparticle growth and size control in aqueous amphiphilic block copolymer solutions at ambient conditions', *Journal of Physical Chemistry B*, vol. 109, no. 16, pp. 7766-77.

56. Alexandridis, P 2011, 'Gold nanoparticle synthesis, morphology control, and stabilization facilitated by functional polymers', *Chemical Engineering & Technology*, vol. 34, no. 1, pp. 15-28.

Chapter 5

RGO-Si Schottky Junctions

Aqueous GO dispersions were used to prepare GO thin films via vacuum filtration. Subsequently, these films were characterised and then investigated for their use in RGO-Si Schottky junction solar cells. The photovoltaic properties of the RGO-Si solar cells were optimised through investigation of the effects of GO film annealing temperature and film thickness and finally through chemical doping.

This chapter contains material previously published in:

Larsen, LJ, Shearer, CJ, Ellis, AV & Shapter, JG 2016, 'Optimization and doping of reduced graphene oxide–silicon solar cells', *The Journal of Physical Chemistry C*, vol. 120, no. 29, pp. 15648-56.

5.1 Introduction

As discussed previously in Chapter 4, there has been increasing interest in nanocarbon-based material-silicon photovoltaic systems with the main focus of current research being CNT-Si heterojunctions [1] and G-Si Schottky junctions [2]. Since the first report of a G-Si Schottky junction [3], the large majority of the work in this field has focused on graphene produced using CVD [2]. While CVD graphene may be favoured due to its relatively homogenous nature and structure, it lacks the ease of processing and the possibility for production at commercial scales which can be achieved by solution processing methods.

There are two main approaches to producing graphene via solution processing, with the main distinction being whether the end product has been chemically modified from the starting pristine graphite material. Non-chemically modified graphene can be exfoliated from graphite in the solution phase through a variety of methods, including the use of surfactants [4, 5], organic solvents with sonication [6-8], and more recently shear [9, 10]. GO is the most well-known form of chemically modified graphene. It is generally produced using either the Hummer’s [11] or modified Hummer’s methods [12-14], with these methods capable of producing large quantities of single-layer GO, which due to its highly oxidised basal surface can be easily suspended in water at high concentrations. However, these same oxygen moieties cause a large decrease in the conductivity and transparency of resultant GO films, and hence numerous reduction methods [15] using either temperature or chemical reduction, are employed to produce RGO films with more desirable physical properties.

While Chapter 4 presented an investigation into the application of solution processed graphene that has not been chemically modified in the G-Si Schottky junction, this chapter instead focuses on the use of GO to make thin films which can then be reduced to form RGO-Si heterojunctions. The application of solution processed pristine graphene has seen little research by others but there have been a number of recent papers investigating GO and RGO-Si heterojunctions [16-19]. Additionally, there have been several other reports which use GO or RGO in some capacity in nanocarbon-based material-silicon systems, whether as an intermediate layer between another carbon layer, such as the semiconducting polymer PEDOT:PSS [20, 21], or as a surfactant for the suspension of CNTs to produce CNT:GO-Si cells [22].

The device architecture of RGO-Si solar cells is an important feature, as the achievable power conversion efficiencies (PCEs) differ vastly between architectures. The most simple of the architectures consists of an *n*- [17-19] or *p*-type [16] Si substrate upon which a thin film of RGO is deposited as a transparent conducting layer (see Figure 1.15 for a representative energy level diagram). These have achieved PCEs ranging from 0.02 % [16] to 0.31 % [19]. GO has also been used as a buffer layer or filler material, or both, in systems which typically also contain PEDOT:PSS to great success. Liu et al. [20] used a partially thermally reduced GO as a buffer layer between a Si substrate and a PEDOT:PSS:GO composite and achieved a PCE of 10 %, while a 2.4 nm thick buffer layer of GO was used by Khatri et al. [21] between a PEDOT:PSS:GO-Si interface for a PCE of 11 %. GO can also be used to help suspend CNTs in aqueous solutions, with the resultant dispersion then filtered to produce CNT:GO-Si cells with a PCE of up to 6 % [22].

Previous work investigating RGO-Si solar cells have so far not investigated the effect chemical doping has on their photovoltaic performance. This is despite numerous examples in the literature of the beneficial effects of chemical doping of CVD G-Si solar cells [23-27], as well as the work shown in Chapter 4 for surfactant assisted exfoliated graphene. This chapter thus investigates the optimisation of a readily scalable RGO film production method, along with an investigation of the resultant RGO-Si solar cell performance upon chemical doping with common chemical dopants, $SOCl_2$ and $AuCl_3$.

5.2 Experimental Methods

5.2.1 GO Film Fabrication

The GO suspensions used in the production of GO films for this chapter were first prepared by evaporating the ethanol from 2 mL of a commercial single-layer GO dispersion in ethanol (5 mg·mL^{-1}, 0.5-2.0 µm flake size, Advanced Chemicals Supplier, USA). Once dried, the remaining solid GO (5.2 mg) was resuspended in MilliQ water (10 mL) via ultrasonication (Elmasonic Elma S30H, 80 W) for 30 min, producing an aqueous GO dispersion (0.5 mg·mL^{-1}). GO films were then prepared as per Chapter 2 Section 2.1.1.

5.2.2 Solar Cell Fabrication

Solar cell fabrication details followed those previously described in Chapter 2 Section 2.1.2.

5.2.3 Film Annealing

All film annealing was performed as per Chapter 2 Section 2.1.4, with the tube furnace operating at temperatures from 150 ºC to 400 ºC.

5.2.4 Doping of Solar Cells

Solar cells were doped with $SOCl_2$ and $AuCl_3$ following the procedures described in Chapter 2 Section 2.1.3.

5.3 Characterisation of the Temperature Dependence of Reduced Graphene Oxide

To investigate the effect of annealing temperature on the GO films, films of the same thickness, deposited on glass slides, were annealed at 150 ºC, 200 ºC, 300 ºC and 400 ºC. Film thickness was controlled in this study by using the same volume of GO dispersion per unit area of film each time a set of films was produced (66 μL·cm-^{2}). The UV-Vis spectrum (Figure 5.1(a & b)), Raman spectrum (Figure 5.1(c)) and sheet resistance (Figure 5.1(d)) of each film was measured prior to annealing, and immediately after annealing once cooled to room temperature. As expected (Chapter 2 Section 2.2.1 Figure 2.2(c)), the UV-Vis spectra of the GO and RGO films were broad and featureless (Figure 5.1(a)), with a large decrease in the transmittance at 550 nm observable from the lowest annealing temperature of 150 ºC (Figure 5.1(b)). The optical bandgap of the GO and RGO films can be determined from a Tauc plot, using the relationship:

$$\alpha h\nu = (h\nu - E_G)^{1/2}$$

Equation 5.1

where α is the extinction coefficient, $h\nu$ is the photon energy and E_G is the optical bandgap of the GO or RGO [16, 17]. Representative Tauc plots of both GO (blue trace) and RGO reduced at 400 ºC (red trace) can be seen in Figure 5.2, while Table 5.1 summarises the optical bandgaps of all films. Table 5.1 shows a change in the optical bandgap of the films from 3.2 eV for the GO films to 2.9 eV for the RGO films reduced at 150 ºC and 200 ºC. While Kalita et al. [17] and Behura et al. [16] reported larger optical bandgaps of 3.6 eV for drop cast GO films, this value can be modified by changing the sp^2/sp^3 ratio of carbon in the GO. As such, different GO production methods should introduce a level of variability to these bandgaps due to the varying oxidation levels of the GO. The final optical bandgap however, is in line with the findings of Kalita et al. [17] who reported partial reduction of GO films in a hydrogen atmosphere resulted in a drop in optical bandgap to 2.8 eV. Despite the changes in optical bandgap of the 150 ºC and 200 ºC films, there is no apparent change in the sheet resistance of the films, with sheet resistances constant at approximately 2×10^6 Ω·square^{-1} (Figure 5.1(d)). This lack of change in sheet resistance is not unexpected as at low temperatures the predominant mechanism behind changes to the film’s properties is due to desorption of water molecules and other physisorbed species present in the film [28, 29]. Furthermore, electron percolation between sp^2 regions of GO flakes has been shown to occur at 220 ºC [30], which significantly improves the conductivity of the flakes. Upon annealing at 300 ºC and 400 ºC, the bandgap further drops to 2.8 eV (Table 5.1). There is also a decrease in sheet resistance compared to that at lower temperatures of the RGO films to $3.9 \pm 0.6 \times 10^3$ Ω·square^{-1} at 300 ºC and $4.2 \pm 0.2 \times 10^3$ Ω·square^{-1} at 400 ºC. This reduction in sheet resistance was observed to be stable over at least a 96 h period (Figure 5.1(d)) and is comparable with other reported RGO films of similar transmittance using numerous reduction techniques [30]. While this is consistent with the expected effects of the changing chemical structure of the now reduced films, there is no appreciable difference in either the peak position or intensity ratios seen in the Raman spectra of the GO and RGO films, as seen in Figure 5.1(c) and Table 5.1 indicating that although the GO is reduced, the defects in the graphene are not fully returned to sp^2 hybridised carbon.

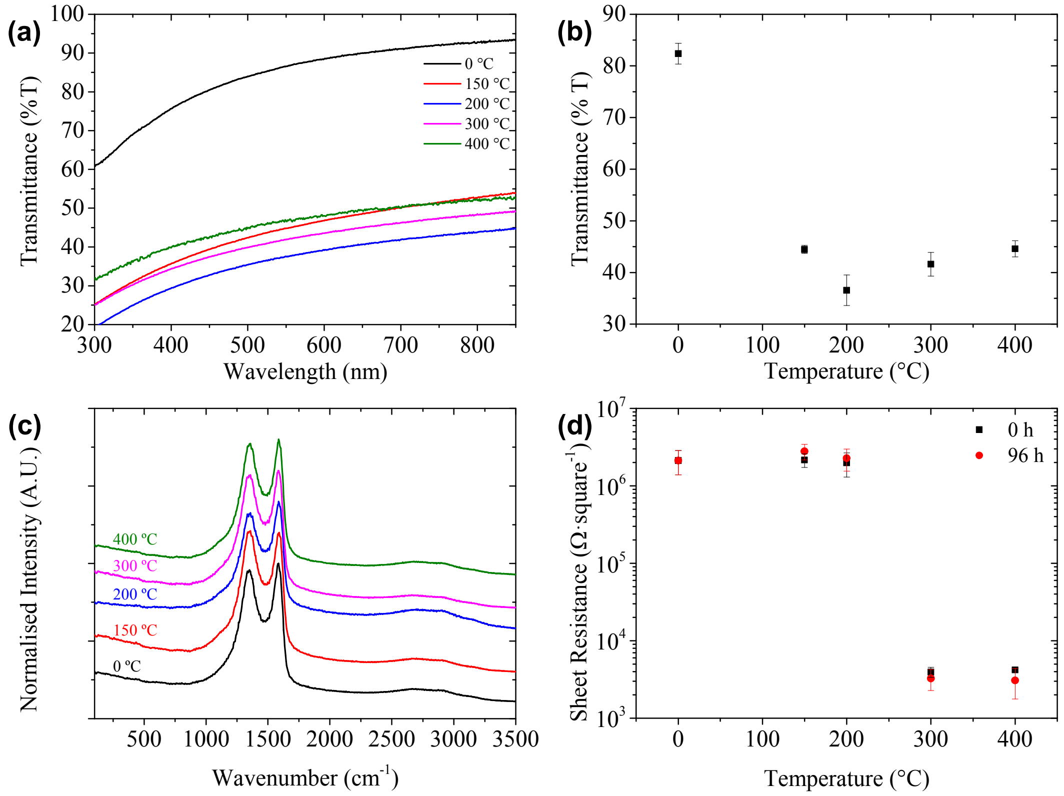

Figure 5.1: (a) UV-Vis spectra of GO and RGO films at different annealing temperatures, (b) Average UV-Vis transmittance at 550 nm, (c) normalised Raman spectra of GO and RGO films (offset for clarity) and (d) sheet resistance of GO and RGO films at different temperatures both immediately after annealing and 96 h later.

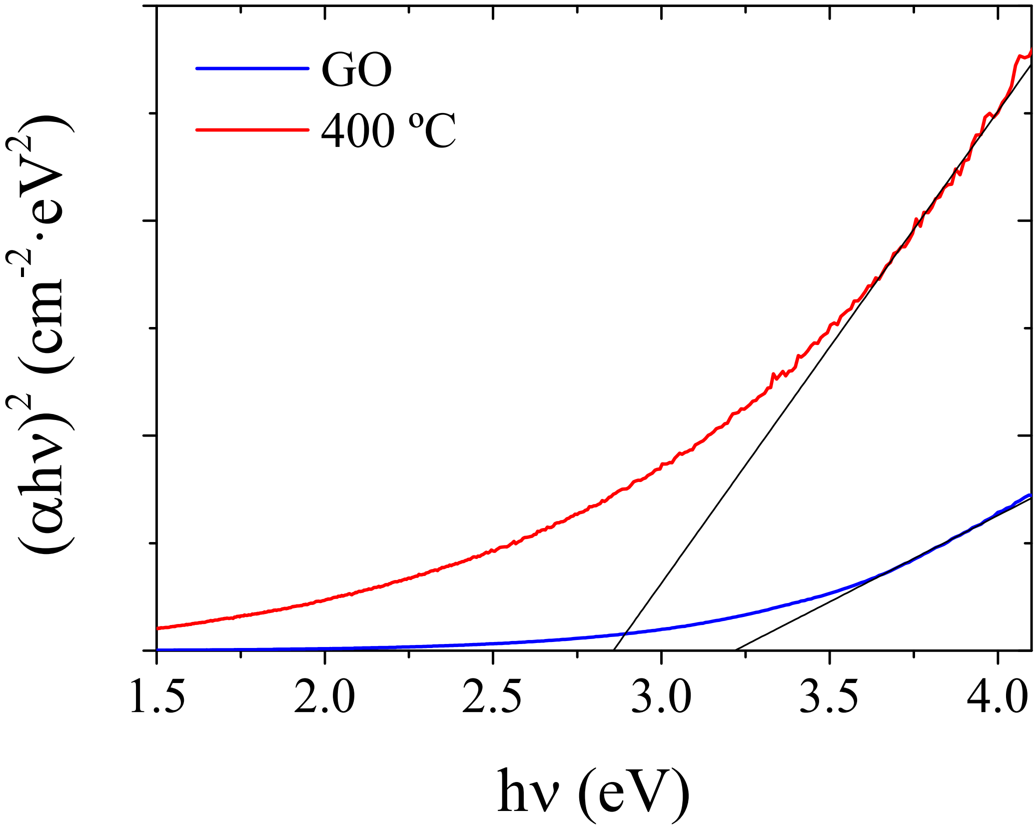

Figure 5.2: Representative Tauc plots for a GO film (blue) and a RGO film annealed at 400 ºC (blue).

Table 5.1: Average optical bandgap of GO and RGO films with standard deviation at different annealing temperatures from Tauc plot analysis of UV-Vis spectra and the corresponding D:G Raman intensity ratio of the respective spectra.

	GO	150 °C	200 °C	300 °C	400 °C
Bandgap (eV)	3.2	2.9	2.9	2.8	2.8
St. Dev.	0.024	0.0075	0.0073	0.047	0.042
D:G Ratio	0.96	1.0	0.95	0.98	0.98

5.4 Effect of Annealing Temperature on the Photovoltaic Properties of RGO-Si Schottky Junctions

As expected, GO-Si substrates showed no photoresponse when tested under illumination (black series of Figure 5.3(a-d)) due to the insulating nature of GO films. Figure 5.3(a-d) also shows the photovoltaic properties of solar cells made with films annealed at 150 ºC, 200 ºC, 300 ºC and 400 ºC. The plots show several notable points. In particular, despite there being a decrease in optical transparency and negligible decrease in the sheet resistance of RGO films produced at annealing temperatures of 150 ºC and 200 ºC, there is a photoresponse present in RGO-Si cells annealed at these temperatures (red and blue series respectively of Figure 5.3(a-d)). Furthermore, there appears to be a clear positive trend in both J_{SC}, Figure 5.3(a), and thus PCE (Figure 5.3(d)) of these RGO-Si solar cells as the annealing temperature is increased. However, this increase is again not easily explained by changes in the optical transparencies or sheet resistances previously discussed. While annealing at 300 ºC and 400 ºC did decrease the sheet resistance of the films by three orders of magnitude there was not a correspondingly large increase in the J_{SC} of the cells, nor in their FF (pink and green series respectively of Figure 5.3(c)). These results are in contrast to those of Zhu et al. [19] who found a clear positive trend in J_{SC} and FF with increasing annealing temperature. Their study, however, only analysed the photoresponse of cells to a 445 nm laser at lower power levels, not AM1.5G solar simulation, as used in this study. Also of note is that the V_{OC} (pink and green series of Figure 5.3(b)) of the cells annealed at 300 ºC and 400 ºC was significantly reduced compared to the lower annealing temperatures, a result also observed by Zhu et al. [19] albeit, at much lower voltages of 0.15 - 0.3 V.

Of most interest is the response of the RGO-Si cells annealed at 300 ºC and 400 ºC after being stored in ambient conditions for 96 h. Upon retesting, the cells annealed at 300 ºC and 400 ºC showed a 240 % and 150 % increase in J_{SC} (Figure 5.3(a)) and a 190 % and 150 % increase in V_{OC} (Figure 5.3(b)), respectively. These increases come despite there being negligible changes in the film sheet resistance or transmittance. The increased photovoltaic performance may be a result of either interfacial native oxide growth occurring between the RGO film and Si, slight doping of the RGO by atmospheric oxygen, or a combination of both. In the absence of chemical changes to the GO films seen at 150 ºC and 200 ºC, atmospheric doping cannot sufficiently induce enough change in the films to change the photoresponse and hence any interfacial native oxide growth can also not exert any influence on the solar cell performance. At 300 ºC and 400 ºC, atmospheric doping is able to induce photoresponse changes in the films and this effect can then also be increased with interfacial native oxide growth. This effect is also quite stable, with the cells retaining their high performance for at least another 96 h (total time 192 h), with representative dark and light J-V curves 0 h after annealing and 196 h after annealing seen in Figure 5.4(a) and the light J-V curves in the power quadrant only seen in Figure 5.4(b). Also of note is that the FF of these cells is within experimental error for all annealed cells and remains constant over time regardless of the annealing temperature.

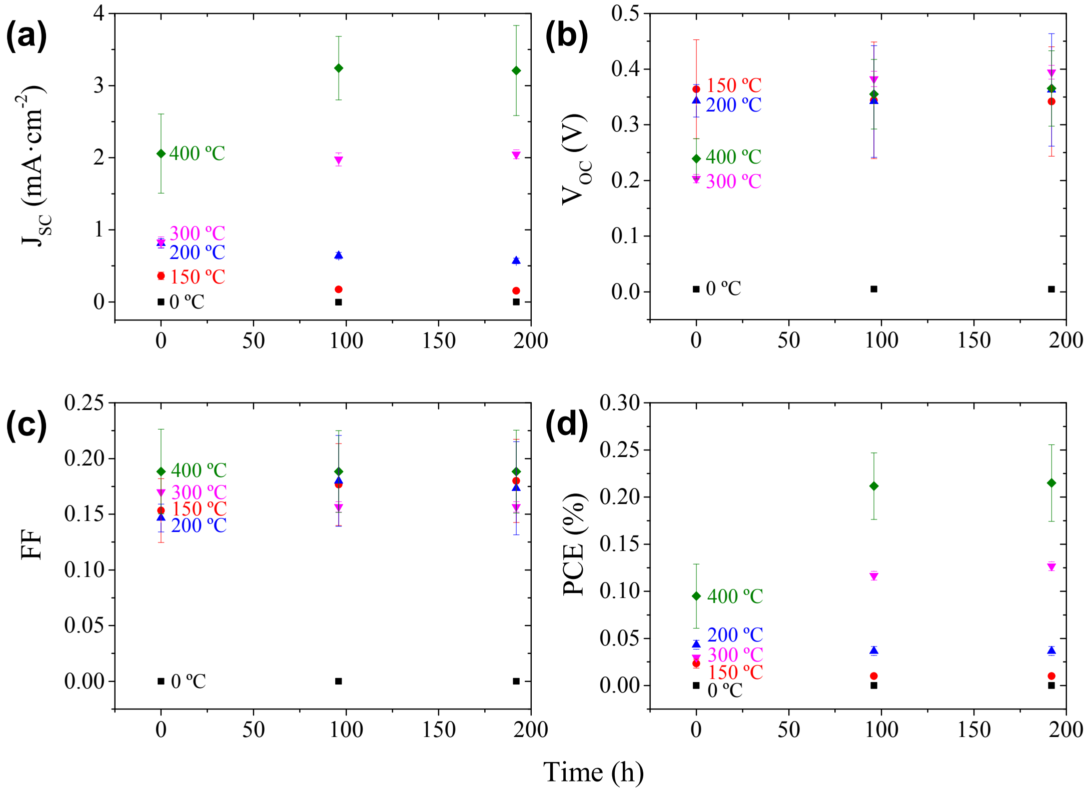

Figure 5.3: Summary of photovoltaic properties of GO-Si and RGO-Si solar cells showing variation in (a) Jsc, (b) Voc, (c) FF and (d) PCE of pristine and aged GO and RGO cells.

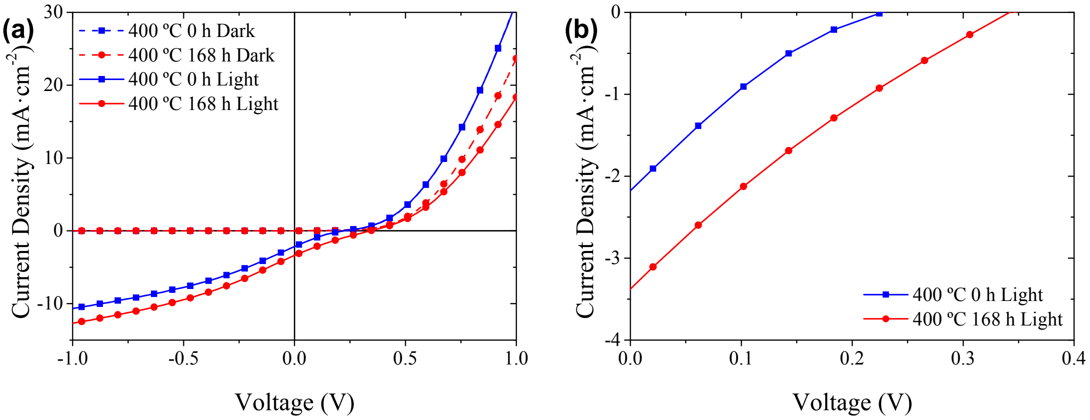

Figure 5.4: Representative dark (dashed lines) and light J-V curves (solid lines) of RGO-Si solar cells annealed at 400 ºC 0 h after annealing (blue) and 168 h after annealing (red) over the range -1 to 1 V, with (b) showing the light J-V curves in the power quadrant only.

5.5 Effect of Chemical Doping on Graphene Oxide-Silicon Schottky Junctions Annealed at Different Temperatures

As previously mentioned in Section 5.1, the effects of chemical doping have not been investigated in previous RGO-Si photovoltaic studies. In this chapter, the effects of two common chemical dopants, namely, $SOCl_2$ and $AuCl_3$, have been investigated, with Figure 5.6 showing the effect of both $SOCl_2$ doping and $AuCl_3$ doping on the J_{SC} (a & b), V_{OC} (c & d), FF (e & f) and PCE (g & h) of the RGO-Si solar cells, with Figure 5.5 showing representative J-V curves for cells annealed at 400 ºC both pre- and post-$SOCl_2$ and $AuCl_3$ doping. $SOCl_2$ (Figure 5.6(a)) and $AuCl_3$ (Figure 5.6(b)) doping both have a significant positive effect on the J_{SC} of RGO-Si cells annealed at 400 ºC (green series), with $AuCl_3$ also doubling the J_{SC} of the 300 ºC cell (pink series). Doping a 400 ºC cell with $SOCl_2$ resulted in an increase in V_{OC} (Figure 5.6(c)), while $SOCl_2$ had a negative effect on the cells annealed at lower temperatures. In contrast to this, all cells except the 150 ºC cell showed improvements in V_{OC} when doped with $AuCl_3$ (Figure 5.6(d)). An increase in V_{OC} is generally caused by an increase in the built-in potential of the Schottky junction due to p-doping of the RGO films by $AuCl_3$ [31]. $SOCl_2$ has been previously shown to p-dope RGO films [32], and as such the increase in V_{OC} of the 400 ºC film is expected. However, $SOCl_2$ has also been shown to cause oxidation of the underlying Si substrate in CNT-Si solar cells [33]. If the native oxide layer between the RGO-Si interface is too thick this could result in a decrease in V_{OC} analogous to those observed in CVD G-Si systems as well as a reduction in J_{SC} and FF as seen in CVD G-Si systems [34]. Neither dopant resulted in significant changes to the FF of cells annealed at any temperature (Figure 5.6(e &f)). While it appears that the GO-Si cells did show a marked improvement in FF, it should be noted that the J_{SC} and V_{OC} of these cells were so low that the calculation and hence any changes to the FF of the J-V curves in effect becomes redundant. Ultimately, the trends discussed in the aforementioned J_{SC}, V_{OC} and FF result in an increase in PCE after $SOCl_2$ doping of the 400 ºC films (green series of Figure 5.6(g)) and an increase in the PCE of the 300 ºC and 400 ºC films after $AuCl_3$ doping (pink and green series respectively of Figure 5.6(h)). That the doping is only effective on cells which have been annealed at high temperatures further indicates that these films have been chemically reduced by the thermal treatment. This in turn allows the dopants to induce effective p-type doping in the RGO films. While both $SOCl_2$ (0.1 % – 0.31 % for a 400 ºC annealed film) and $AuCl_3$ (0.13 % – 0.33 % for a 300 ºC film and 0.25 % – 0.81 % for a 400 ºC film) were quite effective at increasing the PCE of the highly annealed cells, this improvement was not stable, with the PCE decaying back to its pre-doped level after 24 h of storage. This was not observed in $AuCl_3$ doping of surfactant-assisted exfoliated G-Si Schottky junctions discussed previously in Chapter 4, although it is broadly consistent with the instability under ambient conditions that has been previously shown in $SOCl_2$ doped CNT-Si cells [33, 35] and CNT:GO-Si cells [22]. The lifetime of the doping effect in these systems can be lengthened by hermetically sealing the solar cells via polymer coating or encapsulation [33], and as such this constitutes a possible area for further research for RGO-Si solar cells.

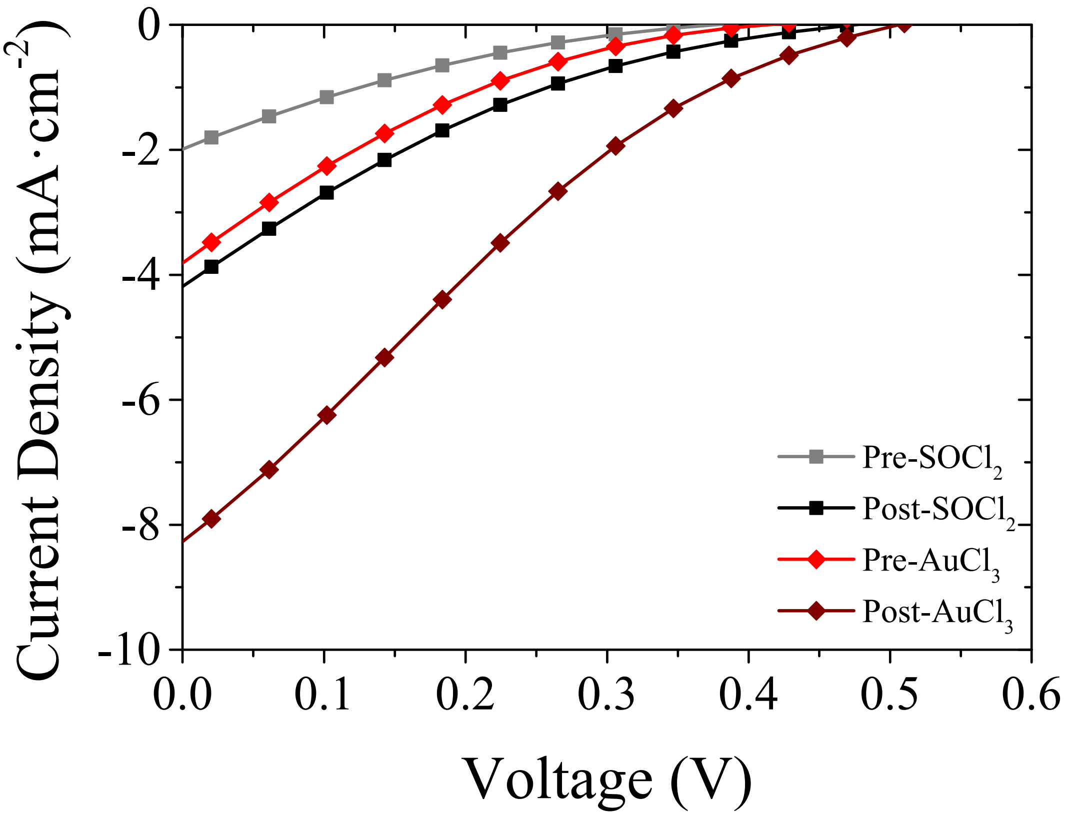

Figure 5.5: Representative J-V curves for both pristine and doped RGO-Si solar cells annealed at 400 °C.

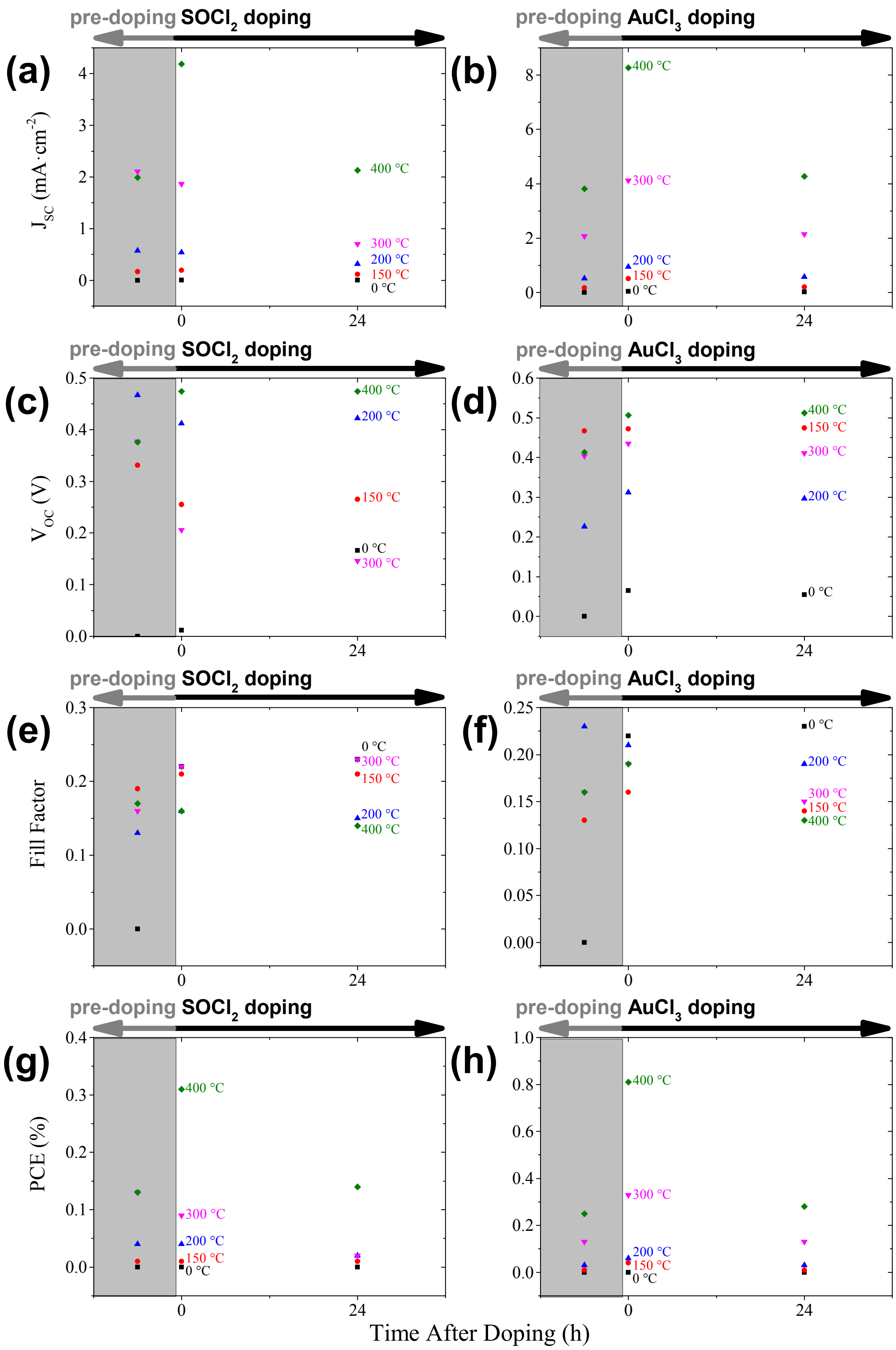

Figure 5.6: J_{SC} (a & b), V_{OC} (c & d), FF (e & f) and PCE (g & h) of GO- and RGO-Si solar cells both pre- (grey shaded area) and post-doping with both $SOCl_2$ and $AuCl_3$ respectively.

5.6 Characterisation of the Effect of Film Thickness on Graphene Oxide Films

The effect of film thickness on the performance of the RGO-Si cells was investigated once the optimal annealing temperature of 400 ºC was found. The initial thickness of the films was controlled by adjusting the volume of the 0.5 $\text{mg}\cdot\text{mL}^{-1}$ GO suspension filtered per unit area of film from 66 $\mu\text{L}\cdot\text{cm}^{-2}$, used in the temperature study, down to the thinnest 4 $\mu\text{L}\cdot\text{cm}^{-2}$ films. AFM was performed on both pristine GO films and RGO films annealed at 400 ºC to determine the thickness of the films, seen in Figure 5.7(a), while representative AFM images can be seen in Figure 5.8, Figure 5.9 and Figure 5.10. Films produced using 66 $\mu\text{L}\cdot\text{cm}^{-2}$ approached the upper limit of the reliable thickness (66 nm) manufacturable via filtration onto predefined areas, as beyond this concentration, the films became less permeable to water flow than the underlying template filter papers and the dispersion was filtered through these extra areas. Below this concentration, the technique was capable of producing well controlled GO film thicknesses as low as 9 nm, as evident in Figure 5.7(a).

Once annealed at 400 ºC, the thickness of most films was reduced by approximately 30 %, due to the removal of water and other adsorbates previously intercalated within the films [28, 29], enabling RGO film thicknesses as low as 2.3 nm (2-3 layers of RGO) [36]. Again, annealing reduces the UV-Vis transmittance of these films at 550 nm (Figure 5.7(b)), with the thinnest 2.3 nm films having a transmittance of 85 % (from 97 %) and the thickest 58 nm films having a transmittance of 35 % (from 80 %). This decrease in transmittance is concurrent with a decrease in sheet resistance (Figure 5.7(c)), as the thickness of the films increases with a decrease from $1.1 \pm 0.6 \times 10^6\ \Omega\cdot\text{square}^{-1}$ for the thinnest 2.3 nm films $3.9 \pm 0.3 \times 10^3\ \Omega\cdot\text{square}^{-1}$ for the thickest 58 nm films. It is interesting to note that while the decrease in sheet resistance appears linear for the three thinnest films, there is a large decrease in resistance post-annealing in the two thicker films (Figure 5.7(c)). This implies that between 17 and 29 nm, the electron transport properties of the films are changed markedly.

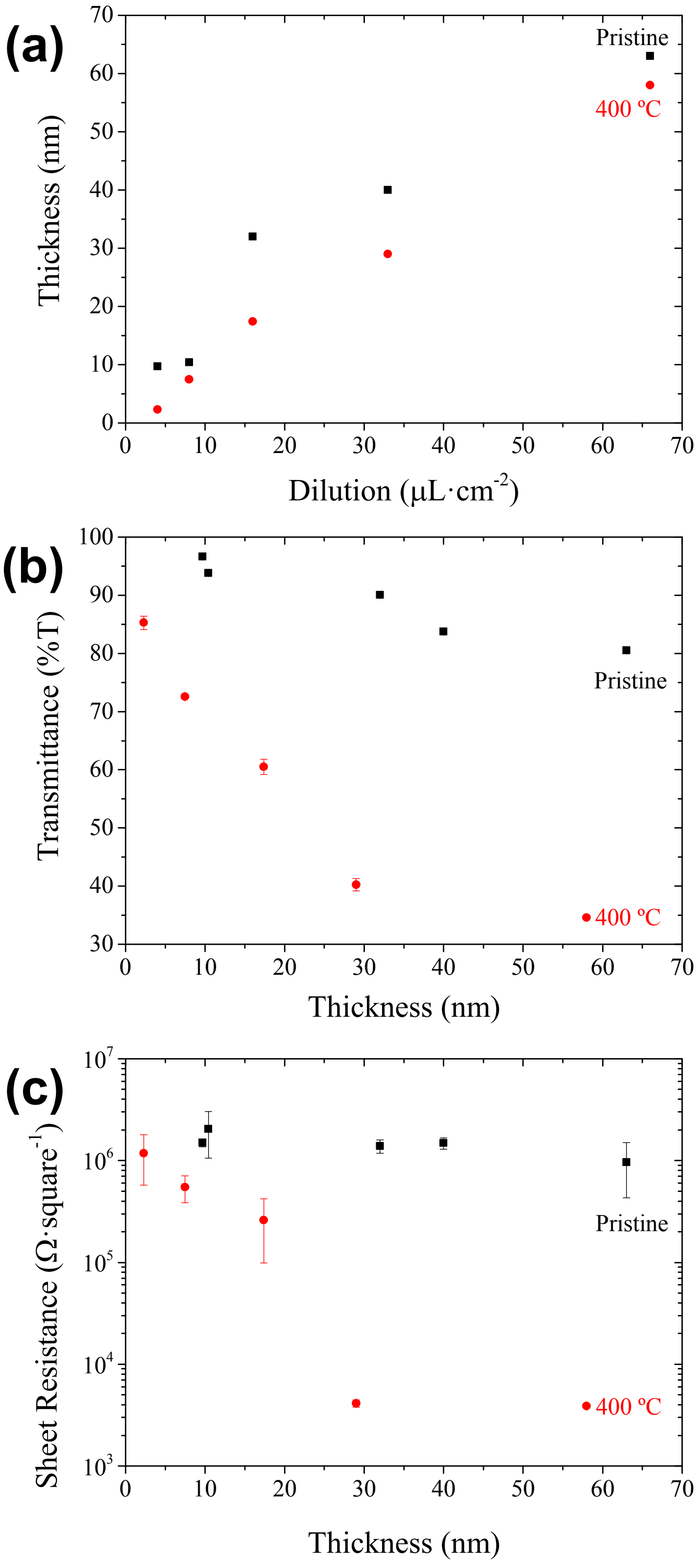

Figure 5.7: Plots of (a) AFM measured GO film thickness vs filtered GO suspension per unit area, (b) UV-Vis transmittance at 550 nm of GO films and RGO films annealed at 400 °C and (c) sheet resistance of GO and RGO films at 400 °C (error bars represent standard deviation of sheet resistance).

To investigate the physical structure of the GO and RGO films, films of varying thickness were deposited onto Si substrates and scratched with a scalpel. Prior to annealing, the films were imaged using AFM and the film thickness determined, as seen in Figure 5.8. Prior to annealing the imaged areas of these films all appear to be continuous, with the thicker films showing characteristic GO wrinkling throughout [37]. After this initial investigation with AFM, the films were annealed at 400 ºC and then reimaged with AFM, the results of which can be seen in Figure 5.9. It can be seen in Figure 5.9(a) that the 4 μm·cm^{-2} film, which when annealed had a thickness of 2.2 nm, has incomplete areas where the underlying substrate is clearly visible throughout regions of the film, with Figure 5.10(a & b) showing this more clearly. These features are consistent with other ultrathin vacuum filtered RGO films previously reported [38]. Such features are not present in thicker films, e.g. the 16 μL·cm^{-2} film shown in Figure 5.9(b), where the film is much more uniform across the covered region and no underlying substrate other than the premade scratch on the left hand side of the image is seen throughout. The two thickest films, seen in Figure 5.9(c & d) are also quite dense and show the typical folded and wrinkled nature of RGO films. The formation of complete films is desirable for these RGO-Si solar cells as it allows holes (charge carriers) to travel efficiently throughout the RGO film to the front electrode contact, decreasing the chance of recombination within the film and the need for a hopping transport mechanism. The AFM investigation of the films does not however, suggest further obvious reasons for the aforementioned large drop in sheet resistance observed between the 17 nm films and 29 nm films, as unlike the graphene films in Chapter 4 Section 4.3, there are no clear morphological differences between these films.

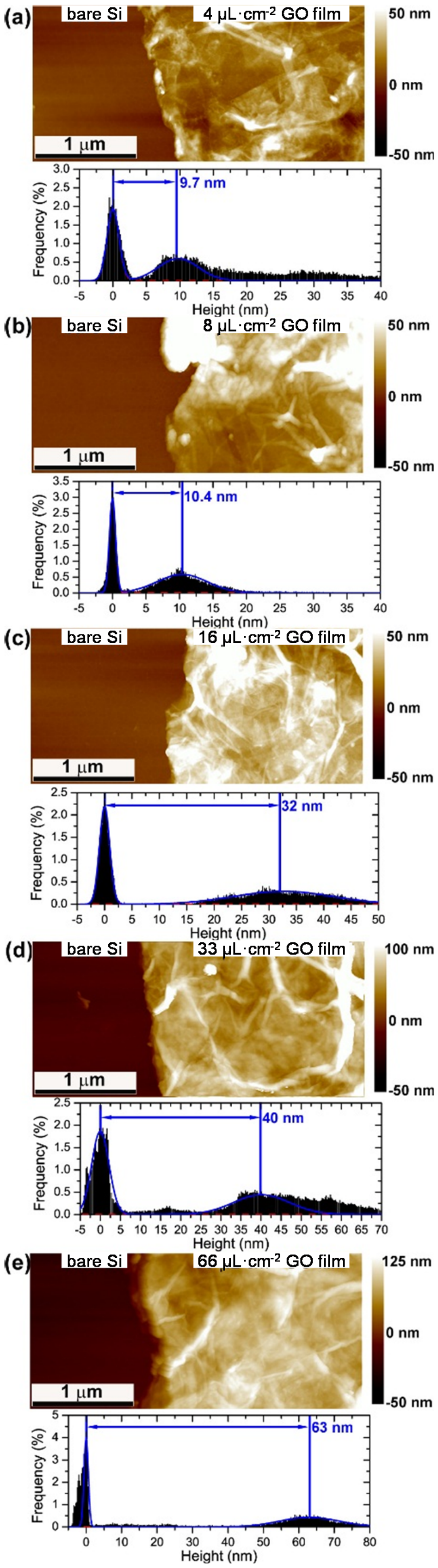

Figure 5.8: AFM height images and histograms of a (a) 4 µL·cm^{-2} film, (b) 8°µL·cm^{-2} film (c) 16 µL·cm^{-2} film, (d) 33 µL·cm^{-2} film and (e) 66 µL·cm^{-2} GO films. The flat area on the left of each image is the bare substrate exposed by the scratch.

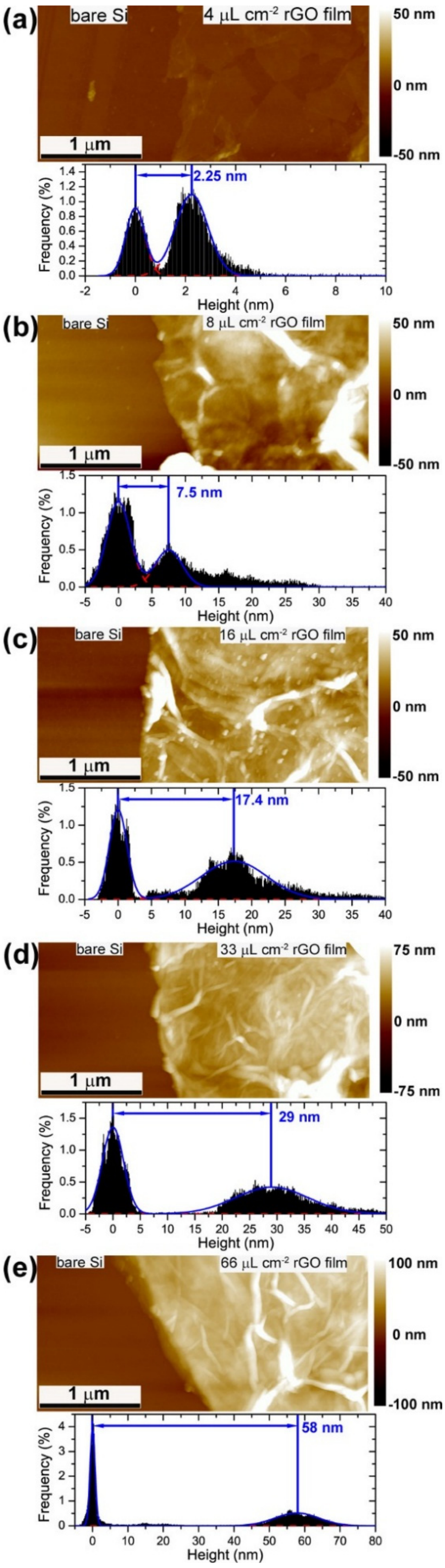

Figure 5.9: AFM height images and histograms of a (a) 4 μL·cm^{-2} film, (b) 8 μL·cm^{-2} film (c) 16 μL·cm^{-2} film, (d) 33 μL·cm^{-2} film and (e) 66 μL·cm^{-2} RGO film annealed at 400 ºC. The flat area on the left of each image is the bare substrate exposed by the scratch.

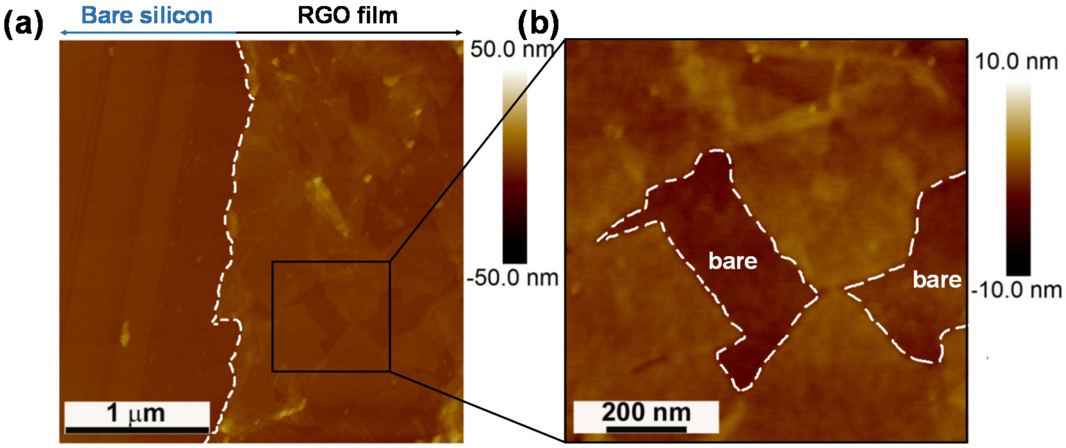

Figure 5.10: AFM image of 4 µL·cm^{-2} film annealed at 400 ºC, with dashed lines added to image to show (a) bare silicon substrate area obtained using a scalpel and (b) areas of coating in RGO film which do not cover the substrate.

5.7 Effect of Film Thickness on Photovoltaic Performance

The effect of RGO film thickness on the photovoltaic performance of these RGO-Si cells was also investigated, with the evolution of cell performance over time shown in Figure 5.11(a-d). Figure 5.11(a) shows the J_{SC} evolution of the cells over a 72 h period, with the cells stored in ambient conditions between testing times. It is apparent that all film thicknesses except the thinnest 2.3 nm film (black series) undergo the same increase in J_{SC} performance observed during the temperature dependence study. Further, this data shows that the improvement actually occurs within the first day, before plateauing in the case of the 58 nm (again, as seen in the temperature study) and 29 nm cells (green and pink series respectively). Interestingly, cells produced with thinner RGO films of 7.5 nm and 17 nm exhibit a decrease in J_{SC} after the initial increase, while the thinnest 2.3 nm film only decreases in J_{SC} over the 72 h period.

In contrast to these patterns, the V_{OC} of the cells over the same period of time is consistent across thicknesses (Figure 5.11(b)). The 2.2 nm thick cells (black series) have a slight V_{OC} increase of 8 % over the 72 h period, while all other cells show increases of between 34 – 53 % after 24 h, which then remained constant over the testing period. As discussed in Chapter 4, increases in V_{OC} observed over time in G-Si solar cells are due to the growth, or regrowth, of the native oxide layer at the G-Si interface [34]. This same effect is at play at the RGO-Si interface in these cells, with the gradual regrowth of the native oxide layer occurring over time. As such, the fact that the 2.2 nm film cells show very little change in their V_{OC} is to be expected, as the previously discussed incomplete nature of the films with many areas of exposed Si would allow oxygen much easier access to the RGO-Si junction and hence result in a fast oxide growth. The thicker films, however, are much less permeable to oxygen diffusion, and as such the growth of the oxide layer is much slower and the improvement in V_{OC} is not seen as quickly.

In general, the FF of the cells, seen in Figure 5.11(c) does not change significantly between thicknesses, or over time, and it can be seen in Figure 5.11(d) that the PCE of the cells is therefore controlled mainly by the trend observed in the J_{SC} (especially in the case of the 2.3 nm films) and V_{OC} measurements. Although there are decreases in J_{SC} for the 7.5 nm and 17 nm cells over time, the subsequent increases in V_{OC} of the four thickest cells is enough to offset these, resulting in net increases in

PCE for all but the 2.2 nm cells. Figure 5.12 shows that while the 7.5 nm cells initially have the best performance of the cells, after 72 h, all of the cells from 7.5 nm to 58 nm have the same performance, within experimental error, despite these films allowing various amounts of light through to the RGO-Si junction (Figure 5.7(b)). However, cells made with the three thickest films do improve their overall performance after 72 h (red series compared with the black series of Figure 5.12) showing the usefulness of such aging procedures. The best performed cells were thus found to be those made with 58 nm films, having a PCE of 0.21 ± 0.04 %.

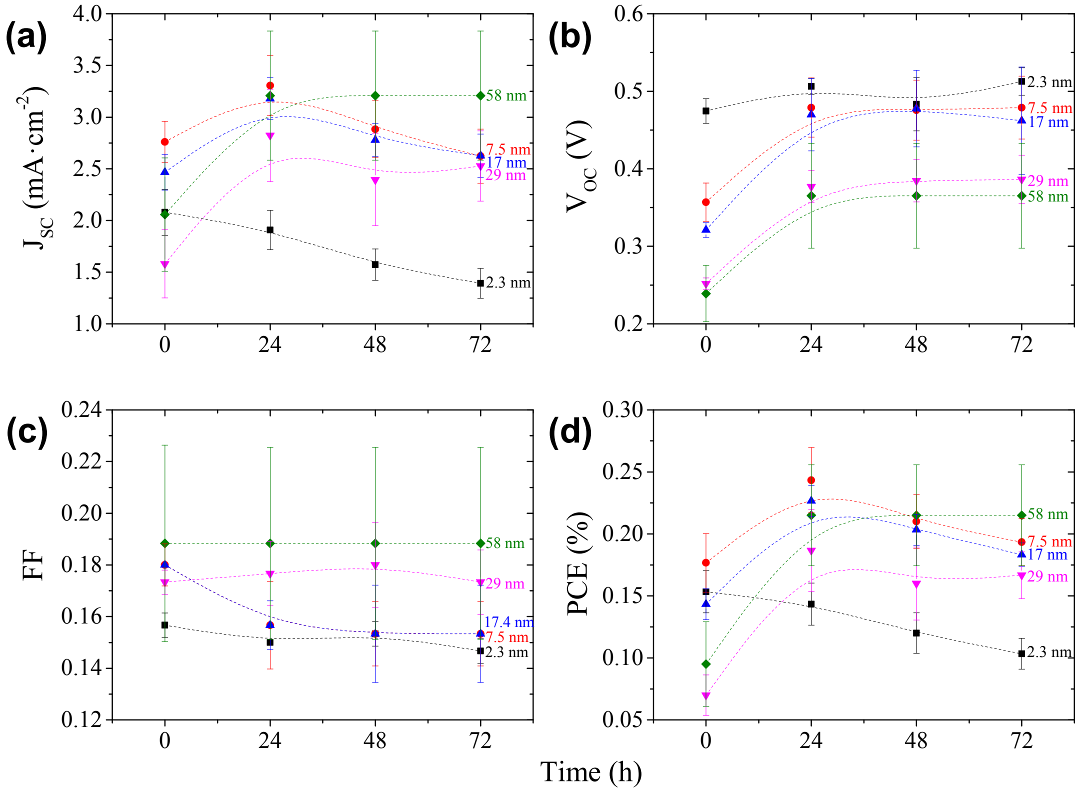

Figure 5.11: Photovoltaic properties of RGO-Si cells of different film thicknesses annealed at 400 ºC from pristine, 0 h, to 72 h aged (a) J_{SC}, (b) V_{OC}, (c) FF and (d) PCE (lines added to guide the eye).

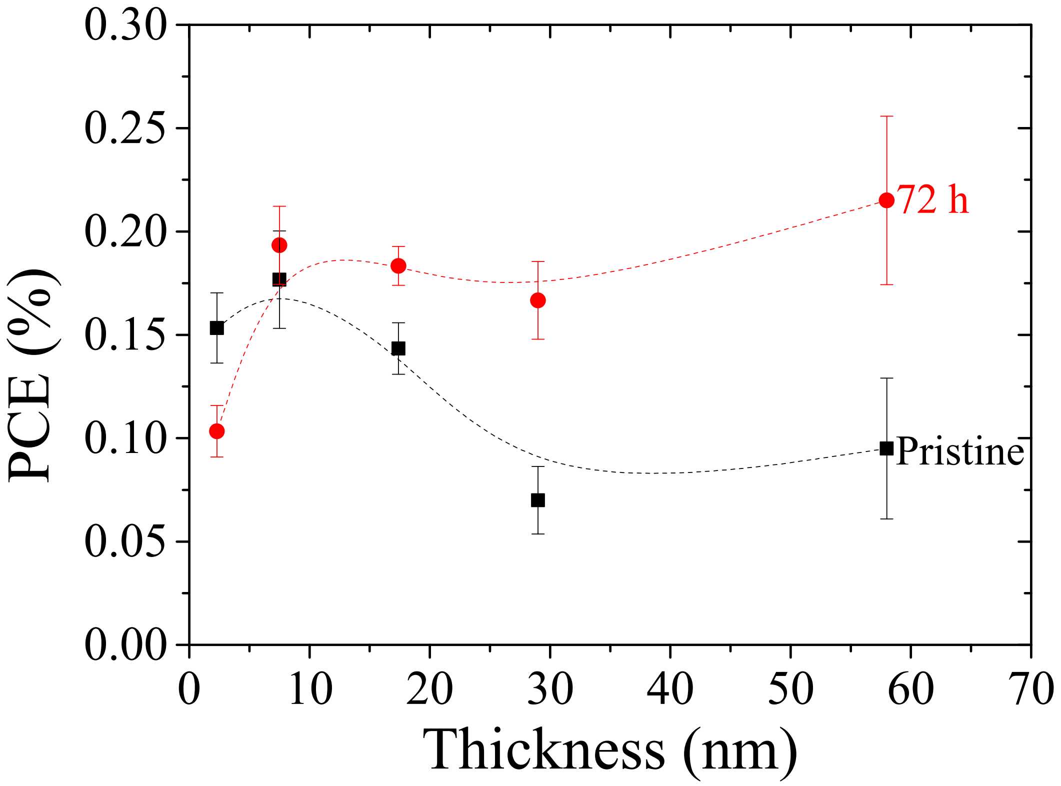

Figure 5.12: PCE of RGO-Si solar cells made with RGO films of varying thicknesses tested in pristine condition after having cooled from annealing (black series) and after having been aged 72 h (red series) (lines added to guide the eye).

5.8 Effect of Chemical Doping on Photovoltaic Performance of Different Film Thicknesses

The effect of chemical doping on the photovoltaic performance of RGO-Si solar cells made with varying film thicknesses was again investigated using $SOCl_2$ and $AuCl_3$. Figure 5.13(a) shows representative dark and light J-V curves for both $SOCl_2$ and $AuCl_3$ doping with Figure 5.13(b) showing the light J-V curves in the power quadrant only. Figure 5.14 shows the effect of doping on the J_{SC} (a & b), V_{OC} (c & d), FF (e & f) and PCE (g & h) for $SOCl_2$ and $AuCl_3$ respectively. Both $SOCl_2$ (Figure 5.14(a)) and $AuCl_3$ (Figure 5.14(b)) have a positive initial impact on the J_{SC} on cells of all thicknesses, showing that the sheet resistance of the RGO films of the cells is reduced upon chemical doping. However, in the case of both dopants, this increase is short lived, with decreases seen for all cells after 24 h of ambient storage which continue over a period of 168 h, at which time the J_{SC} is lower than its pre-doped level.

Both $SOCl_2$ and $AuCl_3$ had mixed initial effects on the V_{OC} of the RGO-Si cells, but it can be seen in Figure 5.14(c & d) that exposure to both dopants again resulted in the V_{OC} dropping to pre-doped levels after 168 h of storage, except for the 2.3 nm RGO-Si cell exposed to $SOCl_2$ (black series of Figure 5.14(c)).

While exposure to $SOCl_2$ generally resulted in little overall change to the FF of the RGO-Si solar cells over a period of 168 h (Figure 5.14(e)), $AuCl_3$ had a beneficial effect on all cells except for that of the thickest 58 nm film (green series of Figure 5.14(f)). Ultimately however, in the case of both dopants, the overall PCE of the cells after doping was determined mainly by the J_{SC} response, as can be seen in Figure 5.14(g & h). Doping with $SOCl_2$ results in at least a 47 % relative improvement in cell PCE and up to a maximum of 138 % relative improvement in the 7.5 nm film case. While $AuCl_3$ doping has minimal effect on the thinnest cell PCE, all other thicknesses show an improvement of at least 24 %, up to a maximum of 224 %, seen in this case in the thickest 56 nm cell. It is interesting to note that in the surfactant-assisted exfoliated G-Si Schottky junction cells presented in Chapter 4, $AuCl_3$ doping results in a stable increase in cell performance, while in this case the RGO-Si cell performance decreases to values below pre-doping levels. This is again consistent with CNT-Si and GO/CNT-Si cells, where it has been shown that introducing anti-reflective polymer coatings can reduce this instability [33].

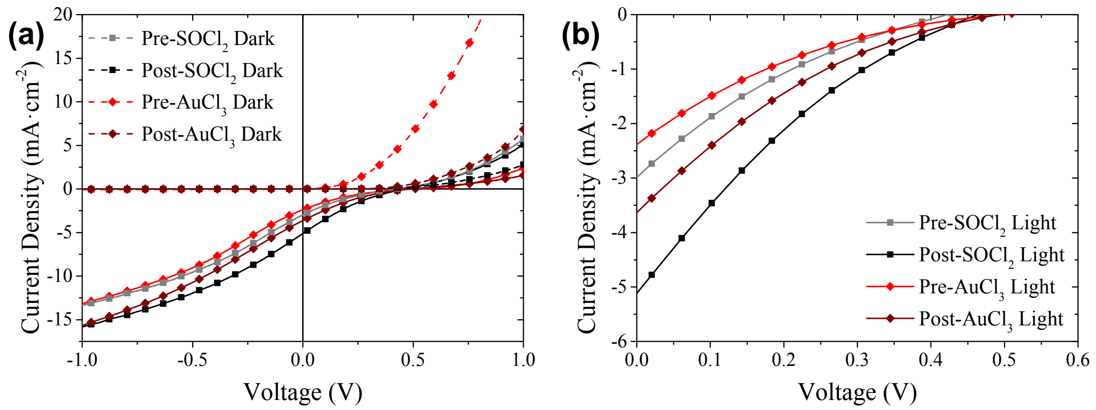

Figure 5.13: (a) Representative dark (dashed lines) and light (solid lines) J-V curves for both pre- and post- doped RGO-Si cells made with 7.5 nm ($SOCl_2$) and 56 nm ($AuCl_3$) films, and (b) the representative light J-V curves in the power quadrant only.

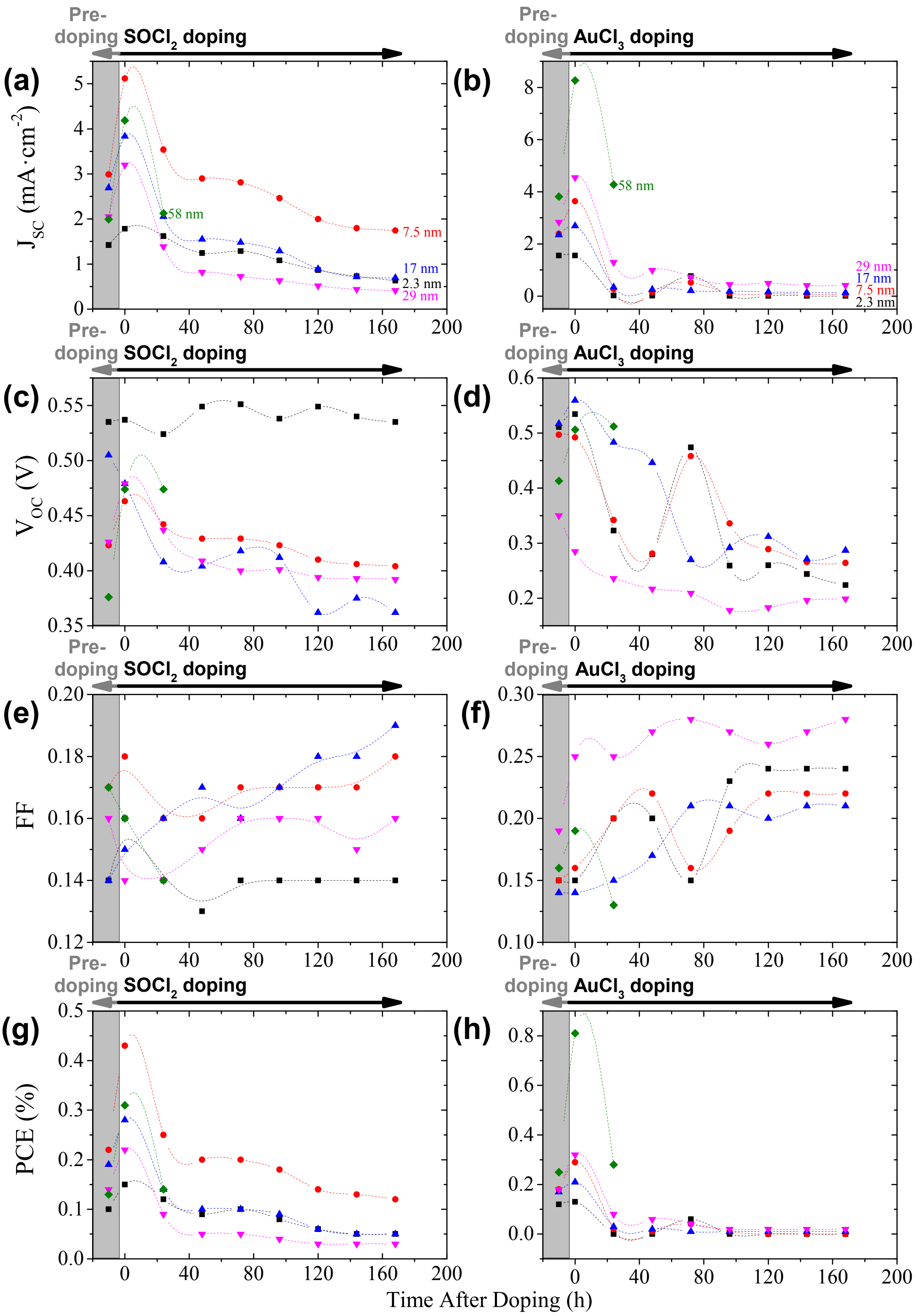

Figure 5.14: (a & b) J_{SC}, (c & d) V_{OC}, (e & f) FF and (g & h) PCE of RGO-Si cells of different film thicknesses annealed at 400 ºC both pre-doping (grey shaded areas) and post-doping with $SOCl_2$ and $AuCl_3$ with respectively (lines added to guide the eye).

The results presented here show that there still remains a number of important factors that must be considered when designing RGO-Si solar cells, but that they present a viable direction for further work. Annealing RGO-Si cells at 400 ºC produces the best J_{SC} and V_{OC} response to AM1.5G solar simulation conditions, but critically, only once a cell has been allowed to age. Once a proper aging condition has been satisfied, the thickness of the RGO layer can be further optimised. This is an important consideration, as this chapter shows that for raw solar cell PCE performance thicker films in fact perform better than thin film cells. Alternatively, thin films produced larger V_{OC}, which may be desirable in other fields such as photodetectors and gas sensing.

Furthermore, doping of these RGO-Si solar cells with common dopants has seen increases in PCE to yield PCE maxima of up to 0.4 % for $SOCl_2$ and 0.8 % for $AuCl_3$. This level of PCE performance is larger than previously reported undoped RGO-Si solar cells of 0.31 % [19], and is also close to the values reported for chemically doped surfactant-assisted exfoliated graphene-Si solar cells (maximum of 0.9%) described in Chapter 4. While these PCEs are low in the context of other architectures such as CVD graphene-Si solar cells or hybrid GO-Si heterojunctions, such as PEDOT:PSS:GO-GO-Si solar cells, there are a number of advantageous features that are promising for future work in the field. This chapter also only investigated the thermal reduction of GO, leaving open the potential for investigation of chemically reduced GO-Si cells, combining both thermal and chemical reduction techniques, and investigating plasma reduced GO. Further investigation can also explore other chemical dopants, such as nitric acid, and further optimisation of the doping methods themselves, along with combining these doping methods with encapsulation methods to seek to improve the longevity of the cells.

5.9 Performance Variability Between Batches

The previous sections of this chapter have shown that aqueous GO dispersions can be successfully used to create thin, scalable RGO films for use in RGO-Si solar cells with acceptable reproducibility between films and cells. However, one common problem faced when working with any nanoscale carbons with variable chemical and physical structure, such as carbon nanotubes, graphene flakes and graphene oxide, is the reproducibility between different batches of nominally the same material. Differences in production methods and starting materials can cause vast changes to the final composition of the material, and indeed, even seemingly small differences in methods, such as changing the type of filter used to filter GO films from aluminium oxide to Teflon, can result in a film which is either water stable or readily disintegrable [39]. This variability between different batches of GO was noticed when comparing preliminary research carried out on these RGO-Si solar cell systems. As such, the experiments detailed in Sections 5.3-5.8 were all conducted using the same batch of GO.

To investigate the effect that using different GO samples would have on the performance of the cells, three individually sourced bottles of nominally the same graphene ethanol dispersion detailed in Section 5.2.1 were used to prepare three different batches of aqueous graphene dispersions. The intent was to then characterise the physical properties of GO and RGO films of the same thickness made from these individual batches of GO as well as the performance of RGO-Si solar cells made using these films. To prepare the aqueous dispersions, a volumetric pipette was used to pipette 2 mL of each dispersion into pre-weighed bottles.

Table 5.2 shows that despite all three bottles being nominally 5 $mg \cdot mL^{-1}$, there was a range of 3.9 mg in the amount of GO between the three batches. In order to have a sufficient volume of aqueous dispersion, 10 mL of MilliQ water was used to make the three batches of aqueous GO dispersions, resulting in the concentrations seen in Table 5.2.

Table 5.2: Mass of GO left after evaporation of ethanol for each batch of GO and the resultant concentration of the aqueous GO dispersions.

Batch	**Mass (mg)**	**Concentration ($mg\cdot mL^{-1}$)**
1	3.8	0.38
2	5.9	0.59
3	7.7	0.77

The thickness of the films made from the aqueous dispersions can be controlled by varying the amount of dispersion filtered per unit area of the desired films, as discussed in Chapter 2 Section 2.1.1. However, the mass of GO being filtered will affect this value when the concentration of each batch is different. As such, the mass of the best performed films from Section 5.7 (58 nm thick) was calculated, and this value of 0.118 mg was set as a target mass for the films to be made from the three GO batches. Using this target mass and the concentrations for each batch of graphene, the initial amount of dispersion to filter for each batch was calculated, as seen in Table 5.3. However, upon filtering this target volume for each batch, visual examination of the filter papers revealed that the desired thickness of films had not been achieved. As such, subsequent aliquots of each batch were repeatedly filtered in an attempt to produce the desired thicknesses. While Batch 2 quickly appeared to reach the desired thickness, considerably more dispersion was required for Batch 1 and 3, despite Batch 3 having the highest concentration of the three dispersions.

Table 5.3: Target volume needed for filtering, actual volume filtered and actual mass filtered for each batch of graphene.

Batch	Target Volume (µL)	Actual Volume (µL)	Actual Mass (mg)
1	303	3624	1.38
2	195	975	0.58
3	149	4768	3.67

The resultant films for each batch were then deposited onto glass substrates following the procedure set out in Chapter 2 Section 2.1.1 and their UV-Vis transmittance at 550 nm and sheet resistance were investigated, as per Chapter 2 Section 2.1.5. Figure 5.15(a) shows the UV-Vis transmittance of the films, both pristine and after annealing at the optimal 400 ºC. Of note is that the mass of the film does not correlate with the optical thickness of the film, as would be expected (black series of Figure 5.15(a)). Indeed, the film with the largest mass of GO filtered, Batch 3, has the highest optical transmittance of all three batches. Upon annealing at 400 ºC the films undergo the expected decrease in transmittance (red series of Figure 5.15(a)). Comparison of the pristine and annealed transmittances with the target films transmittances discussed in Section 5.6, seen in Table 5.4, shows that Batch 1 and 2 have lower optical transmittances when pristine and annealed than the target film (58 nm), with Batch 3 having a slightly higher transmittance in both cases.

Figure 5.15(b) shows the sheet resistance of the films from all three batches both pristine (black series) and post-annealing (red series). Despite the differences in their optical transmittances, the sheet resistance of the films are within experimental error of each other, both in their pristine and post-annealed state. Comparison of these values with the target film's sheet resistance, also seen in Table 5.4, shows that despite the clear differences in mass and optical transmittance, the films all have the same sheet resistance, within experimental error, as the target film (58 nm).

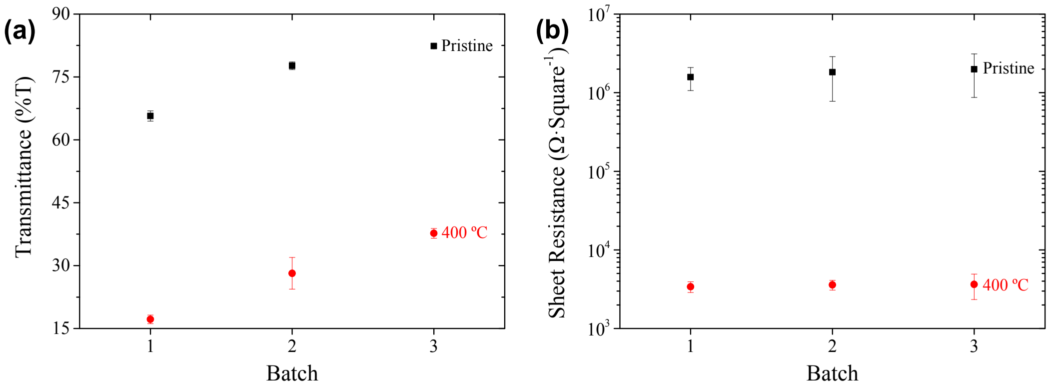

Figure 5.15: (a) UV-Vis transmittance of pristine GO and 400 ºC annealed RGO films made from three different batches of GO and (b) their corresponding sheet resistances.

Table 5.4: Table showing comparison of UV-Vis transmittance at 550 nm and sheet resistance of films made using three different batches of GO and the target film's properties.

State	Property	Batch 1	Batch 2	Batch 3	Target
Pristine	**Transmittance (%T)**	66 ± 1.2	78 ± 0.89	82 ± 0.33	80 ± 0.27
	Sheet Resistance ($\Omega\cdot$square^{-1})	$1.5 \pm 0.51 \times 10^{6}$	$1.8 \pm 1.0 \times 10^{6}$	$2.0 \pm 1.1 \times 10^{6}$	$9.6 \pm 5.3 \times 10^{5}$
Annealed	**Transmittance (%T)**	17 ± 1.0	28 ± 3.8	38 ± 1.1	35 ± 1.0
	Sheet Resistance ($\Omega\cdot$square^{-1})	$3.4 \pm 0.53 \times 10^{3}$	$3.6 \pm 0.51 \times 10^{3}$	$3.6 \pm 1.3 \times 10^{3}$	$3.9 \pm 0.035 \times 10^{3}$

Following the investigation of the optical transmittance and sheet resistance of these films, new films were produced to make RGO-Si solar cells for each batch of GO, with the representative dark and light J-V curves shown in Figure 5.16(a) with the light J-V curves shown in the power quadrant only in Figure 5.16(b) and the photovoltaic properties of the resultant cells displayed in Figure 5.17. It is immediately apparent from the representative J-V curves shown in Figure 5.16(a & b), as well as Figure 5.17, that despite their similar sheet resistances, the films exhibit vastly different short circuit current densities. Also of note, is that the trend in J_{SC} observed between the batches is the reverse of the trend observed in optical transmittance. That is, the films with the lowest optical transmittance have the highest J_{SC} and vice versa, with Batch 3 (blue series of Figure 5.16(b) and Figure 5.17) clearly exhibiting very poor photoresponse. Batch 1 (black series of Figure 5.16(b) and Figure 5.17) clearly shows the same aging behaviour observed in Sections 5.4 & 5.7, with Batch 2 (red series of Figure 5.16(b) and Figure 5.17) displaying similar, but less significant, behaviour with the performance of Batch 3 being so close to zero that any aging effect cannot be observed. This same behaviour is observed for both the V_{OC} (Figure 5.17(b)) and FF (Figure 5.17(c)) of the cells made from Batch 1 and 2, although for both of these properties the experimental error prohibits cross batch comparison. Figure 5.17(d) shows that when the overall PCE is considered, there is a clear difference between cells made with different batches, which follows the main trend observed in the J_{SC} of the cells.

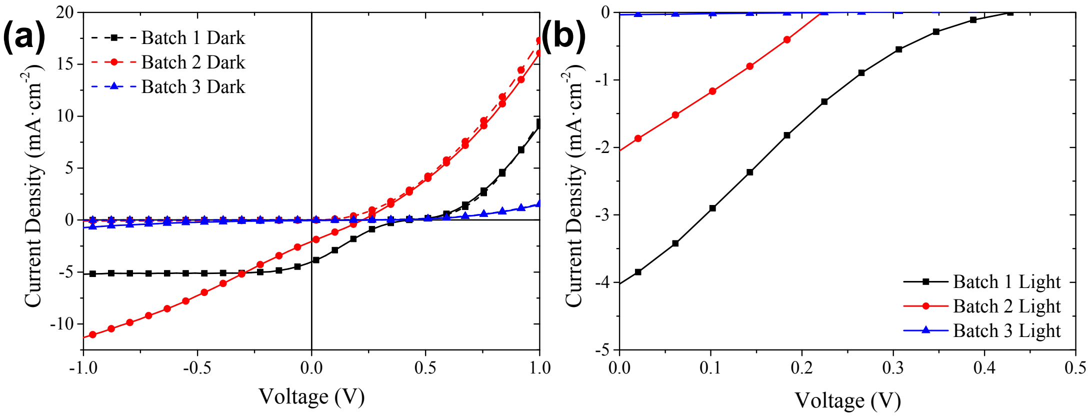

Figure 5.16: (a) Representative dark (dashed lines) and light (solid lines) J-V curves of RGO-Si solar cells made with films using three different batches of GO, aged to 72 h and (b) the representative light J-V curves in the power quadrant only.

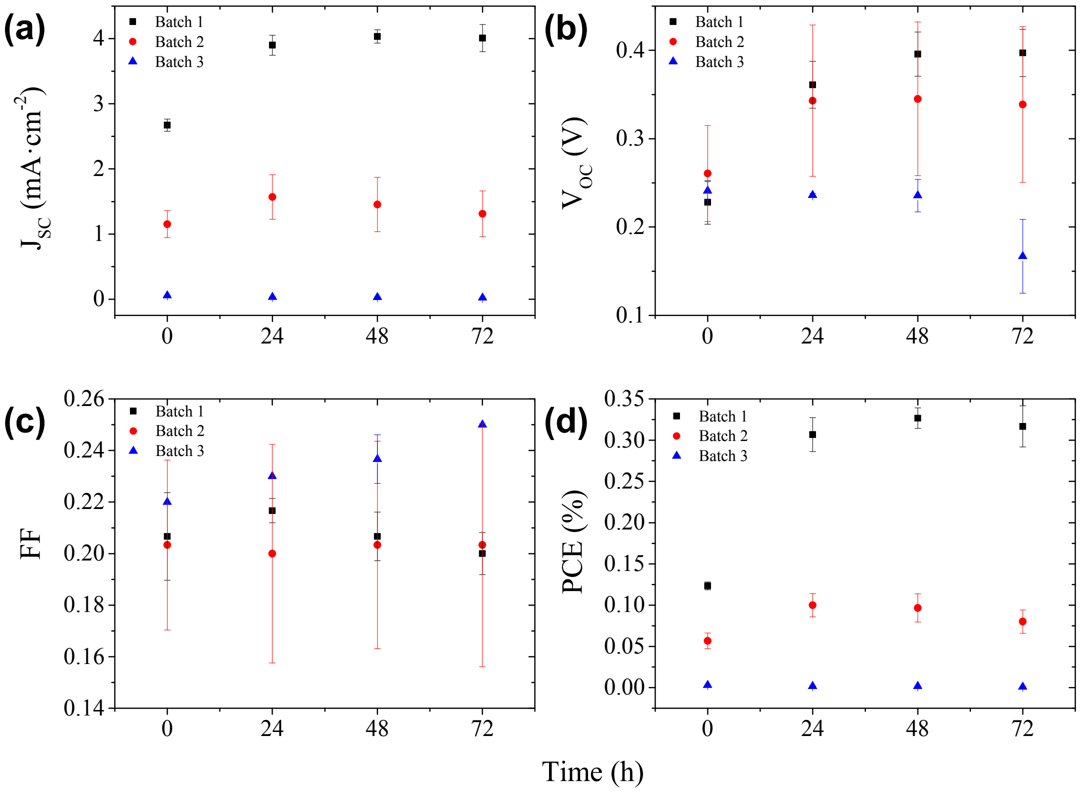

Figure 5.17: Summary of the photovoltaic properties of RGO-Si solar cells made with films using three different batches of GO showing the variation in (a) Jsc, (b) Voc, (c) FF and (d) PCE over time.

Comparison of the photovoltaic properties of the RGO-Si solar cells made with these three batches of GO with that of the target cell, as seen in Table 5.5, shows that cells made with films of each batch have reasonable reproducibility within their own data set, but there is considerable variability between cells made with films from different batches. Indeed, RGO-Si solar cells made with GO from Batch 1 actually show the highest undoped PCE observed within this chapter and are on par with the highest previously reported PCE of 0.31 % for undoped RGO-Si solar cells [19].

Table 5.5: Comparison of RGO-Si solar cell photovoltaic properties after 72 h made from films of different GO batches along with the target cell's properties after 72 h.

Property	Batch 1	Batch 2	Batch 3	Target
J_{SC} (mA·cm^{-2})	4.0 ± 0.21	1.3 ± 0.35	0.021 ± 0.0020	3.2 ± 0.62
V_{OC} (V)	0.40 ± 0.027	0.34 ± 0.088	0.17 ± 0.042	0.37 ± 0.068
FF	0.20 ± 0.0082	0.20 ± 0.047	0.25 ± 0.00	0.19 ± 0.037
PCE (%)	0.32 ± 0.021	0.08 ± 0.014	$(8.7 \pm 2.7) \times 10^{-4}$	0.22 ± 0.041

Lastly, the response of the RGO-Si solar cells made with films from different batches of GO to chemical doping was investigated, with Figure 5.19 showing the photovoltaic properties of the cells both pre- and post-doping with both $SOCl_2$, Figure 5.19(a, c, e & g) and $AuCl_3$, Figure 5.19(b, d, f & h). Representative J-V curves of these cells both pre-and immediately post-doping with $SOCl_2$ and $AuCl_3$ can be seen in Figure 5.18(a & b) respectively. Comparing the trends observed throughout Figure 5.19 for the Batch 1 and Batch 2 cell, with those seen in Figure 5.14, the effects of both $SOCl_2$ and $AuCl_3$ are broadly consistent, showing an initial improvement in PCE followed by eventual degradation. This is especially evident when observing the overall trend represented by the PCE of the cells after $SOCl_2$ (Figure 5.18(g)) and $AuCl_3$ (Figure 5.18(h)) doping. Also of interest is that despite initially having poor photovoltaic performance, when cells made with Batch 3 films were exposed to $SOCl_2$ and $AuCl_3$ their already poor V_{OC} and FF were reduced further. This again highlights the poor applicability of that particular batch of GO to photovoltaic applications.

These results suggest that although the RGO-Si solar cells discussed within this chapter can be optimised through control of the RGO film thickness, annealing temperatures and chemical doping, their future applicability may be limited if work is not also done to control the variability introduced when using GO from different sources.

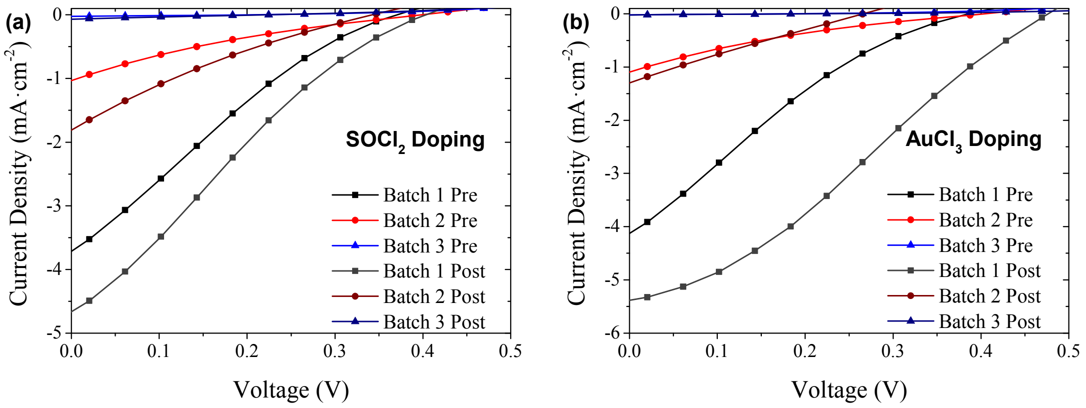

Figure 5.18: Representative J-V curves of RGO-Si solar cells made with films using three different batches of GO, both pre- and post-doping with (a) $SOCl_2$ and (b) $AuCl_3$.

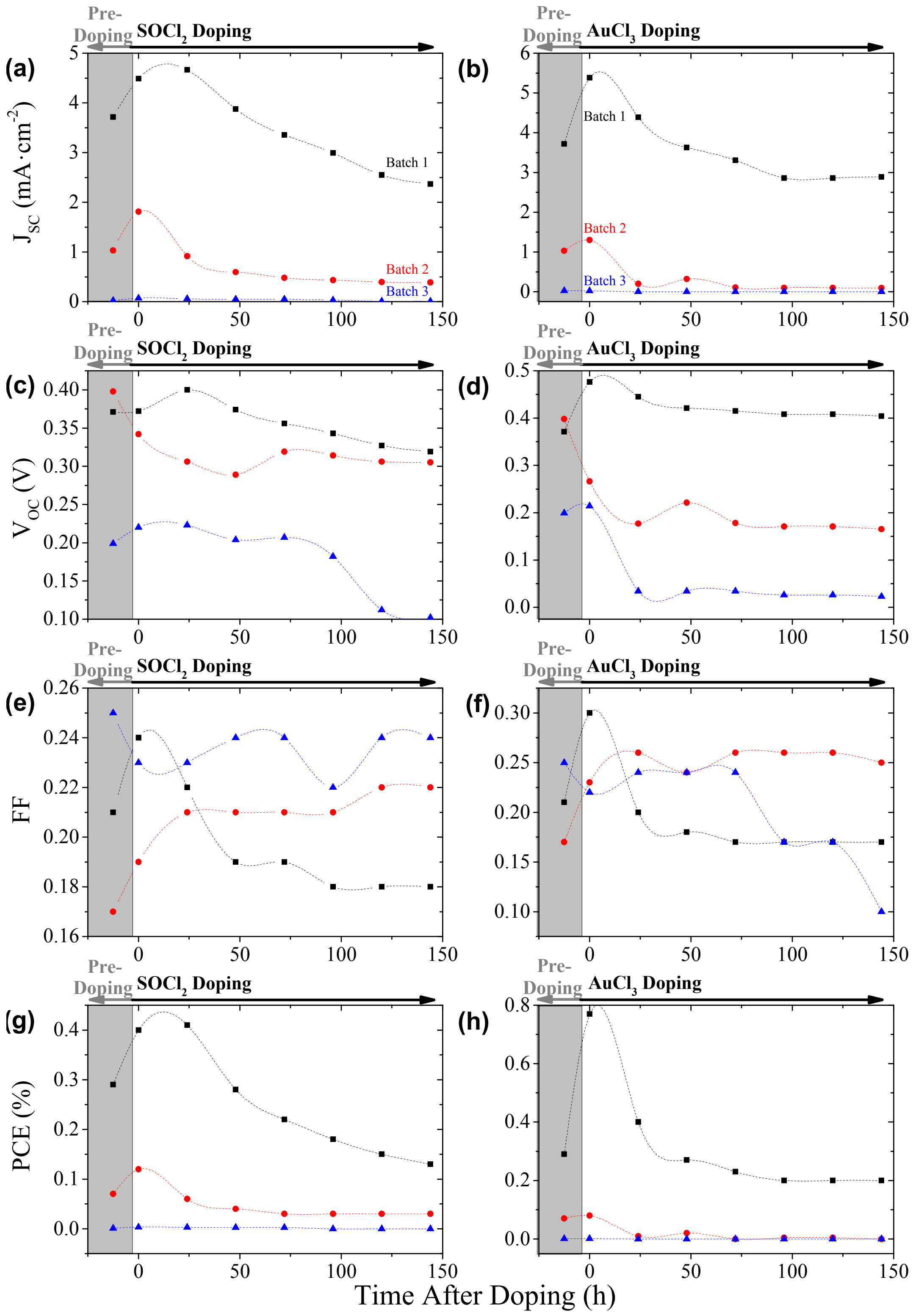

Figure 5.19: (a & b) J_{SC}, (c & d) V_{OC}, (e & f) FF and (g & h) PCE of RGO-Si cells made with three different batches of GO both pre-doping (grey shaded areas) and post-doping with $SOCl_2$ and $AuCl_3$ with respectively (lines added to guide the eye).

5.10 Conclusions

Scalable vacuum filtration methods were used to produce RGO-Si solar cells. Thermal reduction under a forming gas atmosphere at 400 ºC, with an optimal annealed film thickness of 56 nm were found to be the optimal conditions for RGO-Si solar cell performance. These cells were found to improve upon their initial performance after ambient storage and remain stable over time. Chemical doping with $SOCl_2$ was able to improve solar cell PCE from between 45 and 135 %, with $AuCl_3$ doping improving PCE from between 20 and 220 %. Maximum doped efficiencies reached as high as 0.8 %, close to three times higher than previously reported for undoped RGO-Si cells, and hence these cells show potential for further development.

However, significant variability was found when comparing RGO-Si cells made using different batches of GO from different sources. While the photovoltaic properties were found to be consistent within each set of cells, cross batch reproducibility was shown to be a significant issue.

Hence future work, while potentially focusing on the production and alternative reduction methods of GO, should also include investigations that aim to reduce variability in the RGO films and resultant RGO-Si solar cells made with them.

5.11 References

1. Tune, DD, Flavel, BS, Krupke, R & Shapter, JG 2012, 'Carbon nanotube-silicon solar cells', *Advanced Energy Materials*, vol. 2, no. 9, pp. 1043-55.

2. Ye, Y & Dai, L 2012, 'Graphene-based Schottky junction solar cells', *Journal of Materials Chemistry*, vol. 22, no. 46, pp. 24224-9.

3. Li, X, Zhu, H, Wang, K, Cao, A, Wei, J, Li, C, Jia, Y, Li, Z, Li, X & Wu, D 2010, 'Graphene-on-silicon Schottky junction solar cells', *Advanced Materials*, vol. 22, no. 25, pp. 2743-8.

4. Lotya, M, King, PJ, Khan, U, De, S & Coleman, JN 2010, 'High-concentration, surfactant-stabilized graphene dispersions', *ACS Nano*, vol. 4, no. 6, pp. 3155-62.

5. Guardia, L, Fernández-Merino, MJ, Paredes, JI, Solís-Fernández, P, Villar-Rodil, S, Martínez-Alonso, A & Tascón, JMD 2011, 'High-throughput production of pristine graphene in an aqueous dispersion assisted by non-ionic surfactants', *Carbon*, vol. 49, no. 5, pp. 1653-62.

6. Blake, P, Brimicombe, PD, Nair, RR, Booth, TJ, Jiang, D, Schedin, F, Ponomarenko, LA, Morozov, SV, Gleeson, HF, Hill, EW, Geim, AK & Novoselov, KS 2008, 'Graphene-based liquid crystal device', *Nano Letters*, vol. 8, no. 6, pp. 1704-8.

7. Hernandez, Y, Nicolosi, V, Lotya, M, Blighe, FM, Sun, Z, De, S, McGovern, IT, Holland, B, Byrne, M, Gun'Ko, YK, Boland, JJ, Niraj, P, Duesberg, G, Krishnamurthy, S, Goodhue, R, Hutchison, J, Scardaci, V, Ferrari, AC & Coleman, JN 2008, 'High-yield production of graphene by liquid-phase exfoliation of graphite', *Nature Nanotechnology*, vol. 3, no. 9, pp. 563-8.

8. Khan, U, Porwal, H, O'Neill, A, Nawaz, K, May, P & Coleman, JN 2011, 'Solvent-exfoliated graphene at extremely high concentration', *Langmuir*, vol. 27, no. 15, pp. 9077-82.

9. Paton, KR, Varrla, E, Backes, C, Smith, RJ, Khan, U, O'Neill, A, Boland, C, Lotya, M, Istrate, OM, King, P, Higgins, T, Barwich, S, May, P, Puczkarski, P, Ahmed, I, Moebius, M, Pettersson, H, Long, E, Coelho, J, O'Brien, SE, McGuire, EK, Sanchez, BM, Duesberg, GS, McEvoy, N, Pennycook, TJ, Downing, C, Crossley, A, Nicolosi, V & Coleman, JN 2014, 'Scalable production of large quantities of defect-free few-layer graphene by shear exfoliation in liquids', *Nature Materials*, vol. 13, no. 6, pp. 624-30.

10. Chen, X, Dobson, JF & Raston, CL 2012, 'Vortex fluidic exfoliation of graphite and boron nitride', *Chemical Communications*, vol. 48, no. 31, pp. 3703-5.

11. Hummers, WS & Offeman, RE 1958, 'Preparation of graphitic oxide', *Journal of the American Chemical Society*, vol. 80, no. 6, p. 1339.

12. Marcano, DC, Kosynkin, DV, Berlin, JM, Sinitskii, A, Sun, Z, Slesarev, A, Alemany, LB, Lu, W & Tour, JM 2010, 'Improved synthesis of graphene oxide', *ACS Nano*, vol. 4, no. 8, pp. 4806-14.

13. Hirata, M, Gotou, T, Horiuchi, S, Fujiwara, M & Ohba, M 2004, 'Thin-film particles of graphite oxide 1: High-yield synthesis and flexibility of the particles', *Carbon*, vol. 42, no. 14, pp. 2929-37.

14. Wu, Z-S, Ren, W, Gao, L, Liu, B, Jiang, C & Cheng, H-M 2009, 'Synthesis of high-quality graphene with a pre-determined number of layers', *Carbon*, vol. 47, no. 2, pp. 493-9.

15. Pei, S & Cheng, H-M 2012, 'The reduction of graphene oxide', *Carbon*, vol. 50, no. 9, pp. 3210-28.

16. Behura, SK, Nayak, S, Mukhopadhyay, I & Jani, O 2014, 'Junction characteristics of chemically-derived graphene/p-Si heterojunction solar cell', *Carbon*, vol. 67, pp. 766-74.

17. Kalita, G, Wakita, K, Umeno, M & Tanemura, M 2013, 'Fabrication and characteristics of solution-processed graphene oxide–silicon heterojunction', *physica status solidi (RRL)-Rapid Research Letters*, vol. 7, no. 5, pp. 340-3.

18. Phan, DT, Gupta, RK, Chung, GS, Al-Ghamdi, AA, Al-Hartomy, OA, El-Tantawy, F & Yakuphanoglu, F 2012, 'Photodiodes based on graphene oxide–silicon junctions', *Solar Energy*, vol. 86, no. 10, pp. 2961-6.

19. Zhu, M, Li, X, Guo, Y, Li, X, Sun, P, Zang, X, Wang, K, Zhong, M, Wu, D & Zhu, H 2014, 'Vertical junction photodetectors based on reduced graphene oxide/silicon Schottky diodes', *Nanoscale*, vol. 6, no. 9, pp. 4909-14.

20. Liu, Q, Wanatabe, F, Hoshino, A, Ishikawa, R, Gotou, T, Ueno, K & Shirai, H 2012, 'Crystalline silicon/graphene oxide hybrid junction solar cells', *Japanese Journal of Applied Physics*, vol. 51, no. 10S, p. 10NE22.

21. Khatri, I, Tang, Z, Hiate, T, Liu, Q, Ishikawa, R, Ueno, K & Shirai, H 2013, 'Optical and carrier transport properties of graphene oxide based crystalline-Si/organic Schottky junction solar cells', *Journal of Applied Physics*, vol. 114, no. 23, p. 234506.

22. Yu, L, Tune, D, Shearer, C & Shapter, J 2015, 'Heterojunction solar cells based on silicon and composite films of graphene oxide and carbon nanotubes', *ChemSusChem*, vol. 8, no. 17, pp. 2940-7.

23. Liu, X, Zhang, XW, Yin, ZG, Meng, JH, Gao, HL, Zhang, LQ, Zhao, YJ & Wang, HL 2014, 'Enhanced efficiency of graphene-silicon Schottky junction solar cells by doping with Au nanoparticles', *Applied Physics Letters*, vol. 105, no. 18, p. 183901.

24. Liu, X, Zhang, XW, Meng, JH, Yin, ZG, Zhang, LQ, Wang, HL & Wu, JL 2015, 'High efficiency Schottky junction solar cells by co-doping of graphene with gold nanoparticles and nitric acid', *Applied Physics Letters*, vol. 106, no. 23, p. 233901.

25. Miao, X, Tongay, S, Petterson, MK, Berke, K, Rinzler, AG, Appleton, BR & Hebard, AF 2012, 'High efficiency graphene solar cells by chemical doping', *Nano Letters*, vol. 12, no. 6, pp. 2745-50.

26. Li, X, Xie, D, Park, H, Zhu, M, Zeng, TH, Wang, K, Wei, J, Wu, D, Kong, J & Zhu, H 2013, 'Ion doping of graphene for high-efficiency heterojunction solar cells', *Nanoscale*, vol. 5, pp. 1945-8.

27. Cui, T, Lv, R, Huang, Z-H, Chen, S, Zhang, Z, Gan, X, Jia, Y, Li, X, Wang, K & Wu, D 2013, 'Enhanced efficiency of graphene/silicon heterojunction solar cells by molecular doping', *Journal of Materials Chemistry A*, vol. 1, no. 18, pp. 5736-40.

28. Jung, I, Vaupel, M, Pelton, M, Piner, R, Dikin, DA, Stankovich, S, An, J & Ruoff, RS 2008, 'Characterization of thermally reduced graphene oxide by imaging ellipsometry', *The Journal of Physical Chemistry C*, vol. 112, no. 23, pp. 8499-506.

29. Jeong, H-K, Lee, YP, Jin, MH, Kim, ES, Bae, JJ & Lee, YH 2009, 'Thermal stability of graphite oxide', *Chemical Physics Letters*, vol. 470, no. 4–6, pp. 255-8.

30. Mattevi, C, Eda, G, Agnoli, S, Miller, S, Mkhoyan, KA, Celik, O, Mastrogiovanni, D, Granozzi, G, Garfunkel, E & Chhowalla, M 2009, 'Evolution of electrical, chemical, and structural properties of transparent and conducting chemically derived graphene thin films', *Advanced Functional Materials*, vol. 19, no. 16, pp. 2577-83.

31. Shi, Y, Kim, KK, Reina, A, Hofmann, M, Li, L-J & Kong, J 2010, 'Work function engineering of graphene electrode via chemical doping', *ACS Nano*, vol. 4, no. 5, pp. 2689-94.

32. Eda, G, Lin, Y-Y, Miller, S, Chen, C-W, Su, W-F & Chhowalla, M 2008, 'Transparent and conducting electrodes for organic electronics from reduced graphene oxide', *Applied Physics Letters*, vol. 92, no. 23, p. 233305.

33. Yu, L, Tune, DD, Shearer, CJ & Shapter, JG 2015, 'Implementation of antireflection layers for improved efficiency of carbon nanotube–silicon heterojunction solar cells', *Solar Energy*, vol. 118, no. 0, pp. 592-9.

34. Song, Y, Li, X, Mackin, C, Zhang, X, Fang, W, Palacios, T, Zhu, H & Kong, J 2015, 'Role of interfacial oxide in high-efficiency graphene–silicon Schottky barrier solar cells', *Nano Letters*, vol. 15, no. 3, pp. 2104-10.

35. Yu, L, Tune, DD, Shearer, CJ & Shapter, JG 2015, 'Application of polymer interlayers in silicon–carbon nanotube heterojunction solar cells', *ChemNanoMat*, vol. 1, no. 2, pp. 115-21.

36. Stankovich, S, Dikin, DA, Piner, RD, Kohlhaas, KA, Kleinhammes, A, Jia, Y, Wu, Y, Nguyen, ST & Ruoff, RS 2007, 'Synthesis of graphene-based nanosheets via chemical reduction of exfoliated graphite oxide', *Carbon*, vol. 45, no. 7, pp. 1558-65.

37. Becerril, HA, Mao, J, Liu, Z, Stoltenberg, RM, Bao, Z & Chen, Y 2008, 'Evaluation of solution-processed reduced graphene oxide films as transparent conductors', *ACS Nano*, vol. 2, no. 3, pp. 463-70.

38. Eda, G, Fanchini, G & Chhowalla, M 2008, 'Large-area ultrathin films of reduced graphene oxide as a transparent and flexible electronic material', *Nature Nanotechnology*, vol. 3, no. 5, pp. 270-4.

39. Yeh, C-N, Raidongia, K, Shao, J, Yang, Q-H & Huang, J 2015, 'On the origin of the stability of graphene oxide membranes in water', *Nature Chemistry*, vol. 7, no. 2, pp. 166-70.

Chapter 6

Conclusions

6.1 Conclusions

The application of solution processed nanocarbon-based materials in a number of photovoltaic systems was investigated and the performance of these systems optimised. This included the sensitisation of vertically aligned arrays of SWNTs as a replacement working electrode in a DSC design, the use of surfactant-assisted exfoliated graphene in G-Si Schottky junction solar cells and the use of RGO in RGO-Si solar cells.

Vertically aligned arrays of photoactive SWNTs were chemically attached to FTO substrates. These arrays were then sensitised by the addition of a spin coated layer of TIPS-DBC, creating a new working electrode for use in DSC-like photoelectrochemical cells. The addition of TIPS-DBC to the working electrode resulted in significant enhancements to both the J_{SC} and V_{OC} of the solar cells, due to the photoresponse of TIPS-DBC. It was found that the J_{SC} and V_{OC} of the subsequent cells, and thus PCE, could be tuned by controlling the concentration of TIPS-DBC solution used to deposit the TIPS-DBC layer, as well as controlling the spin speed used during the deposition. The optimal working electrode was found to occur when a 30 $mg \cdot mL^{-1}$ TIPS-DBC solution was deposited at a spin speed of 2000 rpm. Using these optimised conditions, the maximum J_{SC} was found to be (68 ± 3) $\mu A \cdot cm^{-2}$, four times higher than the previous maximum achieved by similar SWNT working electrode cells (16.4 $\mu A \cdot cm^{-2}$ from Bissett et al. [1]) and the maximum V_{OC} was found to be (98 ± 2) mV, two times higher than the previous maximum (47 mV from Tune et al. [2]). Despite the low maximum PCE (~0.002%) achieved in this work, the improvements here represented the best improvements seen in these cell designs, with a thirty fold increase in PCE when compared to untreated SWNT electrodes.

The exfoliation of graphite in aqueous dispersions of Tween-60 was investigated and found to produce FLG. These dispersions could be vacuum filtered to make conductive films with highly reproducible transparencies and sheet resistances. These films were found to form in two different regimes, a thin regime, consisting of non-continuous flake coverage and exposed substrate and a thick regime, consisting of continuous films with thicknesses on the order of hundreds of nanometres. G-Si Schottky junction solar cells were made with these solution processed films for the first time and were found to be highly durable, sustaining repeated testing over a period of 966 h, while also being quite responsive to the growth of an oxide layer at the G-Si interface. G-Si Schottky junction solar cells made with films of differing thicknesses revealed that there was both a thin film regime maximum PCE (0.05 % at 60 %T) and a thick film regime maximum PCE (0.06 % at 23 %T). Thermal annealing of solar cells made with these 23 %T graphene films doubled cell PCE (0.13 %). Solar cells made with either pristine or annealed thick films responded well to chemical doping with both HNO_3 and $AuCl_3$ doping significantly improving cell J_{SC} and hence PCE. Pristine cells achieved maximum PCEs of up to 0.5 % with HNO_3 doping and 0.4 % with gold chloride doping, with $AuCl_3$ doping found to be surprisingly stable over a 96 h period. A maximum PCE of 0.9 % was achieved by HNO_3 doping an annealed 23 %T cell, while $AuCl_3$ doping of annealed 23 %T cells appeared to be less effective than with pristine cells, achieving a maximum 0.3 %, with this effect less stable than the pristine cells.

Aqueous dispersions of GO were prepared and used to form thin GO films via vacuum filtration. These films were then deposited onto silicon substrates and annealed at a range of temperatures under forming gas, from 150 ºC to 400 ºC to form RGO-Si Schottky junction solar cells. Increasing annealing temperatures initially resulted in increased J_{SC}s but decreased V_{OC}s. However, a novel effect was seen after aging of the cells annealed at temperatures of 300 ºC and 400 ºC, with these cells subsequently showing a significant improvement in both J_{SC} and V_{OC} and thus PCE. In contrast to G-Si Schottky junction solar cells, 400 ºC annealed RGO-Si cells responded positively to $SOCl_2$ doping, seeing improvements in both J_{SC} and V_{OC}, while also seeing similar improvements upon $AuCl_3$ doping. In contrast to the G-Si system however, both of these effects were short lived, with cells returning to performance levels similar to their initial testing 24 h after doping. After investigation of annealing temperature, the effect RGO film thickness was investigated, with two distinct thickness regimes again observed. The performance of all but the thinnest films measured were within error of each other, while the four thicker films all displayed the same improvement in PCE seen previously with the initial 400 ºC annealed films. The performance of cells of all thicknesses was improved after chemical doping with $SOCl_2$ and $AuCl_3$, driven mainly by increases in cell J_{SC}. A maximum PCE of 0.4 % was observed with $SOCl_2$ doping, with 0.8 % for $AuCl_3$. Although these were of similar performance levels to the G-Si Schottky junction solar cells, and considerably larger than previously reported un-doped RGO-Si solar cells

(0.31 % by Zhu et al. [3]) they were again short lived, with cells returning to their pre-doped levels within 24 h and reaching even lower levels after 168 h.

6.2 Future Directions

The research presented in this Thesis presents numerous avenues for future research.

Although the optimisation of TIPS-DBC/SWNT/FTO electrodes presented in this Thesis was impressive when compared to previous attempts, the PCE of these cells, at just 0.002 %, still remains much too low to present viable commercial prospects. This low PCE is due to a number of issues, including the amount of SWNTs present on the electrode, and the large number of electron-hole recombination and shorting events this presents. It may be tempting to think that other solution processing deposition methods, such as vacuum film filtration and electrophoretic deposition, or direct CVD growth of CNTs would help to reduce these issues. However, as mentioned in Chapter 1 Section 1.6.5, previous work by with electrophoretically deposited SWNTs also show very low conversion efficiencies [4], as do their porphyrin sensitised counterparts [5]. Likewise, Bissett et al. [1] have shown chemically attached SWNT arrays outperform CVD SWNT arrays, and indeed CVD growth of CNTs requires temperatures too high for TCO substrates as well as flexible substrates.

While these TIPS-DBC/SWNT/FTO electrodes could potentially find use as cheap photodetectors, especially for detection in the 450 – 550 nm range, the real potential for SWNTs, and CNTs in general, within DSC systems appears to be either as an additive for the mesoporous TiO_2 layer, as a catalytic layer in the CE [6, 7] or as a TCO replacement in either electrode [8, 9]. Indeed, CNTs as an additive in the mesoporous TiO_2 layer have already seen PCEs of 10 % achieved [10, 11]. These achievements however were all reported in the early parts of this decade, and PCE enhancements in this area appear to have stalled in recent years. This mimics PCE enhancement in the DSC field itself, with the last independently verified record PCE of 11.9 % also achieved in 2012 [12] and an unverified record PCE of 14.3 % achieved in 2015 [13].

This lack of progress may well be due to the scientific community's new found interest in perovskite solar cells, a solid-state descendent of the DSC [14, 15]. These cells use a perovskite material as a replacement for the conventional dyes used in DSCs and separated holes are transported to the CE via hole transport layers, rather than liquid electrolytes. This design would allow for the use of CNTs in the hole transport layer and counter electrode, and again as potential candidates for systems that help to replace the TCO layer of the working electrode [16]. In all of these instances, the ability to use solution-processed CNTs, or indeed nanocarbon-based materials in general, would help to improve the energy efficiency of these systems, as well as improving new avenues for fabrication, such as their production on flexible substrates [17].

With a maximum PCE of 0.9 % achieved after HNO_3 doping, and a stabilised PCE of 0.4 % after $AuCl_3$ doping, the solution processed G-Si Schottky junction solar cells presented in this Thesis show good promise. The initial report of a CVD G-Si Schottky junction produced a PCE of 1.65 % [18], albeit with pristine conditioning. Since 2010, the maximum PCE of CVD G-Si cells has risen due to improvements in design such as native oxide growth and anti-reflection layers, as well chemical doping, with a maximum PCE of 15.6 % recorded in 2015 [19]. While solution processed G-Si Schottky junction solar cells may not reach PCE levels this high, the potential scope of their improvement is easy to see.

No attempts were made within this research to optimise the nature of the graphene dispersions obtained using Tween-60. Indeed, it is highly likely that the quality of the graphene dispersion could be improved with regards to flake size and thickness, and this could potentially lead to improvements in film conductivity and hence photocurrent collection. Photocurrent collection would be further improved in this scenario as films made with graphene flakes with few layers will also be more transparent, allowing more photons to the G-Si interface and hence the creation of more photogenerated excitons. Reducing the number of layers in the graphene flakes could also allow for more uniform and stronger doping to occur throughout the individual flakes and the film itself, allowing for stronger n-Si band bending and subsequently, potential improvements in V_{OC} of the cells, leading to improved separation of photogenerated excitons. For example, DGU has been shown to separate sodium cholate surfactant-exfoliated graphene into fractions containing graphene flakes one to three layers thick [20]. This process could allow for a systematic investigation of flake thickness versus photovoltaic performance in solution-processed G-Si Schottky junctions. However, it has been shown by Lotya et al. [21] that increasing the spin speed of centrifugation reduces the length of sodium cholate surfactant-assisted exfoliated graphene flakes. Alternatively, increasing the ultrasonication time used when creating the graphene dispersion with a low powered ultrasonicator can effectively reduce flake thickness while maintaining larger flake lengths [21]. The Tween-60 surfactant-assisted exfoliated graphene used within this Thesis was ultrasonicated for 2 h and thus extending the ultrasonication time in line with Lotya et al. [21] (approximately 200 h) could allow for thinner flakes while maintaining the larger flake sizes necessary to reduce the total number of flake-flake interactions charge carriers experience while travelling through thin films.

Furthermore, the addition of an anti-reflection layer is another obvious route for improving the performance of these cells. While deposition of colloidal TiO_2 systems has been popular in the CVD G-Si community [19, 22], polymeric anti-reflection layers seen in CNT-Si heterojunction solar cells would present another good option [23]. Another potential improvement could come in the form of either hole-transporting anti-reflection layers or carrier doping antireflection layers, as seen in the application of molybdenum oxide layers in CNT-Si heterojunctions [24]. This would be particularly useful in the case of solution processed G-Si Schottky junction solar cells, as if holes were injected into a hole-transporting layer, they would be transported much more efficiently to the front electrode than if they were still forced to percolate through individual graphene flakes throughout the film. Another less common technique that has been applied in CVD G-Si systems is the "self-healing" of cracks in CVD graphene with gold nanoparticles [25] before subsequent cell completion and chemical doping. Here the gold nanoparticles effectively fill in the cracks present in the graphene, enhancing its conductivity. This process may also work in solution processed graphene films, due to the large number of "cracks" available at flake-flake interfaces.

Finally, the presence of a thin insulating oxide layer at the G-Si interface was shown here to be beneficial for cell performance in solution processed G-Si Schottky junction solar cells. This layer helps in a similar fashion to MIS cells. With this in mind, the introduction of very thin insulators may also help further improve cell performance. This could possibly be achieved by the addition of a very thin layer of GO, shown to be quite possible in Chapter 5, to the bare n-Si interface before application of the graphene film. This has previously been shown to be an effective method in RGO-Si solar cell systems [26]. One caveat to the application of this GO layer however, would be that cell annealing may interfere with the performance of the cell by reducing the GO. The G-Si cells in this work were annealed at 250 °C, the limit at which GO reduction will start to take place. As such, there would need to be careful investigation as to the effect that this annealing would have on cell performance, if the

GO layer was indeed beneficial. Alternatively, this method may work better with cells produced from graphene dispersions with lower amounts of, or no, surfactant, or with films treated with acidic rinsing to help reduce surfactant content prior to their application to the cell.

Although short-lived, the maximum PCE of 0.8 % achieved via chemical doping of RGO-Si solar cells, when compared with previous "pristine" values of 0.3 % again shows there is good scope for their future development. One of the main areas for improvement is the reduction method used to produce the RGO, with thermal annealing at the low temperatures used within this Thesis known to not be the most beneficial in terms of subsequent RGO film properties. Now that these systems have been shown to be viable with this technique however, more reduction techniques can be employed, including for example chemical reduction such as that achieved via hydrazine treatment, further heat treatment after chemical reduction or plasma assisted reduction [27]. It would also be of interest to investigate more "green" reduction methods [28], such as the vitamin C approach mentioned in Chapter 1 Section 1.4.4, as hydrazine for example is not an environmentally friendly chemical treatment and reducing the need for elevated temperatures in the range of 400 °C would further help the energy efficiency of the production techniques used.

Owing to their shared architecture with G-Si Schottky junction solar cells, RGO-Si solar cells would also potentially greatly benefit from the application of anti-reflection layers and or hole transporting layers to help increase photocurrent generation and collection.

Even though the solution processed carbon deposition methods used throughout this Thesis have a low energy cost, the design of the solar cells themselves still contain a number of issues. The DSC-like SWNT cells from Chapter 3, use FTO coated electrodes, with many DSC and perovskite designs using ITO electrodes as well. FTO and ITO layer performances both suffer when deposited on flexible substrates, and ITO contains the rare element indium, the availability and pricing of which is becoming a concern for a number of industries [29]. The G-Si and RGO-Si solar cells made in Chapter 4 and Chapter 5 respectively use silicon substrates and gold front electrodes. The production of n-doped silicon substrates is itself an energetically expensive process and the use of expensive rare elements like gold for front electrodes will not help uptake and mass production of these types of cells.

One of the best ways to overcome these problems would be the development of all-carbon solar cells, based solely on solution processed materials. Some work already exists in this area with CNT-C_{60} heterojunction solar cells, for example, showing promising performances [30-32] and Tune and Shapter [33] demonstrating the potential of photovoltaic cells in which SWNTs are the only photoactive material. Ultimately, these cells would be produced using solution processed nanocarbon-based materials as the photoactive material, sandwiched between two electrodes also produced using less expensive materials. These could include nanocarbon-based material films for contact electrodes, and transparent conducting nanocarbon-based material films deposited onto flexible substrates, examples of which already exist within the literature [34]. While it is possible that these types of cell designs may not rival the top efficiencies produced by traditional silicon based cells, or new up and coming designs like perovskite solar cells, their cheap production and flexibility, and hence wearable nature, could allow for a paradigm shift to personal portable power production, reducing people's reliance on the grid during their daily activities.

This Thesis does however present one roadblock in the eventual success of the all-carbon cell described in the previous paragraph, viz. the issues of nanocarbon-based material batch to batch reproducibility discussed in Chapter 5 Section 5.9. While the performance of cells made with the same nanocarbon-based material solution can show good reproducibility, the reproducibility between cells made with different batches of nanocarbon-based material solution can vary substantially. This issue is not unique to GO dispersions, with the same issues faced when making new graphene or CNT dispersions as well. This is a major problem facing any solution processing approach when attempting to scale it up to industrial scale production. As such, efforts should be made by the scientific community to investigate, and report, the reproducibility of their results both within batches of cells made at the same time, and at other times with other materials that are nominally the same. This would ideally happen in conjunction with investigations looking at the ability to consistently reproduce dispersions of nanocarbon-based materials.

While this will require a lot of further work and investigation, it appears that there is still much progress to be made from photovoltaic systems produced with solution processed nanocarbon-based materials and that this work is indeed warranted.

6.3 References

1. Bissett, M, Barlow, A, Shearer, C, Quinton, J & Shapter, JG 2012, 'Comparison of carbon nanotube modified electrodes for photovoltaic devices', *Carbon*, vol. 50, no. 7, pp. 2431-41.

2. Tune, DD, Flavel, BS, Quinton, JS, Ellis, AV & Shapter, JG 2010, 'Single walled carbon nanotube network electrodes for dye solar cells', *Solar Energy Materials and Solar Cells*, vol. 94, no. 10, pp. 1665-72.

3. Zhu, M, Li, X, Guo, Y, Li, X, Sun, P, Zang, X, Wang, K, Zhong, M, Wu, D & Zhu, H 2014, 'Vertical junction photodetectors based on reduced graphene oxide/silicon Schottky diodes', *Nanoscale*, vol. 6, no. 9, pp. 4909-14.

4. Barazzouk, S, Hotchandani, S, Vinodgopal, K & Kamat, PV 2004, 'Single-wall carbon nanotube films for photocurrent generation. A prompt response to visible-light irradiation', *The Journal of Physical Chemistry B*, vol. 108, no. 44, pp. 17015-8.

5. Umeyama, T, Fujita, M, Tezuka, N, Kadota, N, Matano, Y, Yoshida, K, Isoda, S & Imahori, H 2007, 'Electrophoretic deposition of single-walled carbon nanotubes covalently modified with bulky porphyrins on nanostructured SnO_2 electrodes for photoelectrochemical devices', *The Journal of Physical Chemistry C*, vol. 111, no. 30, pp. 11484-93.

6. Ramasamy, E, Lee, WJ, Lee, DY & Song, JS 2008, 'Spray coated multi-wall carbon nanotube counter electrode for tri-iodide reduction in dye-sensitized solar cells', *Electrochemistry Communications*, vol. 10, no. 7, pp. 1087-9.

7. Lee, WJ, Ramasamy, E, Lee, DY & Song, JS 2009, 'Efficient dye-sensitized solar cells with catalytic multiwall carbon nanotube counter electrodes', *ACS Applied Materials & Interfaces*, vol. 1, no. 6, pp. 1145-9.

8. Liu, C-T, Wang, Y-C, Dong, R-X, Wang, C-C, Huang, K-C, Vittal, R, Ho, K-C & Lin, J-J 2012, 'A dual-functional Pt/CNT TCO-free counter electrode for dye-sensitized solar cell', *Journal of Materials Chemistry*, vol. 22, no. 48, pp. 25311-5.

9. Kyaw, AKK, Tantang, H, Wu, T, Ke, L, Peh, C, Huang, ZH, Zeng, XT, Demir, HV, Zhang, Q & Sun, XW 2011, 'Dye-sensitized solar cell with a titanium-oxide-modified carbon nanotube transparent electrode', *Applied Physics Letters*, vol. 99, no. 2, p. 021107.

10. Sawatsuk, T, Chindaduang, A, Sae-kung, C, Pratontep, S & Tumcharern, G 2009, 'Dye-sensitized solar cells based on TiO_2–MWCNTs composite electrodes: Performance improvement and their mechanisms', *Diamond and Related Materials*, vol. 18, no. 2–3, pp. 524-7.

11. Dang, X, Yi, H, Ham, M-H, Qi, J, Yun, DS, Ladewski, R, Strano, MS, Hammond, PT & Belcher, AM 2011, 'Virus-templated self-assembled single-walled carbon nanotubes for highly efficient electron collection in photovoltaic devices', *Nature Nanotechnology*, vol. 6, no. 6, pp. 377-84.

12. Green, MA, Emery, K, Hishikawa, Y, Warta, W & Dunlop, ED 2016, 'Solar cell efficiency tables (version 47)', *Progress in Photovoltaics: Research and Applications*, vol. 24, no. 1, pp. 3-11.

13. Kakiage, K, Aoyama, Y, Yano, T, Oya, K, Fujisawa, J-i & Hanaya, M 2015, 'Highly-efficient dye-sensitized solar cells with collaborative sensitization by silyl-anchor and carboxy-anchor dyes', *Chemical Communications*, vol. 51, no. 88, pp. 15894-7.

14. Kojima, A, Teshima, K, Shirai, Y & Miyasaka, T 2009, 'Organometal halide perovskites as visible-light sensitizers for photovoltaic cells', *Journal of the American Chemical Society*, vol. 131, no. 17, pp. 6050-1.

15. Heo, JH, Im, SH, Noh, JH, Mandal, TN, Lim, C-S, Chang, JA, Lee, YH, Kim, H-j, Sarkar, A, NazeeruddinMd, K, Gratzel, M & Seok, SI 2013, 'Efficient inorganic-organic hybrid heterojunction solar cells containing perovskite compound and polymeric hole conductors', *Nature Photonics*, vol. 7, no. 6, pp. 486-91.

16. Batmunkh, M, Shearer, CJ, Biggs, MJ & Shapter, JG 2015, 'Nanocarbons for mesoscopic perovskite solar cells', *Journal of Materials Chemistry A*, vol. 3, no. 17, pp. 9020-31.

17. Roldan-Carmona, C, Malinkiewicz, O, Soriano, A, Minguez Espallargas, G, Garcia, A, Reinecke, P, Kroyer, T, Dar, MI, Nazeeruddin, MK & Bolink, HJ 2014, 'Flexible high efficiency perovskite solar cells', *Energy & Environmental Science*, vol. 7, no. 3, pp. 994-7.

18. Li, X, Zhu, H, Wang, K, Cao, A, Wei, J, Li, C, Jia, Y, Li, Z, Li, X & Wu, D 2010, 'Graphene-on-silicon Schottky junction solar cells', *Advanced Materials*, vol. 22, no. 25, pp. 2743-8.

19. Song, Y, Li, X, Mackin, C, Zhang, X, Fang, W, Palacios, T, Zhu, H & Kong, J 2015, 'Role of interfacial oxide in high-efficiency graphene–silicon Schottky barrier solar cells', *Nano Letters*, vol. 15, no. 3, pp. 2104-10.

20. Green, AA & Hersam, MC 2009, 'Solution phase production of graphene with controlled thickness via density differentiation', *Nano Letters*, vol. 9, no. 12, pp. 4031-6.

21. Lotya, M, King, PJ, Khan, U, De, S & Coleman, JN 2010, 'High-concentration, surfactant-stabilized graphene dispersions', *ACS Nano*, vol. 4, no. 6, pp. 3155-62.

22. Shi, E, Li, H, Yang, L, Zhang, L, Li, Z, Li, P, Shang, Y, Wu, S, Li, X, Wei, J, Wang, K, Zhu, H, Wu, D, Fang, Y & Cao, A 2013, 'Colloidal antireflection coating improves graphene–silicon solar cells', *Nano Letters*, vol. 13, no. 4, pp. 1776-81.

23. Yu, L, Tune, DD, Shearer, CJ & Shapter, JG 2015, 'Implementation of antireflection layers for improved efficiency of carbon nanotube–silicon heterojunction solar cells', *Solar Energy*, vol. 118, no. 0, pp. 592-9.

24. Wang, F, Kozawa, D, Miyauchi, Y, Hiraoka, K, Mouri, S, Ohno, Y & Matsuda, K 2015, 'Considerably improved photovoltaic performance of carbon nanotube-based solar cells using metal oxide layers', *Nature Communications*, vol. 6, p. 6305.

25. Ho, P-H, Liou, Y-T, Chuang, C-H, Lin, S-W, Tseng, C-Y, Wang, D-Y, Chen, C-C, Hung, W-Y, Wen, C-Y & Chen, C-W 2015, 'Self-crack-filled graphene films by metallic nanoparticles for high-performance graphene heterojunction solar cells', *Advanced Materials*, vol. 27, no. 10, pp. 1724-9.

26. Liu, Q, Wanatabe, F, Hoshino, A, Ishikawa, R, Gotou, T, Ueno, K & Shirai, H 2012, 'Crystalline silicon/graphene oxide hybrid junction solar cells', *Japanese Journal of Applied Physics*, vol. 51, no. 10S, p. 10NE22.

27. Eigler, S, Grimm, S, Enzelberger-Heim, M, Muller, P & Hirsch, A 2013, 'Graphene oxide: Efficiency of reducing agents', *Chemical Communications*, vol. 49, no. 67, pp. 7391-3.

28. Thakur, S & Karak, N 2015, 'Alternative methods and nature-based reagents for the reduction of graphene oxide: A review', *Carbon*, vol. 94, pp. 224-42.

29. U.S. Geological Survey 2015, *Mineral commodity summaries 2015: U.S. Geological survey*, U.S. Department of the Interior, Reston, Virginia.

30. Bindl, DJ & Arnold, MS 2013, 'Efficient exciton relaxation and charge generation in nearly monochiral (7,5) carbon nanotube/C60 thin-film photovoltaics', *The Journal of Physical Chemistry C*.

31. Bindl, DJ, Shea, MJ & Arnold, MS 2013, 'Enhancing extraction of photogenerated excitons from semiconducting carbon nanotube films as photocurrent', *Chemical Physics*, vol. 413, no. 0, pp. 29-34.

32. Ramuz, MP, Vosgueritchian, M, Wei, P, Wang, C, Gao, Y, Wu, Y, Chen, Y & Bao, Z 2012, 'Evaluation of solution-processable carbon-based electrodes for all-carbon solar cells', *ACS Nano*, vol. 6, no. 11, pp. 10384-95.

33. Tune, DD & Shapter, JG 2013, 'The potential sunlight harvesting efficiency of carbon nanotube solar cells', *Energy & Environmental Science*, vol. 6, no. 9, pp. 2572-7.

34. Stapleton, AJ, Yambem, S, Johns, AH, Gibson, CT, Shearer, CJ, Ellis, AV, Shapter, JG, Andersson, GG, Quinton, JS, Burn, PL, Meredith, P & Lewis, DA 2015, 'Pathway to high throughput, low cost indium-free transparent electrodes', *Journal of Materials Chemistry A*, vol. 3, no. 26, pp. 13892-9.